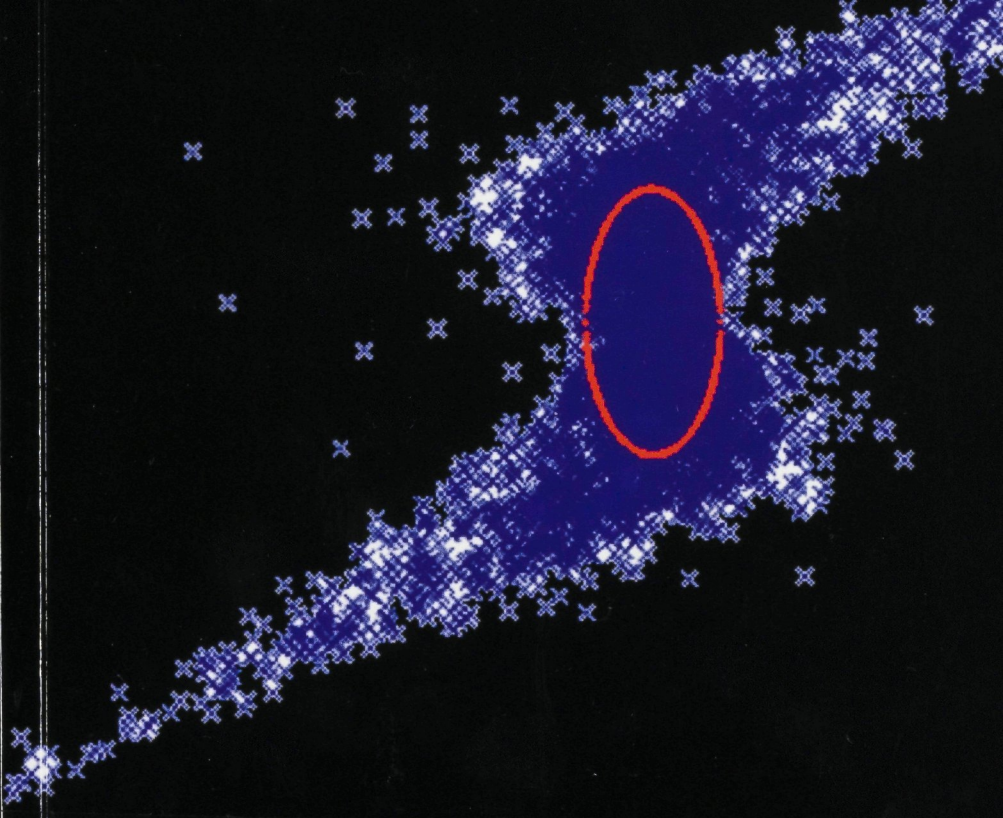

Ben Cook

Brightness Limitations In Sources For Static & Ultra-Fast High Resolution Electron Microscopy

Ben Cook

PhD Thesis
Date: 31st October 2013

Cover: The 50 percent emittance method from Chapter 9, figure 2.

BRIGHTNESS LIMITATIONS IN SOURCES FOR STATIC & ULTRA-FAST HIGH RESOLUTION ELECTRON MICROSCOPY

PROEFSCHRIFT

ter verkrijging van de graad van doctor
aan de Technische Universiteit Delft,
op gezag van de Rector Magnificus prof. ir. K.C.A.M. Luyben,
voorzitter van het College voor Promoties,

dinsdag 19 november 2013 om 15:00 uur

door

Benjamin John COOK

Master of Science
Imperial College of Science Technology and Medicine
University of London
geboren te Chesire, United Kingdom

Dit proefschrift is goedgekeurd door de promotor:
Prof. dr. ir. P. Kruit

Samenstelling promotiecommisie:

Rector Magnificus,	voorzitter
Prof. dr. ir. P. Kruit,	Technische Universiteit Delft, promotor
Prof. P. Hommelhof,	Friedrich Alexander University
Prof. dr. ir. O.J. Luiten,	Technische Universiteit Eindhoven
Prof. dr. ir. L.J. van Vliet,	Technische Universiteit Delft
Dr. C.W. Hagen,	Technische Universiteit Delft
G. Schwind,	FEI Company
Prof. dr. H.W. Zandbergen,	Technische Universiteit Delft, reservelid

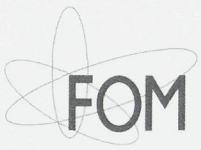

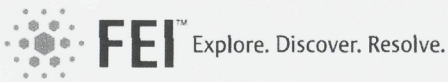

ISBN: 978-94-6191-975-5

Printed in The Netherlands

As I write, highly civilized human beings are flying overhead, trying to kill me

- George Orwell

Acknowledgments

There are of course many people to thank and if I miss anyone out then I'm sorry. First must be my parents who probably initiated my interest in science and encouraged me to pursue it. I want to thank Maria for understanding the time spent working on my thesis and not with her. The next people to thank are the academic staff in the Charged Particle Optics (CPO) group at Delft. Thanks to Pieter Kruit, Kees Hagen, Jacob Hoogenboom and the late Jim Barth for putting up with my disorganised working style, terrible writing and sometimes incredible stupidity. The technicians helped me a great deal, one of them Vladimir Kutchoukov was my roommate and perhaps he had it worst, thank you Vladimir for putting up with me. Carel Heerkens helped me to build my blanker chip and invested hours of time and patience in helping me, thanks! Jacques Nonhebel, built me a lot of things and helped with many electrical measurements and also has a very extensive bird database. Jan de Looff our vacuum technician was a man with some unique sayings and always very obliging until of course someone more attractive came along! Also Franz Berwald, Franz managed to keep out of most of my stupid projects, but he did advise me extremely well with regards to Belgium beers, and finally Han van der Linden who came along a little later. The three secretaries that helped me with my administrative turmoil Margaret van Fessem, Elly van der Most and Anjella van Vliet deserve medals! I also have to thank the people from FEI, Greg Schwind, Frank de Jong, and their teams in Eindhoven and Portland respectively they assisted with the project giving useful advice and assistance. Also helpful to my work on ultra-fast electron microscopy was the staff in Jom Luitens, group at Eindhoven university, Edgar Vredenbregt, Bas van der Geer ,Jom himself, and also Jom's PhD student Adam Lassie. I had two students who helped me with my work Musa Alaydrus who worked on single electron emission from a quantum dot, and Thomas Verduin who worked on Coulomb interactions and Schottky emission, and was co-author on two of my publications.

My friends and colleagues with whom I shared my experiences at Delft deserve also thanks, first Merijn Bronsgeest who helped me a lot at the start of my PhD and is co-author on one of my papers. The rest of my friends and colleagues who helped to make my life fun and enjoyable, in no particular order, Vincenzo Castaldo, Ali Gheidari, Aurélien Botman, David Jun, Alex Kostenko, Chris Post , Daan Van Oosten Slingeland , Willem van Dorp, Sander den Hoedt, Andries Effting, Anand Dokania, Thijs Hosman , Marco van der Heijden, Christian Zonnevylle and Nalan Liv, Angela Narváez Gonzalez, Sangeetha Hari, Ivan Lazić,

and Leon van Kouwen.

Ben Cook

Summary

Brightness Limitations In Sources For Static & Ultra-Fast High Resolution Electron Microscopy

Ben Cook

Electron sources suffer from fundamental limitations. These limit their brightness and increase their energy spread. This thesis starts with a general introduction and is then split into two parts. Part one looks at limitations for traditional static high resolution electron microscopy and part two focuses on the new field of ultra-fast electron microscopy. The conclusion and summary are again general bringing everything together. Chapter 1) is a straightforward introduction to some concepts of the thesis and briefly touches on some historical points.

Chapter 2 shows us how to calculate the brightness and energy spread of a combined photo, thermal and field emitter. These two properties are compared to experimental results and then compared to a more conventional Schottky emitter. Next in chapter 3 we look at the heating effects of photo excitation with a very simple analytical model. Chapter 4 takes a look at the influence of electron-electron interactions on a photo, thermal and field emitter in comparison to a Schottky emitter, and in chapter 5 we decided to try and find out what was the brightest source we could have (assuming limitations by statistical electron-electron interactions) and therefore examined the relationship between source size and maximum brightness of cold field emitters. Part I ends with chapter 6 which is an N-body simulation of electron-electron interactions for a cold field emitter gun to see whether the previous semi-analytical method we used is correct, along the way we also examine the influence of the energy spread for probe forming.

The second part starts with a in depth review of guns used for ultra-fast electron microscopy (chapter 7) we use simple metrics like brightness, energy spread, pulse charge and pulse length to discuss what type of imaging these guns could be used for and what they can not. Chapter 8 is an idea for using the existing and proved Schottky source for ultra-fast electron microscopy by adding an ultra-fast, and ultra small blanker. Finally (chapter 9) we look at using a photo field emitter for ultra-fast electron microscopy concentrating on how Poisson emission statistics can destroy brightness even at seemingly small currents.

The last chapter contains conclusions and a summary of the actual results.

Samenvatting

Gedistribueerd Regeling een Identificatie: een Ontleiding Benaderen

Ben Cook

Er zijn fundamentele grenzen aan de helderheid en energiespreiding van elektronenbronnen. Dit proefschrift beschrijft deze begrenzingen geldend voor traditionele, statische, hoge resolutie elektronen microscopie, en voor de recentelijk ontwikkelde ultrasnelle elektron microscopie. 1) introduceert de belangrijkste begrippen waarbij enkele historische ontwikkelingen kort worden besproken. In het eerste deel van I worden de bronnen besproken die gebruikt worden voor statische hoge resolutie elektronen microscopie. Het tweede deel is gewijd aan de bronnen voor ultrasnelle hoge resolutie elektronen microscopie. Hoofdstuk 2 beschrijft hoe de helderheid en energiespreiding voor een gecombineerde photo-, thermische- en veldemitter te berekenen zijn. Deze eigenschappen worden vergeleken met experimentele resultaten en met gegevens van de meer conventionele Schottky emitter. Hoofdstuk 3 beschrijft een eenvoudig analytisch model voor de opwarming die gepaard gaat met photo excitatie. Hoofdstuk 4 beschrijft de invloed van electron-electron interacties bij een gecombineerde photo- thermische- en veld emitter. Ook wordt de vergelijking gemaakt met een Schottky emitter. In hoofdstuk 5 proberen we te bepalen met welke bron de hoogste helderheid bereikt kan worden. Hiertoe wordt de relatie tussen bron grootte en maximale helderheid bij koude veld emitters besproken, rekening houdend met de statistische elektron-elektron interacties. Part Iwordt afgesloten met hoofdstuk chapter6waarin een N-body simulatie wordt besproken van elektron-elektron interacties in een koude veld emitter ter verificatie van de semi-analytische methode uit hoofdstuk 5 Het tweede deel van dit proefschrift begint met hoofdstuk (chapter 7) waarin een uitgebreid overzicht gegeven wordt van de bronnen die gebruikt worden voor ultrasnelle elektron microscopie. Aan de hand van eenvoudige karakteristieken als helderheid, energiespreiding, puls lading en puls lengte wordt besproken voor welke beeldvormende technieken deze bronnen wel en niet geschikt zijn. Chapter 8 beschrijft een concept hoe de beproefde Schottky bron geschikt te maken valt voor ultrasnelle elektron microscopie door toevoeging van een extreem snelle en extreem kleine blanker. In hoofdstuk (chapter 9) bekijken we hoe de Poisson verdeling van de emissie van photo-, veld emitters de helderheid al bij lage stroom sterk begrenst.

Het laatste hoofdstuk bevat de conclusies en een samenvatting van de resultaten.

Contents

1 CHAPTER

Introduction

Work is a necassary evil to be avoided

Mark Twain

I want this introduction to be accessible to everyone, so there are no equations (OK maybe one), and plenty of pictures, since I was once told "Physics is difficult enough, why make it harder". Thats not to say that this thesis is difficult, but there are enough formulas and theories in the next chapters. In the following introduction I will try to give an overview of what I think is interesting for the casual reader, and what can give a better understanding of the rest of this thesis.

1.1 Microscopy

In this introduction we will first talk about microscopy giving a quick overview of light and electron microscopy, as well as how that has developed from looking at photos to watching videos of atoms moving. Then I will explain a few concepts, which are important for electron sources namely, emittance, brightness, energy spread, and the physics of electron emission. Finally I will address what was the purpose of this thesis, in other words; what was the problem and how did we solve it.

1.1.1 Light Microscopes

Initially microscopes were simple with only a few small lenses because making clear glass was very difficult. One of the first microscopes shown in figure 1.1 was

by Delft born Antony van Leeuwenhoek [1]. The microscope was an improvement on previous work and he was able to examine for example bacteria from his mouth, the world of biology and materials has since started to open up.

In the 18th and 19th century microscopes started to become more familiar, although one is unlikely to find anything quite so ornate as those in figure 1.2 in the labs at Delft today.

The workings of all these microscopes are pretty similar. A microscope magnifies an object. It does that by using lenses as can be seen in figure 1.3 where a candle illuminates an object which is magnified and an image formed on the retina of the eye with many times magnification.

In the simple ray diagram of figure 1.3 one would imagine that we can go on magnifying indefinitely, but since light is a wave it diffracts, blurring the image. The best resolution we can hope to achieve is around half the wavelength, for visible light this means that two lines 250 nm apart would be seen as two lines, but below this they would appear as one.

1.1.2 Electron Microscopes

Bacteria and viruses can be even smaller than the 250 nm a light microscope can see, and atomic structure is some $1,000$ times smaller, therefore people try to use shorter and shorter wavelengths of light to perform imaging. Using shorter wavelengths of light (e.g X-rays) has many technical challenges, another alternative is to use electrons since they have a wavelength which is small enough to view atomic structure.

The concept of the electron microscope is exactly the same as the light microscope, and a schematic drawing is shown in figure 1.4 The glass lenses are replaced with magnetic or electric ones, the candle is replaced with an electron source and since the human eye is not sensitive to electrons the image is formed onto a screen, modern electron microscopes use a CCD camera directly and older models have a luminescent screen which can be viewed by eye. Finally the whole system must be run in vacuum since electrons interact with the air and can not travel even a mm. In figure 1.5 there are three TEMs which are on display at the Deutches Museum in Munich, at the base of each is what was nicked named the "Gold Fish Bowl", in this area the image was formed on the luminescent screen and could be viewed in more detail using binoculars (left picture) or a telescope (centre picture).

A Modern TEM shown in figure 1.6 has a resolution of well below one nm and can routinely examine the atomic structure of a material. Although as can be seen it still has the 'Gold Fish Bowl' with a set of binoculars, however the imaging can also be done using a camera connected to a computer.

Another form of electron microscope is called the Scanning Electron Microscope see figure 1.7, in this system the beam of electrons is focused to a fine point on the sample and then scanned, the primary electron beam interacts with the sample to create secondary electrons which are detected. The image is formed

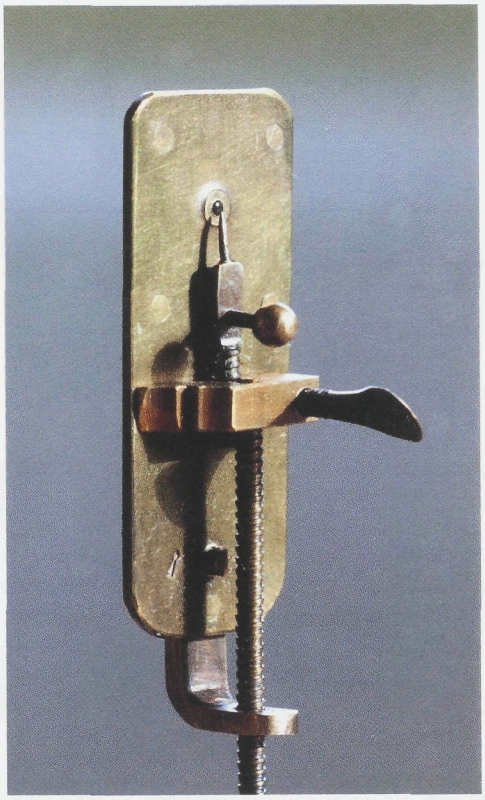

Figure 1.1: Improved microscope from Anton van Leeuwenhoek, need to reference this properly to wikipedia page

Figure 1.2: Examples of antique microscopes on display at the Deutsches in Munich

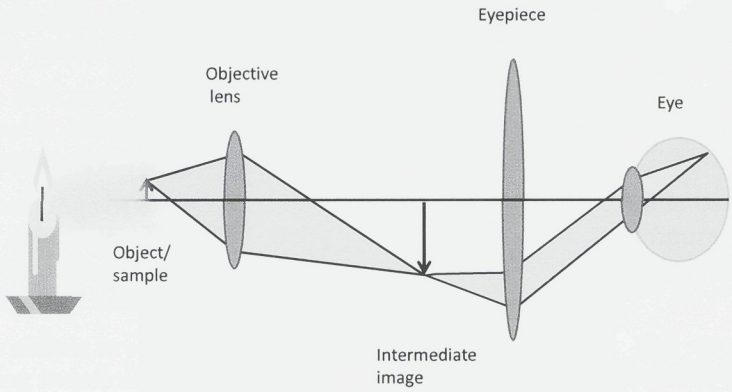

Figure 1.3: Simple ray diagram of a microscope

on a computer screen point by point. The SEM does not have atomic resolution (except in diffraction mode) but gets very close, it is however much easier to use than the TEM and much more versatile. This is the type of instrument I have used at Delft, and it is used as the basis for the ultra-fast blanker described in chapter 8.

1.1.3 Ultra-fast Electron Microscopy

All these instruments can make excellent pictures of static or slow moving things.

However don't move about slowly and we want to be able to understand how chemical reactions occur or how solids change to liquids. These things tend to happen in a few picoseconds, therefore ultra-fast microscopy was invented see figure 1.8. The big leap was the invention of reliable ultra-fast lasers which meant that the sample could be illuminated for only a few 100 fs. The sample must be made to do something first, and in figure 1.8 we assume that the red laser excites or pumps the sample to some new state, and the purple laser later interrogates or probes the sample to find out what that new state is. The sample replies with a green pulse and the signal can be recorded on the CCD camera. Unfortunately although the state of the atom can be recored its location remains unknown with the light microscope.

In Stanford they have taken the idea of ultra-fast light microscopy to a new level and have a microscope several miles long called the Linear Coherent Light Source LCLS. The LCLS generates an ultra-short laser pulse of X-rays with a few nm wavelength and can be used for recording the location of atoms on an ultra-fast timescale. This location however is only available as diffraction pattern, which can be interpreted as the average location of atoms.

Another approach for ultra-fast atomic imaging is to use an ultra-fast electron microscope. This is not several miles long and can fit into most labs, in fact many universities and research labs already have a normal electron microscope which

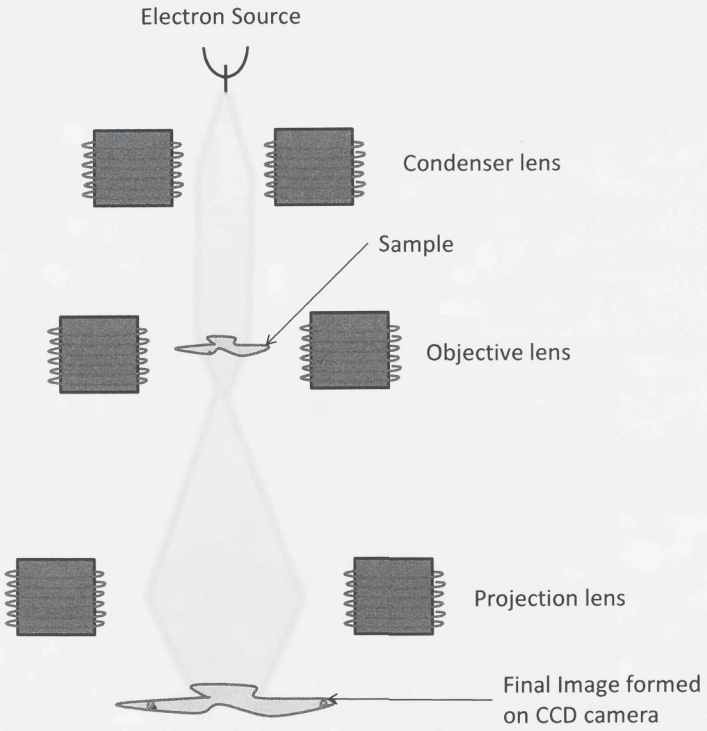

Figure 1.4: A schematic drawing of a Transmission Electron Microscope (TEM)

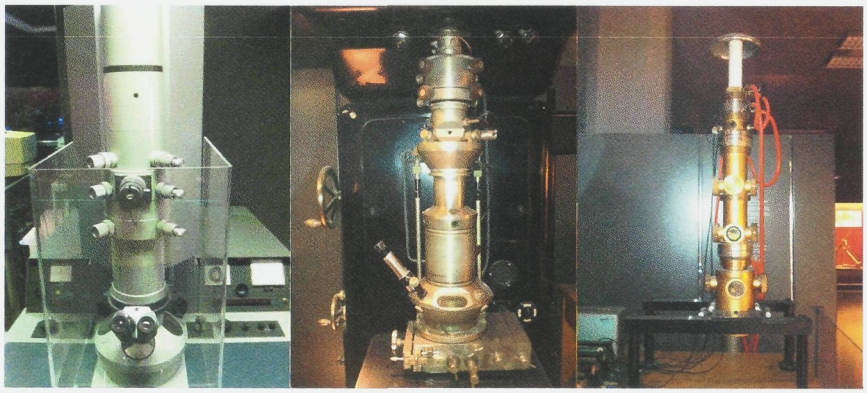

Figure 1.5: Vintage electron microscopes from the Deutsches Museum Munich

Figure 1.6: A modern TEM from FEI called Titan

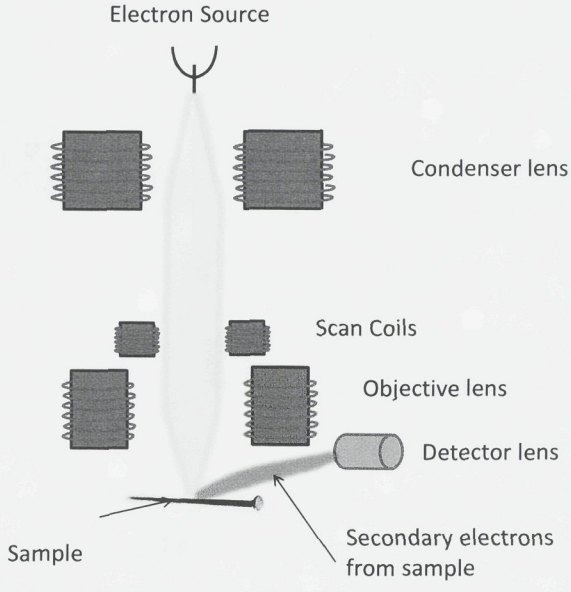

Figure 1.7: Cartoon of a Scanning Electron Microscope

could in comparison to the LCLS be quite simply modified to become an Ultra-fast Electron Microscope UFEM.

The UFEM is quite similar to its light equivalent, and is described in figure 1.10. The sample is pumped by an ultra-fast laser and then later after the sample has changed it is imaged by a pulsed electron source. The electron source is pulsed in this example because it is photo-excited by the purple laser.

With this method ultra-fast atomic images can be made in the lab with out a trip to California, appealing as that may be.

1.2 Electron Sources

The electron source is the most important part of an electron microscope and the phrase "rubbish in rubbish out" applies. Most electron sources are made of metal, some are made of semiconductors and there are of course many exotic materials used as well. Many electron microscopes use a Schottky electron source, shown in figure 1.11 this is a tungsten wire with a special Zirconium and oxygen coating

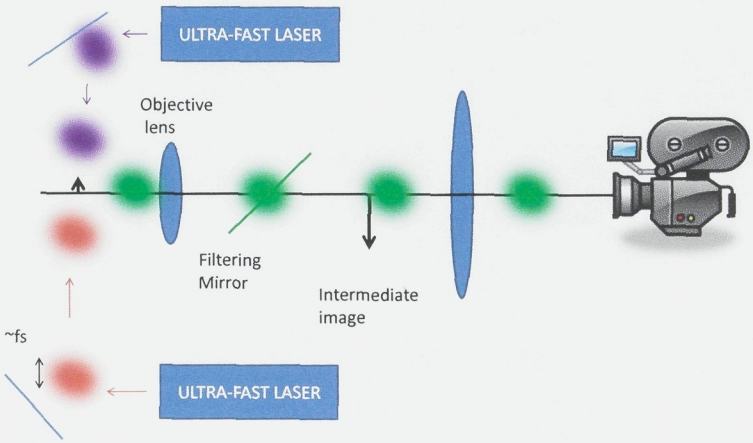

Figure 1.8: A diagram of an ultra-fast light microscope

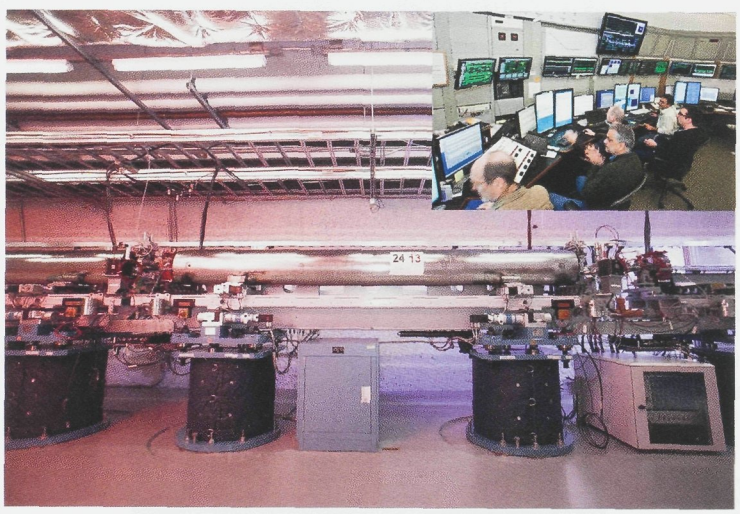

Figure 1.9: Main: A small section of the beam line at the LCLS. Inset: The control room housing part of the team of scientists and engineers required to run the complex machine

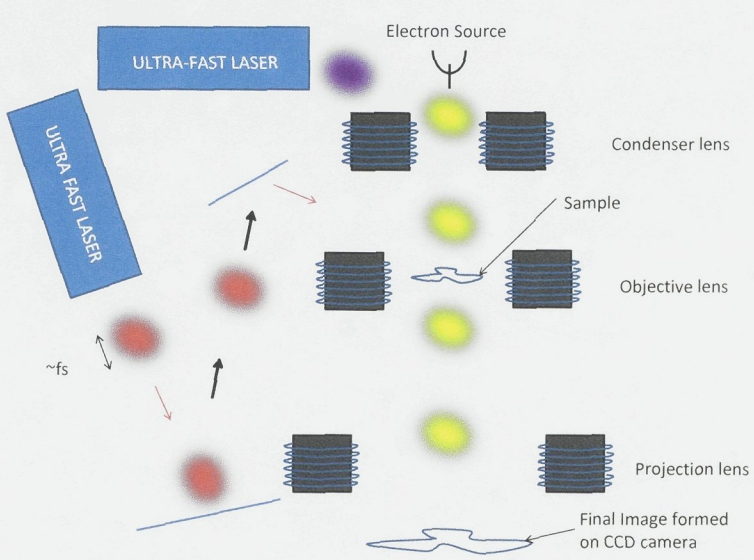

Figure 1.10: Schematic of Ultra Fast Electron Microscope (UFEM)

which helps to improve the emission properties. On the left of figure 1.11 there are two legs which are used to heat the Schottky source to around 1800K, and electrons are evaporated from the tip. At the sharp end of a Schottky source the tip radius is ≈ 200 nm, when the tip is in an electric field, field lines are concentrated around the tip. The strong electric field allows electrons to tunnel out of the metal. Therefore the Schottky source is sometimes called a thermal field emitter since it uses a combination of thermal and field emission. A fuller picture of this process is given in chapter 2.2, where we also examine a third important method of getting electrons from a material, photo emission. Photo emission is less used than the other methods for reasons that will be explored in this thesis. However photo emission is important for creating ultra-fast pulses.

1.2.1 Describing the Quality of an Electron Source

There are several parameters which describe the quality of an electron source, they are, emittance, reduced brightness, energy spread, stability and lifetime. The last two are reasonably self explanatory, but the first three deserve a little attention. For a more depth overview see section 7.2.

Emittance The emittance ϵ is a combination of how much the beam expands (the angle) and its size. Figure 1.12 shows three different electron sources, with source (a) all the electrons come from a single point (size=0) and therefore ϵ is 0, in source (b) the angle is 0 and again ϵ is 0. No source has $\epsilon = 0$, and source (c) is more realistic showing that because the electron source must have some size and some

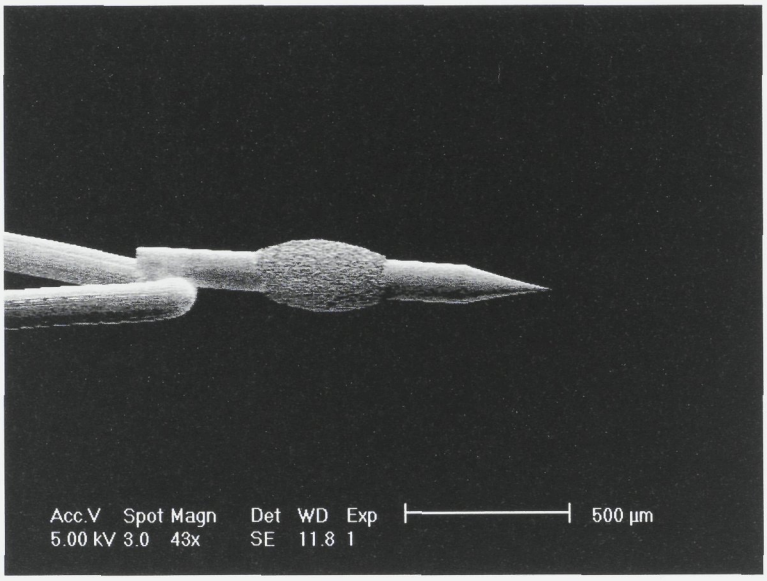

Figure 1.11: A ZrOx Schottky Source

angle the rays cannot be focused to a perfect spot. If no apertures are included in the optical system and the beam voltage remains constant then the emittance at the electron source is the same or worse at the specimen.

Reduced Brightness The reduced brightness B_r at the electron source is the same or worse at the specimen, regardless of whether the beam voltage (V) is changed or if the beam is apertured.

$$B_r = \frac{I}{\pi^2 \epsilon^2 V} \tag{1.1}$$

here I is the beam current. B_r is extremely useful since no matter the optical system you can immediately know its ultimate performance by knowing the B_r at the electron source. The calculation of B_r for the case of a combined thermal, field and photo emitter is discussed in chapter 2. Chapters 4, 5, 9 and 6 deal with the repulsive nature of the electron-electron interactions which cause B_r to be worsened.

Energy Spread The energy spread ΔE is a measure of the distribution of energies that the electrons have. Unless a filter or some time dependent optics are used the ΔE at the electron source is the same or worse at the specimen, regardless of whether the beam voltage (V) is changed or the beam is apertured.

A typical energy distribution is shown in figure 1.13, the yellow section represents the smallest width where 50 percent of the current is found, we call this

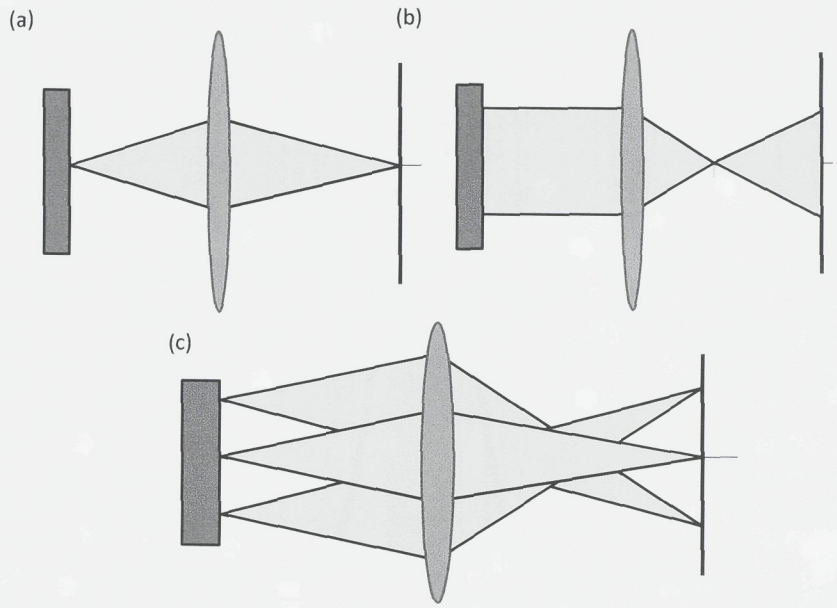

Figure 1.12: Each picture shows an electron source, and a focusing lens. (a) An Electron source which all electrons come from an infinitely small point (commonly called a point source). (b)An electron source where the electron have no angle, this is analogous to a laser beam (which actually does expand but with a very small angle). (c) A realistic electrons source with a finite source size and an angle.

the Full Width 50 or F50 for short. This is a good measure of ΔE since it gives two pieces of information, ΔE and the amount of current with ΔE. Measures such as the standard deviation or the full width at half the maximum may contain any amount of current.

1.3 Electron-electron interactions

Coulomb discovered that electrons repel each other, and this gets worse the closer they are together scaling with the inverse square of their separation. This might not be such a big problem if electrons came in well ordered distributions, but they escape from the electron source with Poisson statistics. We are taught in school that Poisson statistics explain why you will wait for a bus then two come along together. If two electrons "come along together" than they will repel each other more than if they were evenly spaced, some consequences of this for ultra-fast electrons sources are discussed in chapter 9.

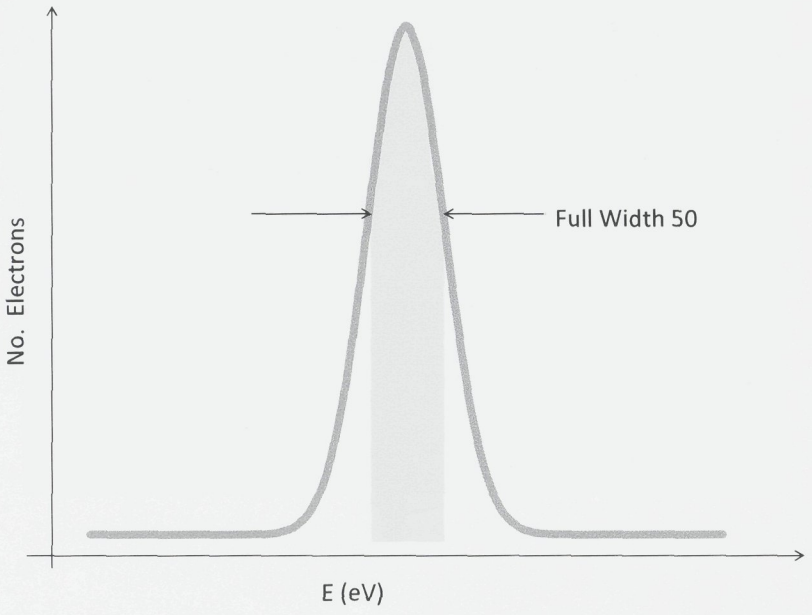

Figure 1.13: Energy Distribution

Electrons come out in a mess if they didn't their emittance would be 0 (see section 7.2), and when we try to squeeze them together with a lens the interactions between them grow. The interactions also cause the emittance to grow, and when it is bad enough it fundamentally limits the quality of an electron microscope.

There are no exact formulas to describe what happens when more than two particles collide, and we have to describe billions of them per second. We can use computer simulations with thousands of electrons till we get good statistics, or we can use some approximate formulas to predict what we think the blur will be. Chapters 4 and 5 discuss the applications of formula created by G Jansen [2] to electron sources, and chapter 6 compares them to computer simulations.

In the end it seems that the statistical Coulomb interactions are a fundamental limit to the reduced brightness of an electron source.

1.4 Historical events that made this thesis possible

In this section we will discuss the historical events which I believe made this thesis possible. Figure 1.14 gives a time line of important events

We start at the beginning of the century when Richardson first described the thermal emission of electrons from metal [3], for which he later received the Nobel

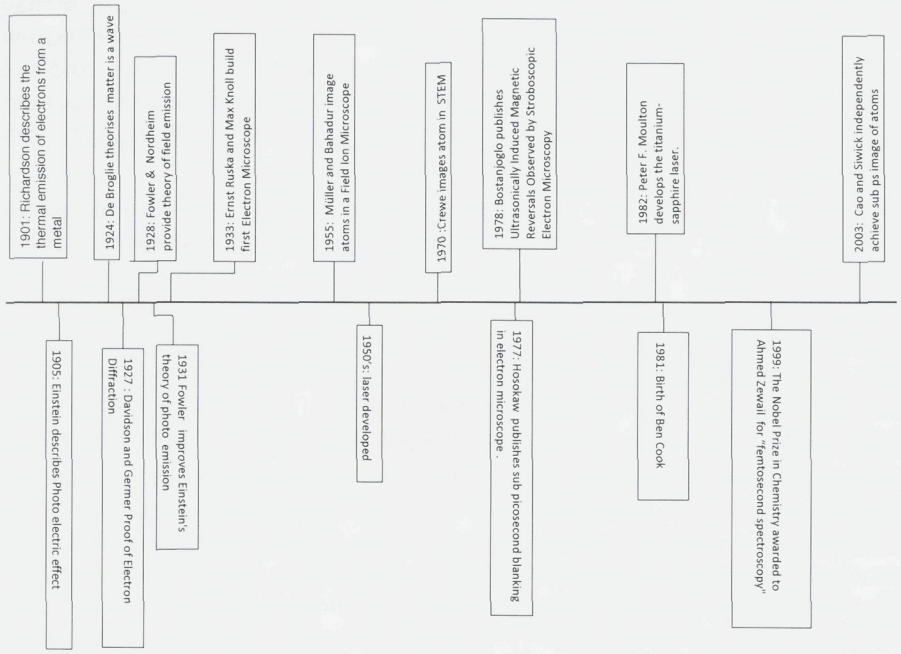

Figure 1.14: A time line of events I think were important for this thesis. (References can be found in the main text.)

prize in physics, this is really the basis of all the later forms of electron emission. It would be unthinkable not to include Einstein's work somewhere here, since without his work we would not understand photo emission, we would not have lasers, and relativistic effects on electrons would not be understood. The next big break through comes in 1924 when De Broglie theorized that matter is a wave [4], this lead the way for Fowler and Nordheim [5] to describe Field emission in 1928, only one year after Davidson and Germer [6] performed electron diffraction proving conclusively that electrons have a wavelike nature. Fowler than went on in 1931 to write a useful paper about photoemission from a metal [7] which is the basis of chapter 2.

In 1933 we get the first electron microscope designed and made by Ernst Ruska and Max Knoll [8], we might describe this as one of the first applications of the new science of free electrons.

In the next 20 years science was extremely busy for example improvements to the electron microscope were going on at Delft university with LePoole, and rather unfortunately we had a war and developed the atomic bomb. However the next important event for my thesis came in the 1950's with the invention of the laser and it's development during the 1950s which earned Charles H. Townes, Nikolay Basov, and Aleksandr Prokhorov the 1964 Nobel Prize in Physics.

In 1955 we enter the age of atomic imaging as Mueller and Bahadur manage to image individual atoms on a field ion microscope [9], and then in 1970 Crewe is able to image atoms in his STEM [10] (possibly because he used a cold field emitter). Crewe's achievement proved to be more useful since there are not many field ion microscopes in the world, but there is probably a TEM in every good university.

So now with the ability to visualize atoms we start to explore the fast and ultra-fast world. In the 70s there was interest in using very fast electron microscopes in the semiconductor industry. For this reason Hosokawa developed an SEM which could blank the beam by using an electric field to swing the electrons over a slit, in this way Hosokawa created sub picosecond bunches of electrons see papers [11] and [12]. A year later Bostanjoglo started to use a blanker which gave nanosecond pulses to look at things that were more interesting to physicists and material scientists, [13]. This is the start of ultra-fast electron microscopy.

1982 saw Peter Moulton of MITs Lincoln Laboratory develop the titanium-sapphire laser [14], this laser can easily generate short pulses in the picosecond and femtosecond ranges, with excellent power and there are many of them used routinely in research labs around the world. The titanium-sapphire laser really helped ultra-fast chemistry and ultra-fast light microscopes to become easy to use and opened up the field. In 1999 Ahmed Zewail received the Nobel prize for his work on chemical reactions using femtosecond light microscopes. Zewail then went on to build ultra-fast electron microscopes which made use of ultra-fast lasers to generate via the photo-electron effect sub picosecond bunches of electron. According to the time line of King et al in [15] the first ultra-fast atomic (diffraction) imaging was made by Cao [16] and Siwick [17] independently in 2003, not far behind however was Zewail with his publication [18] also in 2003.

1.5 Reasons For This Thesis

Initially the idea was to improve the B_r of a Schottky source for use in microscopy. Although higher B_r sources such as CFE already existed for around 100 years their stability has never really been good enough. We hopped that by combining a Schottky source with a laser we could improve its B_r. We theoretically proved that due to excessive heating this was a bad idea and along the way we came up with equations and a method of finding the B_r of a combined photo thermal and field emitter.

Whilst trying to find our way around the heating problem we decided to investigate the effect of electron-electron interactions on the system. This actually made everything even worse, and showed nicely that it is necessary to consider electron-electron interactions in gun design.

From the heating and electron-electron interactions we were lead to examine pulsed electron beams, and it seemed the most obvious place to use such a beam was ultra-fast electron microscopy. Since none existed we first made a comprehensive literature review of all the existing guns, and then from this decided that

the current solutions for UFEM where focused on high current and not resolution. We thought there were two possible solutions for high resolution UFEM, either an ultra-fast blanker, or a photo assisted cold field emitter with an ultra fast laser, we investigated both possibilities begining with the ultra-fast blanker.

We wanted a blanker which could easily be integrated into our SEM and would not deteriorate the beam. To do this we designed and built the first Giga Hertz frequency ultra-fast micro blanker. We were able to show numerically that it should produce pulses of around 400 fs with out affecting the beam quality.

Regarding the CFE with an ultra fast laser we knew that there where examples of this however there were no measurements of B_r and we suspected that electron-electron interactions would play a large role. Therefore we looked at how the number of electrons in an ultra-fast pulse alters the beam quality, finding that the optimum number of electrons in a pulse is 1 - depending of course to some extent on geometry. We also wondered what the maximum B_r of a cold field emitter was since in the literature claims had been made of B_r at the absolute quantum limit. We suspected electron-electron interactions would limit the emission long before the quantum limit, and after investigating various radii of tungsten CFEs we found this to be true, and further found that there is a worst case scenario for tip radius. Since this work was done semi-analytically we wanted to check this and so using a fully computational model we checked some points and found them to be good, and then examined how CFE's compare to thermal field emitters for low voltage electron microscopy where the energy spread of the emitter becomes important. Often a CFE is used because of their low energy spread however this might be lost by Coulomb interactions, we found that this is not the case and a CFE performs well for low voltage electron microscopy, when compared to a Schottky source.

Part I

Part 1- Electron Sources for Static Imaging

2 CHAPTER

Combining Photo, Thermal and Field Electron Emission

Work keeps at bay, three great evils – boredom, vice and need

Voltaire

Using a relatively simple model of photo emission we derive an expression for the reduced on axis brightness of a photo-thermal-field emitter. We then show that it is theoretically possible to reduce the energy spread of a Schottky (thermal field) emitter whilst increasing the reduced brightness. This can be achieved by illumination of the tip with high intensity laser light. We call the source PHAST - PHoto Assisted Schottky Tip. We find that due to the strong E-fields applied PHAST may operate at photon energies below the (Schottky reduced) work function, thus removing the need for UV lasers. We will show that it is in fact preferable to work in the red, or green. The necessary laser intensities probably limit the application to pulsed operation. *This chapter was published in Ultramicroscopy vol 109 issue 9 in April 2009 under the title Improving the energy spread and brightness of thermal-field (Schottky) emitters with PHAST–PHoto Assisted Schottky Tip.*

2.1 Introduction

The Schottky electron source (tungsten needle thermal-field emitter with a layer of ZrO_x see figure 2.1) is used for many SEMs, TEMs, Auger spectrometers and semiconductor inspection tools. Electron emission arises due to a combination of thermal and field effects. The ZrO_x lowers the work function of the tungsten

to about 2.9 eV. Schottky sources are normally operated at fields between 0.4-1.0 V/nm, provided by an extractor plate in front of the tip. A temperature of approximately 1800 K is obtained from resistive heating. Typical parameters are an ΔE of between 0.3-0.8 eV Full Width 50(FW50) and an experimentally measured reduced brightness B_r of ¿ 10^7 $Am^{-2}sr^{-1}V^{-1}$ [19]. The brightness B is a key concept in optics, it measures the current density per solid angle. Unfortunately B is not invariant to an accelerating /decelerating voltage so we use the brightness per volt, this quantity is called the Reduced Brightness. ΔE and B_r are limiting factors in many applications, and in many situations B_r and ΔE uniquely determine the amount of current that can be focused into a spot of a particular size [20], [21].

We intend to control ΔE and / or increase B_r by illuminating a Schottky tip with a laser. Thus making a "PHoto Assisted Schottky Tip" - PHAST.

In the rest of this paper we will first bring together Shimoyama's work [22] and the Fowler-Dubridge method [7] [23] [24] to derive equations for the reduced brightness of a photo emitter. This will be the main topic of section 2.2.1 but it will also include current density calculations which are useful when comparing theory to experiment. Section 2.2.2 will give an equation to find the ΔE. In section 2.2.3 we will discuss the Fowler Dubridge method and what we call Fowler's approximation. Section 2.2.4 gives a short overview on how we deal with the transmission coefficient, and section 2.2.5 is on scattering in metals. Section (2.3.1) will include a comparison of our theory to experimental and analytical results. In section 2.3.2 we will use our model to show that PHAST can improve B_r and ΔE of a Schottky emitter. Finally we will have a discussion about the usefulness of PHAST and make some conclusions.

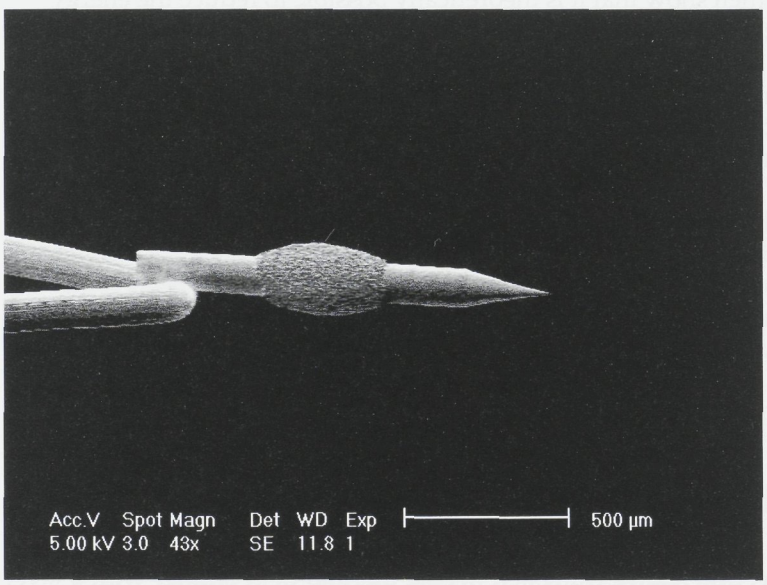

Figure 2.1: *Electron microscope picture of a standard Schottky tip, the lump is the ZrO_x reservoir. The legs are for heating.*

2.2 Introduction To PHAST

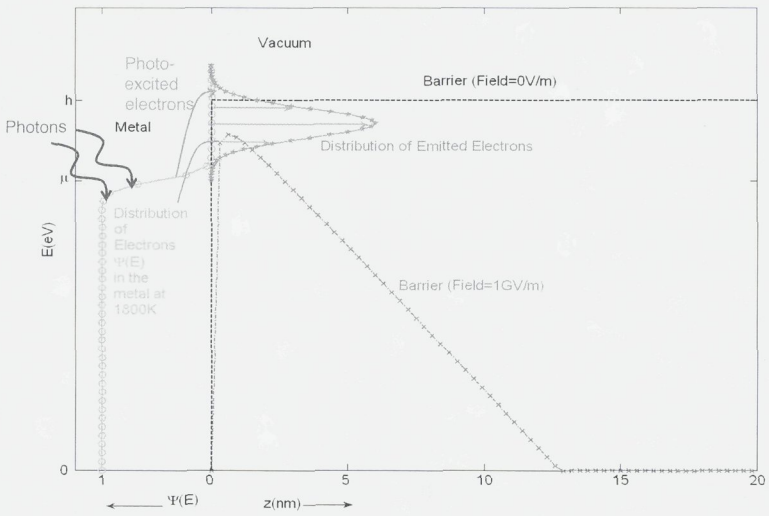

Figure 2.2: Schematic of the emission processes contributing to PHAST. The dashed and x marked lines show how the barrier shape changes with the introduction of a strong E-field, this allows tunneling to occur. In the case of a Schottky emitter the tunneling is mainly from thermal electrons as the field is not strong enough to allow significant tunneling from around μ (the electron chemical potential). With PHAST we have the addition of photons which excite electrons from lower levels to (if available) an energy level $h\nu$ higher. These excited electrons have the possibility to escape either directly, or by tunneling through the barrier. If the electrons are already thermally excited and are subsequently excited by a photon, and escape, then they become thermal photo-(field) emitted electrons. The distribution of emitted electrons for PHAST is shown with the line marked with *s.

The basic concepts of PHAST emission are schematically shown in figure 2.2. For most cathodes electrons can escape by any of three basic processes; thermal emission over the top of the barrier (see fig. 2.2), field emission by tunneling through the barrier, or photo-emission, where an electron interacts directly with a photon and escapes over the barrier. In the present situation we have a strong field, a high temperature and a focused laser beam applied to the tungsten tip of fig 2.1. This means that we can have emission by combination of any of the three previously mentioned inputs.

(1) The strong field, will act to lower the barrier height from height h (0 field barrier height) (see fig. 2.2), this is the Schottky effect [25]). The barrier shape changes as shown in fig. 2.2 for a field strength of 1 GV/m. If the field is strong enough the barrier will become thin enough for electrons to tunnel through.

(2) The high temperature changes the energy distribution of the electrons giving it a long tail at higher energies. Some of the electrons in the tail will have an energy above the barrier height and can then escape. This may be assisted by the Schottky effect, which will reduce the temperature required for a particular current. Thermally excited electrons may also tunnel through the top of the barrier where it is thin enough.

(3) The focused laser beam (ignoring any thermal aspects) will promote electrons to higher energy levels. The electrons can then do one of three things: (i) escape directly (ii) escape in combination with their prior thermal energy (iii) they may be photo excited and then if there is sufficient field, tunnel.

We want to use the three inputs to maximise the output of PHAST for the highest brightness and lowest ΔE.

We will need equations to describe B_r, ΔE. We will also want equations for the quantum efficiency / current density so that we can compare our model to experimental results. For thermal-field emission these are well documented in textbooks and in the literature, see for example [26] and [27]. Photo-emission literature is often based on the Fowler-Dubridge model [7], [23]. With this we may calculate ΔEs, and currents or quantum efficiencies and even account for multi-photon excitation [28]. However up to now the Fowler-Dubridge model does not include a method of finding B_r. This is what we will now do.

2.2.1 Brightness

To derive an expression for B_r from a photo emission source we will start by looking at the work of Shimoyama [22]. We will follow part of his derivation of B for a thermal-field emitter. Then we will combine Shimoyama's work with Jensen's work on photo(field) cathodes (see for example [24]).

According to Shimoyama [22] to derive a complete (at every point in space) expression for B, we must ray trace the emitted electrons. The full expression for brightness is shown in eq. 2.1 and illustrated in fig. 2.3.

$$B(r,\theta) = \frac{d^2I(r,\theta)}{d\Omega dS cos\theta} \tag{2.1}$$

Here r and θ refer to coordinates on a cylindrical coordinate system, d^2I is the current, dS a cathode surface element, $d\Omega$ is the solid angle element, and θ the angle normal to dS. For some cases, analytical solutions can be found to eq. 2.1, but not in general, we therefore seek alternatives. In electron optics the maximum brightness is often used, or using the terminology of Shimoyama, the axial brightness B_0 - the brightness on the axis in the axial direction. We however will drop

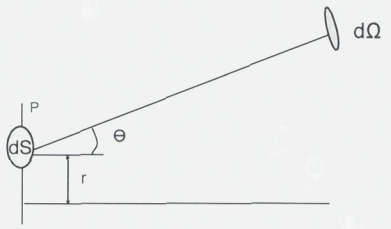

Figure 2.3: An Illustration to help with the definition of optical brightness, please see main text for explanation.

the subscript $_0$ and just use B. So ρ and θ become zero and we assume a uniform current distribution and replace I/dA with J the current density.

$$B = \frac{dJ}{d\Omega} \tag{2.2}$$

But we would like to have B_r i.e the brightness per volt B_0/V.

$$B_r = \frac{dJ}{d\Omega V} \tag{2.3}$$

We will now find the on axis(maximum) reduced brightness of PHAST, starting from an expression for the non-reduced on axis brightness; eq. (15) in [22] which is in general valid,

$$B = \frac{e^2}{\pi}\Phi^* \int_{-\infty}^{\infty} N(E_n, E_t = 0)dE_n \tag{2.4}$$

here Φ^* is the relativistically corrected accelerating voltage, $N(E_n, E_t = 0)$ is the energy distribution at 0 tangential energy (E_t). E_n is the energy of the electron normal to the cathode surface. This may also be written as

$$B = \frac{e^2}{\pi}\Phi^* N(E_t = 0) \tag{2.5}$$

where $N(E_t = 0)$ is the emitted energy distribution at 0 tangential energy. The tangential energy distribution of the emitted electrons is simply

$$N(E_t) = \int_{-\infty}^{\infty} N(E_n, E_t)dE_n \tag{2.6}$$

We now skip to section 5 in Shimoyama [22] and eq. (24) where the expression for the emitted tangential energy distribution $N(E_t)$ is given for thermal field emission as:

$$N(E_t)dE_t = dE_t \int_{-\infty}^{\infty} P(E_n, E_t)D(E_n)dE_n \tag{2.7}$$

where

$$P(E_n, E_t) = \frac{A}{ek^2}\left[1 + exp(\frac{E_n + E_t + \phi_w}{kT})\right]^{-1} \tag{2.8}$$

Here $D(E_n)$ is the transmission factor(an analytical approximation is given by Shimoyama and a numerical method is described here in section 2.2.4). P is a 2D thermal supply function, with $A = \frac{4\pi mek^2}{h^3}$,$e$ is the elementary positive charge m is the electron mass in free space, k is Boltzmann's constant, h is Planck's constant. T is the thermodynamic temperature. ϕ_w is the energy gap between the zero energy point and the chemical potential. Shimoyama defines the zero energy point as the energy of an electron at an infinite distance from the metal with 0 field. In the energy scale shown in fig. 2.2 this would be the barrier height h. In fig. 2.2 ϕ_w is $h - \mu$ where μ is the chemical potential (We neglect the temperature dependence of μ and assume $\mu = \mu(T = 0K)$). Now with our expression for P substituted in equation 2.5 we may write down an expression for the reduced on axis brightness of a thermal field emitter as

$$B_{rtf} = \frac{e^2}{\pi}\int_0^{\infty} P(E_n, E_t = 0)D(E_n)dE_n \tag{2.9}$$

We are now ready to combine the expression of Shimoyama for the axial brightness with Jensen's work on photo cathodes. We want eq. 2.9 in the presence of photons.

Jensen works with the same energy scale as fig. 2.2 so we must convert Shimoyama's scale to fig. 2.2 so we can have an equivalent expression for the reduced on axis brightness. We begin with the 2D thermal supply which function becomes

$$Q(E_n, E_t) = \frac{A}{ek^2}\left[1 + exp(\frac{E_n + E_t - \mu}{kT})\right]^{-1} \tag{2.10}$$

Where for clarity we have used the new variable Q. The new transmission coefficient becomes $D'(E_n)$= $D(E_n - h)$. Now eq. 2.7 (again using a new variable M instead of N becomes

$$M(E_t)dE_t = dE_t \int_0^{\infty} Q(E_n, E_t)D'(E_n)dE_n \tag{2.11}$$

Now eq. 2.9 becomes

$$Brtf = \frac{e^2}{\pi}\int_0^\infty M(E_t = 0)dE_t = \frac{e^2}{\pi}\int_0^\infty Q(E_n, E_t = 0)D'(E_n)dE_n \tag{2.12}$$

We may now note that if we carry out the integration of $M(E_t)$ in eq. 2.11 with respect to E_t over all energies we would end up with an expression for the flux of emitted thermal field electrons, more precisely for flux we mean the number of thermal field emitted electrons per second per metre squared. Multiplying this flux by e gives the current density.

$$J_{tf} = e\int_0^\infty M(E_t)dE_t = e\int_0^\infty\int_0^\infty Q(E_n, E_t)D'(E_n)dE_n dE_t \tag{2.13}$$

As a side note Eq. 2.5 for the reduced on axis brightness can be re-writen in the form used by Fransen [29],

$$B'_0 = \frac{e}{\pi}\frac{dJ}{dE_t}|_{E_t=0} \tag{2.14}$$

Now linking to Jensen we find that integrating Q over E_t we will end up with (excluding some pre-factors which will in any case cancel out) what Jensen refers to as the 1D supply function.

$$F(E_n) = \frac{A}{k}T\ln\left(1 + \exp\left[\frac{(\mu - E_n)}{kT}\right]\right) \tag{2.15}$$

In [30] he writes this as

$$f(E) = \frac{m\pi}{\beta\hbar^2}\ln\left(1 + \exp\left(\mu - E(k)\right)\beta\right) \tag{2.16}$$

And in eq. (47) of [31] in a form closer to that derived here. Jensen uses β to represent $\frac{1}{kT}$ and E (as a function of the quantum wave number k not Boltzmann's constant) is our E_n.

We now need to combine Shimoyama and Jensen. We want to find the brightness in the presence of photons. So we will need an expression for $M(E_t = 0)$ (the tangential ΔE at zero tangential energy) when illuminated by a laser. To include laser illumination we need some idea about the quantum efficiency, which relates laser intensity at the cathode to the emitted current density in the following way:

$$J = \frac{(1 - R)Ie}{h\nu}\gamma \tag{2.17}$$

Where R is the reflectivity of the cathode, I is the laser intensity (not to be confused with the current of eq. 2.31), and γ is the quantum efficiency. In [30] Jensen tells us that based on the Fowler Dubridge method [7], [23] (see section

2.2.3 of this thesis for a discussion of this) the quantum efficiency of a photo cathode is the number of emitted electrons per absorbed photon and he gives this as (equation 4 of [30]),

$$QE = \frac{\int_0^W \left(\int_0^\infty f(E) D'(E + h\nu) dE \right) \exp((\frac{-\rho}{\rho_0})^2) \rho d\rho}{\int_0^W \left(\int_0^\infty f(E) dE \right) \exp((\frac{-\rho}{\rho_0})^2) \rho d\rho} \tag{2.18}$$

W, ρ, and ρ_0 are factors introduced from the geometry of the cathode and the distribution of the laser beam. In our simple model we work on the assumption of a semi-infinite plane cathode, and a uniform laser beam so the integrals over $d\rho$ and all terms with ρ in can be replaced by current densities and laser intensities. For a first approximation of a photo-emitter this simplification will tell us roughly what laser powers are needed, further in microscopy we aperture the beam, and thus see only a fraction (10's of nm) over this area the laser beams intensity will be relatively constant.

We are almost ready to use this expression for the quantum efficiency to calculate our total current density for PHAST. First we need to include the scattering of the electron on the way to the surface of the cathode. We do this in a slightly different and more simple manner than Jensen who discusses his method in [24]. We include the scattering term $S(E_n)$ in the upper integral of eq. 2.18, so we define the quantum efficiency with γ and write,

$$\gamma = \frac{\int_0^\infty S(E_n) F(E_n) D'(E_n + h\nu) dE_n}{\int_0^\infty F(E_n) dE_n} \tag{2.19}$$

The scattering term S is discussed later in section 2.2.5. Jensen, also states that photo emission current simply adds to the thermal field current [32]. So now we may write an expression for total the current density from PHAST using $F(E_n)$ instead of $f(E_n)$,

$$J_{PHAST} = J_{tf} + \frac{I(1 - R(h\nu))e}{h\nu} \frac{\int_0^\infty S(E_n) F(E_n) D'(E_n + h\nu) dE_n}{\int_0^\infty F(E_n) dE_n} \tag{2.20}$$

We would like to make the form of the equation more clear, so will rewrite it.

$$J_{PHAST} = J_{tf} + \kappa \int_0^\infty S(E_n) F(E_n) D'(E_n + h\nu) dE_n \tag{2.21}$$

$$\kappa = \frac{I(1-R(h\nu))e}{h\nu} \frac{1}{\int_0^\infty F(E_n)dE_n} \tag{2.22}$$

We may think of κ as a correction or scaling factor for photo-emission where the integral in the denominator is the maximum current available from all the electrons in the metal, and the remaining terms represent the total charge which the photons have interacted with, or the number of photons absorbed by the metal multiplied by eZ. With this in mind it follows from eq. 2.13 that,

$$J_{PHAST} = J_{tf} + \kappa \int_0^\infty \int_0^\infty S(E_n)Q(En, Et)D'(E_n + h\nu)dE_n dE_t \tag{2.23}$$

and so the reduced axial photo brightness $B_{rph} = \frac{e}{\pi}\frac{dJ_{ph}}{dE_t}|_{E_t=0}$ is

$$B_{rph} = \frac{e}{\pi}\kappa \int_0^\infty S(E_n)Q(E_n, E_t = 0)D'(E_n + h\nu)dE_n \tag{2.24}$$

and

$$B_{rPHAST} = B_{rph} + B_{rtf} \tag{2.25}$$

The reduced on axis brightness is widely used in microscopy for thermal and field emission, and so the expression works well as a source comparator.

Let's see how our PHAST emitter compares with a standard Schottky tip. If we define brightness efficiency as $\frac{B_r}{J}$, then we find that a photo-emitter is less efficient than a thermal field emitter operating at 1800K (The manufactures recommend operating temperature for our Schottky tip), this is illustrated in fig. 2.4. We see that $\frac{B_{rPHAST}}{J_{PHAST}}$ decreases with increasing photon energy, and for sub-threshold photon energy the reduced on axis brightness is equivalent to a thermal-field emitter $B_{rtf} = \frac{eJ}{\pi kT}$ [22] (if tunneling can be ignored). This result and an expression for the brightness with zero field and zero temperature will be derived. We start with the sub-threshold photo-emission (with zero field) here electrons escape only by a combination of thermal energy and photo excitement. We will begin by adopting Shimoyama's notation, and energy scale (which will prove easier here). With $E + \phi_w$ large compared to kt, we may write eq. 2.8 as

$$P^* = \frac{A}{ek^2} \exp\left(-\frac{E_n + E_t + \phi_w}{kT}\right) \tag{2.26}$$

Now if we may neglect quantum mechanical effects, assume an averaged scattering factor $\overline{S}$, ande a step like barrier function of height $h = \phi_W + \mu$, then for sub threshold 0 field, photo emission we can write,

$$J^* = \kappa\overline{S} \int_0^\infty \int_0^\infty \frac{A}{k^2} \exp\left(-\frac{E_n + E_t + \phi_w - h\nu}{kT}\right) dE_n dE_t \tag{2.27}$$

Where we have moved the effect of the photon to act directly on the work function ϕ_w. This makes the derivation more clearly follow that of the thermal field derivation.

$$J^* = \eta \overline{S} A T^2 \exp\left(\frac{\phi_w - h\nu}{kT}\right) \tag{2.28}$$

and the reduced on axis brightness B^*_{rph} will be with $E_t = 0$

$$B^*_{rph} = \eta \overline{S} \int_0^\infty \frac{e}{\pi}\frac{A}{k^2} \exp\left(\frac{E_n + \phi_w - h\nu}{kT}\right) dE_n \tag{2.29}$$

$$B^*_{rph} = \eta \overline{S} \frac{e}{\pi} A \frac{kT}{k^2} \exp\left(\frac{\phi_w - h\nu}{kT}\right) \tag{2.30}$$

finally we see that

$$B^*_{rph} = \frac{eJ^*}{(\pi kT)} \tag{2.31}$$

Now for the 0 temperature, 0 field photo-emission. We will start with the expression for the current density eq. 2.20. As T=0 and E=0 there is no thermal field current so $J_{tf} = 0$ and again we use $\overline{S}$. We can then write,

$$J_{T=0} = \left[\frac{I(1 - R(h\nu))\overline{S}e}{h\nu}\right] \frac{\int_{(\phi_W + \mu - h\nu)}^{\mu} (\mu - E_n) dEn}{\int_0^{\mu} (\mu - E_n) dEn} \tag{2.32}$$

Integrating gives us,

$$J_{T=0} = \left[\frac{I(1 - R(h\nu))\overline{S}e}{h\nu}\right] \frac{(h\nu - \phi)^2}{\mu^2} \tag{2.33}$$

Now for the reduced on axis brightness we may write

$$B_{rphT=0} = \left[\frac{I(1 - R(h\nu))\overline{S}e}{h\nu}\right] \frac{e \int_{(\phi_W + \mu - h\nu)}^{\mu} (1) dEn}{\pi \int_0^{\mu} (\mu - E_n) dEn} \tag{2.34}$$

integrating once more leads to,

$$B_{rphT=0} = \left[\frac{I(1 - R(h\nu))\overline{S}e}{h\nu}\right] \frac{e(h\nu - \phi_W)}{\pi\mu^2} \tag{2.35}$$

It is normal to relate the expression back to the current density J,

$$B_{rphT=0} \frac{e(J)}{\pi(h\nu - \phi_W)} \tag{2.36}$$

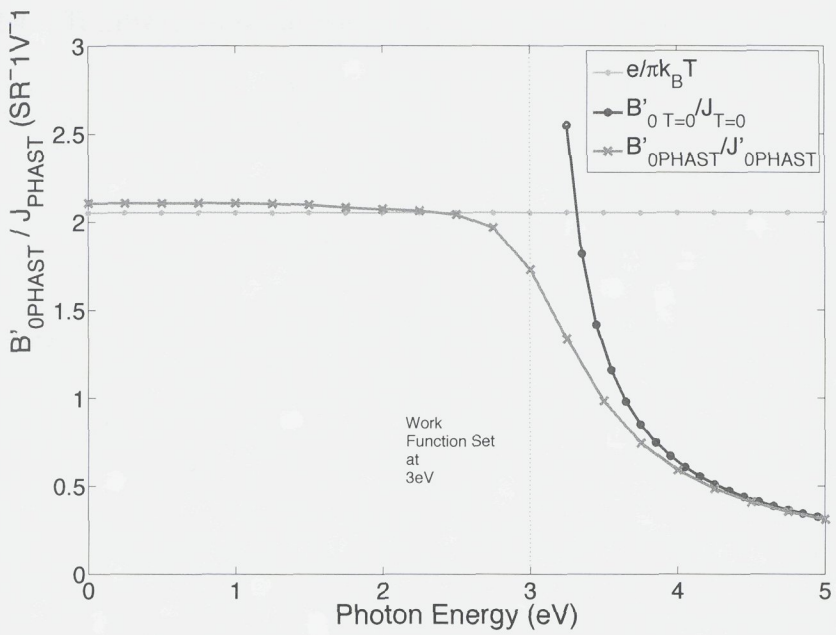

Figure 2.4: Reduced on axis brightness (B_{rPHAST}) divided by current density (J_{PHAST}) vs photon energy (red with x markers) and for comparison $\frac{e}{\pi kT}$ which if multiplied by J_{tf} gives the reduced on axis brightness of a (low field) thermal emitter. The two lines do not quite match because of numerical inaccuracies and the approximation of eq. 2.26. The third line (blue with circle markers) is for cold photo emission and so we see this form dominates for high photo energies. For low photon energies $B_{rphT=0}/J_{0T=0}$ tends toward infinity, but for any situation where a reasonable amount of current is produced it is below the line of $\frac{e}{\pi kT}$. $T = 1800K$

Eqs. 2.31 and 2.36 are shown in fig. 2.4 and compared to a numerical calculation with 0 field, at a temperature of 1800K. We see that for photon energies less than ϕ_W the reduced on axis brightness follows that of a thermal emitter, and for photon energies sufficiently over threshold it follows equation 2.36.

2.2.2 Energy Spread

We have still not considered the ΔE. This can be calculated by consideration of a total energy distribution, the end results matches closely with Dubridge's [23] exact expression for the distribution of photo excited electrons using a step barrier function. We will simply quote the result because the derivation is so similar to the one for the brightness and well documented for thermal field emission see for

example [27] (also used in a similar way for photon emission in [33]).

$$\frac{dJ_{tf}}{dE} = \eta \frac{A}{k^2} S(E) \left[1 + exp(\frac{E-\mu}{kT})\right]^{-1} \int_0^E D'(E_n) dEn \tag{2.37}$$

and for photo emission this will be,

$$\frac{dJ_{ph}}{dE} = \frac{I(1-R(h\nu))e}{h\nu} \eta \frac{A}{k^2} S(E) \left[1 + exp(\frac{E-\mu}{kT})\right]^{-1} \int_0^E D'(E_n + h\nu) dEn \tag{2.38}$$

Where we use E to describe the total energy of the electron. The problem with this is that the location of the emitted electrons will not be correct in comparison with the thermal field electrons. The solution to this is to shift the supply function (instead of shifting the transmission coefficient to lower energies) to higher energy and so we get

$$\frac{dJ_{ph}}{dE} = \eta \frac{A}{k^2} S(E) \left[1 + exp(\frac{E-(mu+h\nu)}{kT})\right]^{-1} \int_0^E D'(E_n) dEn \tag{2.39}$$

finally the two terms can be added,

$$\frac{dJ_{PHAST}}{dE} = \frac{dJ_{tf}}{dE} + \frac{dJ_{ph}}{dE} \tag{2.40}$$

2.2.3 The Fowler Dubridge Model and Fowler's Approximation

Fowler suggested an approximation for near threshold emission where E' equals the barrier height. Allow the photon's energy to add only to the E_n component, $E'_n = E_n + h\nu$. This is reasonable, since $E' = E'_t + E'_n$, so at threshold E'_t must be zero to allow emission. This is what we shall call Fowler's Approximation. Fowler did not include field emission in his original paper, so he used a step like barrier, $D'(E_n + h\nu) = 0$ $E_n < h$ and $D'(E_n + h\nu) = 1$ $E_n > h$ which can be easily taken account of with integration limits. Jensen takes account of the photon energy with a transmission co-efficient so we can include field emission. Fowler's approximation is validated and used countless times in the literature for example [7] [23] [34] [35] [36] [37]. As well as in this paper, see figs. 2.8, 2.9 and 2.10.

A better theory would be for the photons energy to add to the total energy of the electron, $E' = E + h\nu$ but we are not aware of this leading to an easily manipulated form. Fowler was the first to create a successful theory of photo emission [7] with an analytical form that could be easily applied. He was interested in a theory which could deal with the 'thermal tails' which made determining work functions from photo emission data difficult.

It is worth noting that our expression for the reduced on axis brightness does not suffer from Fowler's approximation. E_t must be zero, so E'_t must also be zero, and $E' = E'_n = E_n + h\nu$.

2.2.4 Transmission Factor

To find $D(E_n)$ we assume a uniform field electric field E is applied at the cathode surface and then consider the potential of an image charge to find the barrier potential $V(z)$ the result is given in equation 2.41 (see [26]).

$$V(z) = \mu + \phi_W - \frac{e^2}{16\pi\epsilon_0 z} - Eze \tag{2.41}$$

Where ϕ_W is the zero field barrier height, E is the field strength and ϵ_0 is the permittivity of free space. Eq. 2.41 is taken only for positive values of $V(z)$ and is zero everywhere else see fig. 2.5.

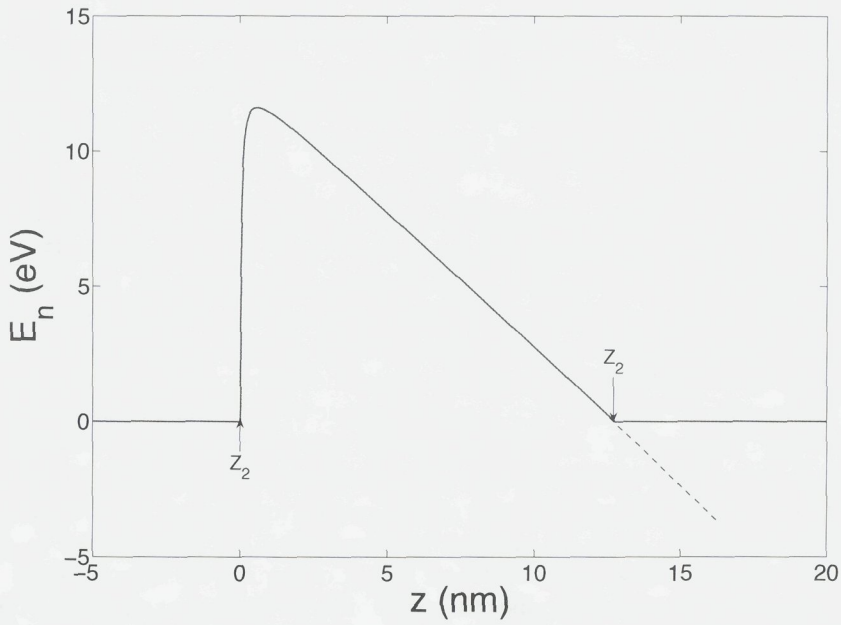

Figure 2.5: Potential energy barrier for calculating transmission coefficient $D(E_n)$ calculated from eq. 2.41. Zero is taken as the lowest energy level in the conduction band of the metal. The dotted line shows the true potential which continues to decline toward the anode.

Now we may solve the Schrödinger equation as on both sides at z_1 and z_2 there is zero potential. We end up with a wave function ψ made up of three waves/components:

$$\begin{aligned} \psi(z) &= C_1 \exp ik_z z + C_2 \exp(-ik_z z) \quad for\ z < z_1 \\ \psi(z) &= C_3 \exp(ik_z z) \quad for\ z > z_2 \end{aligned} \tag{2.42}$$

Where C_1 and C_2 are the amplitudes of the electron waves traveling left and traveling right inside the metal, and C_3 is the amplitude of the electron wave in the vacuum at zero potential. Using a 4th order Runge Kutta method we step through the barrier from right to left and solve to obtain eq. 2.43

$$D(E_n) = \left| \frac{C_3}{C_1} \right|^2 \tag{2.43}$$

Now we may find J_{tf} at a range of fields and temperatures. J_{tf} has been plotted in fig. 2.6 where we can see how it compares to its analytical counterparts, and in fig. 2.7 where we can see how it compares to experimental data. However to calculate the photocurrent J_{ph} we must first consider the scattering.

2.2.5 Scattering

The previous section would be sufficient for calculating emission from a metal if the photoelectric effect was purely a surface phenomenon, which would mean no scattering, since this is not the case we must include a scattering term which is now discussed.

Although there is plenty of data on mean free paths and escape depths of electrons for the energy range 50eV and above, below 50eV the data is sparse. Thus we use tabulated values of the thermal conductivity and infer the mean free path (λ_e) from this [38]. In our case we are mainly interested in electrons close to threshold and thus we again make the approximation that the electrons only travel the perpendicular distance to the surface. We also make the assumption that one collision is enough to prevent escape which is probably true at such low photon energies. The probability of an electron being transported to the surface is governed by the following exponential decay law $exp(-\frac{x}{\lambda_e(E_n)})$ where x is the distance to the surface in the normal direction. This must also be related to the absorption depth δ of the light (again governed by an exponential decay law). δ is a function of $h\nu$ and values are taken from the CRC handbook [39]. Combining these parameters we obtain equation 2.44 which describes the probability of a photo excited electron to scatter.

$$S(E_n) = \frac{\int_0^\infty exp(-\frac{x}{\delta(h\nu)})exp(-\frac{x}{\lambda_e(E_n)})dx}{\int_0^\infty exp(-\frac{x}{\delta(h\nu)})dx} = \frac{1}{1+\frac{\delta(h\nu)}{\lambda_e(E_n)}} \tag{2.44}$$

Where x is the distance from the surface of the cathode ,λ_e is the electron mean free path and δ is the penetration depth of the light. When calculating the total energy distribution the approximation becomes $S(E_n)$ =$S(E)$ because we do not have a term for E_n.

Eq. 2.44 is not new, Spicer has used this in [40]. What is perhaps different is the simple use of thermal conductivities in combination with the approximation

of only normal traveling electrons, because of this it is a very crude approximation. In fact these values are only really valid around the Fermi energy so our extrapolation to other values is quite unjustified. Luckily the results seem to fit well previous experimental data see figs. 2.8,2.9, and 2.10, so we are for the time being happy with this method.

2.3 Results

2.3.1 Comparison With Existing Data

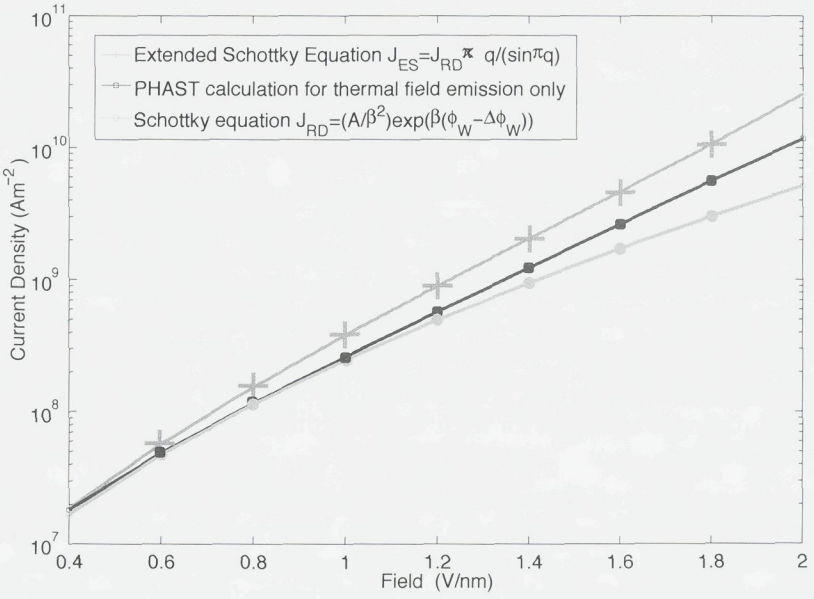

Figure 2.6: Current density for thermal field emission. The temperature is 1800K and the work function is 2.7 eV, and the field is varied from 0.4V/nm to 2V/nm. + line shows the extended Schottky current density. The squares line is numerically calculated using the model described in section 2.2. Circles are for the Schottky equation. Note that there is a large difference (the vertical axis is log scale) between the three lines at high fields. In the equations $\phi_W - \Delta\phi_W$ is the Schottky lowered work function and q is a function of field and temperature which deals with the tunneling [29])

We must check that our model is correct, to do that we first compare our results with the analytical equations of thermal field emission, and with experimental results. Also we will check the photo efficiency (number of emitted electrons divided by number of incident photons) against experimental data.

Figure (2.6) compares our results for thermal-field emission with the Schottky and Extended Schottky equation equations 2.45 and 2.46.

$$J_S = (A(k_B T)^2) exp(\frac{(\phi_W - \Delta\phi_W)}{k_B T}) \tag{2.45}$$

$$J_{ES} = J_s \frac{\pi q}{(sin(\pi q))} \tag{2.46}$$

Where $\phi_W - \Delta\phi_W$ is the Schottky lowered work function and q is a function of field and temperature which deals with the tunneling. Eqs. 2.45 and 2.46 are derived and compared with experimental values in [29]. Essentially the Schottky equation deals with the lowering of the emission barrier by the high applied field, this goes into $\Delta\phi_W$ but does not include tunneling. The extended Schottky model was developed to include tunneling, which becomes significant at high field and temperature.

At low fields all three lines agree, but diverge at higher fields where electron tunneling becomes significant, and is either over estimated (Extended Schottky) or neglected (Schottky)
Now if we compare our numerical results with some experimental data (figure 2.7) for Schottky emission we find excellent results. No fitting factor is used, constants such as work function are the same as reported in [41]. There is some deviation between the two lines at lower fields, this might be explained by realignment of the ZrO layer on the tip, or tip facet radius growth at low field and high temperature.

These two results show that it is extremely worthwhile to numerically integrate the Schrödinger equation for high temperature emitters when electron tunneling becomes important.

We look now at actual photoemission photo efficiencies and compare with the results presented in [42]- see figures 2.8 and 2.9 . The simulation is fitted for zero field and room temperature. We assume these were the experimental details. It is clear that with potassium there is a significant difference depending on the cleaning method used, as from the figure we see this makes a big difference to the work function or more accurately the threshold wavelength for emission (for the simulation we used the work function listed in the CRC handbook [39]). We see immediately the problem of obtaining reliable measurements. Three different sets of data are obtained for potassium none of which appear to agree with the work functions presented in the CRC handbook and verified in other locations. Thus it is clear that small surface imperfections dramatically changes the photo efficiency, and we are happy with the results here as they have the same shape as the experimental data and in the case of potassium sit in the 'middle' of the experimental data. We see with gold and silver that at shorter wavelengths (higher photon energies) we over estimate the photo efficiency, this is probably because of the approximation of Fowler (see section 2.2) but we still catch the shape, and closer to threshold where the majority of the electron's energy is in the normal direction we match well considering the uncertainty in surface conditions. We conclude that the simulation matches reasonable well the experimental data. The

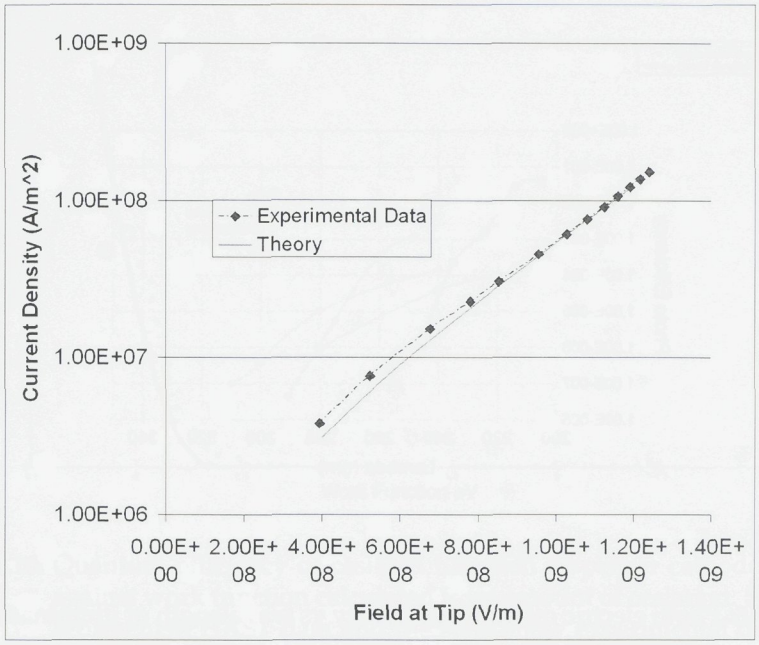

Figure 2.7: Current Density derived from Experimental data (dotted line diamond markers) and numerical (solid line) results for a standard Schottky emitter. Temperature is 1800K, Work Function =2.95eV other data is taken from [41] . Note there is good agreement between the numerical and the experimental data especially at higher fields where analytical methods tend to fail.

only fitting was to infer the work function/barrier height from the experimental data, all other data was obtained from the CRC handbook [39] and [43]. We can also examine how our results compare with the recent work of N.A Moody who is developing cesiated photo cathodes for use in free electron lasers and accelerators. This should be closer to the PHAST situation because of the work function lowering ZrO layer on the tip. In this case the fit is excellent (see figure 2.10). The situation here is more complex having to calculate how the amount of cesiation relates to work function. This was done graphically by comparison with figure 17 in [44]. We believe that a Schottky tip should behave in a similar way, and that it has a constant work function lowering effect from the coating of ZrOx, assuming we maintain a steady temperature.

2.3.2 Simulation Results For PHAST

What we want with PHAST is a bright monochromatic electron source. We believe that this is possible by illuminating a Schottky cathode with a focused laser beam. By combining these two qualities (reduced on axis brightness and energy spread) on one graph (figure 2.11) we see that the upper left hand section of the graph

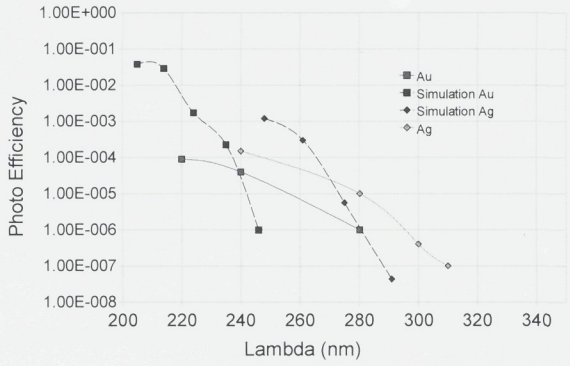

Figure 2.8: Photo electric quantum efficiency vs wavelength of illuminating light. Experimental data from [42] for Gold (squares), Silver(diamonds) plotted with our PHAST simulation data (dotted lines).

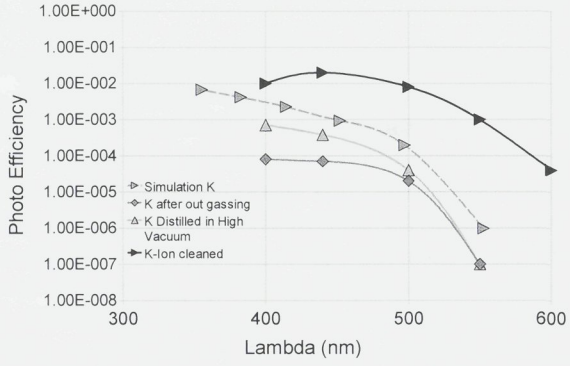

Figure 2.9: Photo electric quantum efficiency vs wavelength of illuminating light. Experimental data from [42] for Potassium (circles after ion cleaning, triangles after vacuum distillation, diamond after out gassing), plotted with our PHAST simulation data (dotted lines).

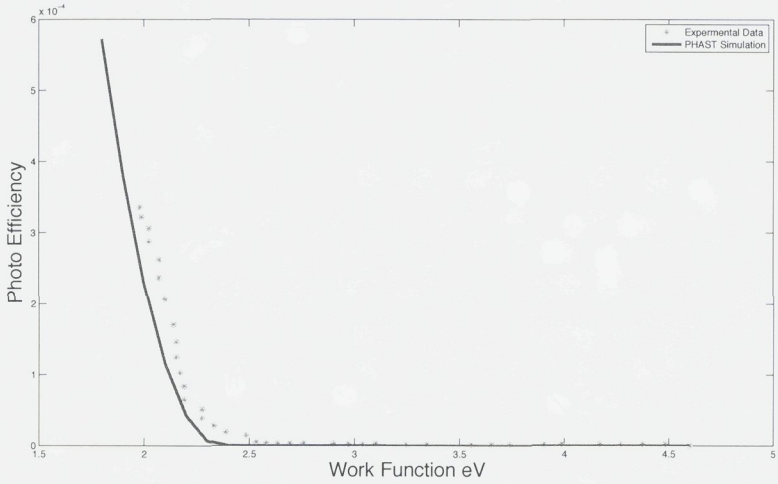

Figure 2.10: Quantum efficiency of cesiated tungsten dispenser cathode plotted against work function calculated from amount of cesiation. Solid line represents PHAST data and the stars show experimental data. The laser wavelength used was 532nm (2.34 eV) assumed temperature of 300K and 0 or very low electric field. Many thanks to N.A Moody for supplying this data.

represents what is achievable with thermal-field emission, and the bottom right is what we hope to achieve with PHAST. The most striking feature is the increase in brightness with either a drop or zero increase in energy spread, this is simply due to the energy location of the photoelectrons. Each mark on the photo assisted solid lines corresponds to an increase in photon energy of 0.2eV. Initially there is very little increase in the brightness and so the points are close together. Eventually we get significant tunneling and then emission over the barrier, once the photon energy is roughly 0.4eV above the Schottky barrier the energy spread races away. This is nicely demonstrated in figure 2.12, which shows how the distribution of emitted electrons changes with laser energy $h\nu$.

2.4 Discussion

We can see from our simulations that the model we are using is reasonable, it fits almost perfectly with the experimental data of cesiated tungsten in fig. 2.10 and follows roughly the curve for different metals shown in figs 2.8 and 2.9. Fowler's approximation of adding the photon energy only to the normal component of the electron energy is clearly reasonable. Dubridge also used this to describe the energy distribution and showed that this reproduces nicely experimental data [23]. From the work of Jensen we have included electron tunneling, and obtained quantitative results. In this paper we have arrived at an expression

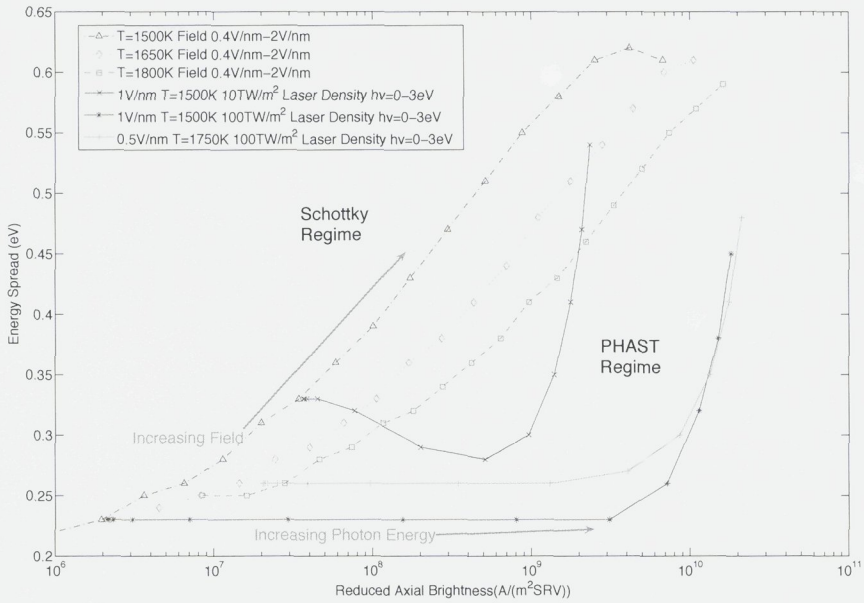

Figure 2.11: Energy spread (FW50) and reduced on axis brightness. thermal field emission with increasing field left to right (dotted lines) marker spacing of 0.1V/nm and PHAST emission with increasing photon energy left to right (solid lines) marker spacing of 0.2eV. The region in the upper left denotes the regime available to traditional thermal field sources, where as the regime in the bottom right (PHAST Regime) represents what is available to PHAST. A description of what each line represents is given in the key for this graph.

(eq.2.24), based on their work for the reduced on axis (maximum) brightness of a photo-field emitter. This expression does not suffer from Fowler's approximation and is in this sense exact.

However the increase in brightness and control of energy spread in fig. 2.11 is only available at extremely high laser intensities around $10TWm^{-2}$. With a CW laser we can not achieve the high laser intensities needed because we quickly calculate that the tip will be well above 1800K (The manufacturers recommended operating temperature). In fact we can roughly calculate that if we laser heat a Schottky tip to 1800K then in addition to the thermal field brightness of around 10^8 we add only a photo induced reduced on axis brightness B_{rph} of 4×10^4 $Am^{-2}sr^{-1}V^{-1}$, which is negliable .

We therefore conclude that a radical design change is required.

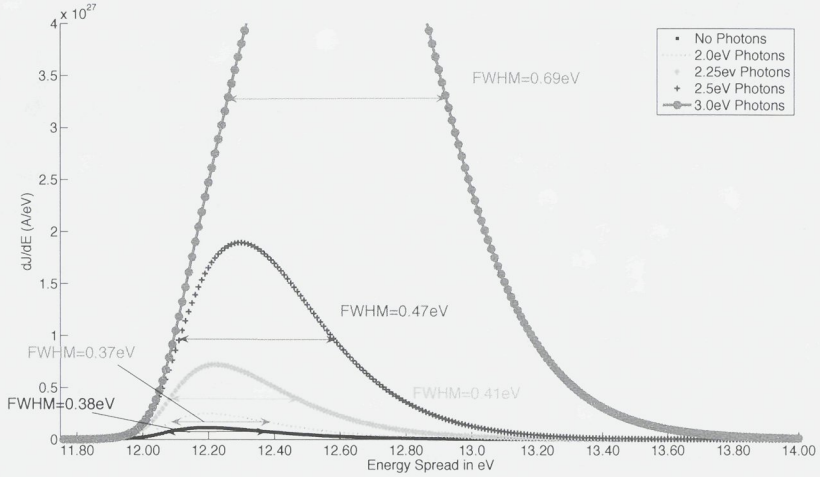

Figure 2.12: Distribution of emitted electrons from the bottom: (1)pure thermal field emission, (2) 2.0eV (622nm) photons, (3) 2.25eV (550nm) photons,(4) 2.5eV (497nm) photons, (5) 3eV (412nm) photons. Here we look at the Full Width at Half Maximum (FWHM) which is only valid for symmetric distributions, but the distribution of emitted electrons is clearly not symmetric. However it is much clearer to see the FWHM than the Full Width 50. We show here that with red photons we are able to produce more current and at the same time reduce the energy spread from 0.38 to 0.37eV (FWHM) compared with the pure thermal field case. The difference is a little bit small for the FWHM measurement but is more noticeable when using the FW50. For shorter λ the distribution will spread faster.

2.4.1 Design Change

It has long been known that a side illuminated tip should have a better quantum efficiency than a front illuminated mainly from the polarisation sensitivity of the electronic surface states. Experimental evidence suggests that an increase of up to 7 times may be possible [45].However this is still not enough to get us the factor 10^4 needed to compete with the standard Schottky source.

We anticipate that by applying a thin film of tungsten to a diamond substrate and super cooling the diamond we may be able to increase the power applied by at least 2 orders of magnitude without significant problems.

Further solutions lie in the use of materials with higher thermal conductivities or inherently better quantum efficiencies such as semi-conducting materials.

For the present time we think that the primary application of PHAST is in the pulsed regime with pulse times sufficiently short to prevent overheating of the tip.

2.5 Conclusions

PHAST presents a new and exciting idea for an electron source with higher brightness and lower energy spread than state of the art thermal field emitters. Also the use of photons with energies less than the barrier height (photofield emission) can make a useful contribution to the brightness via tunneling. Adding photo emitted electrons does not necessarily damage the energy spread and may sometimes even improve it, merely by the location on the energy scale of the emitted photo electrons. This opens up the use of both green and red lasers which are considerably cheaper than their UV cousins.

We hope that with more radical design and engineering we may overcome the heating problems. However it is uncertain as to how non-linear effects may cause problems.

We have also shown that we are using a valid theory of electron emission which follows well the experimental results, and allows us to make useful predictions.

To continue further theoretically, we hope to move to a fully quantum description of emission and thus include polarisation sensitivity and band structure. Experimentally we will first explore the pulsed mode, allowing us to verify the theoretical predictions, this will also have applications in for example ultra fast microscopy.

3 CHAPTER

Heating Effects

The radiation left over from the Big Bang is the same as that in your microwave oven but very much less powerful. It would heat your pizza only to minus 271.3C - not much good for defrosting the pizza, let alone cooking it.

Stephen Hawking

Laser heating is a big problem for photo emitters, so here I examine its influence. I have tried to make it as simple as possible and leave out as much as possible to allow it to be studied analytically with out complex mathematics. We will find out at which point the thermal emission is greater than the photo emission and how that relates to work function and photo efficiency. Surprisingly we find that it is beneficial to have a higher rather than a lower work function.

3.1 Introduction

In [46] we discussed using a laser to improve on the electron emission characteristics of a Schottky tip. As shown in figure 3.1 we planned to shine a laser onto the front part of a Schottky tip kept in vacuum. The photons in the laser would interact with the metal, and the process of photo emission would deliver electrons from the metal to the vacuum.

Due to the large laser intensity required for photo emission, heating of the tip is a major concern in such a situation. Having neglected this in [46], we are now going to address it.

We can already tell that heating will not be negligible : the intensities - $>$ 1 TW/m^2 - we discussed in [46] are considerably greater than those used for laser

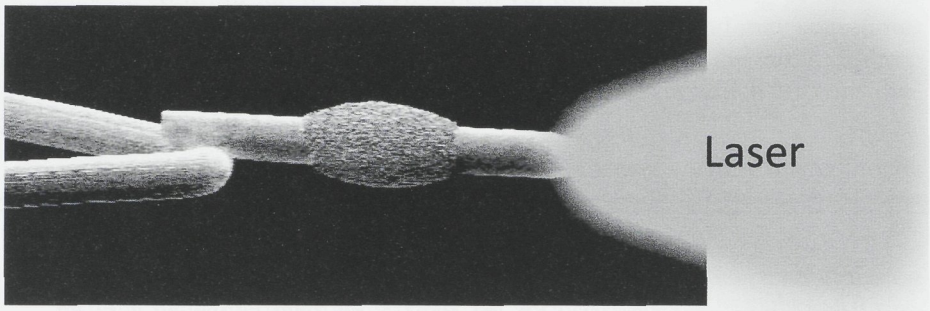

Figure 3.1: Cartoon of Schottky tip being illuminated by a laser

welding $\approx 1\ \mathrm{MW/m^2}$ [47]. We should therefore expect that adding a laser will as a minimum induce some unwanted thermal emission of electrons from the Schottky tip. Although it may not be immediately clear from [46], we can argue that if the thermal emission outstrips the photo emission then the extra effort of adding a laser is wasted. To be improving the characteristics of a Schottky source, the photo emission should play a starring role. Our task in this section is to identify the temperature rise due to laser heating in order to determine the current density of the thermally emitted electrons J_{th}. We can also include melting effects. To do this we will first look at a few models for heating and choose the most appropriate. Then we will use these to examine the thermal emission, and to compare it to the photo emission.

3.2 Models for Heating

There are four methods of heat transfer, convection, conduction ,(infra-red) radiation and Nottingham Cooling. Since our Schottky tip is in vacuum convection can not occur. The laser radiation heats the tip, the manner that this works is discussed by, for example, [28], and also in the rest of this section. Looking next at conduction we will show this is the most important cooling mechanism. Most models ignore the changes in material properties with temperature as these fur-

ther complicate matters, however they are important in accurately determining a temperature. In this case we we opt for simplicity and ignore them.

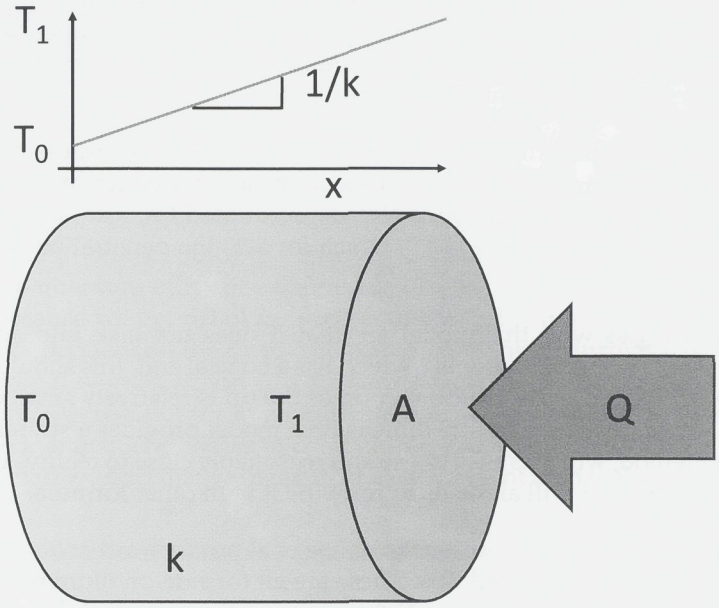

Figure 3.2: Static planar heating of a cylindrical rod, with graph above showing the temperature distribution in the rod

The most simple model, for laser heating a Schottky tip is a time independent one dimensional model, with a heat source Q (in this case our laser) at one end and a fixed temperature T_0 at the other, see figure 3.2, and equation 3.1.

$$\frac{Q}{tA} = \frac{k(T - T_0)}{L} \tag{3.1}$$

Here t is time, A is the area over which Q is spread (in our model, the area of the exposed surface of the rod). The rod has a thermal conductivity k which for tungsten is around 100 W/m/K [39]. The length of the rod is L, and T is the temperature at the surface A.

Radiative cooling of a Schottky tip can be neglected in a first order approximation since according to Dokania [48] it is only around $1/6^{th}$ of the total. The radiated power output is $Q/t = \epsilon\sigma A_{TS}T^4$, where ϵ is the emissivity factor σ is the Stefan-Boltzmann constant $\approx 6 \times 10^{-8}$ $\mathrm{Wm^{-2}K^{-4}}$, A_{TS} is the total surface area of the tip and T is the temperature of the emitter. To ignore radiative cooling $k >> \frac{\epsilon 2L^2T^3}{r}$ for a typical Schottky tip this is the case (take $\sigma = 1$, $r = 200$ µm $T = 1800k$, $k = 100$ W/m/K and $L = 1$ mm).

Nottingham cooling [49] occurs because of electron emission this is also negliable. Nottingham cooling comes from the energy difference between the electron leaving the metal into vacuum and the electron arriving from the power supply which travels at the Fermi energy. if we call this difference $\Delta E_s(\ \mathrm{eV})$ then the power lost to Nottingham cooling is $Q/t = I * \Delta E_s$ therefore to ignore Nottingham cooling $k > \frac{I \delta E L}{T}$ which for the same numbers we applied for radiative cooling assuming even a large current of 1 A is fulfilled.

This model assumes that a heat sink can maintain T_0 regardless of the input heat Q. In reality the sink will warm, this can be accounted for by increasing T_0. In Q the heat absorbed, reflection is already accounted for; also, the penetration depth of the laser is assumed to be 0, which for a 20 nm penetration depth and a 1 mm rod is reasonable.

Further worries with this model are that it does not take into account the change in radius of the Schottky tip, which has a conical end; this should however not be a problem, since the conical section of the tip is relatively small compared to the cylindrical section. The one-dimensional model provides a straightforward first-order method, which is easy to use and reasonably close to reality. The simple nature of equation 3.1 will allow us to combine it with other formula.

In [50], and other papers such as [51], Lee et al put forward analytical models of heating for laser illuminated tips. These are all for side-on illumination, which is not the situation we are investigating. They take into account the shape of the tip, and the laser distribution, thus they can be a little cumbersome, for example in [50] equation 10 needs the error function. There are formulae (equations 12 and 14) for the temperature rise at the emission site of the tip only, which is enough for our purposes, that are easier to manipulate. However as they are investigating a side illuminated tip, they are not of direct application here.

Betchel [28] theoretically investigated heating of semi-infinite materials with picosecond pulsed lasers. He posed two methods of laser heating, a volume and a surface interaction, both give roughly similar results. There are analytical formula which are usable, but not easily manipulated. This method would work for large tips, with short pulses such that the deposited energy is small enough to disperse as if the tip was infinitely large. However for the static case this method can not be used.

It is also possible to use a finite element method to investigate heating. This can include all relevant physics and parameters known, it should therefore give more accurate results. The problem with computational methods is time, both in calculation and in setting up the model. Further since the underlying physics is hidden by the program the affect of changing a variable is not always clear. To investigate the heating effects of different laser intensities, different materials and different geometries would be a complete thesis on its own. Therefore we will also not use this method.

We will use the simple 1D model due to it's ease of use and because we can easily manipulate and include in it our model of photo emission.

3.3 Theory

If each photon excites one electron, then the current density J_{ph} will scale linear with the laser intensity $\frac{Q}{tA}$. We define a constant of proportionality η to account for the fraction of excited electrons which can not escape into vacuum. 3.2

$$J_{ph} = \eta \frac{Q}{tA} \tag{3.2}$$

By dimensional analysis $\eta = \frac{N_{ee}}{N_{ap}} \frac{e}{h\nu}$, where N_{ee} is the number of emitted electrons, N_{ap} is the number of absorbed photons, e is the elementary charge and $h\nu$ is the energy of the photons. Since the term $e/(h\nu)$ is ≈ 1 our η will have a similar value to the quantum efficiency defined in [46] as N_{ee}/N_{ap}. Our definition of η is useful because we get rid of $h\nu$ from equation 3.2. From [46] we know that η is actually dependent on the $h\nu$ in a complicated manner. Further η is dependent on the material work function ϕ, a scattering factor S, the applied field and the temperature. We will not try to include these in our analysis since they will only complicate matters. The goal is to compare J_{th} caused by laser-heating with J_{ph}, to first order. If we find that we need further refinement then we can use the model of [46].

First we will extend equation 3.1 so it includes η.

$$\frac{Q(1-\eta)}{tA} = \frac{K(T - T_0)}{L} \tag{3.3}$$

We add the factor $(1 - \eta)$ since energy used for photoemission can not also create heat and for semi-conductor η can approache unity.

To determine J_{th}, we can use Richardson's law,

$$J_{th} = \frac{4\pi me}{h^3}(k_B T)^2 \exp \frac{-(\phi - \Delta\phi)}{k_B T} \tag{3.4}$$

here m is the electron mass, h is Plank's constant, k_B is Boltzmannn's constant, ϕ is the work function, and the Schottky lowering of the work function $\Delta\phi = \sqrt{\frac{e^3 E}{4\pi\epsilon_0}}$ where E is the electric field, and ϵ is the permittivity of free space.

By substituting equation 3.3 into 3.4 we find J_{th} as function of laser intensity. Letting $T_0 = 0$ K and the laser intensity $I = \frac{Q}{tA}$, then we may write

$$J_{th} = \frac{4\pi me}{h^3} \left(k_B \frac{I(\eta - 1)L}{k} \right)^2 \exp \frac{-(\phi - \Delta\phi)k}{k_B I(\eta - 1)L} \tag{3.5}$$

3.4 Results and Discussions

We are now going to investigate equations 3.2 and 3.5. The first thing to do is look analytically what can be done. We would like to know when does $J_{ph} = J_{th}$,

this gives us the boundary between thermally driven electron emission and photo driven. Typically for metals $\eta << 1$ [46],so $(\eta - 1)^2 = 1$ in equation 3.5. Then by equating equations 3.2 and 3.5 we may write,

$$\eta = \frac{4\pi me}{h^3}(k_B)^2 I \left(\frac{L}{k}\right)^2 \exp \frac{(\phi - \Delta\phi)k}{k_B I L} \tag{3.6}$$

Equation 3.6 will give us a chance to understand what η we need to create a workable photo assisted Schottky tip, we can investigate how several variable change η. For a laser illuminated Schottky source the variables we can easily change are I and $\Delta\phi$ the others are essentially fixed, L is at least 1 mm, and $k \approx 100$ W/m/K, and $\phi = 2.8$. The field on a Schottky tip is never more than 1.5 V/nm, thus $\Delta\phi$ varies in the region 0 eV to 1.5 eV [46].

From [46] we can see (despite the different definition of η) that metal photo cathodes have at best $\eta = 0.01$, so we will adjust I such that η is around this region.

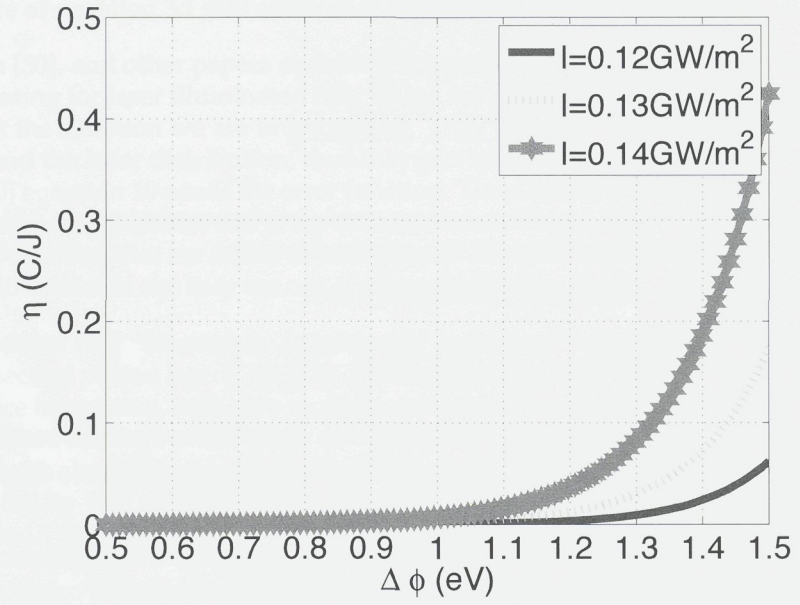

Figure 3.3: For the special case $J_{th} = J_{ph}$, η plotted against $\Delta\phi$ for three values of I

To learn from figure 3.3 we must remember that a higher η is worse since it means that for photo current to dominate we must somehow find a special material with large η. Therefore increasing $\Delta\phi$ is actually not helpful in this case.

We plot figure 3.4 to further illustrate the point that as $\Delta\phi$, increases the photo current is more rapidly dominated by thermal emission. For microscopy the cur-

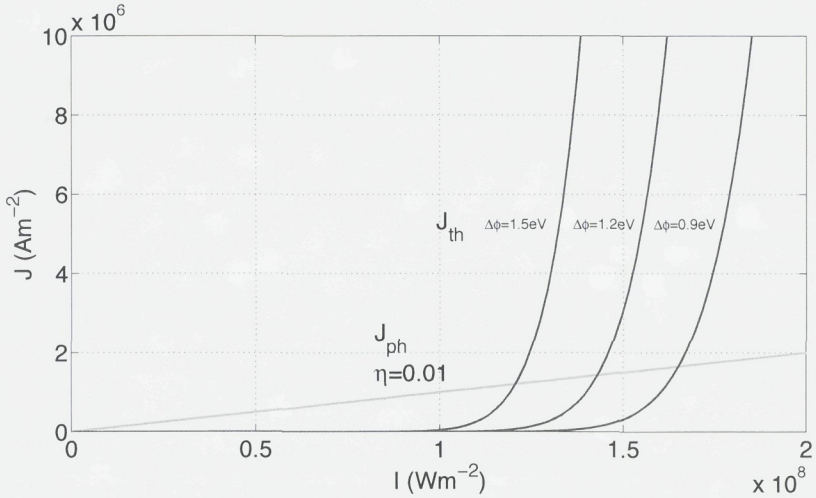

Figure 3.4: Emitted current density J for photo emitter with $\eta = 0.01$ in green and the thermal emission from laser heating (J_{th}) in blue, as functions of I. J_{th} is plotted for $\Delta\phi = 1.5, 1, 2, 0.9$ eV

rent density is not the most important factor, we should consider the reduced brightness B_r for a photo emitter this is given in [46] as $B_{rph} = \frac{eJ_{ph}}{\pi h\nu_X}$, where $h\nu_X = h\nu - \phi - \Delta\phi$ is the excess photon energy. For the thermal emitter $B_{rth} = \frac{eJ_{th}}{\pi kT}$, the total B_r is the sum of these two. Looking at B_r adds a further dimension to investigate since we must include the photon energy, we see this in figure 3.5.

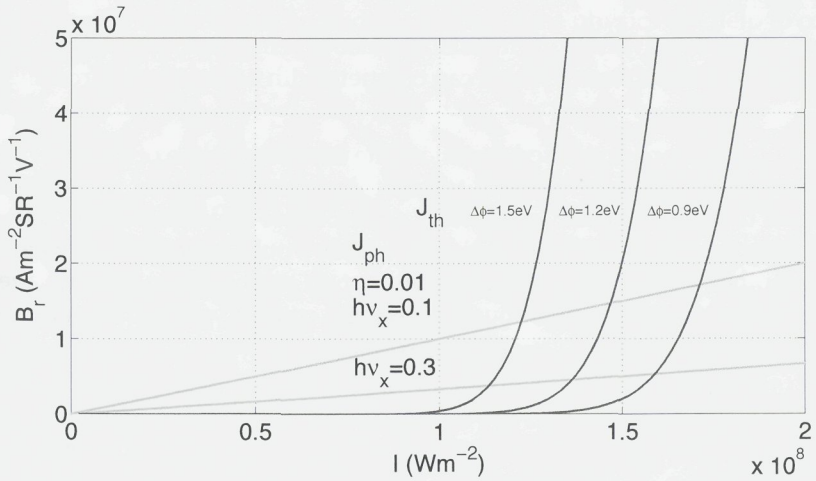

Figure 3.5: Brightness as a function of laser intensity I B_{rph} for photo emitter with $\eta = 0.01$ in green and the thermal brightness from laser heating B_{rth} in blue

To have sufficient B_r from our laser assisted Schottky emitter we need to have $B_{rph} > 10^8$ A/ $(\mathrm{m}^2\mathrm{srV})$ this is not possible even with an $\eta = 0.01$ C/J, and $h\nu_X = 0.1$ eV. We must conclude that there is very little probability of photo assisted Schottky tip working since the η required is several orders of magnitude greater than is typical for Tungsten, or any other metal.

3.4.1 Semiconductors

Semiconductor materials have a much higher η with the possibility of η approaching 1. Taking silicon as an example, in this case of course we must include the factor $1 - \eta$ in equation 3.5, and we find if we let $\eta = 0.1$ C/J and $h\nu_X = 0.1$ eV then by $I = 0.1$ GW/m^2 we reach $B_{rph} = 10^8$ A/ $(\mathrm{m}^2\mathrm{srV})$, with $T = 600K$ this is less than tungsten since silicon has $k = 150$ W/m/K [39]. Thus if we can reach this high quantum efficiency, keep the tip clean, and the high temperature does not make the semiconductor melt, then we might be able to have a viable semiconductor photo emitter. In this thesis we did not investigate semiconductor emitters, because we do not expect that they will be stable enough for microscopy.

3.5 Conclusions

A Schottky source made from a tungsten tip is unlikely to be improved by adding a laser for photo assisted emission. The heating caused by the laser results in an exponentially increasing thermal current, versus the linear photo current.

A high work function material is actually a better photo cathode (given our definition or η) since the thermally emitted current will be low over a larger range of laser intensities.

If we can move away from metals and use a semiconductor, with a high η then a photo emission source which can compete with a Schottky source might be viable.

A final quick word on pulsed emission, the cool down time of a typical tip has been measured by for example [50] to be of the order of at least micro seconds, this means that even pulsed lasers with a reasonable average power must deal with heating since a 100 MHz repetition rate laser would only allow 10 ns for cool down. In other words pulsing is probably not an option for increasing average current, however with a short enough pulse high current within that pulse can be achieved with negliable increase in temperature.

4 CHAPTER

Statistical Coulomb Interactions in a Photo Assisted Schottky Tip

The temptation to form premature theories upon insufficient data is the bane of our profession.

Sherlock Holmes

We show the importance of including the statistical Coulomb interactions in electron source design, in particular we model this for PHAST PHoto Assisted Schottky Tip with and without Laser Illumination . We show that although the statistical Coulomb interactions can not be completely overcome an understanding of the physics can help to considerably reduce them.

4.1 Introduction

The two key parameters of a source for an electron microscope are brightness and energy spread. These two quantities are non-independent, a change in one will effect the other (normally adversely). Brightness and energy spread are so important because they can determine the probe size, at a given current . This is neatly demonstrated in figure 4.1 for details see caption and equation 22 in [20] also of interest is [21].

Electron-electron interactions add an extra element of important physics to consider when designing an electron source. Although many people consider space charge effects, the statistical Coulomb interactions are often overlooked. This is probably due to the inherent complexity of solving multi-body systems. In

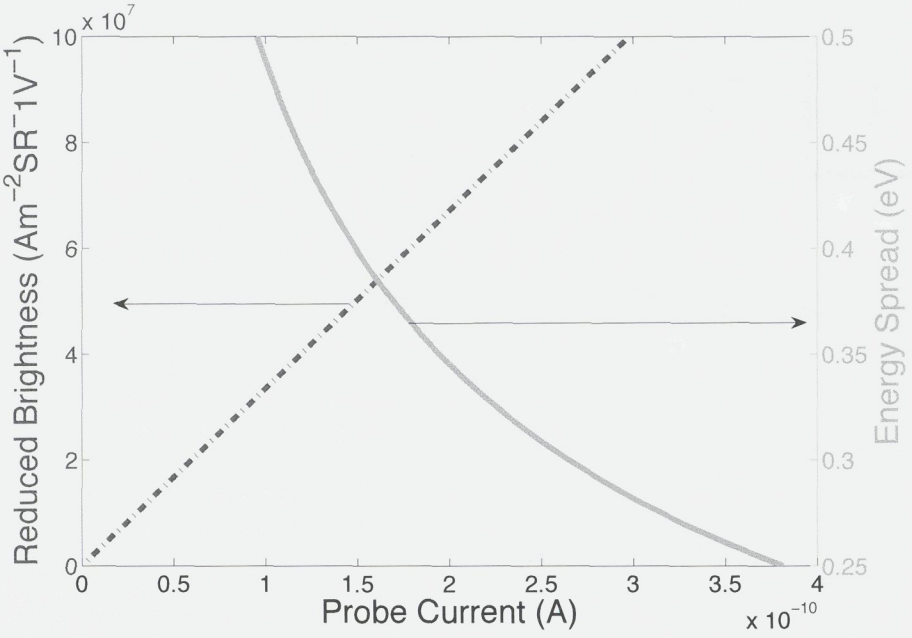

Figure 4.1: Minimum required brightness and maximum allowable energy spread for a 1nm(FW50) probe size, in a system dominated by chromatic aberration, in which the opening angle of the probe forming lens is optimised. Parameters used are electron energy 5keV, chromatic aberration of 0.5mm

many situations analytical solutions (approximate or otherwise) can not be used, and thus Monte-Carlo simulations are often used. This being the case Kruit and Jansen [52] tackled the problem with a combination of simulations and analytical equations and came up with semi-analytical formulas which have been shown to fit well with experimental data, [41] and [19]. These equations allow a designer to quickly calculate the effect of the Coulomb interactions on brightness and energy spread.

We are in the process of exploring the possible benefits of enhancing the emission from a Schottky source [53] by laser illumination. This paper applies the theory of statistical Coulomb interactions to this problem.

4.2 Method and theory

The emission model has been explained in chapter 2 and was calculated numerically. For all simulations the 0 field barrier height is set at 2.8eV, the chemical potential is taken as 10eV and we use a fixed temperature of 1800K.

4.2.1 Statistical coulomb effects

The statistical Coulomb interactions contribute two important effects to a source, these are an increase in energy spread normally known as the Boersch effect, and a trajectory displacement which reduces the intrinsic brightness hence their importance in probe formation. A complete description of the theory is not possible here, instead we give a broad outline with references to earlier work which should the reader be interested allow him or her to reproduce our results.

We calculate for fields from 0.3V/nm to 2V/nm (for figure 4.2 U_{ext}=600V to 10kV) as this covers the operating range of a standard Schottky tip. The conversion factor between field and extraction voltage is found from simulation and is described below.

To estimate the effect of trajectory displacement we follow the method of Van Veen et al. [19]. To get the total trajectory displacement, the angular deflections are calculated from equation 4.1 which comes from [52].

$$\phi_H = 0.128 \frac{m^{1/3}}{\epsilon_0} \frac{(J\pi)^{2/3}}{U(z)^{4/3}} \tag{4.1}$$

where m is the mass of an electron, ϵ_0 is the permittivity of free space, J is the current density, U is the potential. So we first model a 'standard' Schottky electron gun using the program Charged Particle Optics which uses the boundary element method and can ray trace electrons on a nanometre to millimetre scale. This is particularly important as the electric field changes in z extremely quickly near the tip. The geometry file used is shown in fig 4.2. We trace a single electron at 60nm from the centre of the facet , this ray defines our beam envelope. For each coordinate of the ray tracing results we find the FW50 angular displacement due to the statistical Coulomb interactions. This method is only valid in the Holtsmark regime (which for a Schottky source is appropriate [19]) where we can assume a constant current density at each z slice, thus in principle we can choose any starting radius for our beam envelope. We also need the current in the envelope which is calculated from the average field across the facet center (r=0) to r=60nm and the area πr_{60nm}^2. Further we assume a constant potential for each z slice of the ray tracing. These angular displacements are translated to displacements in the virtual source plane as proposed by Van Veen

$$d_{tra} = \int_0^{z'} \frac{r(z)}{\alpha_{vs}} \phi \sqrt{\frac{U(z)}{U_{ext}}} dz \tag{4.2}$$

Where α_{vs} is the intrinsic angle made by the electron envelope at z' and U_{ext} is the extractor potential. The brightness at z' from the emitter is reduced by the trajectory displacement with a factor $\left(\frac{d_{intr}}{(d_{intr}^{2/3} + d_{traj}^{2/3})^{3/2}} \right)^2$ with respect to the intrinsic brightness upon emission (the addition law is found from fitting to fully convoluted data sets). We trace the electrons to 3mm from the source (z'=3mm).

To calculate the Boersch effect we follow Fransen et al.[29] and approximate

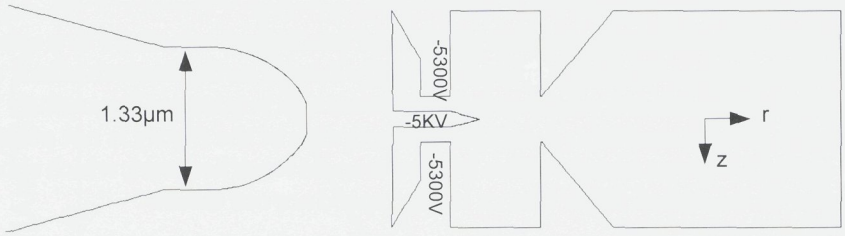

Figure 4.2: The tip (on the left) follows an SEM image of a Schottky emitter with a 143nm facet radius. The geometry of the gun follows a standard FEI microscope. There is a suppressor as marked at -5300V,the extractor (0.4 mm aperture diameter) at 0.50 mm from the emitting surface, this is held at 0V and the tip itself is brought to some negative voltage, in this diagram -5KV. The area to the right of the extractor is field free

the emitter extractor region as field free. We assume uniform current density calculated from the average field across the 60nm radius of the emitter facet. Further we use an emission cone half angle α of 7.5^o [53]. Now we can apply the semi-analytical equations of Jansen. We use the FW50 equations for a cylindrical beam segment containing a crossover. The emitter facet becomes the beam crossover and we divide the equations by two as there is no Boersch effect inside the emitter. In spite of these crude approximations, Bronsgeest et al.[41] have shown this approach gives good agreement with experiment. The Boersch effect is calculated as follows (for FW50 values)

$$\Delta E_H = \frac{4.88(J\pi)^{2/3} r_{facet}}{\alpha U_{ext}^{1/3}} \tag{4.3}$$

$$\Delta E_L = 1.90 \times 10^5 \frac{J\pi r_{facet}^2}{\alpha U_{ext}^{1/2}}; \tag{4.4}$$

$$\Delta E = (\Delta E_H^{-1/4} + \Delta E_L^{-1/4})^{-1/4} \tag{4.5}$$

with r_{facet}. Finally the increased energy spread is found by adding the FW50 Boersch effect to the intrinsic FW50 energy spread with a 1.66 power addition obtained by fitting to numerically calculated convolutions.

4.3 Results

We present the results of our intrinsic (without Coulomb interactions) energy and brightness calculations for the PHAST in figure 4.3. We want to draw the readers attention to the increase in brightness due to laser illumination, and the reduction

in energy spread. At a laser intensity of $30TWm^{-2}$ and a field of 0.9V/nm the energy spread is slightly reduced as we increase the photon energy, until it suddenly accelerates away at a brightness of $10^9 Am^{-2}sr^{-1}v^{-1}$ and $h\nu \approx 2.3eV$.

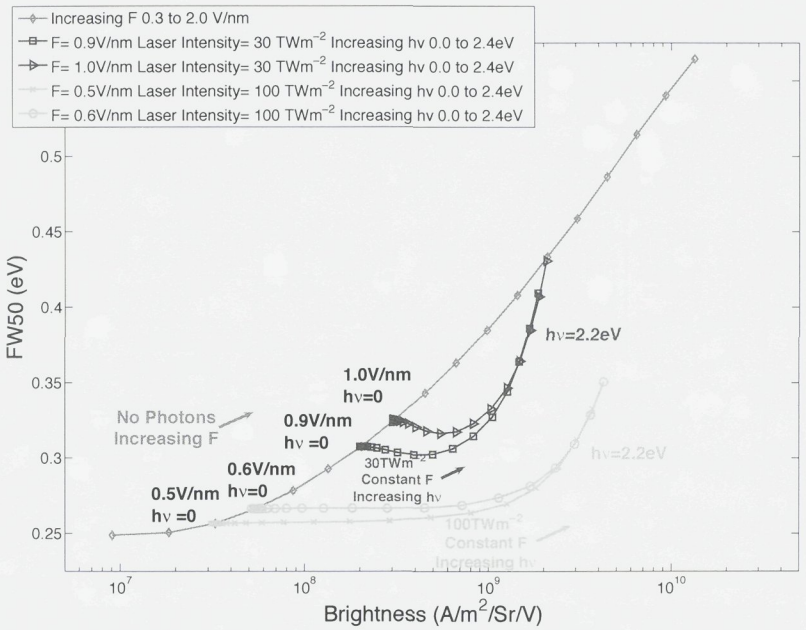

Figure 4.3: Intrinsic Calculated Energy Spread (FW50) and Reduced Axial Differential Brightness, for Schottky emission with increasing field left to right $\diamond$, and PHAST with increasing photon energy left to right $\circ$, X, $\square$ and $\triangle$. The region in the upper left denotes the regime available to traditional Schottky sources, where as the regime in the bottom right the PHAST Regime represents what is available to a PHAST . A description of what each line represents is given in the key for this graph

However this initial intrinsic result is not fully representative of reality, we need to include the statistical Coulomb interactions. First we will simplify our diagram to show only standard Schottky emission- (field and thermal) and laser illumination with a field of 0.9V/nm T=1800K. We are now ready to include the Coulomb interactions and see their effect on the distribution for the parameters described in section 4.2.1 with z'=3mm, see figure 4.4 . Upon doing this we see the Coulomb effect is stronger on PHAST than the Schottky electrons. This happens because, for a given brightness the current density is lower for Schottky emission than for PHAST (this is what we called brightness efficiency and plotted in figure 2.4) . So at a brightness of $10^9 Am^{-2}SR^{-1}V{-}1$ (field=0.9V/nm and $h\nu = 2.2eV$), $J = 8.2 \times 10^8 A/m^2$ for PHAST and $J = 4.8 \times 10^8 A/m^2$ (field=1.3V/nm) for Schottky emission. Also the higher field for Schottky emission (1.3V/nm instead of 0.9V.nm), leads to a higher extraction voltage (9.2 kV instead of 6.5kV) so the electrons move faster and have less time to interact which reduces the Boersch

effect and the trajectory displacement.

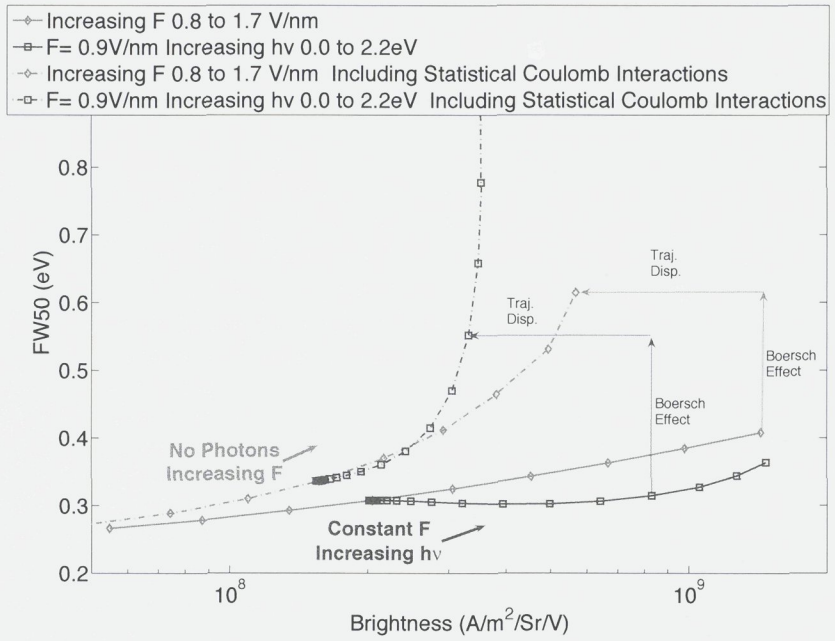

Figure 4.4: Calculated effect of Coulomb interactions on intrinsic energy spread (FW50) and reduced axial differential brightness. As per figure 4.3 but including now with the dashed lines the distributions including both the Boersch effect (Energy Spread) and the trajectory displacement. These two outcomes of the statistical Coulomb interactions are indicated by arrows drawn on the figure, for Schottky emission and PHAST

The statistical Coulomb interactions would therefore seem to upset the intrinsic results of PHAST as an improvement to the Schottky source. Luckily by looking at equation 4.2 we realise that to reduce the trajectory displacement we might aperture the beam near the source, as this determines the upper limit of integration in equation 4.2. After this aperture (the aperture allows our original beam envelope to pass through making it approximately 12 μm in radius) we calculate that the Coulomb interactions are negligible due to the reduced current. We now take z'as 0.6mm (i.e an aperture at 0.6mm from the source) and as figure 4.5 shows it is possible to nearly entirely remove the trajectory displacement. We still have of course the problem of the Boersch effect, and thus we must think again about how to remove this. By going back and looking at equation 4.5 we find that we can reduce the size of the source . However when we do this we affect the trajectory displacement (this will be investigated in a future paper). Thus we plot in figure 4.6 the Boersch effect for a tip with half the facet radius (71nm instead of 143nm) against the intrinsic Energy spread, here we see that for the smaller facet we have reduce the Boersch effect for both case with, and without photons

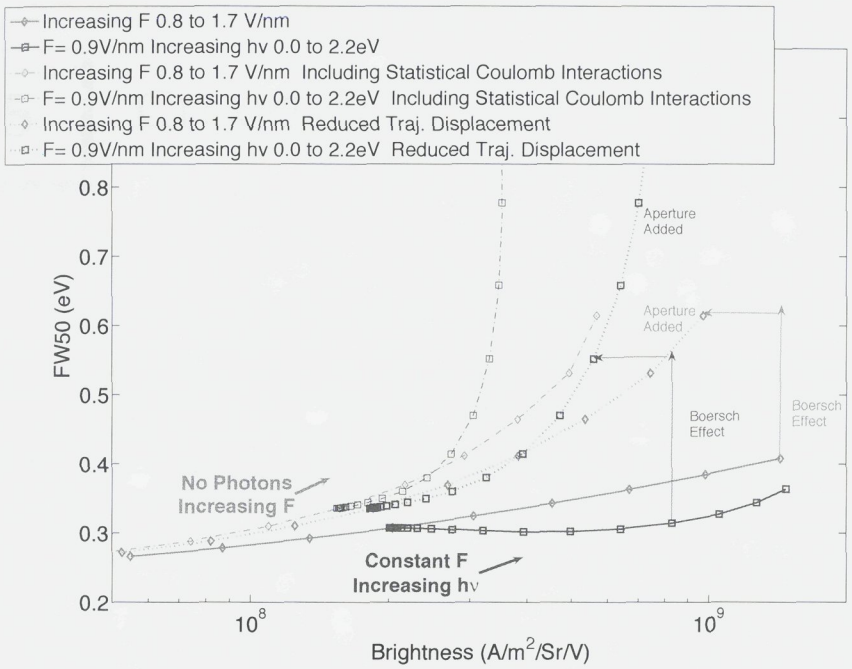

Figure 4.5: Reduced trajectory displacement by aperturing the beam at 0.6mm (equivalent to z'=0.6mm) shown with the dotted lines for both Schottky emission and PHAST. Also included with solid lines are the intrinsic energy spread and the unapertured results dashed lines

4.4 Conclusion

The Coulomb interactions can become particularly important in source design especially at high brightness). By consideration of the equations of Jansen and Kruit it is possible to adapt the source design and thus reduce the Coulomb interactions, thus although Coloumb interactions maybe a limiting factor for PHAST there is perhaps still opportunity for further work.

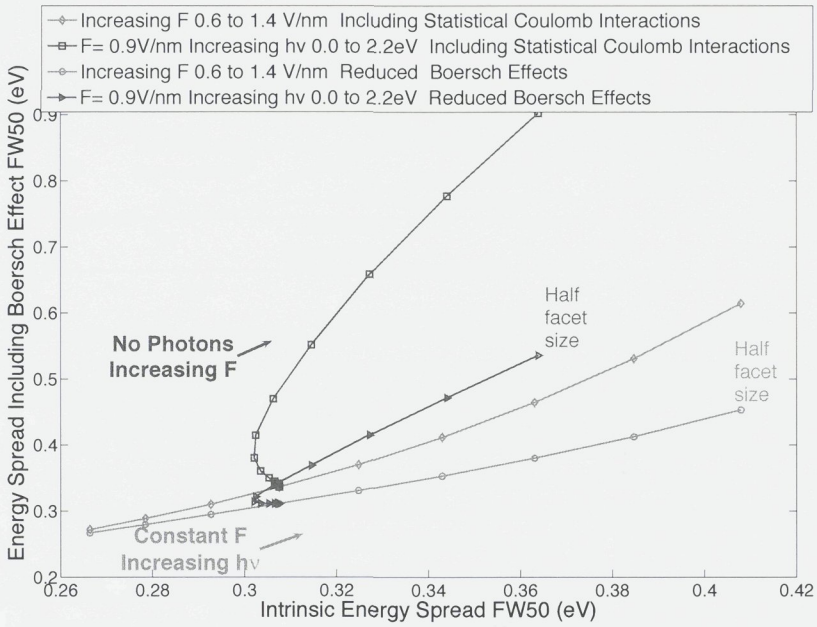

Figure 4.6: Intrinsic energy spread plotted against energy spread including Coulomb effects. □ and ◇ $r_{facet} = 143nm$, △ and X $r_{facet} = 71.5nm$.

5 CHAPTER

Brightness Limits of Cold Field Emitters due to Coulomb Interactions

If there is a God, his plan is very similar to someone not having a plan

Eddie Izzard

Many people have claimed that cold field emitters can enhance imaging in the electron microscope. This is based on theoretically determined values of reduced brightnesses up to $(10^{14}\ \mathrm{A}/\left(\mathrm{m}^2\mathrm{srV}\right))$. However we find that statistical Coulomb interactions limit the reduced brightness of even atomically sharp cold field emitters to $10^{11}\ \mathrm{A}/\left(\mathrm{m}^2\mathrm{srV}\right)$. We also find that for tip radii in the range $1\mathrm{nm}$ to $100\mathrm{nm}$ cold field emitters do not outperform larger Schottky (thermal-field) emitters.

This chapter is published in Journal of Vacuum Science and Technology B Volume 28 Issue 6

5.1 Introduction

Many people believe that cold field emitter will significantly improve the imaging power of an electron microscope. However, despite the hype, field emitters appear not to outperform thermal-field emitters (also known as Schottky-emitters), yet. The reduced brightness, which is constant for conservative fields, is in practice defined as

$$B_r = \frac{I}{\pi\alpha^2 \pi r_{vs}^2 V} \tag{5.1}$$

where r_{vs} is the virtual-source size of the emitter, e.g. the area from which the current appears to come from, $\pi\alpha^2$ defines the solid angle, and V the beam potential.

The reduced brightness B_r decides the amount of current in a probe of radius r_{probe},

$$\left(I_{probe} = B_r \pi \alpha^2 \pi r_{probe}^2 V\right). \tag{5.2}$$

For faster imaging times and even just to overcome signal-to-noise problems, the brightness B_r sets the limit.

The brightness of field-emitters is, according to standard theory (see figure 5.1) [54] [26] [46], virtually limitless. Claims are made of B_r as high as 10^{14} A/ $\left(\mathrm{m}^2\mathrm{srV}\right)$ [55] [56], but – to the best of our knowledge – have never been measured. Some brightness measurements of field-emitters are summarized in [57]. Probably the highest measured B_r's are 3×10^9 A/ $\left(\mathrm{m}^2\mathrm{srV}\right)$ from a carbon nanotube [58] and 4.6×10^9 A/ $\left(\mathrm{m}^2\mathrm{srV}\right)$ from a sharp tungsten tip [59]. In 2001, van Veen measured the brightness of a Schottky-emitter [19]. He found that at high fields – and therefore at high B_r – it is less than theoretically anticipated. This could be due to many reasons. For example, vibrations/stray magnetic-fields can increase the virtual-source size. These will not change with voltage, only acting as a constant blur to the virtual-source size r_{vs}. An error in the emission-model is possible, but this is a well researched, mature field. The most likely conclusion is that brightness B_r is not constant, as there is a non-conservative field introduced by electron-electron interactions. These interactions cause the trajectories of the electrons to be perturbed. The emission process is governed by a transmission probability and the statistical distribution-function of Fermi and Dirac. Therefore, the exact location of the electrons in phase-space (position and velocity) is unknown. This means that the electron-electron forces are also unknown. The trajectory of an electron through such a field can only be described statistically, introducing a blurring term to the virtual-source size r_{vs}, and thus reducing the brightness B_r.

This blurring is likely to be more significant at greater particle densities, and therefore at higher current densities $\left(J = I/(\pi r_{vs}^2)\right)$. Due to equation (5.1), this blurring-effect increases as the brightness B_r increases. This blurring-effect is also influenced by the particle interaction-time. So at higher beam voltages, less interactions should occur. Current-densities at the source are normally high and the potential is close to zero. Therefore most Coulomb-interactions occur in this region, and they should in general always be calculated.

Electron-electron interactions are often calculated by Monte-Carlo simulations. However, Monte-Carlo simulations provide little physical insight, are time consuming, and must be recalculated for every geometry change. We are interested in analytical equations describing the amount of statistical blurring. We therefore use the extended two-particle approximation developed by Jansen [2] [52]. Although it is an approximation, it has been experimentally validated for the trajectory displacement and appears to be accurate, within the experimental error [19].

The objective of this work is to calculate the trajectory displacement due to statistical Coulomb interactions in the gun area, and determine their influence on the brightness of cold field emitters. The amount and distribution of field emitted current is directly dependent on the gun geometry and voltages, which determine the field at the emitter surface. In our model we first calculate the field on the

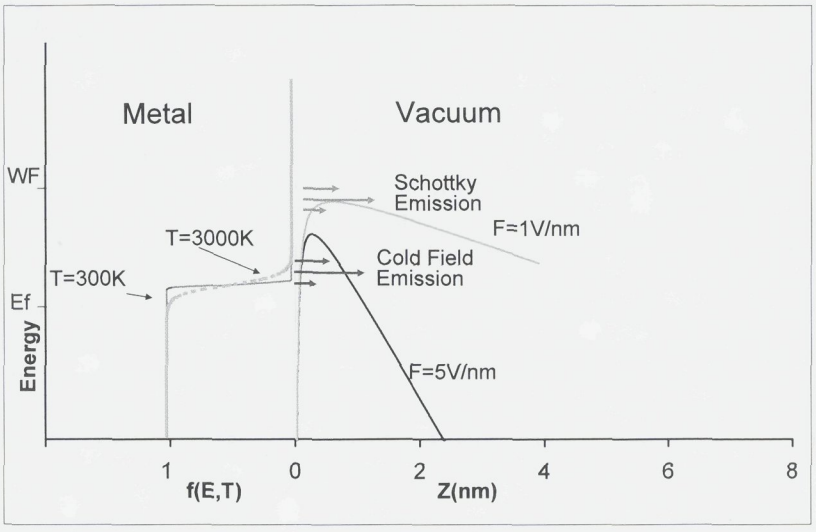

Figure 5.1: Schematic figure of cold-field emission and thermal-emission. On the left, electrons in the metal are distributed according to Fermi-Dirac statistics at T = 300 K and T = 3000 K. On the right, an image-charge barrier is shown at both fields of 1 and 5 V/nm. Due to the small width of the 5 V/nm barrier, electrons near the Fermi-energy E_f can tunnel to the vacuum (indicated by the lower arrows). For the 1 V/nm barrier there is little tunneling near the Fermi-energy and only thermally excited electrons escape. The electrons either tunnel through the top of the barrier, or escape directly due to the Schottky lowered work-function. In this model electron-electron interactions are ignored. Emission is assumed to be from a semi-infinite solid and Nottingham heating, which may cause tip melting, is ignored [49]. Hence the current density J and Reduced brightness B_r can increase almost without limit

emitter surface and then solve the emission equations.

The reader should note that statistical interactions are separate from space-charge. Where the latter creates a conservative field and smooths out the charge. It does not consider the discrete nature of the individual electrons. The interested reader is refered to [52].

5.2 Theory

The extended two-particle method splits the longitudinal and lateral electron interactions. Here we consider only B_r reduction, known as trajectory displacement originating from the lateral interactions. The method is valid for most regimes of interest in imaging and lithography machines.

It is assumed that the particle's positions and velocities are uncorrelated. Then, it approximates the many-body problem to a sum of two-body interactions on a test particle traveling along the axis. This ensures that the space-charge effect is automatically canceled out. It has been shown that an on-axis particle is representative for the beam as a whole [2]. The beam is split-up into segments with constant voltage and either a conical or cylindrical beam envelope. Although exact analytical solutions do not exist, Jansen found different regimes depending on particle density and beam geometry. For these regions, more practical and analytical solutions can be found by fitting and approximating. In order to find the trajectory displacement, we first calculate the angular displacements. The relevant equations and their regimes are shown below. For the Gaussian regime,

$$\phi_G = 0.1667 \frac{m^{1/4} e^{1/12}}{\epsilon_0^{5/6}} \frac{(J\pi)^{1/2} L^{2/3}}{V^{13/12}} \tag{5.3}$$

For the Holtsmarkian regime,

$$\phi_H = 0.128 \frac{m^{1/3}}{\epsilon_0} \frac{(J\pi)^{2/3} L}{V^{4/3}} \tag{5.4}$$

For the pencil-beam regime,

$$\phi_p = 0.429 \frac{m^{3/2}}{\epsilon_0 e^{7/2}} \frac{(J\pi)^3 r^7 L}{V^{5/2}} \tag{5.5}$$

Where m is the electron-mass, ϵ_0 is the permittivity of free space, and L is the interaction-length. The above equations are valid for large particle densities (Gaussian), low particle densities (Holtsmarkian) and low particle densities with a narrow beam (pencil-beam) respectively. These equations are only valid for a cylindrical beam-segment at a constant potential. For an electron-gun with varying potential and beam size we must apply the slice-method. The region to be calculated is divided into small segments over which the voltage and beam size is assumed to remain constant(see figure 2)

Equations (5.3), (5.4), and (5.5) have been interpolated by Jiang, so can be used without knowledge of the regime [60]. The slice-method requires the angular displacement per meter, given by

$$\phi_J = \left[\frac{T_1 D_\lambda^{18/7} D_r^6 I^{18/7} r^{6/7} V^{-15/7}}{T_4 + T_2^{1/7} D_r^6 D_\lambda^2 I^2 r^2 V^{-1}} \right]^{7/6} \tag{5.6}$$

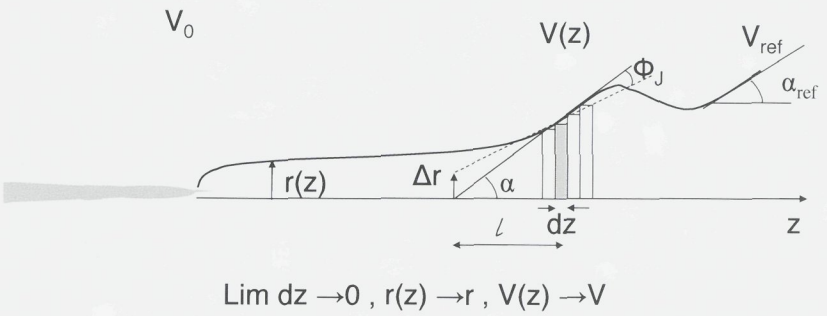

Figure 5.2: From Left to right: The needle cathode, half the beam-envelope (curved line) with beam radius $r(z)$ at potential $V(z)$ traveling along the z-axis to our reference point with voltage V_{ref}. The beam-space is split into small segments dz for which we assume that $V(z)$ and $r(z)$ are constant. The angular displacement ϕ is found from equation (5.6). The trajectory displacement is found by adding the angular displacements for each slice up to Δr_{traj} as given by equation (5.7).

Where $D_\lambda = \sqrt{\frac{m}{2e}}\frac{1}{\epsilon_0 \pi 2^7}$, $D_r = \left(\frac{2\epsilon_0 \pi}{e}\right)^{1/3}$. The constants are $T_1 = 4.618 \times 10^{-2}$, $T_2 = 2.041 \times 10^5$, and $T_4 = 6.250 \times 10^{-2}$. In the interpolation, the Gaussian-regime disappears to zero. One must be careful for large particle densities, as a Gaussian-distribution can still develop. Therefore we are limited to either a pencil-beam or Holtsmarkian-beam.

From the slice-method, the trajectory displacement is calculated by

$$r_{traj} = \int_z \frac{l(z)}{M(z)} \phi_J \left(r(z), V(z), I\right) dz \tag{5.7}$$

We find $l(z)$ from $r(z)/\alpha(z)$, $M(z)$ is the magnification $\left(= \frac{\alpha_{ref}}{\alpha(z)}\sqrt{\frac{V_{ref}}{V(z)}}\right)$. V_{ref} is the voltage at the reference plane in the field free region at 1.2mm. The virtual source radius r_{vs} is defined looking back from this plane.

The trajectory displacement translates as a blurring of the virtual source size, and so we modify B_r as,

$$B_{r(e-e)} = B_r \left(\frac{r_{vs}^2}{(r_{vs}^2 + r_{traj}^2)} \right) \tag{5.8}$$

We use a Gaussian addition rule, as it is generally a good first approximation and as in the case of [19], it seemed to work.

5.3 Method

We have developed our own suite of software at Delft to investigate Coulomb-interactions. This section describes the steps taken by the software to calculate the trajectory displacement.

The initial step is to draw the gun, and assign voltages to each section. The drawing is implemented through our vector graphics routine. Each section is defined from primitive shapes (squares, circles, triangles, ...). This allows us to define more complex geometries such as the needle cathode given by figure 5.3.

The Poisson-solver calculates the electric-field to a user defined precision (see figure 5.4 for a typical geometry). Due to the nature of the problem, we have used spherical coordinates and cylindrical symmetry. The small needle tip is at the centre (where the grid and field-lines are most dense). This is similar to SCWIM developed by Kang et al [61].

With the potential-field known, the outer electrons are ray-traced through the system. This can again be done to user defined precision. Stability criteria are checked before ray-tracing starts. In general, a step size smaller than 10^{-16} s is used. The electrons are launched immediately in front of the tip with no velocity at a height of one fourth of the tip-radius (see figure 5.3). This is somewhat unrealistic, but only serves to underestimate the Coulomb-effect by limiting the current. Experimental evidence suggests that we reach the pencil-beam regime (see section 5.4 for further discussion). This will not happen if the beam is too wide. Also, electrons traveling with large angles will do little.

We take the electric-field at the surface of the tip. If the field allows tunneling (> 0.1 V/nm), we numerically solve Schrödinger's equation with Numerov's method (see for example [62]). Similar results are obtained by using Runge Kutta [46]. Otherwise a step-barrier with Schottky lowered work-function ($\Delta W = \sqrt{Fe^3/(4\pi\epsilon_0)}$) is applied, where F is the electric field. [26]. The emission, in terms of current-density and brightness, is solved as per [46]. This is valid for almost every situation of interest, including all combinations of thermal-, field- and photo-emission.

Next, the slice-method is applied to calculate the trajectory displacement given by equation (5.7). We verify the linear particle density $\left(= Ie/\sqrt{2eV/m}\right)$ and the beam size to insure that we do not work outside the limitations of our equations.

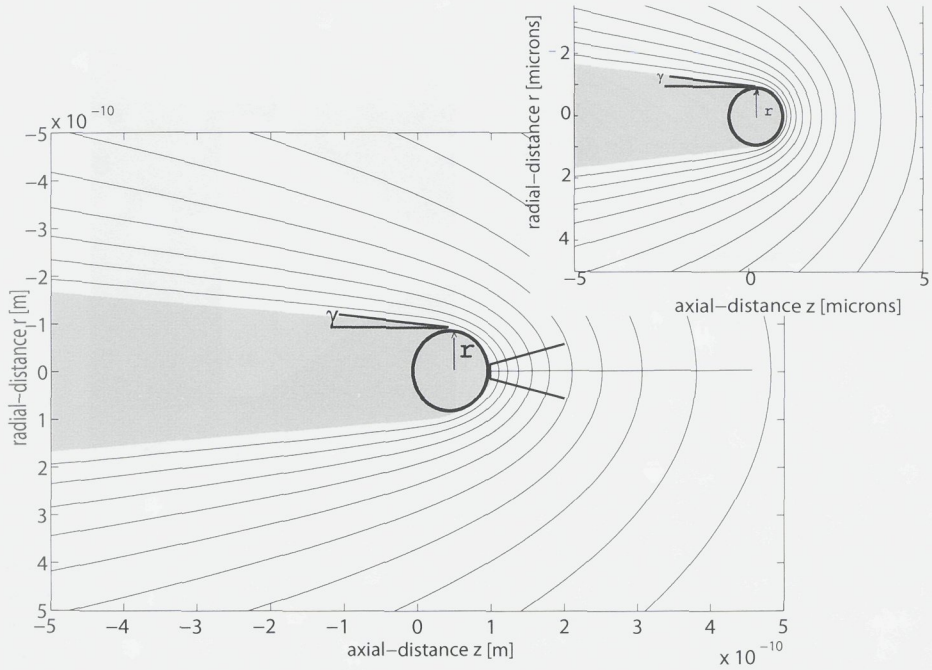

Figure 5.3: Close-up of an atomically sharp tip with equipotential lines. The inset is a close-up of a 1 μm tip. The tip scales with regard to the tip-radius r, having constant cone-angle γ. The field around each tip is smooth and scales as expected. The black cone coming from the end of the field-emission tip indicates where we allow the current to come from. This may be arbitrary, but allowing extra current only increases Coulomb-interactions.

Variables are saved and the whole procedure is repeated with the required variable changed.

5.4 Results and Discussion

After verifying that our software reproduces previously found results [19] [63] [64], we were intrigued to investigate the atomically sharp tips within figure 5.3. Although our atomic tip may be impossible to achieve in reality, they are simple to generate, and a valid shape to start investigating fundamental limits. The intrinsic reduced brightness B_r of a (cold) field emission tip is determined by the field, and the work function of the emitter. Tungsten is widely used, and a work function of 4.3eV is reasonable. To discover how $B_{r(e-e)}$ varied with field we changed the extractor voltage creating figure 5.5. Our expectation was that as the extractor voltage increases so would B_r and $B_{r(e-e)}$. From the experimental results mentioned in section 5.1 we expected that at around $10^9 \mathrm{A}/(\mathrm{m}^2\mathrm{srV})$ $B_{r(e-e)}$

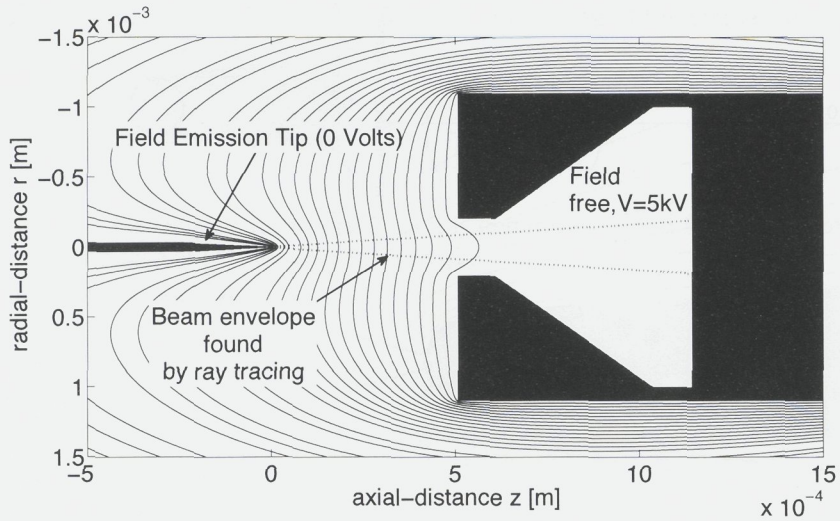

Figure 5.4: Schematic figure of the gun geometry. As indicated, the field-emission tip (for this figure $r = 1\mu\text{m}$) is at ground potential. The extractor for this example is at 5 kV. There is a field-free zone after the extractor. The beam-envelope is shown with a dotted black line. The trajectory appears straight on this scale.

would drop slowly away from B_r. We thought this should be slow due to the inverse proportionality of r_{traj} to V. Hence we were surprised to see it quickly reach a maximum at $5 \times 10^{10}\text{A}/(\text{m}^2\text{srV})$ and fall away. For all points on the graph we are within the Holtsmark /pencil beam regime. Probably mostly influenced by the pencil beam. The behavior stems from the $I^3/V^{2.5}$ in the pencil beam regime, and the exponential dependence of I with surface field.

To see the trend in the maximum brightness we calculated $B_{r(e-e)}$ for several other tip radii. Results are plotted in figure 6. The maxima do not follow directly the tip radius, we expected the brightest would be the atomically sharp tip, and the least bright the $1\mu\text{m}$ tip. Our logic was based on traditional wisdom that sharp tips are best. By reducing the total number of electrons the Coulomb interactions should decrease. However this trend is bucked. The bluntest tip has almost comparable brightness to a 1nm tip. We wanted to check whether this was a computational error. We calculated analytically, using equations (5.4) and (5.5), the trajectory displacement for a cylindrical beam segment with constant radius and voltage. The field on the tip is determined by (V/L) with $L = 0.5\text{mm}$ (see inset figure 5.7), and the intrinsic brightness B_r is calculated as $B_r = \frac{eJ}{\pi d}$. where $J = \frac{4\pi me}{h^3} d^2 exp(-W/d)$ and $d = \frac{ehF}{4\pi\sqrt{(2mW)}}$, $W =$ material's work function, and h is Plancks constant see [54] or [26]. The virtual source contribution of each regime is added together using 1/Total=1/Holtsmark+1/Pencil, according to the addition rule of [52]. This is also a method of interpolating between the two regimes. The result is shown in fig 5.7.

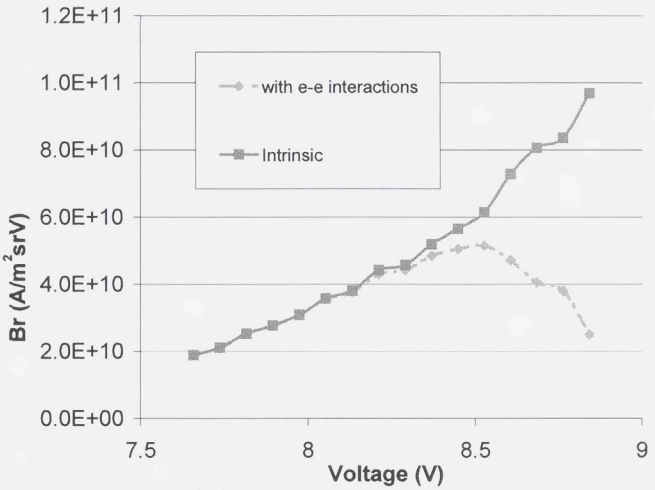

Figure 5.5: Reduced Brightness of an atomically sharp tip (100pmradius) as a function of Extractor Voltage. The upper solid line with □s is the intrinsic B_r without Coulomb interactions, the middle dot-dash line with ◇s includes Coulomb interactions. Initially the Coulomb interactions have very little effect on the brightness, but once r_{traj} becomes comparable to the r_{vs}, $B_{r(e-e)}$ the effect of the trajectory displacement is felt and we quickly reach a maximum at 8.5 Volts and $B_r = 5 \times 10^{10}$

The analytical work is similar to the fully numerical result. We can be certain that the effect is not due to erroneous computations. This analytical approach can never be as accurate as the numerical because around a sharp tip the potential and beam radius change very rapidly, as does the beam radius.

The observed behavior stems from competition between the Holtsmark and pencil beam regimes. To better see the dependence of $B_{r(e-e)}$ we plotted separately the contributions of the pencil beam and the Holtsmark in figure 5.8. The pencil beam scales with I and r, hence as both increase so the brightness of a pencil beam drops off. The Holtsmark regime is dependent on current density so the trajectory displacement is constant for all beam sizes (in this example). The only method to change $B_{r(e-e)}$ is due to the intrinsic source radius (which we specify as S_r). So according to $B_{r(e-e)} = B_r \frac{S_r^2}{(S_r^2 + S_{r(e-e)}{}^2)}$ as we increase S_r the effect of a constant $S_{r(e-e)}$ decreases. This means that if we are in the Holtsmark regime or in fact even the Gaussian (see equation(5.3)) bigger cathodes are less affected by

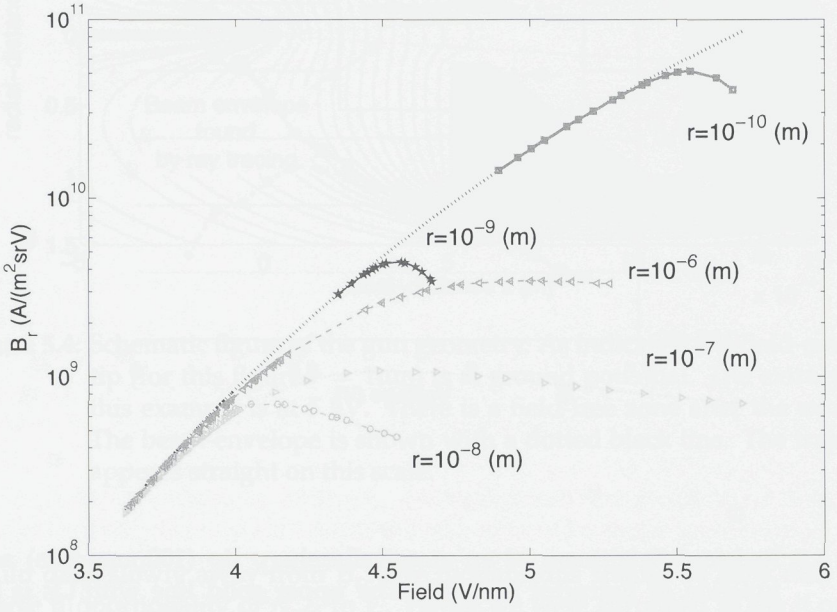

Figure 5.6: Brightness as a function of field for various source radii, with and without Coulomb interactions. Dotted line without marker is intrinsic B_r without Coulomb interactions. Solid line with □s is for a source radius of 10^{-10}m including Coulomb interactions. Solid line with ⋆s is a source radius of 10^{-9}m including Coulomb interactions. Dashed line with ◁s is a source radius of 10^{-6}m. Dotted line with ▷s is a source radius of 10^{-7}m. Dashed line with ◯s is a source radius of 10^{-8}m. The two smallest radii have the sharpest cut off/clearest maximum and as the emitter radius increases so the gradient around the maximum decreases. However the most striking feature of this graph is that the emitter with the $1\mu m$ radius has a brightness well above that of the 100nm and 10nm emitters.

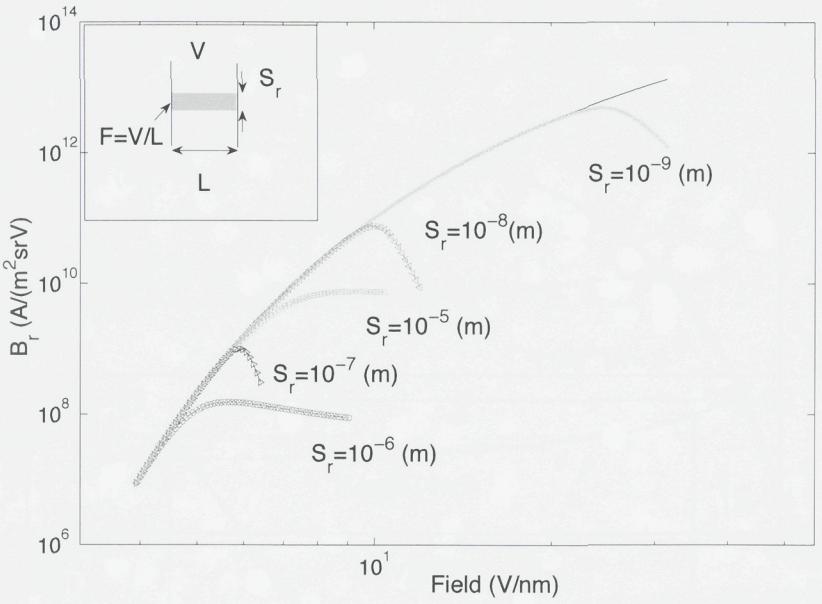

Figure 5.7: Analytical plot of Brightness vs Field for different tip radii. Inset shows the layout used for this experiment. V is not the extractor voltage but the potential of the beam from the start. In other words the beam has a constant velocity. The emission current is calculated from a pseudo field given by (V/L) the solid line without markers is the intrinsic Brightness B_r. The line with $\star$'s is for a 1nm source with Coulomb interactions. $\triangleright$ is 10nm with Coulomb interactions. $\square$ is $10\mu\text{m}$ with Coulomb interactions. $\triangleleft$ is 100nm with Coulomb interactions. $\bigcirc$ is $1\mu\text{m}$ with Coulomb interactions. Just like the numerically produced results the blunter tip has a larger brightness than sharper tips ($1\mu\text{m}$, and 100nm). This demonstrates that the effect is not due to miscalculation of fields or ray tracing

Coulomb interactions than smaller. However, other practical issues involved with generating the fields give difficulties.

For our larger tips we must be careful that we are not in the Gaussian regime, this is not suited to the slice method. At the maximum brightness we are close. However when the brightness drops to 90 % of its intrinsic value ($B_{r(e-e)} = 0.9B_r$), we are still valid for all tip sizes investigated. To summarise our findings we plotted the value of B_r for $B_{r(e-e)} = 0.9B_r$ for different tip sizes in figure 5.9. Included are also a Schottky tip and PHAST, (Photo Assisted Schottky Tip) taken from [64] and [63] respectively. They are from different set-ups with only similar parameters, so care must be taken when making comparisons, however they are brighter than our 100nm tips. It is worth noting that the Schottky tips in [63] [64] have T=1800K, and W=2.8eV. Due to the high temperature it has good stability

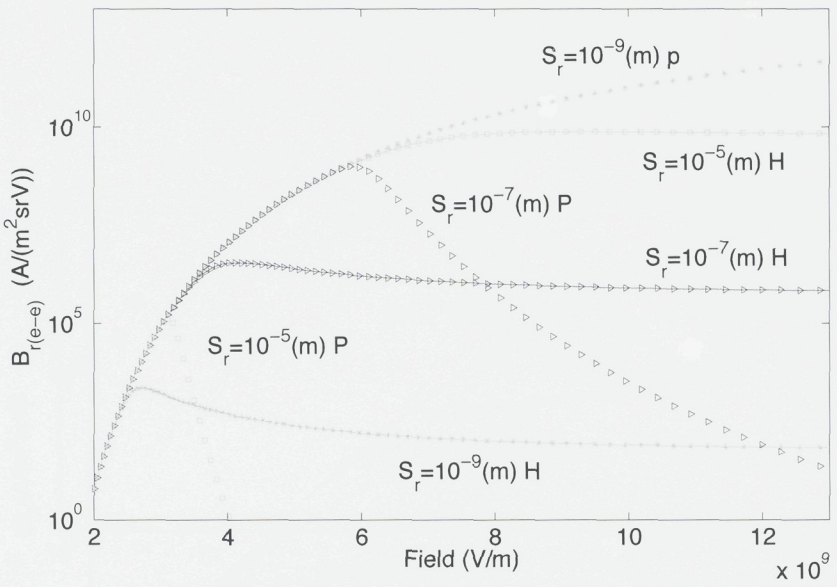

Figure 5.8: Reduced Brightness with Holtsmark and Pencil Beam contributions shown separately labelled H and P respectively. Pencil Beam has no line and Holtsmark a solid line. *s are for $S_r = 10^{-9}$, ▷s for $S_r = 10^{-7}$, □s for $S_r = 10^{-5}$. We can see that the pencil beam scales with $r_v s$ and the Holtsmark regime follows inversely.

(the surface remains free of dirt), and tends to have a longer lifetime than cold field emitters. Thus although intrinsically B_r is less, when Coulomb effects are taken into account, it performs as well as the cold field emitter. We have also included the current used in the calculation for reference. All tips would be suitable for imaging, though perhaps the smaller ones would be limiting for lithography.

5.5 Conclusions

We find that Coulomb interactions significantly limit B_r in cold field emitters. Claims of B_r greater than $10^{12}\mathrm{A}/(\mathrm{m}^2\mathrm{srV})$ should be viewed with caution, we expect that most field emitters have B_r of $10^8\mathrm{A}/(\mathrm{m}^2\mathrm{srV})$ with only a few working at their true potential. Our conclusion is, that when designing electron guns, with cold field emitters, Coulomb interactions must be taken into account, otherwise the extra hassle (ultra high vacuum, regular flash cleaning, short lifetime) associated with cold field emission will be wasted.

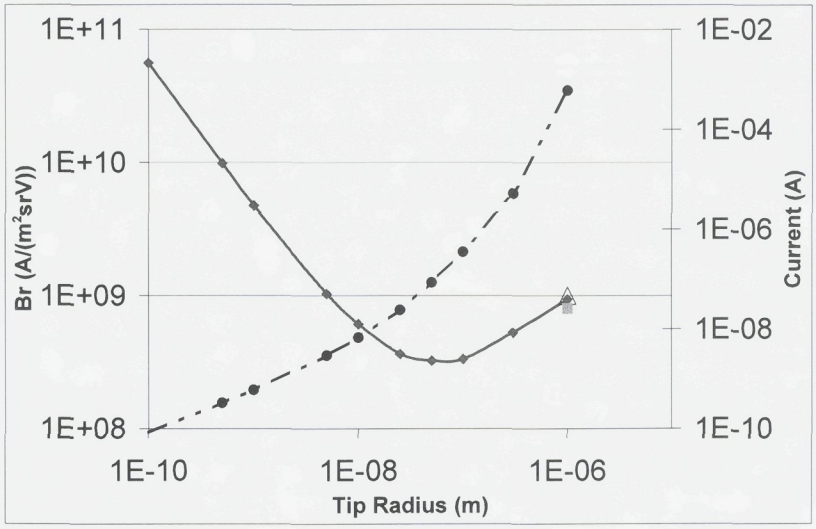

Figure 5.9: Solid Line with ◇s Brightness at 10% reduction ($B_{r(e-e)} = 0.9B_r$), as a function of tip radius, for cold field emitters.Dashsed line with ◯ current at 10% reduction (right axis).The △ and □ are aproximate values for a Schottky emitter and PHAST (see section 5.4) It's important to note the minimum at 10 nm due to the competition between the pencil beam and the Holtsmark regime.

6 CHAPTER

N Body Simulations of Cold Field Emitters

The battlefield is a scene of constant chaos. The winner will be the one who controls that chaos, both his own and the enemies

Napolean

Statistical Coulomb interactions significantly reduce beam quality. For low voltage applications this may be the limiting factor, as the current in a probe of fixed size scales directly with the reduced brightness and the inverse square of the energy spread - $I \propto B_r/(\Delta E.^2)$. We examined statistical Coulomb effects in the gun region of cold field emitters. Two methods are presented a full N body simulation and an approximation called the extended 2 body method [2], adapted for regions of rapidly changing potential -the slice method [65] . We find that for the two tip sizes studied, 10 nm and 50 nm it is the reduction in brightness that is most serious, not ΔE, and in our set-up for both tips a field of around 4.25 V/ nm would maximize probe current.

This chapter was published in the proceedings of the 24th IVNC in 2011 held at Wuppertal under the title Statistical Coulomb interactions in cold field emitters

6.1 Introduction

Low voltage electron microscopy (LVEM) is a useful tool; it has good surface sensitivity, low radiation damage, and contrast mechanisms also change with the voltage. To study nano science we would like a nanoprobe with a large current I, when limited by chromatic aberrations I (for a probe of fixed size) scales as

$I_{probe} \propto \frac{B_r}{\Delta E^2}$ this means a high reduced brightness B_r and low energy spread ΔE are needed. In figure 6.1 we see how I_{probe} scales as a function of field for three different emitters. The Schottky source with its low work function ϕ outperforms the thermal field emitter, yet the Schottky source usually works at around 0.5 V/nm, and a thermal field emitter must work at an even lower field since at such a high temperature the mobile tungsten is deformed. The cold field emitter is typically used at a few volts per nanometre and above 3 V/nm it outperforms a Schottky source working at 0.5 V/nm. The cold field emitter is able to do this because the intrinsic energy spread is many times less than the other two emitters.

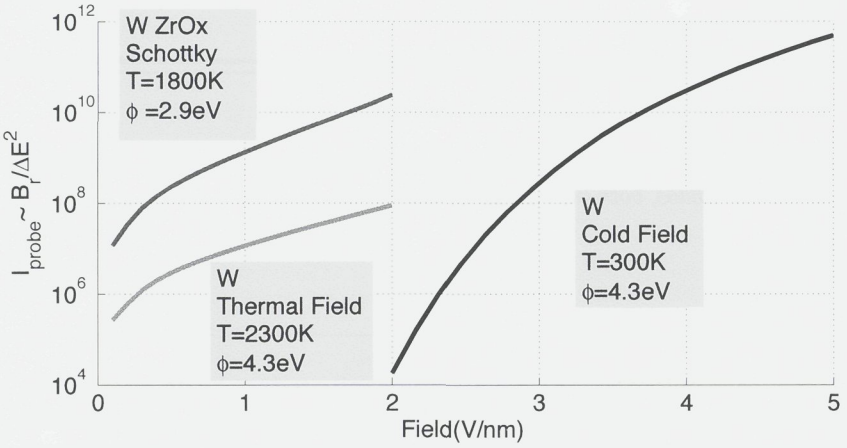

Figure 6.1: $B_r/\Delta E^2$ as a function of field for three different emitters. A Schottky source, a thermal field emitter and a cold field emitter. Units of the y axis are $\mathrm{A}/\left(\mathrm{m^2srV}\right)\left(\mathrm{eV}\right)^{-2}$

Although energy filters can reduce ΔE they also reduce B_r, cold field emitters can be difficult to work with, but are highly monochromatic, and have high B_r. Increasing the field on these emitters increases B_r but also the intrinsic (with out Coulomb interactions) ΔE. However the increase in B_r is fast enough that we do not see any effect from the increase in ΔE. In the literature it is possible to find B_r values as high as $10^{14}(A/m^2SRV)$ [66], yet these are not properly measured, and we do not know of any tool which can form a probe with this B_r. In [65], we suggested that stochastic Coulomb interactions in the gun area limit B_r to at best $10^{11}(A/m^2SRV)$, but for LVEM ΔE should be looked at. In [65] a semi-analytical approximation called the slice method was used (this is based on the extended 2 body model of Jansen see [2]), and now we back this up with N-Body simulations using GPT from pulsar physics .

6.2 Method

We solved the Laplace equation on a spherical grid as per [65], this gives accuracy at the nanometre sized tip, with out excessive grid sizes. Emission characteristics are numerically calculated using Fermi-Dirac statistics, solving the Schroedinger equation and taking the on axis field immediately in front of the tip. The electrons are ray traced over 1 mm and the effect of Coulomb interactions found. This is done either by using a semi-analytical approximation from the extended 2 body method, called the slice method [2] or an N-Body calculation using GPT [67] (with custom field import and high accuracy Barnes Hut method [68]). To compare the slice and N-Body method we must start the electrons with zero energy spread and infinite B_r (0 emittance). The N-body simulation requires more accurate starting parameters than the slice method, so in contrast to [65] we start the electrons on a shell $5nm$ from the tip, with a uniform distribution, and a maximum angle of $\frac{1}{4}rad$. Their velocity (taken from the potential) is pointed directly outwards from the centre of the tip.The brightness is found by adding the increased virtual source size (full width with 50 percent of I FW50) to the intrinsic as $r^2_{total} = r^2_{intrin} + r^2_{Coulomb}$, ΔE is done in the same way. Due to the small virtual source size aberrations and or numerical errors from the finite grid size can be significant. We are not looking at aberrations, so to find $r_{Coulomb}$ we run the simulation with and without interactions turned on. Then we subtract the position of each electron in the focused spot one from the other so only Coulomb interactions contribute to the $r_{Coulomb}$. The gun layout is shown in figure 6.2 Further details are in [65].

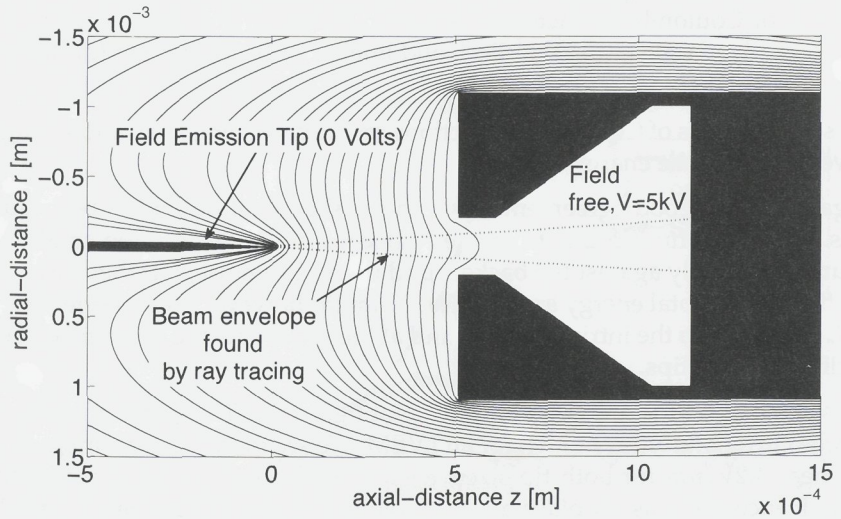

Figure 6.2: Gun geometry simulated,with contour plot showing a calculated field. A typical voltage in the field free region could be 5kV for a large tip.

6.3 Results

In figure 6.3 we see a comparison of the semi-analytical slice method used in [65] and first results of a full N-body simulation using GPT [67] . We looked at a 10nm tip and a 50nm tip. There is good agreement between the two methods. Despite a lack of points for the N-body method, both show a maximum in B_r. If we compare with our previous paper [65] it might seem strange that the $50nm$ tip has a high brightness than the 10 nm. This is not a mistake, in the final figure of [65] we did not plot the maximum brightness, but the B_r at 80% of the B_r without Coulomb interactions. With this measure the $10nm$ tip outperforms the $50nm$ tip.

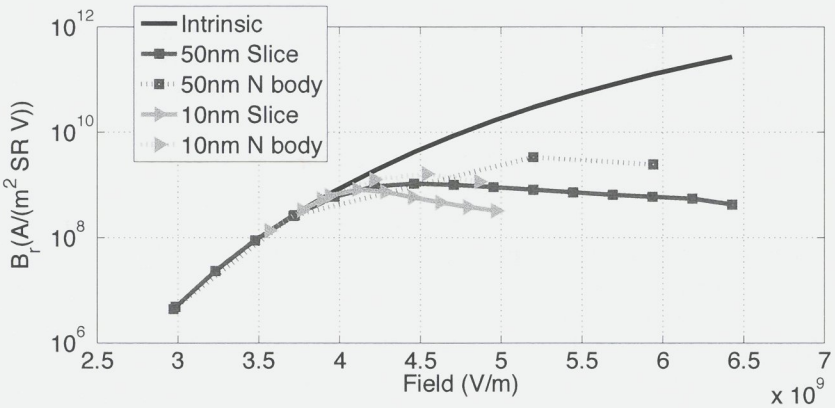

Figure 6.3: Intrinsic Brightness of a field emitter (solid black line) and the effects of Coulomb interactions on a 50nm (blue □) and 10nm (green ▷) tip solved with either the slice(solid line) or N-Body method (dotted line)

To see the effects of Coulomb interactions on the chromatic aberration in figure 1.13 we examined the energy spread.

Again there is good agreement between the slice method and N-body simulations. For the 10nm tip ΔE from the N-Body simulations are too small to be measured accurately against the background numerical noise, but they have very little effect on the total energy spread. The 50nm tip however sees a large increase in ΔE, compared to the intrinsic value, and at the same time the brightness begins to decline for both tips.

To see the effect for probe forming we plot figure 6.5. The y axis is essentially the probe current (arbitrary units) for an LVEM. We see there is a maximum in this graph near $4.2V/nm$ for both tip sizes, even though their energy spreads differ greatly. Hence it seems B_r plays a larger role in limiting the probe current than ΔE . .

In [65] we used the slice method to see how Coulomb interactions effected B_r as a function of tip radius, we can now do the same thing and see how they effect the $B_r/\delta E^2$. In this way we can say what is the best emitter radius for a cold field

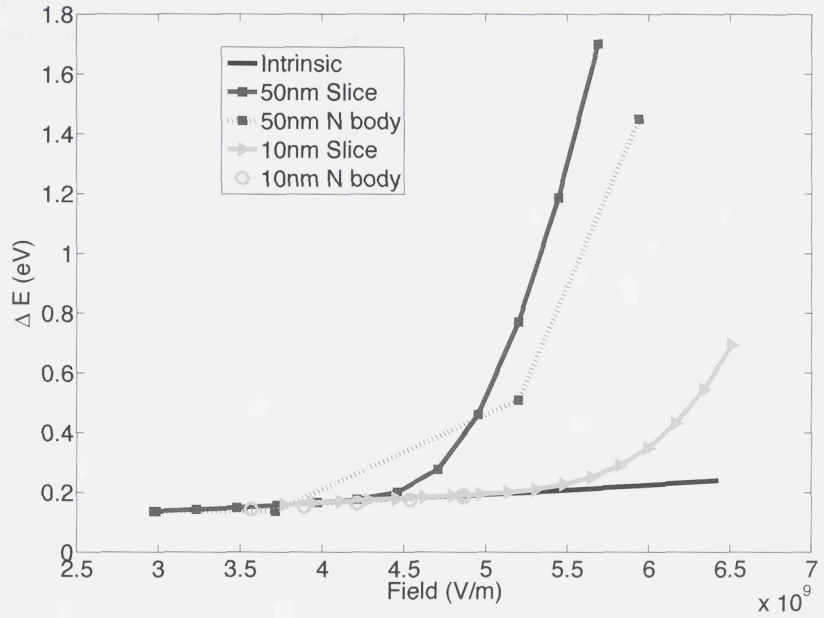

Figure 6.4: Intrinsic Energy spread of a field emitter (solid black line) and the effects of Coulomb interactions on a 50nm (blue □) and 10nm (green ▷ or ◯) tip solved with either the slice(solid line) or N-Body method (dotted line). Note for the 10nm ΔE the N-body is indicated with a large circle to make it visible against the intrinsic, and slice method.

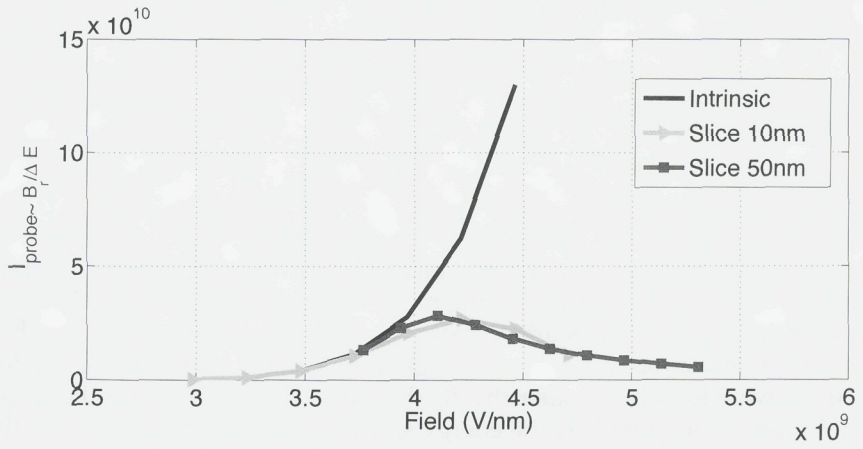

Figure 6.5: Shows probe current with arbitrary scale vs Field at tip for an Intrinsic solid black line), and the effects of Coulomb interactions on a 50nm (blue □) and 10nm (green ▷) tip solved with the slice method.

emitter when working in a chromatically aberrated system. This has been plotted in figure 6.6, where we have used the analytical slice method to calculate the interactions. Looking at the line for the cold field emitter we see that the possible

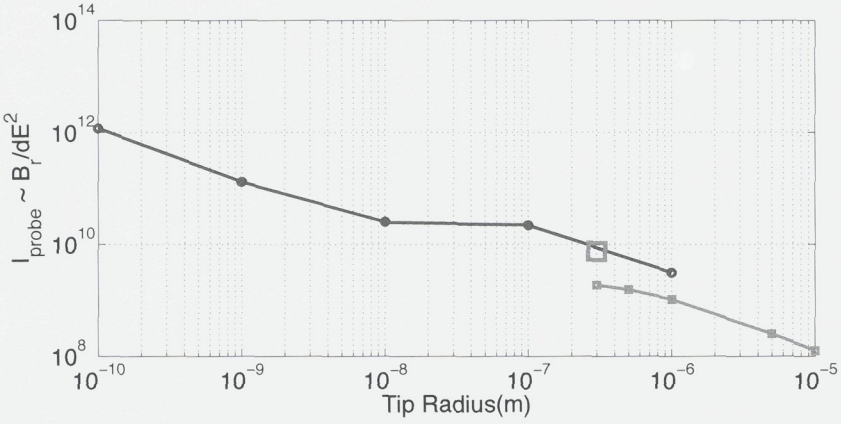

Figure 6.6: Maximum of $B_r/\Delta E^2$ as a function of tip radius for a W cold field emitter blue line with ∘ markers and a Schottky source red line with □ markers, the large red □ is for a Schottky emitter with a monochromator. Units of the y axis are $\mathrm{A}/\left(\mathrm{m}^2\mathrm{srV}\right)\left(\mathrm{eV}\right)^{-2}$

probe current increases for a smaller tip radius, this matches are expectation from [65], and we can that the B_r is increasing much faster than the ΔE. Again in the middle of the graph the curve starts to flatten out, this is again expected from [65] since at this point we found a regime change from a pencil beam to an extended beam. If we were to only consider the B_r the curve would go up for the larger tip radi, however the growth of the energy spread become dominant and so the I_{probe} drops. What we must remember however is that there is a limited current available from a small radius emitter, so it is possible that for some applications the system can become current limited. For example a one nanometre cold field tip would probably not be useful for lithography where high currents are needed.

6.4 Conclusion

Probe current in low voltage electron microscopy is limited by brightness, with the energy spread playing a less significant role. There is a best field to work at (in our case around $4.2V/nm$), increasing that field further will not improve the probe current. Furthermore given the approximations involved there is a good agreement between the slice method and the N-Body simulation. It should be expected that the slice method overestimates the effect of interactions at high B_r however, it does give us the general trend and as such is useful for gun design where the ability to rapidly see the effects of changes is important.

Part II

Part 2 - Electron Sources for Ultra Fast Imaging

7 CHAPTER

A review of Electron Guns for Ultra-fast Microscopy

I love criticism just so long as it's unqualified praise
Noel Coward

Guns for ultra-fast electron imaging are reviewed. We find most can't be brighter than $B_r = 10^6$ A/ $\left(\mathrm{m}^2\mathrm{srV}\right)$, and have an emittance (ϵ) so high only the largest crystals in diffraction mode (LAD) can be examined.

We have tried to appraised all types of guns suitable for ultra-fast electron microscopy (UFEM). The results are presented graphically concentrating on their B_r, emittance, pulse length and pulse charge. The calculations for all guns are in the appendix.

Different types of imaging are analysed (section 7.3) and summarised in tables 7.1 and 7.2 these eventually lead to the conclusion that single shot UFEM is impossible. However single shot LAD is possible, and has been demonstrated [69],[70],[71].

The guns are split into three sections Flat Photo Cathodes, Sharp Tips and Novel Guns. Most UFEM experiments use a DC Flat Photo Cathode (DC - Direct Current i.e a static voltage between cathode and anode). The DC guns have limited B_r due to space charge at the cathode and space charge expansion during flight. We calculate their B_r can not be better than 10^6 A/ $\left(\mathrm{m}^2\mathrm{srV}\right)$, and this is upheld by the reviewed guns. Guns exist which beat space charge leading to an increase in B_r by more than 100 times, unfortunately none have performed a true UFEM experiment yet. This is discussed in section 7.5.5. Sharp tips have a $B_r \approx 10^9$ A/ $\left(\mathrm{m}^2\mathrm{srV}\right)$ and are routinely used in static electron microscopy yet they are surprising uncommon in UFEM. The novel guns are interesting ideas for the future, they are not fully developed at the time of writing, so can not be expected to perform as well as some of the other guns which have had many years of research . We conclude that future gun design should focus on increasing B_r.

7.1 Introduction

Electron microscopes and electron diffraction have been slowly uncovering the world on the nanometer and below scale since the beginning of the 20th century, when Thompson discovered the electron [72], and Davisson and Germer [6], proved the de Brogle hypothesis that electrons have a wave like nature. Modern electron microscopes, allow us to see in real space individual atoms in solids with very little effort.

Dispite this even state of the art commercial Transmission Electron Microscopes (TEM) allow only static or video rate pictures, yet many processes happen on a fast (ns) or ultra-fast (ps) time scale. Thus we need Ultra-Fast Electron Microscopy (UFEM) to learn more about these dynamic processes.

The basic design of a UFEM instrument is shown in figure 7.1. In a UFEM experiment we need to controllably start a dynamic process and then at some later point in time observe what has happened, see caption of figure 7.1 for more detail.

UFEM offers many advantages over the more traditional x-ray analysis such as, real space imaging [73], smaller (10 nm) sample sizes [74], stronger scattering, less damaging, multi-diffraction orders possible per shot , and a table top set-up [75]. UFEM is still in the home made stage yet it is becoming increasingly important, figure 7.2 shows that the number of publications on this topic is growing.

There are many reviews on UFEM, for example [15], or [76], but there are none on the instrumentation. Since the electron gun ultimately determines the performance of a microscope, the phrase 'rubbish in rubbish out' applies. Making a working UFEM system is complicated, time consuming, and first builds are unlikely to work bug free, so a simple approach works best. Today however there appear to be many working set-ups, even 2nd, 3rd or 4th generation systems exist, so it is time for a more considered approach to gun design. In this review, we look at the current state of the art of electron guns, for high resolution, ultra-fast imaging and diffraction. As far as we are aware there are no other reviews with the same depth, which surveys so many guns, or gives a similarly reasoned outlook for the future of UFEM and UFEM guns.

7.1.1 Outline

First in section 7.1.2 we will look at the spatial and temporal performance of recent ultra-fast experiments, then in 7.1.3 we define three UFEM modes and give examples. Next we should talk about the requirements of imaging or creating diffraction patterns, however first section 7.2 gives a list and definition of the parameters that will be used in the rest of the report. We can now show (section 7.3) that to make an image or diffraction pattern the electron gun's parameters must meet certain values. By examining the limitations of guns in section 7.4, we begin to understand, the need for the different UFEM modes, and can make predictions

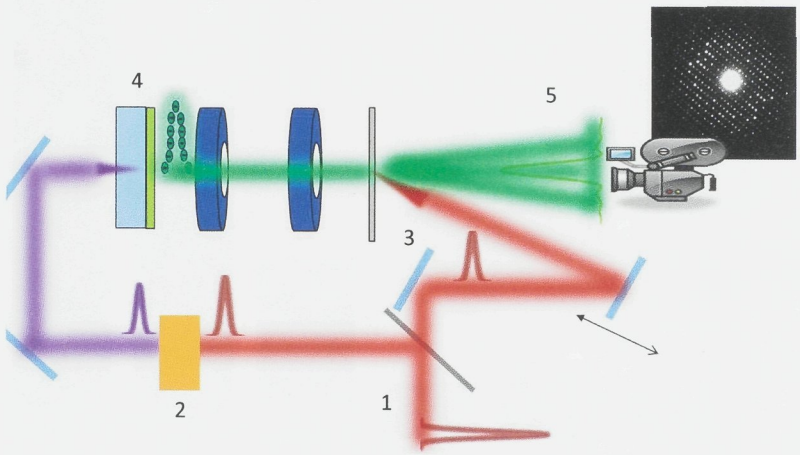

Figure 7.1: Schematic of a UFEM set-up for performing UED (Ultra-fast Electron Diffraction). Imaging set-ups are similar. Following the labels, (1) an ultra-fast (typically) infrared laser pulse is split into two pulses (2) one pulse frequency tripled by a non-linear optical crystal, the other (3) pumps the sample. The first now ultra violet pulse excites the photo cathode (4) creating an electron bunch which then probes the sample (5). The delay between pump and probe is controlled by the path length of the laser.

about the next section, where we review the UFEM guns. Section 7.5 tries to compress a great deal of information about many UFEM guns into several pertinent graphs and parameters, which are directly useful to evaluate the fitness of a gun for a task. We also examine our predictions from the previous section. The final sections look at the different types of guns in more details giving reasons for their current performance and what their ultimate performance might be.

Finally drawing together all the information we conclude with recommendations for any future UFEM guns and an outlook for the general future of UFEM.

7.1.2 Temporal and Spatial Resolution in UFEM Experiments

To see atoms move we will need some minimum temporal and spatial resolution, which we can estimate as follows. Atomic vibrations are of the order of the lattice

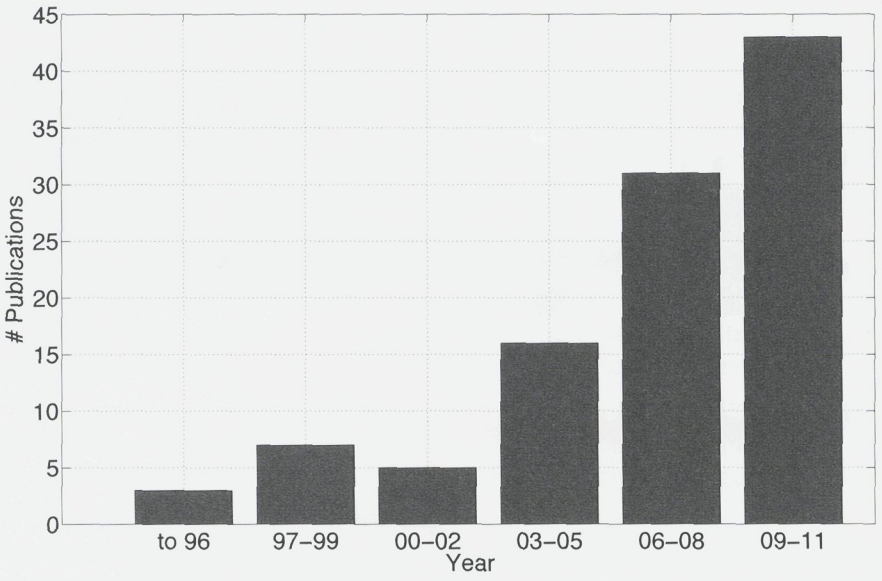

Figure 7.2: Number of publications found on the Web of Science search string " Title=(ultrafast) AND Title=(electron) AND Title=(diffraction OR microscopy) AND Year Published=(X)". Even with this restrictive search string this topic is clearly becoming more and more important.

constant, and occur at the speed of sound in that material. A popular sample is silicon which has a lattice constant of 0.54 nm [39] and the speed of sound in silicon is 8433 m/s [77] at room temperature. For a silicon atom to move one lattice constant would take it 64 fs, the requirements for atomic resolution and are shown in figure 7.3. The red box extends to 0.54 nm and 64 fs, some real experiments are also shown in figure 7.4. We will define $r_{atomic} = 0.1$ nm since this would allow good imaging of the Si lattice and $\tau_{atomic} = 100$ fs even though many experiments are capable of viewing atomic change with longer time scales than the 64 fs we calculated for viewing the vibrations of a silicon lattice. For example another popular experiment is the phase change of ice to water, from a kinetic energy argument we find a root mean squared speed of a water molecules $\approx 2\times10^3$m/s, the lattice constant of water is also a little larger than Si so a temporal resolution of a few 100 fs is reasonable. However we stick with $\tau_{atomic} = 100$ fs as a good order of magnitude estimate, note that as the experiments do not have 64 fs time resolution, then , we can expect that there are many phenomenon still to discover as the temporal resolution improves. Actually work is being done by Baum to achieve attosecond resolution to try and follow the electron motion within a solid [78].

Figure 7.4 gives information on the highest resolution (upper right point of line) achieved in selected ultra fast experiments and the total sampled area and

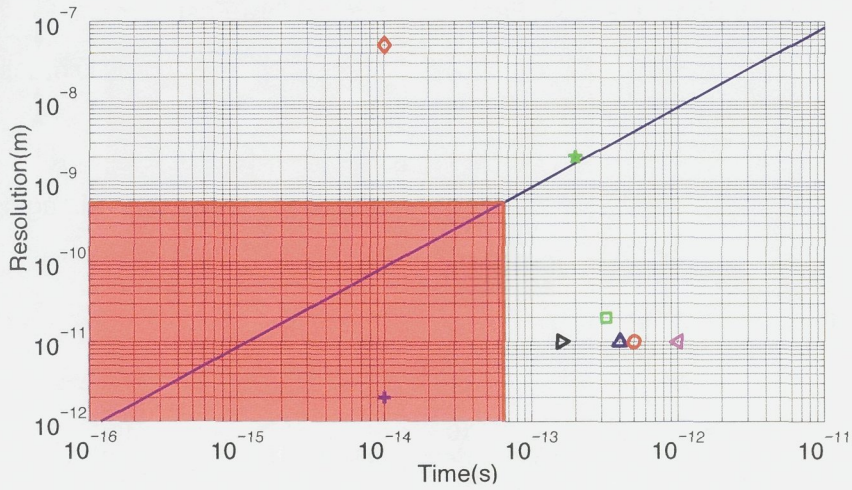

Figure 7.3: Shows the requirement for atomic resolution, as a time distance graph. The gradient of the line is the speed of sound in silicon $8433\ \mathrm{m/s}$. The red box goes from (0, 0) to one lattice constant of Si ($0.54\ \mathrm{nm}$), and the corresponding time $64\ \mathrm{fs} = \frac{0.54\ \mathrm{nm}}{8433\ \mathrm{m/s}}$. The markers indicate experiments and are also shown in figure 7.4. They are from the following publications the green $\star$ [73],blue $+$ [79],red $\diamondsuit$ [80],green $\square$ [81],pink $\triangleleft$ [82],black $\triangleright$ [69], blue $\triangle$ [83], red $\circ$ [74]

time (lower left point of line). The best resolution for an imaging system in figure 7.4 (using electrons) is $200\ \mathrm{fs}$ and $1\ \mathrm{nm}$ however this image was captured over many seconds. The best resolution in diffraction is $160\ \mathrm{fs}$ and $0.01\ \mathrm{nm}$, caution here since the sampled radius is $\approx 100\ \mu\mathrm{m}$ where as the static TEM can take diffraction from samples with $< 10\ \mathrm{nm}$ radius. For comparison, a light microscope and an X-ray free electron laser are included. The static TEM microscope has 10 times better spatial resolution in imaging mode than its ultra fast cousin, but they have the same resolution in diffraction. Please note that the sampled area in diffraction is typically much larger for UFEM than static TEM.

7.1.3 Modes Of Ultra-Fast Electron Microscopy

Ultra-fast Electron microscopy can be split into different modes which we briefly describe. All the modes follow the outline given in section 7.1, and each can be further divided into a diffraction mode and an imaging mode. It should be possible to see how these modes arise, from figure 7.4.

Stroboscopic - few electrons per pulse

In this method a single or few electrons per pulse are used to repeatedly image the same time step in a reversible (and highly repeatable) process. Stroboscopy

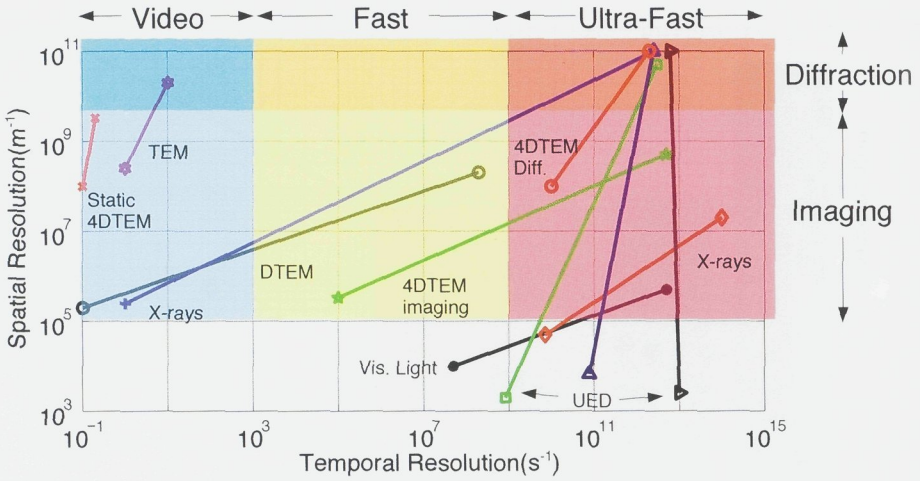

Figure 7.4: Spatial and temporal dimensions of recent imaging and diffraction experiments. The boxes give a rough guide to the type of imaging that can be done. The upper right of a box is the best time and space resolution. The experiments are marked with two points connected by a line, the bottom point is the radius of the area sampled and the top is the resolution achieved. Note that the temporal resolutions in the upper right corner have been altered slightly to make the experiments visible otherwise on this scale they would appear as one point, since this is more of a qualitative than quantitative graph it does not effect the conclusions. The lines come from the following references; red $\times$ [73]; pink $\star$ [84];black $\circ$ [85]; blue $+$[79];green $\star$ [73];pink $\triangleleft$ [82]; black $\bullet$ [86] ;red $\circ$ [74]; red $\diamond$ [80];green $\square$ [81] ; blue $\triangle$ [83];black $\triangleright$ [69]

in its original usage was for viewing a fast process in a single shot with light optics, but according to [87] it can mean illuminating a process by a short pulse of light. The difference between this method and repeated (see section 7.1.3) is the number of electrons included in a pulse. Stroboscopy gives the best resolution (1 nm, 200 fs) for imaging. Most of this work is done at Caltech in the group of Ahmed Zewail. They use a modified TEM, which they call a 4DTEM (please do not confuse the 4DTEM -Four Dimension TEM - with the DTEM - Dynamic TEM - see section 7.1.3 they are two separate microscopes). Looking at figure 7.4, we can see that in imaging mode the 4DTEM is the only solution which gets close to atomic resolution. This is also the only solution for diffraction from small areas, such as convergent beam diffraction. A resolution of 3.4Å is possible in the 4DTEM when with a static image compared to the ultra-fast resolution of 1 nm (figure 1 of [73]). The imaging line on figure 7.4 is from the experiment shown in Figure 7.5 taken from Barwick et al [73], here a gold film is heated and later imaged.

The line marked with red circles in 7.4 from Yurtsever [74] is for stroboscopic convergent beam diffraction (probe radius $10 - 300$ nm), and it comes again from

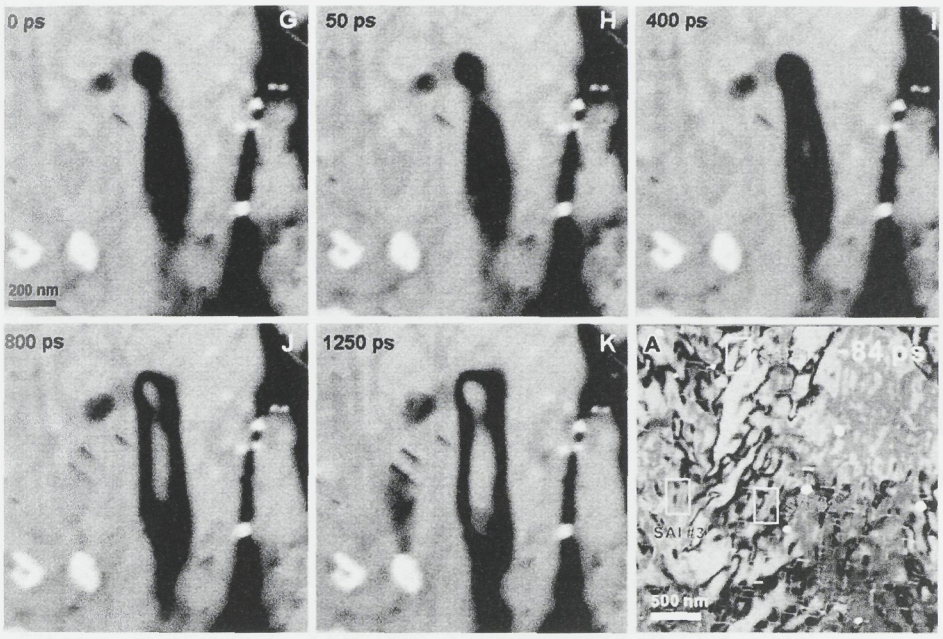

Figure 7.5: Stroboscopic images taken in the 4D microscope at Caltech this comes from figure 2 of [73] reproduced with permission. The sample is an 11 nm thick gold film whas was heated with $1.7\mathrm{mJ}/\ \mathrm{cm}^2$ from a femtosecond laser pulse, and then imaged after a few ps , (time delays indicated top left corner). The first 5 pictures are at high magnification presumably from SAI#2 (Selected Area Image number 2) as marked on the final image.

the 4DTEM at Caltech. They investigated the dynamics of laser heated silicon, the lattice vibrations were measured to decay over a few 10's of picoseconds.
Recently [88] Caltech have also made an ultra-fast scanning electron microscope.

Repeated $\approx$ 10,000 electrons per pulse

For this mode typically a bunch of 10,000 electrons [83] are used to repeatedly image the same time step. The advantage compared to the stroboscopic mode is the reduction in the number of pulses needed. Therefore imaging time, sample repeatability and noise are reduced. As far as we are aware the repeated mode is only used for diffraction of large (> 100 μm) crystals. Hence in figure 7.4 the sampled area for the two lines using this mode are outside of the box for standard electron microscope imaging, so we can see a difference between the repeated and the stroboscopic modes in the area sampled. For example Sciaini et al [83], looked at a non-reversible melting process in Bismuth, by combining 10-12 diffraction images taken at the same time after excitation, but from a different area on the sample, the diffraction pattern was made by averaging. Some results can be seen,

in figure 7.6.

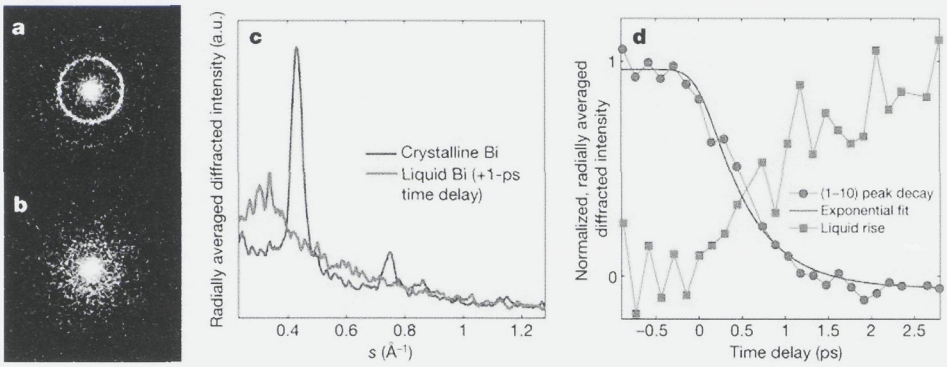

Figure 7.6: Taken from [83] with permission. "Excitation fluence was $18mJcm^{-2}$. a, b, Diffraction patterns recorded without (a) and with (b) pump laser excitation, at $+1$ ps time delay (20 shots averaged). c, Radially averaged intensity profiles of the diffraction patterns shown in a (blue trace) and b (red trace). d, Blue, decay of the (1-10) peak; red, rise of the integrated intensity in the range $0.230.34\text{Å}^{-1}$ (four shots averaged)."

This ability to look at non reversible processes is again very different from stroboscopic, and is due to the relatively low number of shots needed to form the pulse. However this is not our definition of the repeated mode, just one possible way of using it.

Further examples of this technique come from a group at Duisberg Essen, who studied lattice heating in copper and gold films [89] and the group at Caltech [81] who studied vanadium oxide.

Single Shot

The Dynamic TEM at Laurence Berkeley based on the pioneering work of Bostanjoglo in Berlin from the 70's [13], can make single shot real space images, see [90] by La Grange et al, though because it operates in the nanosecond regime it is not an UFEM. Nevertheless it has performed some interesting experiments, see again [90]. The line (black ○) for the DTEM in figure 7.4 is on its own, as far as we know the DTEM is the only one of its kind.

In the femtosecond regime only single shot diffraction of large crystals has been shown. Further there are yet to be any true pump-probe experiments, so the line in figure 7.4, is vertical. An example of the work done at Eindhoven is shown in figure 7.7 [69] . A single shot transmission diffraction pattern from a gold foil has been imaged in less than a picosecond (measured on a streak camera). Further work remains to add a laser excitation path to the sample and perform pump probe experiments.

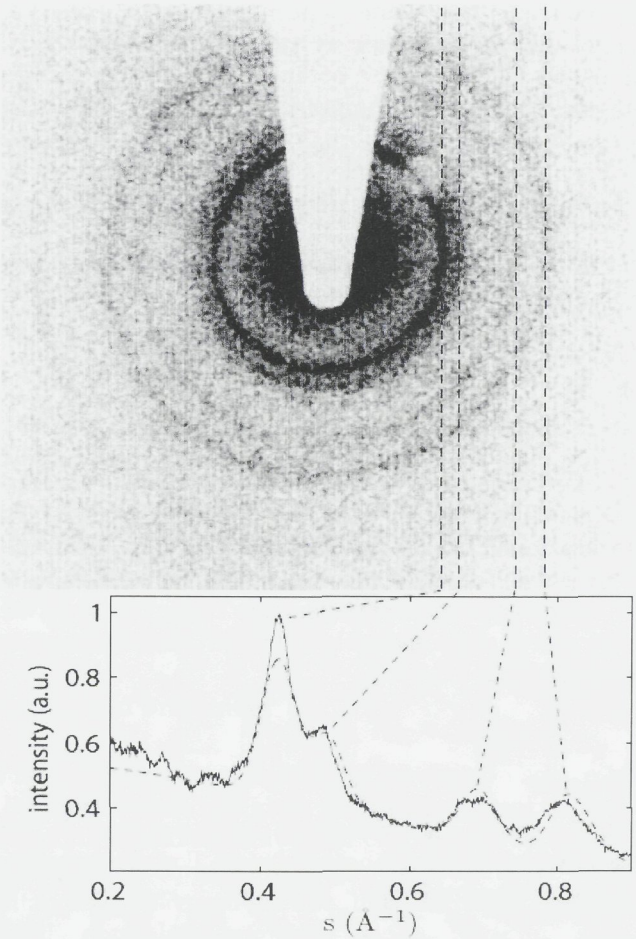

Figure 7.7: Taken from [69] Copyright 2013 by The American Physical Society."Electron diffraction pattern of a polycrystalline gold foil [69] , recorded with a single 200 fC bunch. (bottom) Azimuthal integration (solid line) of the Debye-Scherrer rings in the top panel, and a fit (dashed line) based on kinematic diffraction theory."

7.2 Important Parameters

We will now define the parameters, and also highlight some important relationships that we want to use later in this text. Since there are sometimes differences in definitions (for example pulse length measured as full width or a half width), even the experienced reader may want to check this section. These parameters are important to us because they will allow us to apply a quantitative (if only rough) critique of the guns. By knowing these parameters the reader can perform his or her own analysis whilst reading this paper, and is encouraged to disagree!

Number of electrons in a pulse

The total number of electrons within a pulse N becomes of great significance for single shot imaging, where sufficient signal to noise must be obtained with just N electrons.

Pulse length

The pulse length τ determines the processes we can view, for example the nanosecond pulses of the DTEM can view the formations of defects, but cannot see the lattice vibrations that the 4D microscope (in diffraction mode) is capable of viewing with its sub ps pulse. Ideally we would measure τ as the shortest time containing 50% of N, however since most papers don't state how they measured τ, or the distribution we accept any reasonable full width measurement, and therefore an rms measurement is doubled.

Repetition rate

The repetition rate f is the number of electron pulses per second. This is typically decided by the laser which initiates photoemission. For stroboscopic imaging the repetition rate is of great importance.

Reduced / Normalised emittance

The emittance describes the quality of a beam, and when normalised or reduced it is a conserved quantity (in a system with no aberrations or electron-electron interactions). Further it is a fundamental property of the cathode, and for those attached to using the brightness understanding emittance is the first step to understanding brightness. Therefore it is worth a little effort to explain it.

Liouvilles theorem states that phase space density is constant. Thus for a set of N particles $\int xyzp_xp_yp_zdp_xdp_ydp_zdxdydz$ is fixed where p is momentum and x, y, z are coordinates on a cartesian system. In practice the motion in each direction is decoupled so the emittance can be defined in just one direction. For a

typical TEM electrons are accelerated along the z axis from the electron source towards the sample through a cylindrically symmetric system. At the focus of such a system the emittance can be defined as $\epsilon = r_f\theta$, where r_f is the spot radius and θ is half the angle made by the outer most rays at the focus. The z part of the emittance is normally described by the energy spread (see section 7.2). A more general description valid at any point in the beam is the rms emittance ϵ_x and ϵ_y defined in x as

$$\epsilon_x = \sqrt{< x^2 >< x'^2 > - < xx' >^2} \tag{7.1}$$

x is the position of the electrons within the beam and x' is the angle d_x/d_z. This definition is probably only useful for Gaussian distributions because outliers seriously effect this number. We would prefer to use a FW50% emittance which is the smallest ellipse in x and x' or y and y' that contains half of the particles

The emittance is not conserved under acceleration, so we have the normalised emittance,

$$\epsilon_{nx} = \beta\gamma\epsilon_x \tag{7.2}$$

where $\beta = v_z/c$ and $\gamma = 1/\sqrt{1-\beta^2}$ here v is the velocity and c is the speed of light.

We prefer however to define the reduced emittance at a focus as $\epsilon_r = r_f\theta\sqrt{(V_r)}$ where $V_r = V + (\frac{eV^2}{2m_0c^2})$ is the relativistic corrected voltage, see page 29 of [91].ϵ_r is quicker to calculate since one normally knows the accelerating voltages, and up to 100kV $V_r \approx V$.

Reduced / Normalised Brightness

Perhaps the most important parameter for an electron source is the reduced or normalised brightness since this gives us directly current in a probe, current in a coherent area and is related to many other properties. The reduced or normalised brightness should be the current divided by the phase space volume. However as with the emittance we disregard the longitudinal component to get a phase space area, therefore the normalised brightness is

$$B_n = \frac{I}{\pi^2\epsilon_{nx}\epsilon_{ny}} \tag{7.3}$$

where $I = Nq/\tau$ is the current in emittance $\epsilon_{nx}\epsilon_{ny}$ and q is the elementary charge. (Note Sometimes equation 7.3 is written without the factor of π^2 or multiplied by 2, this is a matter of the definition of I or ϵ.) We however prefer to use the reduced brightness $B_r = \frac{I}{\pi^2\epsilon_r x\epsilon_r y}$, which like the reduced emittance is quicker to calculate than B_n. In practice B_r is expressed as

$$B_r = \frac{I}{\pi r_{probe}^2 \pi\theta^2 V_r} \tag{7.4}$$

here I is the current in a focused, sometimes virtual, spot of area of πr_{probe}^2 and solid angle $\pi\theta^2$. These two brightnesses (equations 7.3 and 7.4) are related as

$$B_n = B_r m_0 c^2/q \tag{7.5}$$

Like emittance brightness is conserved, but unlike the emittance brightness is also conserved after an aperture, this is useful in a system like an electron microscope where there will be at least one aperture between the electron source and the sample. If we know the B_r of the source we can quickly estimate the amount of current in a focused spot.

$$I_f = B_r \pi\theta^2 \pi r_f^2 V_r \tag{7.6}$$

The pulse is charge limited when $I_f > Nq/\tau$, and (7.6) no longer holds.

Further we can see that B_r is determined by the current density J and the lateral energy of the electrons. Substituting $\theta = \frac{v_z}{v_r}$, $J = \frac{I}{\pi r^2}$ and $eV = \frac{1}{2}mv_z^2$ we can write

$$B_r = \frac{eJ}{\pi E_t} \tag{7.7}$$

where $E_t = \frac{1}{2}mv_r^2$. this leads to an expression for the brightness of a photo cathode, which is derived in [46]

$$B_r = \frac{eJ}{\pi(h\nu - \phi)} \tag{7.8}$$

We define the excess energy ΔE_{ex} as the difference between the photons energy $h\nu$ and the work function ϕ.

Coherence length

The coherence length is important for diffraction which can not work without some degree ofcoherence. Also for the high resolution phase contrast imaging performed in TEM.

Rather nicely the Brightness also tells us the amount of current in a coherent area. From Cittert-Zernike theory, the amount of coherence is directly proportional to the Fourier transform of the source image intensity function. For a homogeneously filled disk, the Fourier transform is the Airy function. In a target plane illuminated from that crossover, the coherence function has fallen by 12% at a distance [91]

$$x_{1,2} = \frac{\lambda}{2\pi\theta} \tag{7.9}$$

where λ is the wavelength of the electron.

when the distance grows by a factor of 2π then $x_{1,2} = \frac{\lambda}{\theta}$ and we define complete incoherence. For a practical measure of coherence [91] we take

$$X_{pc} = \frac{\lambda}{2\theta} \tag{7.10}$$

We find that the amount of current in a coherent area is,

$$I_{coh} = B_r V_r \pi (\frac{X_{pc}}{2})^2 \pi \theta^2 = 0.93 \times 10^{-18} B_r \tag{7.11}$$

The coherence length relates to the reduced emittance as

$$\epsilon_r = \frac{r_f}{2X_{pc}} h\sqrt{(2em)} \tag{7.12}$$

Energy Spread

The energy spread ΔE expressed in eV is a measure of the width of the distribution of electron kinetic energies. This should be the total energy, however often the kinetic energy E in the z direction $\frac{1}{2q}mv_z^2$ is used instead. The difference is small and we will not distinguish them.

We believe that the best measure of a width is the smallest full width containing 50% of the electrons FW50, this measure is unaffected by outliers and therefore good for any distribution. As per τ (section 7.2) we try to quote some reasonable measure of the full width of the energy distribution.

The energy spread is important because it increases the bunch length as

$$\Delta t = \frac{\Delta E}{\bar{E}} T_f \tag{7.13}$$

where T_f is the time of flight.

A further issue is chromatic aberration according to [8] the contribution of chromatic aberration to probe size is

$$d_c = C_c \frac{\Delta E}{qV_r} \theta \tag{7.14}$$

Where C_c is the chromatic aberration, which has a typical value of 2 mm [57]

7.3 Creating Images and Diffractograms

In this section we will look at how images and diffractograms are made. We will use the gun parameters we described in the previous section, and assign values to them.

7.3.1 Imaging

In the previous seciont perhaps the most useful and important parameter we defined was equation 7.4 which gave us B_r. We will now adapt 7.4 to show how the brightness of a gun limits the image.

$$B_r = \frac{qN_{im}}{\pi^2 \epsilon_{im}^2 V_r T} \tag{7.15}$$

Where $\epsilon_{Im} = \theta r_{res}\sqrt{N_{pix}}$ is the emittance to form an image, N_{pix} is the number of pixels used in an image, and T is the time taken [1]. We now put values on the variables of equation (7.15), and we will link these to the three modes of UEM we described in section 7.1.3, we start with V_r. Most TEM's operate around $V \approx V_r \approx 100$ keV, some special models operate at mega volts, and nearly all can operate at > 100 keV, but for simplicity of calculation in the rest of this paper and unless otherwise specified we will assume that $V_r = 100$ keV.

Now let's look at finding N_{Im}. For a digital image at least 10 electrons per pixel are required, this works on a signal to noise ratio of 3, based on the Rose criterion [92] and Poisson statistics. Since $Noise = \sqrt{\#electrons}$, then, a signal to noise ratio of $10/\sqrt{10} = 3.2$. Due to detectors efficiencies approx 10% (see section 4 in [93] by Chen) and other losses in practice, 100 electrons per pixel are needed, thus for a 1 mega pixel image, $N_{Im} = 10^8$.

The next variable we will consider is ϵ_{Im}. The N_{Im} electrons should be delivered to the sample in area ($= \pi r_{probe}^2$) and half angle θ, in other words within ϵ_{Im}. A simple system is shown in figure 7.8 where a flat cathode emits a beam with a particular ϵ and I. The beam is described by several rays which could be considered as the path taken by an individual electron. The rays are allowed to expand, then to reduce ϵ to ϵ_{Im} it is apertured, and to get the desired r_{probe} focused by a lens. Paraxial considerations can show that the number of rays per ϵ^2 is conserved.

We know the value of r_{probe} this is our resolution for an atomic image from section 7.1.2 $r_{res} = r_{atomic} = 0.1$ nm multiplied by the length of the image in pixels, $\sqrt{N_{pix}}$, making $r_{probe} = 100$ nm.

To determine θ we should consider spherical aberration , this blurs the resolution as $C_s\theta^3$, including the diffraction contribution $0.61\frac{\lambda}{\theta}$, and assuming addition in quadrature we find an optimised θ of 15 mrad with a spherical aberration coefficient C_s of 3 mm and 100 keV electrons (page 100 of [8]). So we can define a $\epsilon_{rAIm} = 4.7 \times 10^{-7}$ m rad$\sqrt{(\mathrm{V})}$. We used the abbreviation AIm to signify that this is for Amplitude contrast Imaging, caused by variation in absorption or scattering of electrons by the sample.

State of the art TEMs use a much smaller illumination angle, Kisielowski et al in [94] use $\theta = 0.15$ mrad. The small θ means that X_{pc} is maximised -see equation 7.10, and they can make an image using phase contrast (see for example [91] or

[1] We assume a square image field where the size of one pixel is matched to half the resolution of the instrument therefore $r_{res}\sqrt{N_{pix}}$ is the size of the spot used.

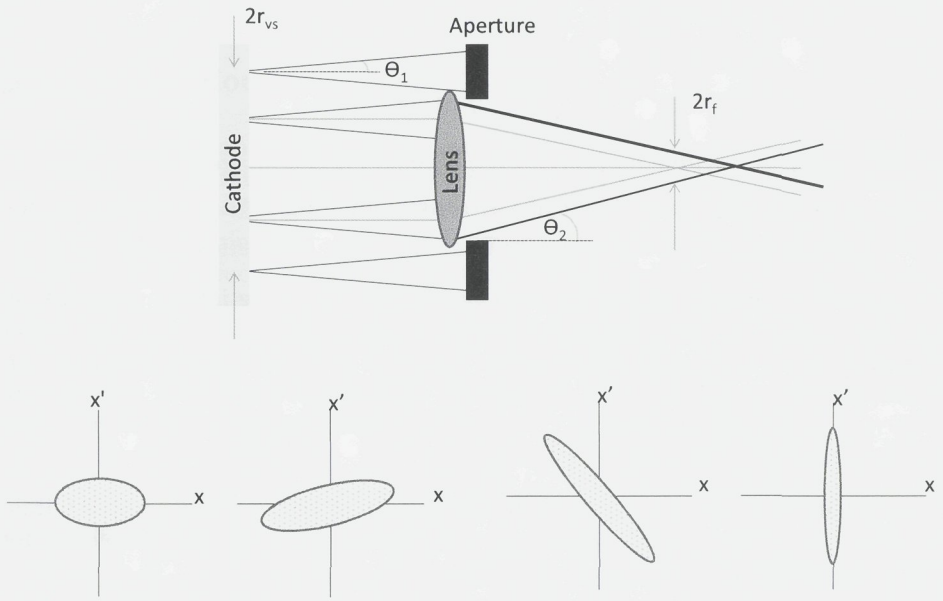

Figure 7.8: Moving from left to right, the top images show a flat cathode emitting electrons with a particular B_r, the x trace space of this system is shown in the first diagram below, the density of the shading represents the electron density. As the electron move towards the lens they expand in x due to their initial v_x. The second diagram shows that the area of the ellipse remains the same as the first diagram. The third shows the effect of the lens and the aperture. The aperture cuts part of the current and therefore the area of the trace space ellipse (and therefore the emittance) is reduced, yet the density remains constant. The lens reverses and increases v_x so that at the focus $\theta_2 > \theta_1$ yet $r_f < r_{vs}$. The density of the system remains constant throughout, thus so does B_r.

[8]), so we make the ϵ_r for phase contrast imaging $\epsilon_{rPIm} = 4.7 \times 10^{-9}$ m rad$\sqrt{(\mathrm{V})}$ here PIm is the abbreviation for Phase Contrast Imaging.

We can also use equation (7.11) to find a theoretical ϵ_r for phase contrast imaging. As a very minimum to see contrast the coherent electrons should cover a square of 4 pixels. So because of signal to noise constraints there should be 400 electrons per coherent area, from equation (7.11) we find that to form a phase contrast image

$$B_r = \frac{400q}{T10^{-18}} \tag{7.16}$$

By comparison with equation (7.15) the total ϵ_r in the image must be $\sqrt{\frac{N_{Im}}{400\pi^2}10^{-18}}$. So theoretically for phase contrast imaging we have $\epsilon_{rPTIm} = 1.6 \times 10^{-7}$ m rad PTIm is therefore short for Phase contrast Theoretical Imaging.

We now determine T, and we will need to consider the imaging modes described in section 7.1.2. For a single shot image $T = \tau_{atomic} = 100$ fs. For repeated imaging we set the number of electrons used to form an image or diffractogram $N = 10^4$ see 7.1.3, so to form an image we need 10^4 pulses, with $\tau = \tau_{atomic} = 100$ fs, therefore $T = 1$ ns. By similar argument in stroboscopic mode we set $N = 1$ $T = 10$ µs.

The electrons traveling with $V_r = 100$ keV must arrive at the sample within the correct ϵ_r, either, ϵ_{rAIm}, ϵ_{rPIm} or ϵ_{rPTIm} and this gives us a requirement for B_r, and is outlined in table 7.1

Mode / ϵ (m rad)	ϵ_{rAIm} $(4.74EE{-}7)$	ϵ_{rPIm} (4.7×10^{-9})	ϵ_{rPTIm} (4.7×10^{-9})
Single Shot	7.2×10^{13}	7.2×10^{17}	6.5×10^{14}
Repeated	7.2×10^{9}	7.2×10^{13}	6.5×10^{10}
Stroboscopic	7.2×10^{5}	7.2×10^{9}	6.5×10^{6}

Table 7.1: Reduced Brightness B_r in $\mathrm{A}/\left(\mathrm{m}^2\mathrm{srV}\right)$ required to operate in the various imaging modes outlined in the main text of this section, the time resolution is $\tau_{atomic} = 100$ fs spatial resolution is $r_{atomic}0.1$ nm with 1000x1000 pixes, the voltage V_r is 100 keV and $N_{Im} = 10^8$.

We want to point out that the times we specified do not take into account the duty cycle of the system. If we assume that $f = 1$ kHz and $\tau = 100$ fs then the waiting time for the user is $T \times 10^{10}$, which for the stroboscopic system is about 1 day.

A further issue with imaging is chromatic aberration restating equation (7.14) the contribution of chromatic aberration to probe size is

$$d_c = C_c \frac{\Delta E}{eV_r}\theta \tag{7.17}$$

which for $V = 100$ keV, $\theta = 15$ mrad, and $C_c = 2$ mm [57] means that the energy spread should be kept below 0.4 eV to achieve r_{atomic} for many gun systems this is a problem, and can limit θ.

Also the expansion of the pulse length τ is a problem For an electron at 100 keV, $v_z \approx 2 \times 10^8$ m/s, the typical length of a column is 1 m, and T_f is $5ns$ during which time, with an energy spread of only 2 eV , $\Delta t = 200$ fs which for a 100 fs pulse is considerable.

7.3.2 Diffraction

A diffraction pattern is proof of the wavelike nature of electrons. The recorded pattern shows the interference caused by the different path lengths created when the electron wave reflects off different lattice planes. As with the previous section on imaging we begin with an equation for B_r (7.18) which we need to determine how brightness affects a diffraction pattern. We then define various parameters that will help us discuss diffraction patterns in a quantitative manner later . Finally we finish with a table showing the B_r needed for different types of diffraction patterns.

$$B_r = \frac{N_{diff} q}{T \epsilon_{diff}^2 V_r} \tag{7.18}$$

We begin by finding a value for N_{diff}.

A diffraction pattern gives an average location of the atoms and therefore less information than an image, in fact we need about 100 times less electrons and $N_{diff} = 10^6$. For example Siwick et al. use 150 pulses with $N \approx 10\,000$ [95] or van Oudheusden [69] who uses slightly less than N_{diff} to form an image.

Now we turn our attention to ϵ_{diff}. To generate a diffraction pattern the coherence length of the electron wave X_{pc} must be several times the lattice spacing, for Silicon 10 times the lattice spacing means $Xpc = 5$ nm [39] and from equation (7.12) and equation (7.4) the reduced brightness can be written as (7.19),

$$B_r = \left(\frac{8mq^2}{\pi^2 h^2} \right) \frac{N_{diff} X_{pc}^2}{r_{probe}^2 T} = 6.7 \frac{I}{r_{probe}^2} \tag{7.19}$$

So by comparison of (7.19) and (7.18) we see that $\epsilon_{diff} = \sqrt{6.7 V_r} r_{probe}$, as in section 7.3.1 $V_r = 100$ keV, but we are still left with r_{probe}. In UEM most work is done on large samples -we call this LAD Large Area Diffraction- with $r \approx 100$ µm, for example [81],[89],[96],[16],[97], and many more, we therefore set $r_{rLADiff} = 100$ µm, and $\epsilon_{rLADiff} = 2.6 \times 10^{-4}$ m rad$\sqrt{(\text{V})}$ where LADiff is short for Large Area Diffraction [2]. In [74] they perform convergent beam diffraction with a r_{probe} from 10 to 100 nm, if $r_{probe} = 100$ nm this gives us a second value $\epsilon_{rCBDIff} = 2.6 \times 10^{-8}$ m rad$\sqrt{(\text{V})}$ here CBDiff is short for Convergent

[2] We have two abbreviates LAD and LADiff which both mean Large Area Diffraction

Beam Diffraction. Finally if we want to have diffraction from a purely coherent beam then we have to look at (7.11), this means that $\epsilon_{rCohDiff} = \sqrt{\frac{10^{-18}}{\pi^2}} = 3.2 \times 10^{-10}$ m rad$\sqrt{(\mathrm{V})}$ to differentiate from convergent beam diffraction we used CohDiff as an abbreviation for Coherent Beam Diffraction.

In the section 7.3.1on imaging we discussed T for different UEM modes. For diffraction single shot remains the same with $T = \tau_{atomic} = 100$ fs. Repeated and stroboscopic diffraction have a decrease in T by a factor of 100 due to a decrease in N, giving $T = 10$ ps, and 100 ns respectively. In table 7.2 we show the B_r required for the combinations of each different mode, single shot, repeated, stroboscopic, and remembering that the N electrons must be delivered to the sample within either, $\epsilon_{rLADiff} = 2.6 \times 10^{-4}$ m rad, $\epsilon_{rCBDIff} = 2.6 \times 10^{-8}$ or $\epsilon_{rCohDiff} = 3.2 \times 10^{-10}$.

Mode/ϵ (m rad)	$\epsilon_{rLADiff}$ (2.6×10^{-4})	$\epsilon_{rCBDIff}$ (2.6×10^{-8})	$\epsilon_{rCohDiff}$ (3.2×10^{-10})
Single Shot	2.4×10^{7}	2.4×10^{15}	1.6×10^{19}
Repeated	2.4×10^{5}	2.4×10^{13}	1.6×10^{15}
Stroboscopic	24	2.4×10^{9}	1.6×10^{13}

Table 7.2: Reduced Brightness B_r in $\mathrm{A}/\left(\mathrm{m}^2\mathrm{srV}\right)$ required to operate in the various diffraction modes outlined in the main text of this section. The time resolution is $\tau_{atomic} = 100$ fs, $V_r = 100$ keV, $N_{diff} = 10^6$. LAD is for diffraction area of radius 100 µm, CBD is from an area of with radius 100 nm and Coherent Diffraction requires a fully coherent beam.

Further let's not forget the duty cycle of the laser is 10^{-10}s (as before $f = 1$ kHz and $\tau = 100$ fs), so the waiting time to perform stroboscopy,is around 15 minutes, and let's not forget that this is for the B_r listed in table 7.2, and that for a lower B_r it would be longer.

Finally the energy spread is typically less of a problem in diffraction, since the wavelength does not vary much and because it is a lensless technique there is no chromatic aberration. However sometimes very large energy spreads are present for example in [98], they suggest that the energy spread in their beam may be reducing the quality of their diffraction patterns.

7.3.3 Section Summary

We have defined values for the number of electrons to make an image or diffraction pattern, we also found values for T, and ϵ for different modes of UEM. These values let us calculate B_r, given in tables 7.1 and 7.2 for imaging and diffraction respectively. We have to remember that the times we calculated for T assume that we can deliver the N electrons within the required ϵ. Importantly we have requirements for imaging and diffraction patterns which can be linked back to the gun.

7.4 Gun Limitations

We have tried to arrange this section in the same order that the electrons would notice the limitations. We start with the restrictions on brightness and energy spread due to Fermi-Dirac statistics within the material, and here we also discuss the effects of using excessive laser power to remove electrons, or too strong a field. The electron density is limited by the Pauli exclusion principle, which sets the maximum phase space density inside and outside the metal. Then in the vacuum we have space charge forces described by Child's law which prevent the electrons from escaping to form a beam. Once the electrons have escaped they can still be affected by Coulomb forces which force them apart, this limits the spatial and temporal resolution of the beam. Finally there are the stochastic electron-electron interactions which destroy the emittance.

7.4.1 Intrinsic Brightness Vs Energy Spread

Unfortunately guns are limited in terms of their brightness and energy spread. This is demonstrated in figure 7.9. We see that for thermal and field emitters, you may not increase the brightness without increasing the ΔE or ϵ, the extra electrons gained come from deeper inside the material and therefore have different energies than those at the Fermi-level. If you are not interested in the energy spread you may be tempted to try using a field emitter at higher and higher fields, however again this leads to heating, often called the reverse Nottingham effect- electrons are emitted from at or below the Fermi level, but must be replaced by electrons traveling just above the Fermi level this causes heating. With photo emission decreasing the photon wavelength, directly increases ϵ and ΔE. You may however increase the laser intensity and therefore B_r, at no cost to the energy spread, but eventually multi-photon effects will start to increase ΔE and the laser will heat the material so that thermal emission becomes problematic. Thermal emission is problematic because it is not prompt like the photo emission, so it increases the pulse length. In [28] there are analytical equations for laser heating, more recently Jensen has looked at the problem [99] using a 2 temperature method. As a rough estimate we can use the specific heat capacity C, the laser solid interaction volume and energy per pulse of the laser to find the temperature rise. In figure 7.9 we see that laser heating dominates photo emission process at high B_r because of the sudden rapid increase in energy spread. We also included a field emitter for comparison. Please note the calculation is very simplified, also Nottingham heating/cooling effects, and Coulomb interactions were ignored here. Further details are in the figure caption.

7.4.2 Quantum Limitations

Pauli Exclusion Principle

The Pauli exclusion principle limits the phase space density, since brightness deals with phase space density this means there is a maximum B_r, which we will now

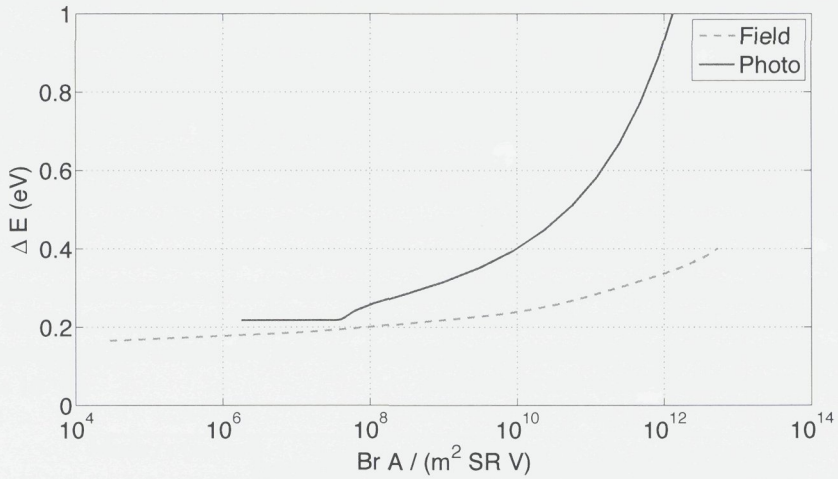

Figure 7.9: Simplified calculation of (solid blue) a photo emitter including laser heating, but excluding Nottingham heating or cooling and excluding Coulomb interactions. Although no numbers should be taken from this purely illustrative graph for completeness the parameters used for generating the graph are given. $C = 10$ K(molJ)$^{-1}$, laser penetration depth $= 20$ nm, volumetric density $= 10.5$ gcm^{-3} and molar density 108 g/mol. The work function is 4.1 eV for the photo emission and 5 eV for the field emission. The laser intensity is varied from $0.1-100$ TW/m^2, at a wavelength of 257 nm, and a quantum efficiency of 10^{-6}. The field on the photo emitter was 0 and for the field emitter it was varied from 5 to 12 V/nm. The tunneling was calculated numerically since a fast (to run and implement) code exists for this. The energy spread is calculated from a full width 50%.

find. The maximum phase space density is $\frac{\Delta p_x \Delta p_y \Delta p_z \Delta x \Delta y \Delta z}{N} \leq 2h^3$. Since all particles have the same mass

$$\Delta x \Delta v_x \Delta y \Delta v_y \Delta z \Delta v_z \leq 2(h/m)^3. \tag{7.20}$$

The brightness is $I/(\pi^2 \epsilon_x \epsilon_y)$ and $\epsilon_x = \Delta x \Delta v_x / v_z$, and the same holds for ϵ_y. Now we have ϵ_z to worry about, however this is normally covered by the energy spread $\Delta E = m v_z \Delta v_z$. So we will use the brightness per unit energy spread (in eV) which can be written

$$\frac{B_r}{\Delta E} = \frac{e\Delta N}{\pi^2 \Delta x (\Delta v_x / v_z) \Delta y (\Delta v_y / v_z) m v_z \Delta v_z \tau \frac{m v_z^2}{2e}} \tag{7.21}$$

Rewriting equation (7.21) noting that $v_z = \frac{\Delta z}{\tau}$ and from equation 7.20

$$\frac{B_r}{\Delta E} = \frac{2e^2 \Delta N}{\pi^2 m^2 \Delta x \Delta v_x \Delta y \Delta v_y \Delta z \Delta v_z} \tag{7.22}$$

So the maximum reduced brightness per unit energy spread is,

$$\frac{B_r}{\Delta E} = \frac{4e^3}{m\pi^2 h^3} = 1 \times 10^{13} \text{ A}/\left(\text{m}^2\text{srV}\right) \tag{7.23}$$

Therefore for a pulse with a $\Delta E = 10$ eV the maximum $B_r = 10^{14}$.

7.4.3 Child's Law

The Child Langmuir law [100],[101] gives the maximum current density J_{max} that can exist in an electron gun made of two parallel infinite plates, with an electric field E_g between them. The law assumes a continuous and uniform J, that fills the area between the plates; electrons start at the cathode with zero velocity; electrons are accelerated towards the anode. The electrons passing between the two plates create their own electric field $E_e(J)$. When $J = J_{max}$ then at the cathode E_e cancel out E and there is no force to move the electrons away from the cathode. Further electrons trying to escape will see a field directed back towards the cathode, and will not be emitted.

To deal with ultra short pulses the Child Langmuir law is not suitable, but if we treat our electron bunch as a flat pancake i.e much wider than it is long, then from Gauss we know that the field the electron bunch creates is,

$$E_e = \frac{Ne}{\epsilon_0 2\pi r^2} \tag{7.24}$$

So to allow emission, E must be greater than this, and according to Valfells to have good beam quality it should be much greater [102]. For $N = 10{,}000$ $E_e > 2.5 \times 10^4$ V/m, with $r = 100$ μm. If we look at figure 7.10 we can see the electric field required to do single shot imaging and diffraction. Typically the maximum DC (DC - Direct Current i.e a static voltage between cathode and anode) field on a flat cathode is 10 MV/m so for single shot imaging the cathode must have a radius of at least 200 μm, where as for diffraction a much smaller 20 μm radius cathode is possible.

From equation 7.24 and 7.8 we can write the maximum B_r for DC photocathodes

$$B_{r-max} = \frac{E\epsilon_0 2}{\pi \Delta E_x \tau}, \tag{7.25}$$

where $\Delta E_x = (h\nu - \phi)$, if the excess energy is 0.1 eV and the field 10 MV/m then for a $\tau = 100$ fs, $B_r = 6 \times 10^9$ A/ $\left(\text{m}^2\text{srV}\right)$

It would seem that equation 7.24 is only good when the bunch is much shorter than the cathode to anode distance, for longer pulses we might use the refined

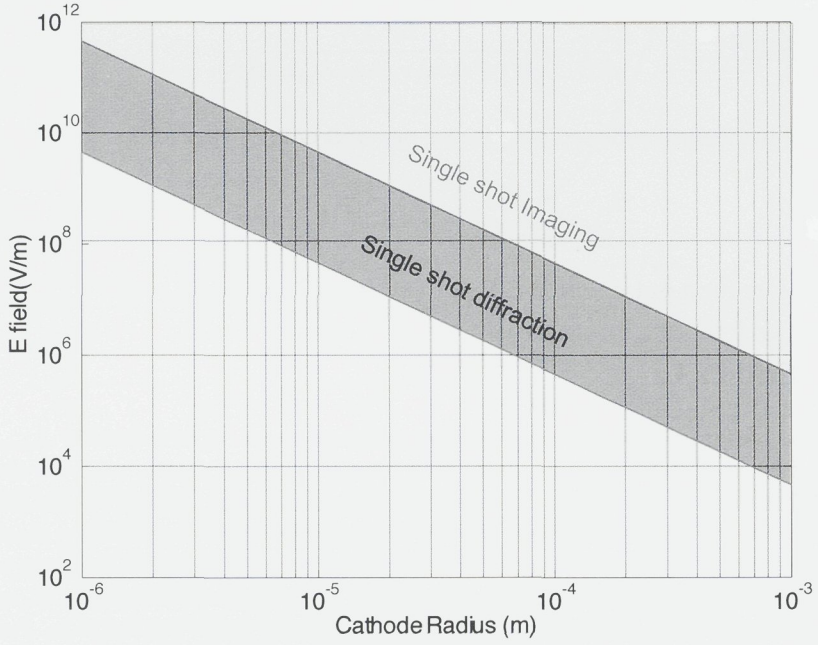

Figure 7.10: For N_{diff} and N_{image}, the acceleration field required to cancel out the space charge field is shown as a function of cathode radius. Please note that at smaller radii the flat pancake approximation of (7.24) used to create this graph becomes increasingly bad.

Child Langmuir law in [102]. However from fig 8 in [102] it would seem that this is not necessary, and we can use equation 7.24 until the pulse fills the gun after which point we should use the normal child Langmuir law [101],[100].

7.4.4 Space Charge Expansion

Temporal Space Charge

After being emitted into vacuum there is still the problem that the electron bunch will expand temporally, due to Space Charge (SC) forces. Most of the literature we reviewed concludes that N must be less than 10^4 This number comes from the mean field model, see for example section 4 of [15] by King et al, or [103] by Gahlmann. We will use the mean field model to estimate a maximum B_r for a cathode limited by longitudinal SC forces. Starting from equation 3 in [103] the longitudinal SC force is

$$\frac{1}{2}\frac{d^2L}{dt^2} = \frac{Nq^2}{2\pi m\epsilon_0 R^2}\frac{2}{1+L/r+\sqrt{1+(L/R)^2}} \tag{7.26}$$

Where L is the length of the pulse in space. Equation (7.26) has no simple solution unless we set $L/R = 0$, for most pulses this is reasonable since $L = 10$ μm and $r \approx 100$ μm for for a 100 fs pulse at $v_z = 10^8$ m/s. Then the square root of equation (7.26) $= 1$; carrying out the integration and substituting in the initial current density $J_i = \frac{qN}{\tau\pi r^2}$ we get (7.27).

$$L = \frac{qJ_i\tau T_f^2}{2m\epsilon_0} + L_0 \tag{7.27}$$

Which could also have been derived from equation 7.24. Compared with (7.26) it overestimates the expansion by only a couple of times for the typical parameters we are interested in ($\tau = 100$ fs,$r = 100$ μm,$L = 10$ μm and the time of flight $T_f = 0.1$ ns which is 1 cm at $v_z = 10^8$ m/s). Also this equation is only for drift space and at the cathode the electrons start with virtually no speed and must first be accelerated, so the time T_f is longer and initially L is less. We want a maximum amount of SC expansion, in order to find our maximum B_r, for the sake of argument we set the maximum value of $L = 2L_0$, we further note that $L_0 = \tau/v_z$ and then we get the maximum J_{max}

$$J_{max} = \frac{2m\epsilon_0 v_z^3}{qz^2} \tag{7.28}$$

z is the distance traveled by the bunch. Putting in the numbers from earlier, we get

$$J_{max} = \frac{100}{z^2} \tag{7.29}$$

With $z = 1$ cm $J_{max} = 10^5 \mathrm{A/m^2}$, this corresponds to around $N = 10,000$ and $R = 100$ μm which is the number we identified earlier as standard limit found in the literature and the number of electrons used in the repeated mode. We still want the maximum B_r, so we must combine equation (7.8), and (7.28) to get

$$B_{rmax} = \frac{2m\epsilon_0 v_z^3}{z^2\pi\Delta E_{ex}} \tag{7.30}$$

We can imagine that ΔE_{ex} would be much less than 0.1 eV and there still be sufficient current therefore $B_{rmax} = 10^6$ A/ $(\mathrm{m^2 srV})$. Note this is only a valid approximation for a flat pulse and the amount of space charge expansion allowed is subjective. Nevertheless B_r will decrease with increasing z, but the resolution that you get will not decrease, nor will the amount of electrons in the image decrease nor can the emittance change, only temporal resolution is lost. It might be more useful to the experimentalist to state the minimum pulse length, this information can be found in [15] ,[103] or other publications, here we want a figure for B_r which we will use later to compare against real cathodes.

Lateral Space Charge

In [103] Gahlman et al expand the mean field model to include focusing lenses, and use N body simulations to check this work.

This is something that must be done for imaging. We will use a back of the envelope calculation to estimate the lateral space charge forces. If we consider the focal spot as a cylinder of length τv_z then for 100 fs at 100 keV this length is already more than 10 μm, so for $r_f = 100$ nm, we might consider that the cylinder is infinitely long. The electric field for such a system is $E = I/v_z \epsilon 2\pi r_f$ with an image forming $I = N_{im} q/100$ fs $= 160$A Then E is an eye watering 100GV/m.

7.4.5 Stochastic Interactions

Unfortunately there will always be a stochastic element to the Coulomb interactions. As a physicist the first idea would be to use a beam temperature, which leads to expression from plasma physics. However for a thermal distribution the time of flight T_f must be much greater than the inverse of the plasma frequency T_f must be $>> \frac{1}{\omega_p} = \sqrt{\frac{m\epsilon_0}{e^2\rho}}$ where $\rho = \frac{J}{v_z e}$. For $N = 10^4$ and τ_{atomic} then $T_f >> 281$ ps, in a 1 cm gun with $E = 10$ MV/m, the time of flight is around 100 ps so we might be better using the extended two body approximation equations of Jansen [2].

The two body approach calculates the effect of a particle distribution on a test particle as a sum of the two body interactions. For the pulse described above we are in the Gaussian regime, and the increase in energy spread δE and angular disturbance $\Delta\alpha$ are given by equations 7.31 and 7.32

$$\frac{\Delta E}{E} = P_{PE} 0.45 \frac{I^{2/3} L^{2/3}}{r V^{13/12}} \tag{7.31}$$

where $P_{PE} \approx 1$

$$\Delta\alpha = P_{PA} 0.23 \frac{I^{2/3} L^{2/3}}{r V^{13/12}} \tag{7.32}$$

and again $P_{PA} \approx 1$ These equations should only be used in drift space, they are not meant for accelerating fields. However using the final cathode voltage as the drift space beam energy we make figure 7.11 which is of course an under estimate. This shows that a relatively large stochastic energy spread can be expected, which according to equation 7.13 could cause a fairly significant lose of temporal resolution.

With the angular deviation (7.32) there is a loss of brightness, which we can estimate by seeing the increase in the virtual source size as $B = B\frac{r_{vs}^2}{r_{vs}^2 + r_C^2}$, where $r_C = \Delta\alpha z$. So for a pulse with 10^4 electrons with a radius 100 μm, after traveling 10 cm there is a 1% loss of brightness, and a beam with $N = 10^6$ will have 10%

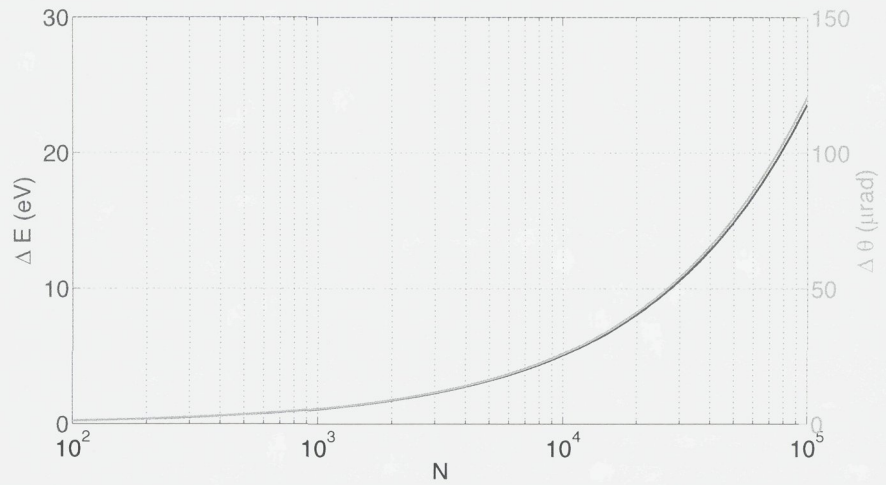

Figure 7.11: Increase in ΔE due to stochastic Coulomb interactions (Boersch effect) on left y axis, and the angular blurring on the right y axis. The parameters used where $L = 1$ cm $E = 10$ MV/m $V = LE$ V $r = 100$ μm $I = Ne/\tau_{atomic}$

loss in brightness. At such high current densities however we might want to be looking into models based on plasma physics.

Note that these formula do not take into account the longitudinal beam expansion caused by space charge, or relativistic effects, so will tend to over estimate the stochastic blurring.

7.5 The Guns

In this section we start by reviewing all the guns together,and in section 7.5.5 there is an overview table showing all the guns. We then look at them more closely as three groups: Flat Photo Cathodes section 7.5.5, Sharp Tips section 7.5.6, and Novel Guns section 7.5.7.

Briefly however, a flat photocathode is normally a flat metal surface illuminated by a UV laser, in complex systems this will also involve a radio frequency electromagnetic field to rapidly accelerate the electron pulse. The sharp tips can be made of thin tungsten wire sharpened to a few 100's of nanometres or even smaller, they are pulsed with lasers of all wavelengths or sometimes pulsed via an electron beam blanker. The novel guns are what is left over and could not be fitted into the other two sections.

Detailed descriptions of each gun is in the appendix, for example see A.1 where we examine a patent that describes gun A.1 used in the 4DTEM at Caltech (this is gun is also known as UEM1). Firstly we describe the gun which is a

LaB6 cathode front illuminated by a UV laser. We then critique the claims in the patent and other related papers to come to a final value for B_r, N, ΔE and Δt.

Coming back to what this section is all about, we have tried to put together as many electron guns as possible, based on the parameters from the previous sections we have made meaningful graphs and figures.

This is difficult, because most papers do not give sufficient information, therefore in some cases we can do little more than guess. The guess work is outlined in the appendices, each gun has a number e.g. $A.1$ which corresponds to a section in the appendix, in the figures we have omitted the letter for brevity. Typically we use equation 7.8 to estimate B_r, this can be quite wrong because work functions are not well known, and Coulomb interactions can change the B_r quickly.

We split the guns up into different types, flat cathodes which includes DC and RF cathodes (Radio Frequency cathodes describes the sinusoidal GHz voltage applied to extract the electrodes) , then sharp tips, this includes sharp tips with lasers and sharp tips with an electron beam blanker or chopper, and finally novel guns which don't really fit anywhere else. The different types of guns are explained in more detail in sections $7.5.5$, $7.5.6$ and $7.5.7$. In this section we will talk about general characteristics, and look at how many guns meet the requirements and predictions we set out earlier.

When stating the brightness, energy, pulse length or other quantity, we suggest using the FW50, this is the smallest width containing 50% of the distribution. This makes more sense experimentally than other measures, as it tells you where half of the signal on the integrating detector comes from, where for example the standard deviation of a narrow function with long tails and a wide tailless function would account for different amounts of the final signal. A Full width at half maximum is easily confused by a strong background and sharp peak. In our full N-body simulations in chapters 9 and6 we often see a very wide range of distributions. Normally, parameters are stated with a Full Width Half Maximum (FWHM) or a Root Mean Square (RMS), often we don't know the distribution, so we don't know the relationship between FWHM and RMS. However we take a full width measurement, so RMS values are doubled, and when the information allows we take the mean value within a pulse Nq/τ, with τ defined as mentioned above (this is sometimes known as the peak current). What this means is for each point on each figure, error bars of around 1 order of magnitude could be added, we do not find that this changes our conclusions.

In the appendix the values as found in the papers consulted are given and our calculations shown or at least outlined, the references which in the graphs for brevity are simply numbers refer to the relevant section in the appendix.

In each figure the guns are coloured according to their pulse length using the false colour map on the right of figure 7.12. In order to make it easier for the reader this colouring is maintained even in graphs with pulse length on the axis. Further, circled numbers indicate that the gun data is experimental, and that the values we calculate from the papers are believable. Numbers without a circle are for simulation work, and unmeasured, unrealistic claims, for example one can not measure the virtual source size of an emitter, at a low current, and assume

that it remains the same at a high current, since stochastic Coulomb interactions are likely to have blurred this. The two dotted circles are for continuous sources in combination with a a ultra-fast beam blanker/chopper. These sources have properly measured B_r however experimental use with an ultra-fast blanker is not yet proven.

7.5.1 Source Brightness Vs Current

In an effort to come up with a single figure containing as much of the fundamental parameters we plotted B_r against I; see figure 7.12. The square in blue contains open circles and so far separates theoretical from the practical.

The diagonal lines show equal ϵ_r for the various modes we outlined in section 7.3, more information in the figure caption.

Most of the guns fall into the LAD area in red, this is not surprising as most are designed for this purpose. Interestingly gun A.1 (no letter only numbered in the figure) which is mainly used for imaging is also in the LAD area, however from section 7.1.3 we know that they do not quite achieve our requirement for atomic imaging. However even though gun A.1 is not in the ϵ_{CBdiff} section it has also been used to perform CB experiments [74], therefore the emittance must be reduced. The emittance was probably decreased by aperturing. When a gun is apertured the B_r remains constant, this means the gun moves to the left. The best gun is the one with the highest B_r, as an example after aperturing gun A.17 to ϵ_{CBdiff} there would still be $\approx$ 100 nA of current where as gun A.1 has around 1 pA. For UEM gun A.17 and the others outside the red area should be apertured, and a lot of the current which is often worked hard for will be lost.

Many of the guns seem to line up as if they have an equal ϵ for example A.9, A.5 and A.6, this is not surprising since they are trying to perform the same type of experiments, and often have the same design (see relevant sections in the appendix).

7.5.2 Brightness, Emittance, Pulse Length and N

From our requirements for imaging and diffraction, B_r (or B_n) ϵ_r (or ϵ_n), τ, and N were the most useful parameters. So in figure 7.13 we plotted four separate graphs butted up to one another. This lets us get quickly all the parameters we want, by drawing a box through them, as shown for the cold field emitter with a red box. The size of the rectangle tells us something about the quality of the gun, essentially the ultimate gun would be at the centre of the figure with a box of zero size. However due to limits such as stochastic interactions, space charge, and quantum limits no guns exist at the centre of the figure. In this graph, it is possible by aperturing to move a gun downwards. In this way the emittance is reduced, so the coherence and resolution increases, but N also decreases. Since the τ and B_r remains the same then, so does the size of the box.

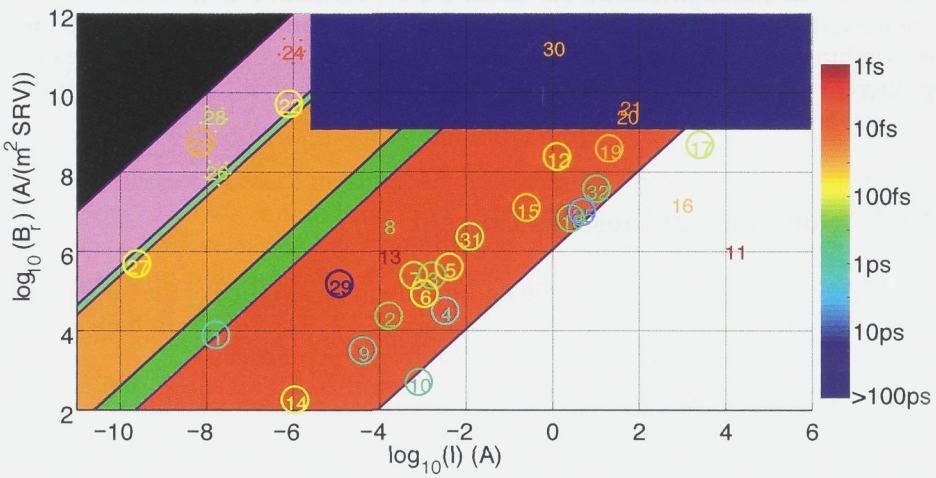

Figure 7.12: Circled numbers are experimentally proven, uncircled numbers are claims or theoretical possibilities. The colour of the marker gives an indication of the pulse length with red as the fastest and blue as the slowest as in the false colour map on the right. The blue area is only occupied by theoretical guns. The diagonal shaded areas show ϵ_r to perform the various imaging or diffraction outlined in section 7.3. Red is ϵ_{LAdiff}, green is ϵ_{Aim} orange is ϵ_{PTim}, light blue ϵ_{CBdiff}, purple is ϵ_{Pim}, and black is $\epsilon_{Cohdiff}$ which requires a completely coherent beam

Due to space charge forces a box will grow horizontally, B_r decreases because τ is increased (I decreases). If this happens with out a change in ϵ_r then the height of the box remains the same. Stochastic electron interactions however will cause the box to expand upwards and outwards, mainly decreasing B_r via increasing ϵ_r.

We can also look at how the guns are grouped for example, guns designed for particle accelerators are all located within the purple rectangle, interestingly half these guns are concepts.

The standard flat photo cathodes are enclosed by a much larger black box than the purple box, meaning they are less good than guns for particle accelerators enclosed by the purple box. Sharp tips and more exotic cathodes have a smaller (red) box than the purple box. The sharp tips have low emittance, for which they sacrifice charge, therefore their box is much lower than the other cathodes. Based on the logic that a smaller box is better it seems that the sharp tips are the best. We will of course examine this further.

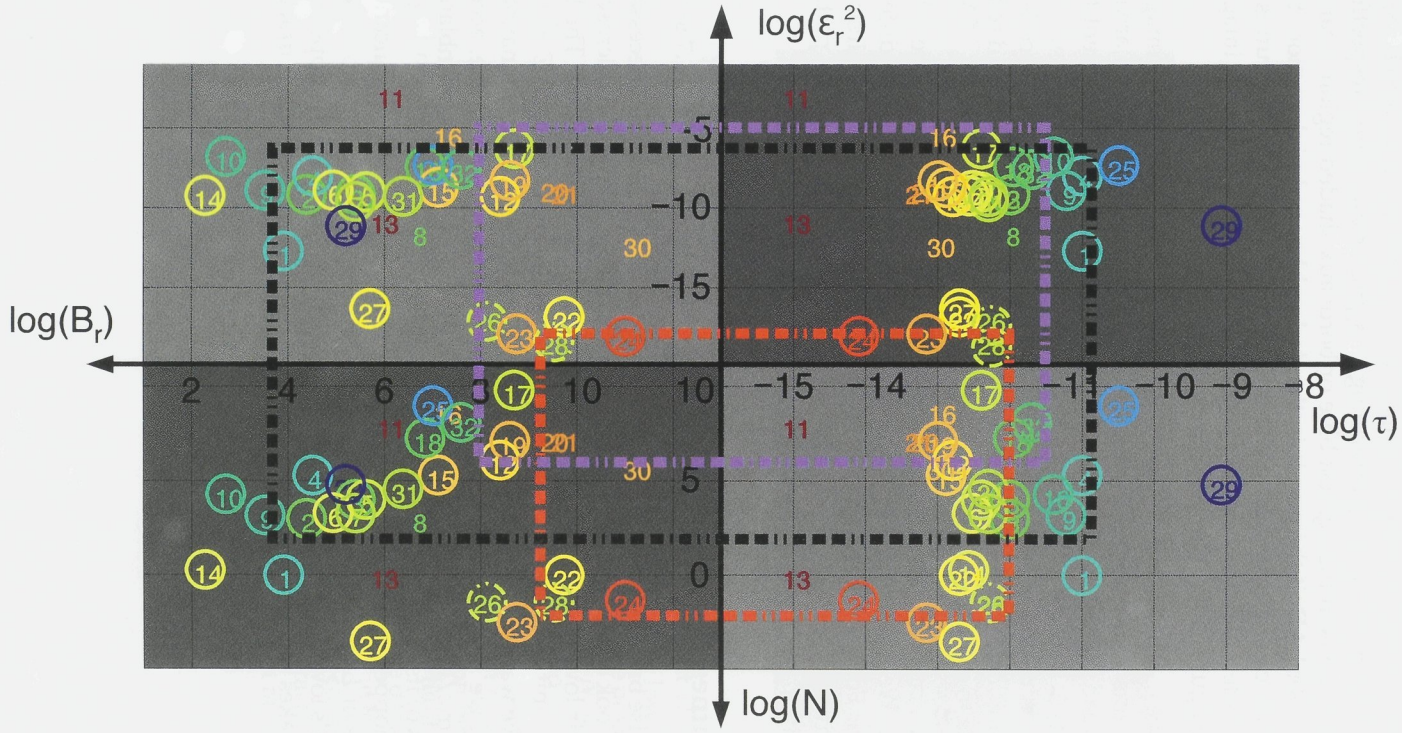

Figure 7.13: Four graphs butted together. The Graphs are plotted on a log scale and show all the parameters needed to calculate B_r. Upper left graph is B_r, against ϵ_r^2. Upper right is τ against ϵ_r^2. Bottom left is B_r against N. Finally Bottom right is N against τ

In section 7.1.2 we set a value for $\tau_{atomic} = 100$ fs, and later in section 7.3 we set $N_{diff} = 1 \times 10^6$ and $N_{im} = 1 \times 10^8$, now we can use them to plot $B_r(\epsilon_r)$ as shown in figure 7.14, we also include a line for ϵ_{rAim} and $\epsilon_{rLADiff}$ which are our maximum (least stringent) ϵ_r for performing imaging or diffraction respectfully. In a nutshell if a gun is in the lightest blue or bordeaux shaded region it can not perform single shot LAD, if the gun is in the darker blue and pink section it can perform LAD but can't perform single shot imaging. If however the gun is not in any of the shaded regions it can perform both LAD and single shot imaging. Please read the figure caption for a fuller explanation.

From 7.14 we can learn that no guns can perform single shot atomic imaging. For example Guns A.17 and A.16 are outside of the light blue shaded areas in 3 of the four quadrants yet not the upper right, where they lack sufficient time resolution. Gun A.16 is very close yet if we look at its ϵ_r we find that $\epsilon_r >> \epsilon_{Aim}$, and since it is inside the bordeaux shaded square we know it's emittance is not even good enough to perform LAD. We can of course aperture the gun and reduce ϵ_r however due to conservation of B_r, N will also fall dropping below $N < N_{im}$.

Several guns can perform single shot diffraction, especially if we are a little lenient with τ. We will see why this is later on when we examine the different groups of guns. For now let us note that only a few guns meet this requirement, and with relatively large ϵ_r, therefore only LAD single shot diffraction patterns are possible with these guns.

7.5.3 Brightness Vs Energy Spread

It's not just pulse brightness that is important, also ΔE. Although not necessarily brighter, (see Cook et al [63]) cold field emitters are often employed in microscopy because of their low ΔE. So we can plot ΔE against B_r, see fig 7.15. The blue shading is the limit from section 7.3.1 for atomic resolution imaging $\Delta E = 1$ eV. In this graph we want to be in the bottom right. Here we see the carbon nanotube A.28, and next we see a photofield emitter A.23. The carbon nanotube, according to this metric/graph is the best source and although so far only unblanked measurements of its B_r has been made, by the use of electromagnetic fields it can probably be chopped to around 0.2 ps (see Hosokawa [11]) without significant aberration or loss of B_r as shown in chapter 8, this gun is only good for stroboscopic work, due to it's low N. The high current guns, such as A.17 are in the upper right corner. This makes them unsuitable for imaging, but they can perform diffraction.

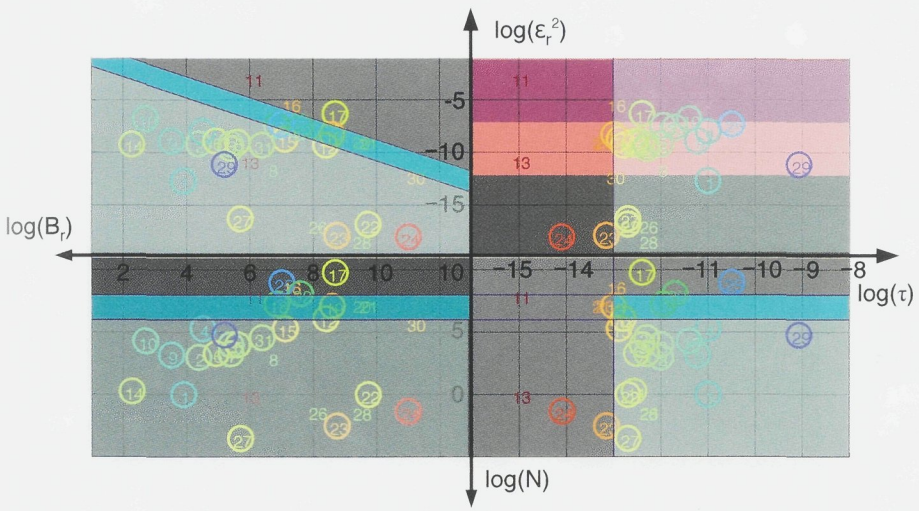

Figure 7.14: As per figure 7.13, but with shading to represent $B_r(\epsilon^2)$ for τ_{atomic}, $N =_{diff}$ and N_{Im}.In the bottom left, quadrant the lowest light blue or gray shading covers guns with $N < N_{diff}$ and the next set of shading in darker blue covers guns with $N > N_{diff}$ but $N < N_{im}$. Moving diagonally the top right quadrant has three shaded area the light blue with a vertical boundary covers guns with $\tau > t_{atomic}$. The pink and bordeaux coloured squares covers guns with $\epsilon_r > \epsilon_{rLADiff}$ and ϵ_{rAim} respectively. The bottom right quadrant combines both τ and N, making a rectangle. The guns inside the first light blue rectangle have both $\tau > t_{atomic}$ and $N < N_{diff}$. Guns in the darker blue square have $N > N_{diff}$ but $N < N_{im}$ and $\tau > t_{atomic}$. The top left quadrant features two quadrilaterals the lower light blue covers guns whose B_r is not good enough to make a single shot diffraction pattern. The darker blue quadrilaterals covers guns which can make a single shot diffraction pattern but not a single shot image.

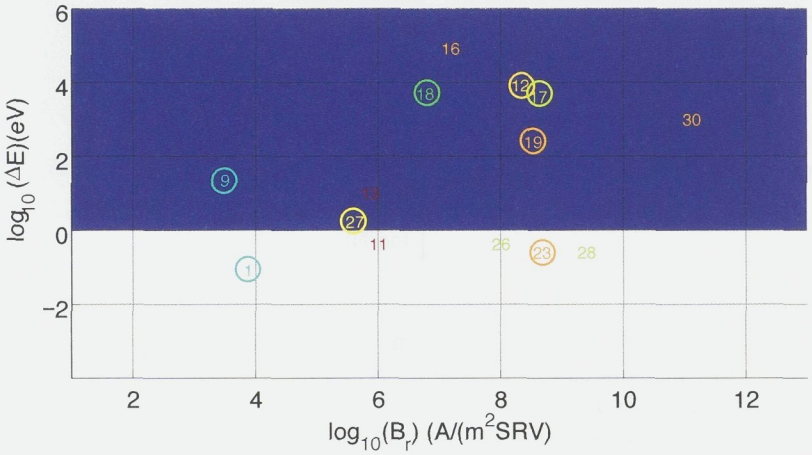

Figure 7.15: Energy spread in eV against mean pulse reduced brightness. Symbols have same meaning as 7.12. The blue shading is for those sources with $\Delta E > 1eV$ which is too great for atomic imaging.

7.5.4 Overview Table

No	$r(\ \mu m)$	$E(MV/m)$	$\tau(\ fs)$	N	$dE(eV)$	ΔE_x	$Br(A/(m^2srV))$	$\epsilon_r mrad mm\sqrt{(V)}$	$f(Hz)$	Exp
A.1	30		10000	1	0.1	0.1	8×10^4	0		y
A.2	75	2.7	1000	1000		0.1	2.8×10^4	26	3×10^1	y
A.3	75	6	1000	10^4		0.1	2.8×10^5	26	1×10^3	y
A.4	100	20	10000	2×10^5		1	3.24×10^4	100		y
A.5	100	9.1	400	10^4		0.1	4.1×10^5	31	1×10^4	y
A.6	100	12	300	2000		0.5	8.9×10^4	35	1×10^4	y
A.7	100	11.6	500	1900		0.1	2.5×10^5	16	1×10^3	y
A.8			1000	1000			5×10^6	2	1×10^3	y
A.9	150	7.5	6000	1500	27	0.1	3.3×10^3	35	5×10^3	n
A.10	1000		4000	2×10^4		0.5	5.09×10^2	399		y
A.11			1	1×10^8	0.5	0.5	1.2×10^6	36800		n
A.12	50	11.2	160	1.25×10^6	10000	0.6	2.5×10^8	23		y
A.13	10	10	1	1	12	1	8.8×10^5	4		n
A.14	70	2	270	1.85		0.6	1.89×10^2	24	2.7×10^6	y
A.15			130	2×10^5			1.3×10^7	44		y
A.16	30000		104	5.88×10^8	100000		1.79×10^7	2270	2.86×10^9	n
A.17	1300	115	400	6.25×10^9	5000		4.96×10^8	715	3×10^3	y
A.18		104	1120	1.81×10^7	6000		7.01×10^6	193		y
A.19			100	1.25×10^7	300		4×10^8	71	1×10^1	y
A.20	100		60	1.88×10^7			3×10^9	41		n
A.21	50		50	1.88×10^7			5×10^9	35		n
A.22	0		200	1		0.3	5.4×10^9	0		y
A.23	0.03		70	0.0031	0.3	0.3	5.6×10^8	0	8×10^8	y
A.24	0.03		8	0.025			1×10^{11}	0	1×10^1	y
A.25	50		32000	9.38×10^8			1×10^7	218	3×10^3	y
A.26		400	500	0.05	0.5		1.2×10^8	0	2×10^2	n
A.27	100		200	3×10^{-4}	2		5×10^5	0	1×10^1	y
A.28	0.01	5000	500	0.044	0.3		3×10^9	0	2×10^2	n
A.29	50		850000	6.25×10^4		3	1.57×10^5	3		y
A.30	30		100	6.25×10^5	1200		1.57×10^{11}	1		n
A.31	500		500	3.75×10^4			2.4×10^6	23		y
A.32	400	75	2000	1.25×10^8			3.91×10^7	161		y

Table 7.3: Parameters for guns reviewed, see appendices for more details

7.5.5 Flat Photo Cathodes

In this section we look in detail at the flat photo cathodes, we have split these into three categories, DC, RF and compressed guns and relativistic RF guns. Each section starts with an explanation of the type of gun, then we discuss how the gun is used and what we can expect from it in terms of imaging and diffraction performance. We use the four quadrant graph from the previous section to compare the guns one against the other. Finally we try to suggest what the ultimate performance of the guns should be and how to get there or modify them to get something better.

DC Flat Photo Cathodes

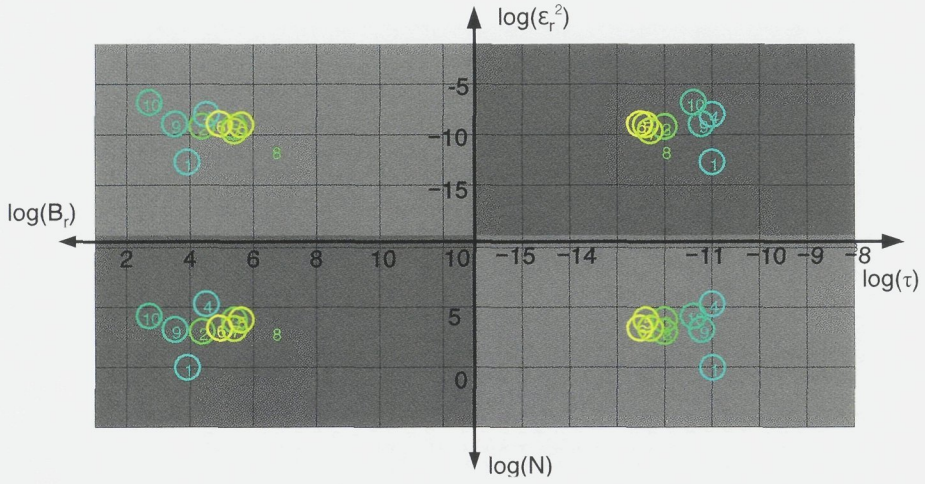

Figure 7.16: Flat Cathodes

This is the type of cathode most used and can be illuminated from the front by a laser, as in figure 7.17 where we see two examples, both taken from [104]. In figure 7.17 the upper gun is a new gun being tested, it was designed by Togawa [105] as a thermal gun but is being investigated as a photo emitter. The lower gun is a less sophisticated design which due to the sharp edges and lack of a Wehnelt causes a reduction in beam quality.

Most of the cathodes in this review are however rear illuminated using a thin film such as the UED4 cathode at Caltech see gun A.4, in this way the scattering length of the electrons, the penetration depth of the photons, and the thickness of the film can be optimised for maximum quantum efficiency. Rear illumination also means they can have smaller laser spot sizes, since the laser path to the cathode does not cross the electron's path, see figure 7.18.

So far all the ultra-fast pump probe electron diffraction experiments we know of, apart from the 4DTEM A.1 and the ultra-fast SEM A.22, used a flat cathode.

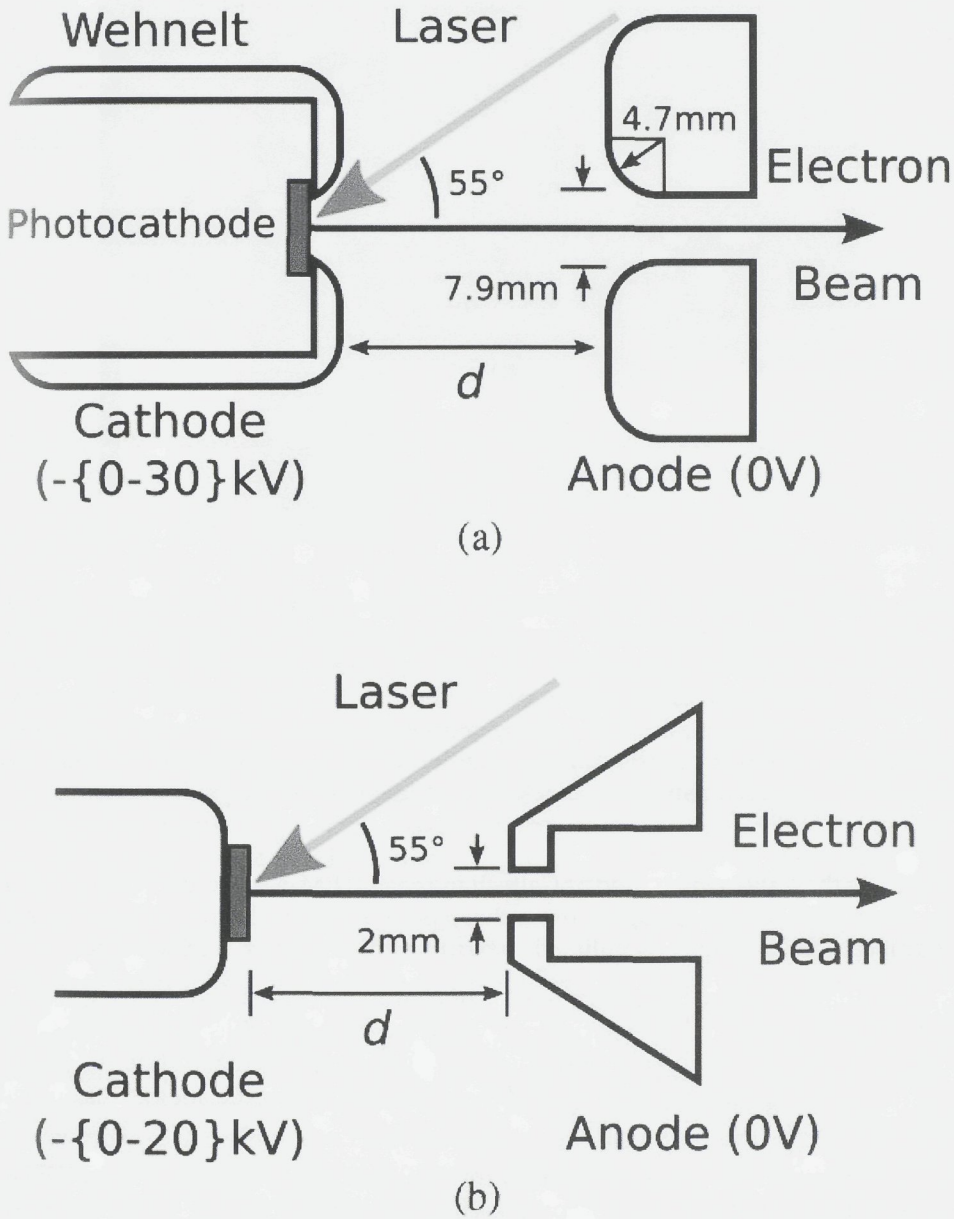

Figure 7.17: Figure taken from [104] with permission. Upper figure is the gun described in [104] based on [105], the lower gun is a more simple gun used as a comparison in [104].

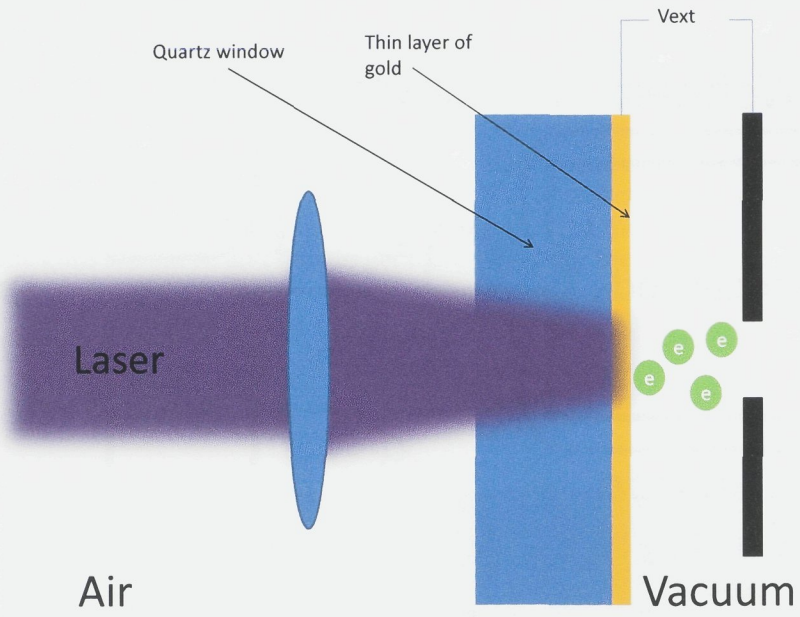

Figure 7.18: Rear Illuminated photocathode. The left side is all in atmosphere and the right side is in vacuum. The laser can be focused to small spot since the objective lens can be close to the cathode. As described in the main text the layer of gold has its thickness matched to the scattering length of the photoelectrons to try and maximise the quantum efficiency of the cathode. An extraction field is applied to a pinhole extractor shown in black here, or in some cases a grid.

Actually the LaB6 source used at Caltech in the 4DTEM A.1 could also be classed as a flat cathode even though it has a sharp point, it is not sharp enough to create significant field enhancement like the sharp tips discussed in section 7.5.6.

The flat cathodes can produce a lot of charge per bunch, so they are useful for multi-shot diffraction experiments. They have a believable B_r of up to 4.1×10^5 $\mathrm{A}/\left(\mathrm{m}^2\mathrm{srV}\right)$ A.5, and our best guess for a gun from Michigan state A.8 is 5×10^6 $\mathrm{A}/\left(\mathrm{m}^2\mathrm{srV}\right)$ although here we find that the data is not sufficient for this outlier so it is not circled.

The minimum $\epsilon_r = 1.8$ mm mrad is also from Michigan, The next lowest which may be better placed in the sharp tip section is the gun from the 4DTEM A.1. N goes from 1 if we include the 4DTEM up to 2×10^5 for the UED4 gun A.4, which also has the longest $\tau = 10$ ps, the shortest pulse 200 fs is again the 4DTEM A.1. The correlation between N and τ is due to space charge forces.

So what can we see with a flat cathode? Let's first look at the imaging possibilities, this was summarised in table 7.1, and all relevant points are indicated with a dotted black line in figure 7.19. We already know that none of the guns can

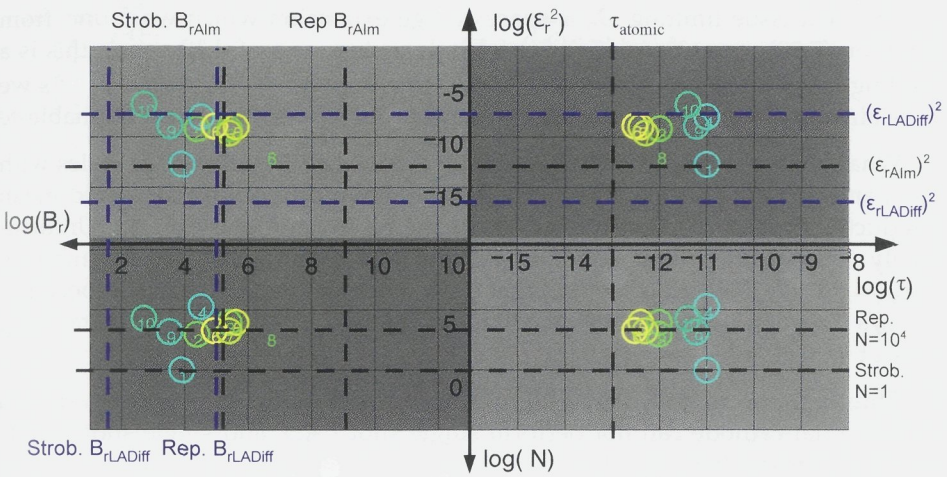

Figure 7.19: Standard Flat Cathodes arranged as per figure 7.13, here we have marked pertinent data points for imaging discussed in the text with a dashed black line and for diffraction with a dashed blue line.

perform single shot imaging with atomic resolution (τ_{atomic} and r_{atomic}). In fact also repeated imaging ($N = 10^4$) is currently not possible with these flat cathodes. The only gun performing imaging is gun A.1, and this doesn't have sufficient B_r according to table 7.1 to do any kind of atomic imaging (assuming $N = 1$), and as expected their pump probe experiments have a resolution of around $1 - 2$ nm. We can always aperture, reduce N, improve ϵ, and we wait a little longer for the higher resolution image to form, unfortunately we think this is limited by the signal to noise. None of the other proven flat cathodes meet the criteria for atomic imaging, although they do have higher B_r, their larger ϵ means aperturing, and whether they could achieve $\tau = 200$ fs like gun A.1 remains to be seen.

For a diffraction pattern, we need to look at table 7.2. As per figure 7.19 where interesting values are shown with a dotted blue line, all guns can perform LAD stroboscopy, not all the guns can perform repeated LAD, and no other type of diffraction should be possible. Again gun A.1 has performed convergent beam diffraction [74], however according to 7.12 we can see that this must have been performed with around $10^{-4}th$ of an electron per pulse to get the required ϵ_r. Some guns such as A.9 don't have the required B_r, however they do perform pump probe LAD experiments, however as we can see they must do them with significantly worse time resolution than τ_{atomic}.

To determine why the guns are not brighter, we need to return to section 7.4 on gun limitations . We can disregard laser heating, quantum limits and Stochastic interactions, but lets check Child's law (7.25), fields above or close to a $10\mathrm{MV/m}$ are difficult to generate and none of them guns have more than this, yet they all have $E > 1\mathrm{MV/m}$ which would limit them to a B_r of around 5×10^8 $\mathrm{A/\left(m^2 srV\right)}$, therefore this is clearly not the problem.

The next issue limiting B_r is space charge expansion which we found from equation (7.30) was 10^6 $\mathrm{A}/\left(\mathrm{m}^2\mathrm{srV}\right)$ for only a single cm of drift space, this is a limiting factor since no flat cathodes have more than 5×10^6 $\mathrm{A}/\left(\mathrm{m}^2\mathrm{srV}\right)$. As we have already said flat cathodes limit themselves to $N = 10^4$ to keep reasonable τ.

What can we do about the space charge expansion? Equation 7.26 scales with $1/r^2$, and although we can not increase the initial radius since this would mean a reduction in B_r we might try to defocus the beam, and let it expand. Unfortunately numerically solving equation (7.26) with $N = 10^6$, $B_r = 10^8$ $\mathrm{A}/\left(\mathrm{m}^2\mathrm{srV}\right)$, $\Delta E_x = 0.1$ eV, $\tau = 100$ fs we find that even when the radial expansion becomes $10^8\mathrm{m/s}$ the pulse has already expanded to more than a picosecond after traveling 1 cm at $v_z = 10^8\mathrm{m/s}$.

Thus it seems unlikely that without some further more radical improvements a simple flat cathode can not perform single shot LAD, and single shot atomic imaging is probably impossible.

There already exist two innovative and radical solutions which solve, or at least reduce the space charge problem. The first allows space charge to linearly expand the bunch then later re-compresses it using RF (Radio Frequency) technology or a static dispersive optical element. The other also uses RF to quickly reach relativistic speeds which decreases the space charge forces.

Non-relativistic RF and Compressed Flat Photo Cathodes

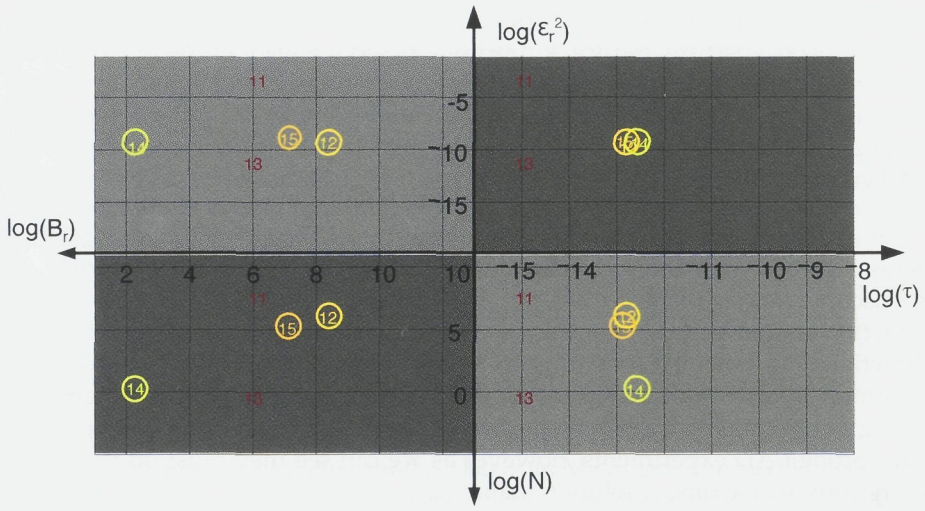

Figure 7.20: RF cathodes

The use of non-relativistic RF compression is so far only implemented by van Oudheusden at Eindhoven [96], [69]. Their goal is to create single shot 100 fs diffraction patterns from crystals of around 100 $\mu\mathrm{m}$. The issue with compression is to have linear space charge forces so that the expansion can be reversed.

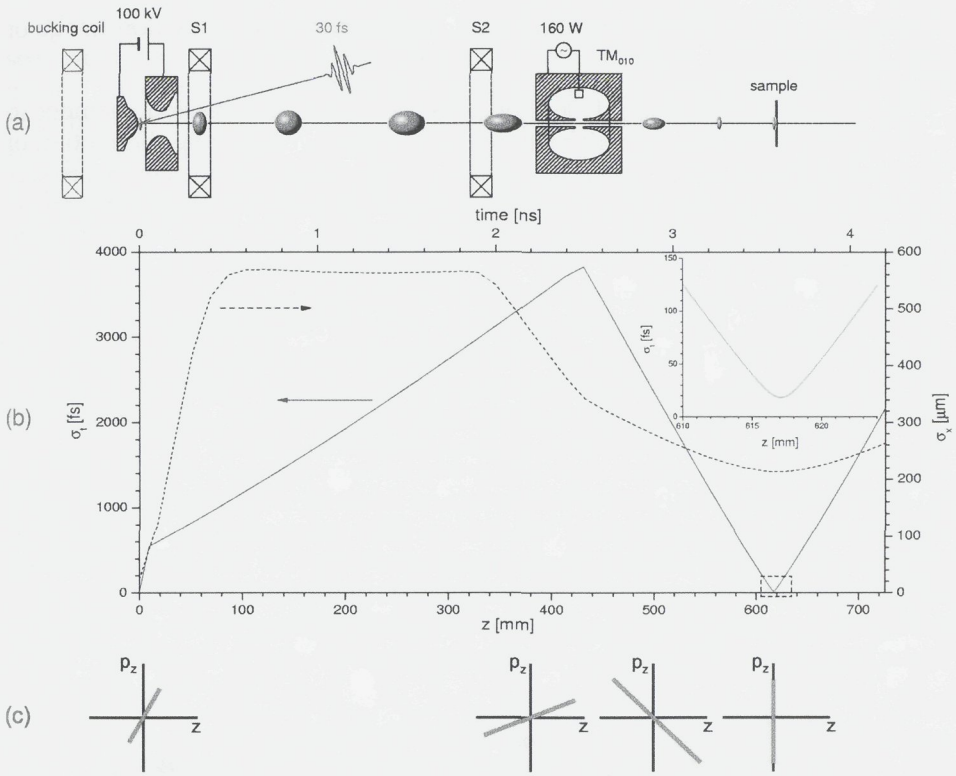

Figure 7.21: Taken from [96] copy right 2013 American Physical Society. (a) The UED set up in, with the red blobs schematically showing the evolution of the electron bunch (b) Solid line shows how τ_σ of the pulse varies with z, dotted line is r_σ (c) Cartoon of the z phase space of the electron bunch.

The design of [96] takes a short ($\tau = 30$ fs) laser pulse with a $\sigma = 50$ μm (where σ is the standard deviation) Gaussian pulse profile truncated at 50 μm. The dome shaped laser pulse results in a pulse with linear longitudinal space charge, which can be reversed with an RF cavity (3 GHz , TM010 E field). The RF cavity focuses the pulse at the sample. In figure 7.21a we see the basic setup, with the red ball representing the pulse. Part b of figure 7.21 gives us the temporal evolution of the pulse, (solid blue line) showing that in the cutaway it is being focused to $\tau_{sigma} = 20$ fs. The dotted line shows the rms beam width, initially there is a huge Coulomb explosion which after the first magnetic lens S1 is suppressed, the second lens S2 focuses the beam, onto the sample to make a 200 μm spot. However the RF cavity adds some defocus, due to the fringe fields. Finally in figure 7.21c we see a cartoon of the z phase space starting with a positive correlation, until the RF cavity at which point the correlation is reversed until finally at the sample it is brought into focus, thus vertical with no correlation between the momentum and position.

In a recent experiment they took a single shot $\approx$ 100 fs diffraction image of gold foil [69].

In the future Peter Baum [106] hopes to use an RF compression chamber to perform sub fs stroboscopic diffraction and perhaps even capture the motion of electrons within a solid. There has also been a simulation paper by Schroeder A.11 and Fill et al A.13 on using RF techniques to compress pulses. Many particle accelerators use RF compression yet they do this at relativistic speeds and rarely do electron imaging.

It is also possible to compress with out using RF techniques, gun A.15 uses a dispersive reflecting element which also bunches the electrons. The big advantage of this is there is no need to synchronise the RF chamber to the laser. The disadvantage is that the electrons must come to a complete stop, lengthening their transit time and allowing statistical electron-electron to increase ϵ.

The Eindhoven gun has an estimated $B_r = 2.5 \times 10^7$ A/ $\left(\mathrm{m}^2\mathrm{srV}\right)$, has a measured compressed pulse length of 160 fs, $\epsilon_r = 2.25e - 5\mathrm{m}$ rad and $N \approx 10^6$. This places the Eindhoven gun in a smaller square on figure 7.13 than the DC flat cathodes, and roughly in the middle of the other RF cathodes in 7.20. The compression and space charge introduce a relatively large energy spread of some keV, so it is in the blue section of 7.15 and unsuitable for imaging.

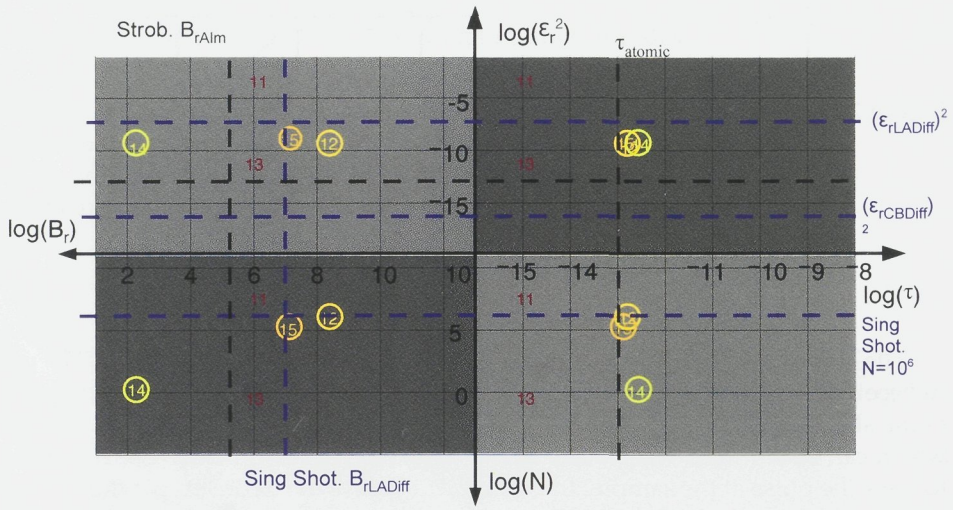

Figure 7.22: Non-relativistic RF and Compressed Flat Photo Cathodes arranged as per figure 7.13, here we have marked pertinent data points for imaging discussed in the text with a dashed black line and for diffraction with a dashed blue line.

Looking at the imaging power with the pertinent values shown in figure 7.22 by black dotted lines we see that these guns can perform stroboscopic imaging but they will need to lose a lot of their electrons since their emittance is orders of magnitude greater than ϵ_{Aim}

However these guns are designed to perform single shot LAD and as can be seen from figure 7.22's blue lines. In fact a successful demonstrations have been made of at least sub ps LAD, [69]. They can not however perform the other types of diffraction with out reducing their emittance, and certainly cannot do this in single shot mode.

Unlike the other photocathodes this type of gun is not limited by temporal space charge, however it is limited by Child's law, according to equation (7.25) with a field of 10 MV/m keeps the $B_r < 5 \times 10^{10}$ A/ $(\mathrm{m}^2\mathrm{srV})$ Compressing the pulse increases I making it brighter, but there are limits to how much it can be compressed. For example the timing jitter between a laser and a cavity was measured to be 14 fs [107]. The stochastic Coulomb interactions also limit the focusing and further problems will arise from aberrations in the RF cavity, path length differences and imperfections in the initial electron intensity distribution.

To beat Child's Law we can use a long thin cigar shaped electron pulse, which also has linear space charge forces and so can be compressed. Equation (7.24) for the short pulse Child's law is independent of τ, yet the long pulse or DC Child's law is dependent on N/τ. So with a long enough cigar pulse we can increase N as desired. Still of course there is a limit to the maximum the pulse can be compressed, this is probably first given by stochastic Coulomb interactions, but the Pauli limit, says that no single shot imaging can be performed, due to the demand of $\Delta E < 1$ eV.

Thus it would appear that there is still no possibility of achieving single shot imaging.

Relativistic RF Flat Cathodes

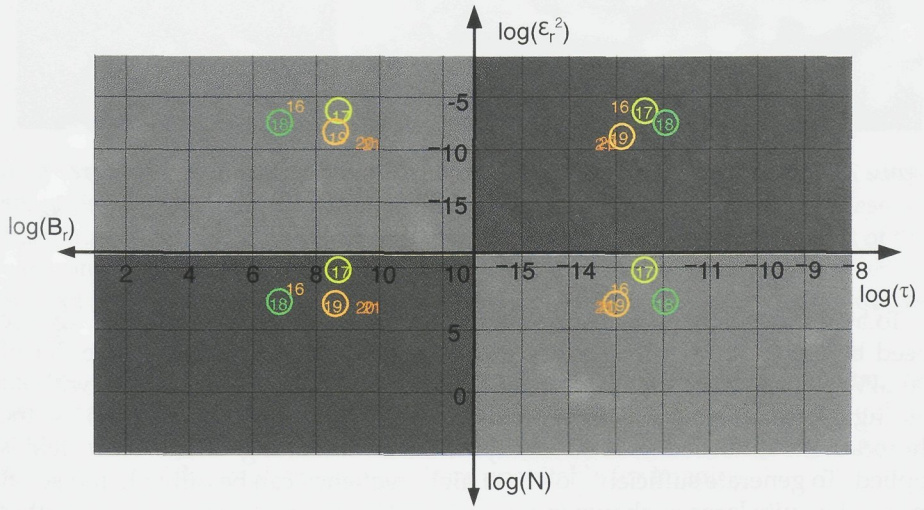

Figure 7.23: Relativistic RF and Compressed Flat Photo Cathodes arranged as per figure 7.13.

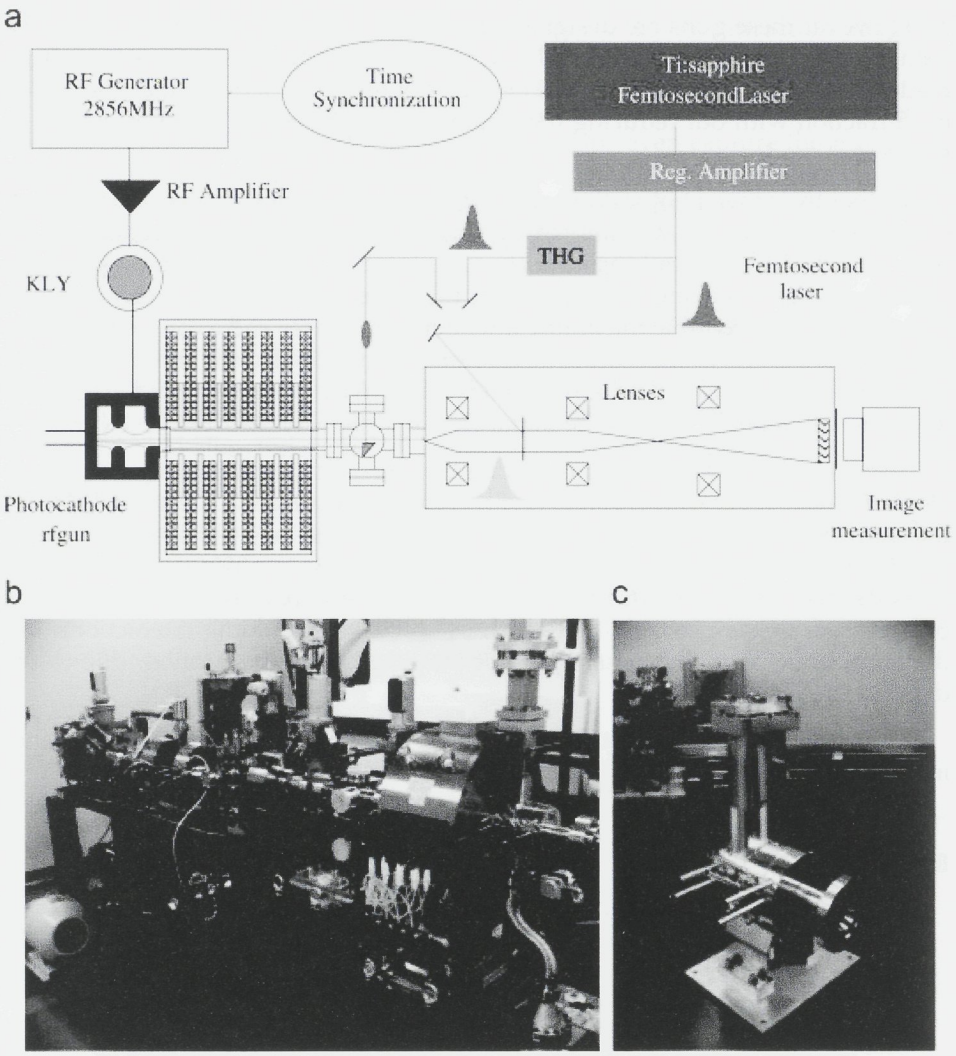

Figure 7.24: taken from [98] with permission. Lower section is a photograph on the MeV gun at Osaka university, above is a schematic showing the layout of all the components picture.

To avoid space charge expansion the electron bunch must reach a relativistic speed before the bunch length has grown. So an acceleration on the order of 100 MV/m is used see for example gun A.17 at SLAC. To have this field without causing a breakdown the field can only exist for a short period of time. So the photocathode is housed in an RF cavity where an oscillating GHz electric field is applied. To generate sufficient power at high frequency can be difficult and so set ups can be quite large as shown in figure 7.24. This is a table top set up, the other relativistic examples are particle accelerators such as those at SLAC.

So far there have been two locations where single shot diffraction experiments

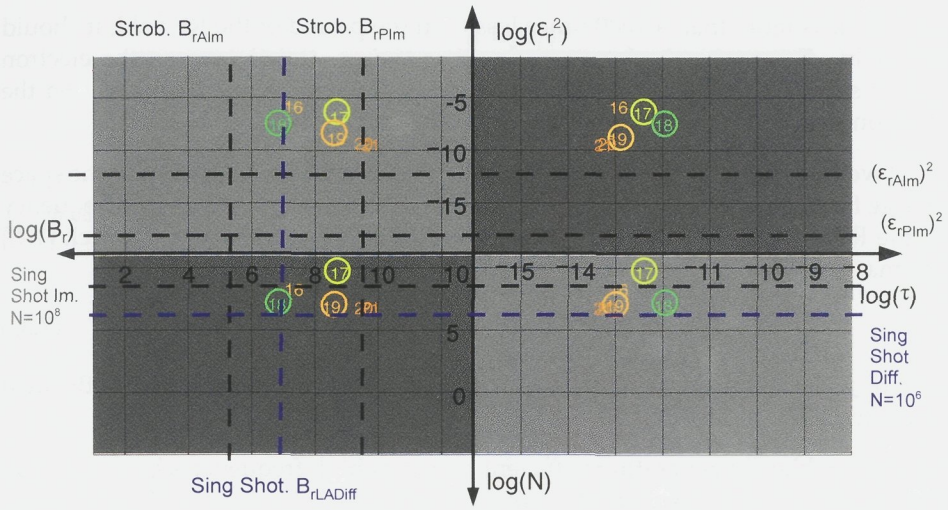

Figure 7.25: Relativistic RF and Compressed Flat Photo Cathodes arranged as per figure 7.13, here we have marked pertinent data points for imaging discussed in the text with a dashed black line and for diffraction with a dashed blue line.

have been performed with relativistic set-ups, Hastings et al, at SLAC [70] with gun A.17 and Murooka et al at Osaka university [98] with gun A.19 . Murooka has taken diffraction patterns of Si thin films with $r_{diff} = 0.25$ mm and Hastings looked at Al films with presumably similar r_{probe} since the starting beam diameter was 2 mm. However even though the work at SLAC was done in 2006 there are still no single shot pump probe experiments performed with relativistic electrons known to the author.

The gun A.19 has $B_r = 4 \times 10^8$ A/ $\left(\mathrm{m}^2\mathrm{srV}\right)$, at $N \approx N^6$, with $\tau = 100$ fs and within an $\epsilon_r = 7.2 \times 10^{-5}$ mrad$\sqrt{(volt)}$. Gun A.18 has $B_r = 7 \times 10^6$, $N = 1.81 \times 10^7$, $\tau = 1.12$ ps and an $\epsilon_r = 1.93 \times 10^{-4}$ mrad$\sqrt{V}$.

From figure 7.25 we see that all of the guns have sufficient B_r to make a stroboscopic image. Further guns A.20 and A.21 have sufficient B_r to make a phase contrast image with ϵ_{Pim}, however for this imaging they will need to lose a lot of their electrons since their ϵ_r is orders of magnitude greater than even ϵ_{Aim}. Therefore we can see that there is no way to perform single shot imaging, which requires a $B_r = 7.2 \times 10^{13}$ A/ $\left(\mathrm{m}^2\mathrm{srV}\right)$.

The ϵ of these guns is very similar to the DC flat photocathodes however they have many more electrons per bunch, which gives them the high B_r and the ability to perform single shot diffraction. Due to the RF field ΔE is pretty high around a few percent of the total, this makes them unsuitable for imaging.

Again these cathodes are limited by Child's law this time due to the $10\times$ increase in field from a $B_r = 10^9$ A/ $\left(\mathrm{m}^2\mathrm{srV}\right)$ to $B_r = 10^{10}$ A/ $\left(\mathrm{m}^2\mathrm{srV}\right)$. We should note that this was Child's law for a DC field, however since the length of the elec-

tron pulse is more than a 1000 times less than the period of the RF field, it should still hold. Even with the huge acceleration and relativistic energy the electron pulses still expand, in the case of gun A.19 it depends roughly linearly on the electron density $(e/cm^2)\ 1.7 \pm 0.2 \times 10^{-8} fs/(e/cm^2)$ [98].

If we increased the E field on the cathode we might be able to reduce the space charge forces acting on the bunch. This could be done by increasing the frequency of the RF cavity, as according to the experimentally determined Kilpatrick [108] the maximum safe field achievable in vacuum is given by

$$f_{MHz} = 1.643(E_{MV/m})^2 \exp(-8.5/(E_{MV/m})) \tag{7.33}$$

Where f_{MHz} is the frequency of the switching field in MHz and E_{MeV} is the field strength in MV/m.

The problem is generating sufficient power at high frequencies becomes challenging, and finding a suitable RF power supply might be difficult. Further significant field emission begins at around 5 V/nm and in section 7.5.6 we discuss field emission at optical frequencies.

We also have the problem of laser heating which now becomes significant, as can be seen from figure 7.15. Another problem is laser ablation of the source, which will limit the lifetime.

So in conclusion even with Relativistic speeds there appears to be no possibility for single shot imaging. Although future advances in technologies like wake-field acceleration might change things, we find it unlikely that single shot imaging can be performed with these types of guns within the next generation. However we look forward to seeing what the relativistic and temporally focused guns can achieve.

7.5.6 Sharp Tips

A sharp tip emitter is typically a tungsten wire etched, to a sharp point, where the radius of the point, can be anything from a 1 μm to in the most extreme case a single atom. In this case cold field emitters are represented by gun A.28 which is a carbon nanotube. The sharp point means fields strong enough to allow the electrons to tunnel out of the atom can be generated with perhaps only a few volts potential difference between tip and extractor [109]. The field is extremely localised and so a controlled break down can occur.

Cold field emitters have been used for microscopy for almost a 100 years since the first field emission microscopes. Cold field emitters according to figure 7.12 are also the brightest proven emitters. It therefore might seem strange that they are not used more often in ultrafast electron microscopy. Probably however this is due to their small size, and therefore low current output, the too late realisation that single electron pulses should be used for high resolution studies and finally because they are typically used for static applications.

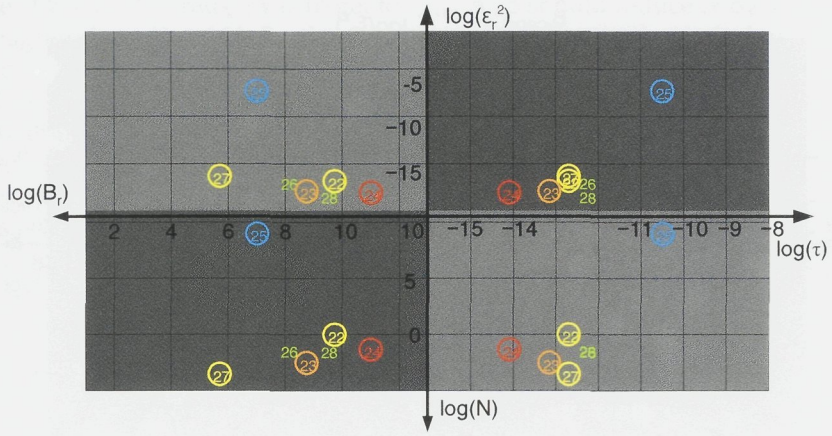

Figure 7.26: Sharp tips

Sharp tips can however become photo-field emitters, or alternatively a DC beam can be blanked, using magnetic or electric fields [110],[12]. In this section we will look at photofield emitters, and then later at blanking for DC beams.

Here are several different methods of using a laser with a sharp tip to generate electrons

- Photo-Schottky emission, here the strong field lowers ϕ (creating a Schottky barrier) this means that instead of a UV laser, a green laser can be used for example this is done by [88] with their new ultra-fast SEM (gun A.22).
- Photo-field emission uses a typically infra red laser to photo excite electrons to a point where the barrier is sufficiently thin that they can tunnel to vacuum, for example [111] and gun A.25 .
- Photo-thermal-field / Photo-thermal-Schottky an already thermally excited electron can be excited further by a photon, so that now it can either escape directly over the Schottky lowered work function or tunnel through a thinner part of the barrier. [46]
- Optical-field (gun A.24) is the process where the optical electric field of the incoming laser pulse, acts directly to increase the DC field, and the electrons can directly tunnel from the metal without being excited by the photon. This is an exciting topic as it is non-linear with the laser power, and still not accepted physics, with many people accrediting this to multi-photon effects.[112] and [113]

Using the ultra-fast SEM with a sharp tip at Caltech Mohammed et al. [88] have examined several materials including time-resolved electron backscattering diffraction (EBSD) of single-crystal InAs(100), where they were able to view the Kikuchi bands (see figure 3 of [88]). This and the other experiments have been

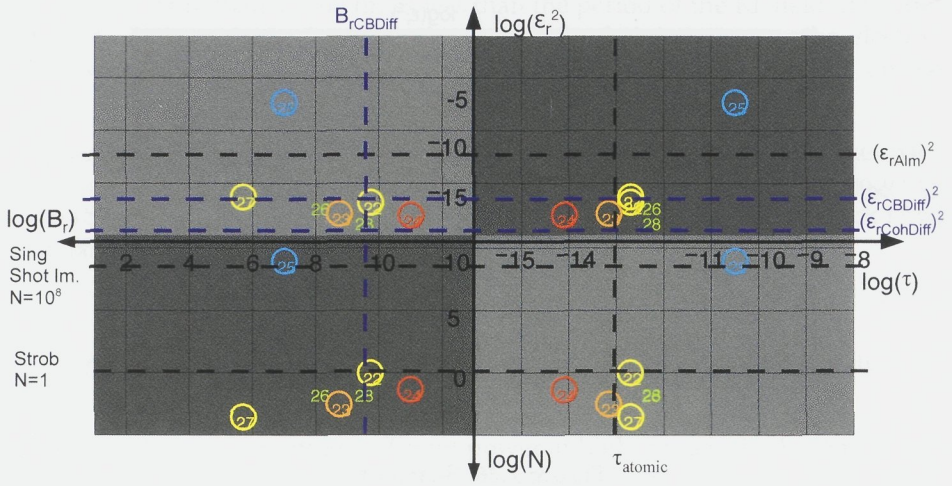

Figure 7.27: Sharp tips arranged as per figure 7.13, here we have marked pertinent data points for imaging discussed in the text with a dashed black line and for diffraction with a dashed blue line.

done in stroboscopic mode. The ultra-fast SEM has an $f = 100$ MHz and so it can do stroboscopic work in a short time. This is possible because the SEM can work on bulk samples where cooling between the pulses used to pump the sample will be much more rapid than the thin films used in TEM.

Others such as Hommelhoff et al. [114], Spence [56], and Barwick et al [113] have also experimented with photo illuminated sharp tips, as possibilities for UFEM.

As early as 1977 others such as Hosokawa [11] used electron blankers in combination with less bright tungsten hairpin emitters A.27 to image Schottky diodes on semiconductors stroboscopically. Although these did not have atomic resolution, the temporal resolution was no more than a few picoseconds, and pulses as short as 0.2 ps have been reported [12].

The performance of sharp tips is impressive, in figure 7.13 the red box around these emitters is the smallest. Gun A.28 was measured at 3×10^9 A/$\left(\mathrm{m}^2\mathrm{srV}\right)$, with an $\epsilon_r = 6.9 \times 10^{-10}\mathrm{mrad}\sqrt{V}$ and a measured ΔE of 0.3 eV. Guns A.28 and A.26 do not have a solid ring around them because they have only been measured in continuous operation, however when properly chopped their B_r should not be affected see chapter 8. Further although unmeasured, 8 fs pulse lengths are reported by gun A.24 (note that this pulse length will increase due to dispersion). What most of these guns lack however is a large N most have less than one electron per pulse. However gun A.25 produced bunches with $N = 6.25 \times 10^9$ although this sharp tip has a radius of 50 μm, and $\tau = 12$ ps.

Let's look at what type of imaging and diffraction the sharp tips can perform. Only gun A.25 has a high enough N for single shot imaging, but it's ϵ_r is far too

large at 2×10^{-4} m rad$\sqrt{(\mathrm{V})}$. To get to ϵ_{Aim} A.25 should reduce N by seven order of magnitude to $N = 166$. Further to get from $\tau = 10$ ps to τ_{atomic} it should reduce the current by another 2 orders of magnitude, so $N = 1$. The higher B_r guns (A.22A.23A.24A.26A.28) will actually be limited by their N if we solve equation 7.4 with ϵ_{Aim} for N then it comes to greater than their actual N. In other words even though these guns are bright enough, they can not supply enough current. However for the more demanding imaging and diffraction they are not limited by N. Also we can see from figure 7.12 that all the guns apart from A.25 have a small ϵ_r, all these emitters are already apertured in some way, however they all need to be further apertured to get a coherent beam and perform coherent beam diffraction.

The tips are capable of an extremely high brightness due to their extremely small virtual source size, and high current density. However the small N also comes from this small virtual source size. The energy spread is typically small because with only one electron in a pulse there can be no Coulomb interactions. Further with single electron in a pulse Child's law is not an issue. This also explains the excellent τ since there is no danger of space charge expansion increasing τ. However Heisenberg's uncertainty principle can limit the temporal resolution, since $\Delta E \Delta \tau = \hbar/2$ then for $\Delta E = 0.1$ eV the best temporal resolution achievable is 3.3 fs.

However as the photofield tip becomes increasingly small (ϵ_r decreases) the amount of laser power to release a single electron grows, and this can lead to tip damage. This is a real problem when the tip has only a few 100 atoms, the source can quickly be ruined.

If $N > 1$ then (depending on the tip size) we immediately create difficulties. For continuous beams, and long enough pulses our work [109], [115] on stochastic Coulomb interactions shows that typically field emitters are limited to a maximum $B_r = 10^{10}$ A/ $(\mathrm{m}^2 \mathrm{srV})$. This is in contrast to some papers by for example Jarvis [66] which discuss the Pauli-Exclusion principle as being the limit. For the short pulses with an average of one electron per pulse Poisson statistics become important see chapter 9. In those pulses with two or more electrons, Coulomb interactions can deteriorate the quality of the pulse. There is an increase in the ϵ, the pulse length and the energy spread.

Sharp tips are probably best suited to stroboscopic work, they have the low emittance required for the highest resolutions. Therefore the ultimate solution would be an atomically sharp tip with just less than a single electron per pulse on average. The only limits on this are the Pauli exclusion principle which also limits the electron density in the tip, the uncertainty principle and tip damage. If we can accept a large energy spread at the sample then the temporal resolution could reach sub fs by bunching, as proposed by Baum [106].

Unfortunately field emitters suffer from poor stability, and short lifetimes and it is likely that photofield emitter will perform similarly. However the Schottky tip A.26 or thermal field emitter, which is a little less bright has much better stability and a longer lifetime.

For single shot applications we will need to temporally focus since according

to equation (7.24) to extract a pulse with $N = 10^6$ in 100 fs from a 100 nm radius a field of $280\mathrm{V/nm}$ is needed. This field would mean that a field emission current of 592A was permanently present, which would be the background against the photo induced pulse.

As a side note: the useful B_r of a field emitter is B_r in a pulse minus B_r background, for example trying to add laser pulses to a Schottky emitter in normal operation would not be worthwhile, the maximum Brightness as limited by the Pauli exclusion principle is $B_r = 10^{13}\ \mathrm{A/\left(m^2 srV\right)}$ with a 1 eV energy spread, the Schottky source has $B_r = 10^8\ \mathrm{A/\left(m^2 srV\right)}$ so the maximum useful $B_r = 10^5\ \mathrm{A/\left(m^2 srV\right)}$

For temporal bunching the limitations are the same as those stated in section 7.5.5.

Thus with a sharp tip the possibility of single shot diffraction is not likely and single shot imaging even less so.

7.5.7 Novel Guns

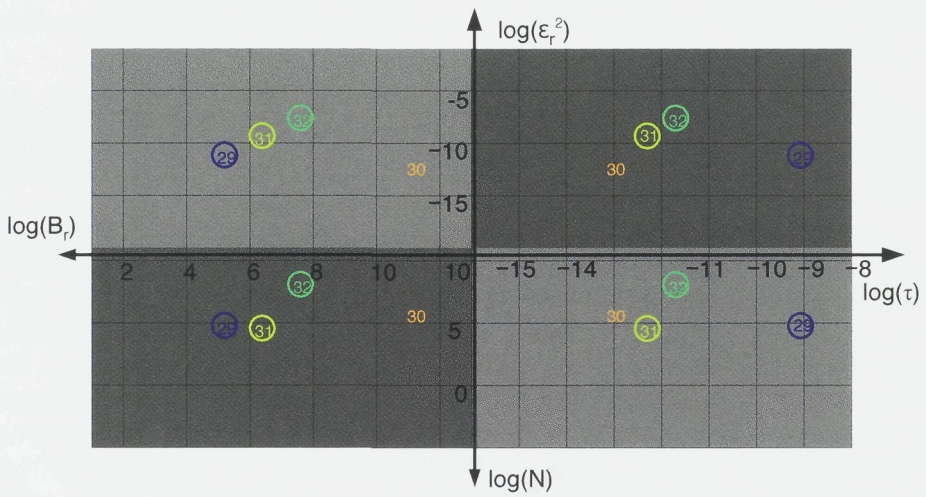

Figure 7.28: Novel guns that are difficult to classify

Here we look at three guns that don't seem to fall into any of the other categories, these are shown on figure 7.28, (one gun has two points). These novel guns are particularly interesting because they have been designed with UFEM in mind. Since they are new their performance is not as good as some others, however for some continued development will reap rewards. The less successful may inspire new ideas and we often learn more from failure than success.

Each of the three guns need to be described separately because of their completely different working principles.

The first gun we will look has two points on figure 7.28 , gun A.29 and A.30, these are two implementations of an ultra-cold atom trap which promises large

bunch charge at low emittance. The next gun A.32 is really a flat cathode from an particle accelerator with a novel RF streak camera which converts temporal information to spatial information, this promises single shot UFEM movies. Finally we examine a gun which uses a vaporised polyethylene film to produce laser accelerated electrons, this offers much larger acceleration than is possible with current RF technology.

Ultra Cold Atom Trap

Guns A.29 and A.30 refer to a magneto optical trap (MOT) which is used to super cool a gas to less than 10K. Since $B_r = Je/(\pi k_B T)$ this gun should have a very high B_r due to it's low T. The electrons are removed from the captured gas in two stages; first lasers excite the gas and then either a pulsed or DC electric field is applied. The process is described in figure 7.29 and its caption in more detail.

The ultra cold gas has a very long scattering length, much larger than the source size, so the quantum efficiency is very high when compared to a metallic source. It also means that the laser beam does not heat the material. Further this cathode will not contaminate or damage in the same way that a typical solid cathode would. According to the authors the biggest advantage is in the large source area which reduces problems with Child's law, unfortunately a large area also increases ϵ remember we stated in equation (7.25) and text next to it that according to Child's law the largest B_r would be around 6×10^9 A/ $\left(\mathrm{m}^2\mathrm{srV}\right)$ and this was independent of the cathode area. This gun has been designed at Eindhoven university and is documented in the thesis of Taban [117]. As far as we know this gun has not been used for pump probe experiments, but this is being investigated. There is also interest from other groups.

The UCAT has a measured B_r of 1.6×10^5 A/ $\left(\mathrm{m}^2\mathrm{srV}\right)$, a pulse length of $\tau = 850$ ps, $N = 6.25 \times 10^4$ and $\epsilon_r = 2.8 \times 10^{-6}$ m rad$\sqrt{(\mathrm{V})}$. This pulse length is too long for UFEM but is limited by measurement and in future implementations the plan is to shorten this pulse.

If we try to use this gun in it's current format to make an image then from table 7.1 and shown graphically in figure 7.30 we do not have enough B_r to perform single electron stroboscopic amplitude imaging. To reach the required ϵ they need $N \approx 1/3$ with τ_{atomic}. This system is limited by the time required to refill the trap between pulses, so if this can be done at $f = 1$ kHz an image would take 4 days to form. A brightness of 2.4×10^5 A/ $\left(\mathrm{m}^2\mathrm{srV}\right)$ (table 7.2) is sufficient to perform repeated LAD, currently this gun could only have $N = 5,000$ and not $N = 10,000$ within ϵ_{LAD}, This guns performance is limited by several things for example, measurement of the pulse, pulse length of the electric field and pulse length of the laser, these can be "fixed" by a change of equipment. The other limitations, Child's law, space charge expansion and stochastic interactions remain.

In [116] by van der Geer describe gun A.30, they computationally look at how this source might be optimised. The first problem discussed is the stochastic interactions which occur in the trap. By looking at this (correctly) as a thermalisation they find that the minimum/optimum T which this trap can achieve is

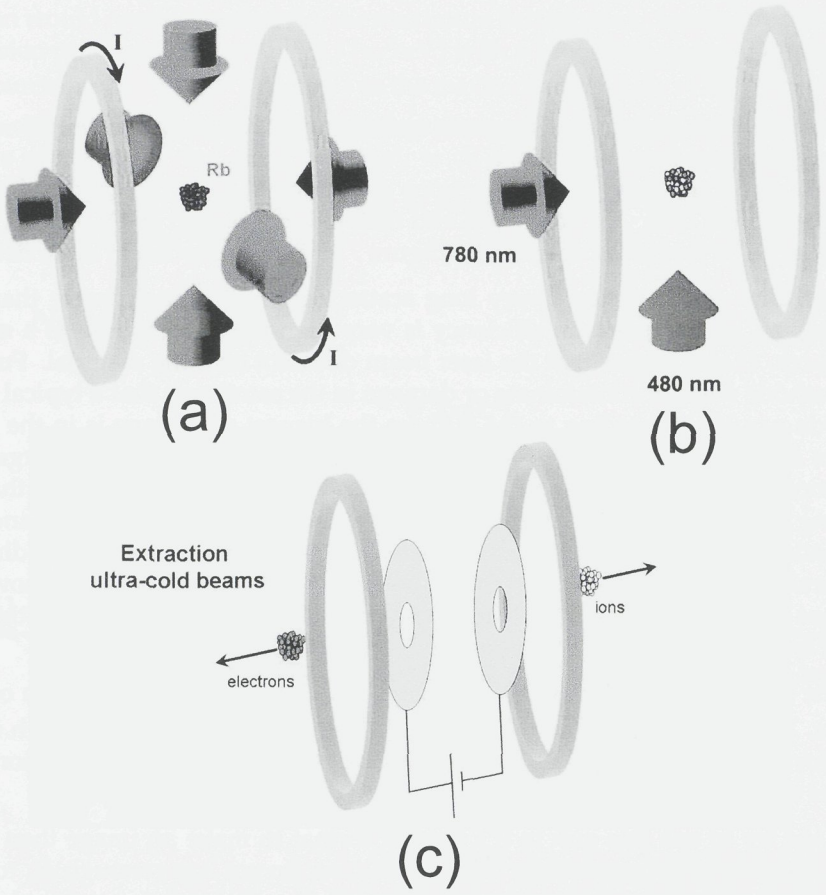

Figure 7.29: Taken from [116] with permission. Cartoon of the Ultra Cold Atom Trap UCAT, in picture (a) a gas of Rb atoms are captured and cooled using six laser beams. (b) the gas is ionised in two stages first by a $780nm$ laser and then a tunable $\approx$ 480 nm laser. (c) The atoms are now a fully ionised plasma or in a Rydberg state and are extracted from the trap by a strong electric field.

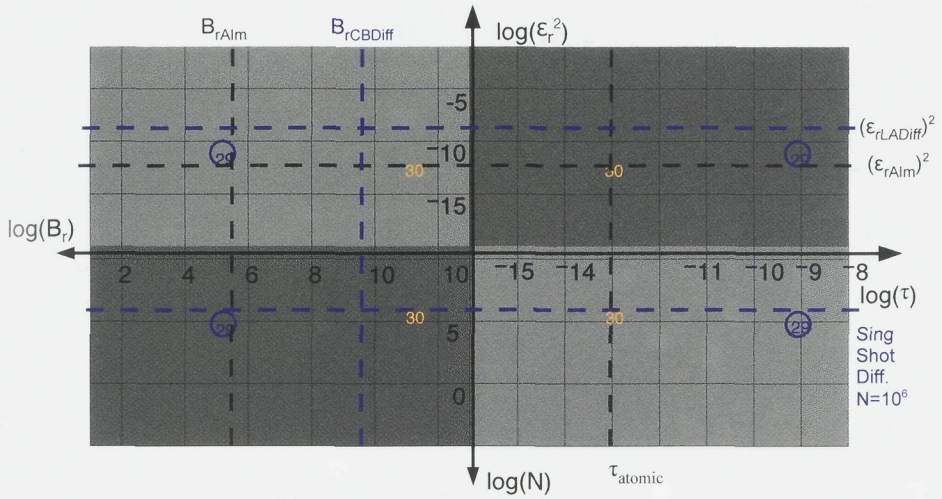

Figure 7.30: Ultra Cold and Ultra Cold Bunch Atom Trap arranged as per figure 7.13, here we have marked pertinent data points for imaging discussed in the text with a dashed black line and for diffraction with a dashed blue line.

10K. The next issue regarding a strong enough and fast electric field is solved by building the trap in an RF chamber. The bunch will still expand however they resolve this with a 2nd RF cavity which compresses the bunch. The bunch can be compressed because it has a long thin cigar like shape which has linear space charge forces. The bunched UCAT has $\tau = \tau_{atomic}$, $N = 6.25 \times 10^5$,$B_r = 1.6 \times 10^{11}$ A/ $\left(\mathrm{m}^2\mathrm{srV}\right)$,with $\epsilon_r = 8.04 \times 10^{-7}$ m rad$\sqrt{(\mathrm{V})}$. Despite a design criteria of low ϵ this gun cannot have low ϵ because of the large source area, and therefore it does not have low enough ϵ to perform stroboscopy (see table 7.1) without aperturing. It is bright and could even manage repeated imaging on all but ϵ_{Pim}. Howevever it can not perform single shot imaging as this needs a B_r two orders of magnitude greater. The ΔE is also far too large to perform high resolution imaging.

This gun meets it's design criteria of performing single shot LAD, the other forms of diffraction are still out of reach except stroboscopically, which due to the slow filling time of the trap is not a suitable way to use this gun.

Novel RF Streak Camera

Gun A.32 uses a long pulse to probe the sample and then using a streak camera rotates the pulse so that the z axis, (which for fixed velocity is equivalent to time $z = vt$) of the pulse is imaged into x. This method loses a spatial dimension, however for symmetric diffraction patterns that may not be an issue. The big advantage is that pulse can be long, but for gathering the information we still expect

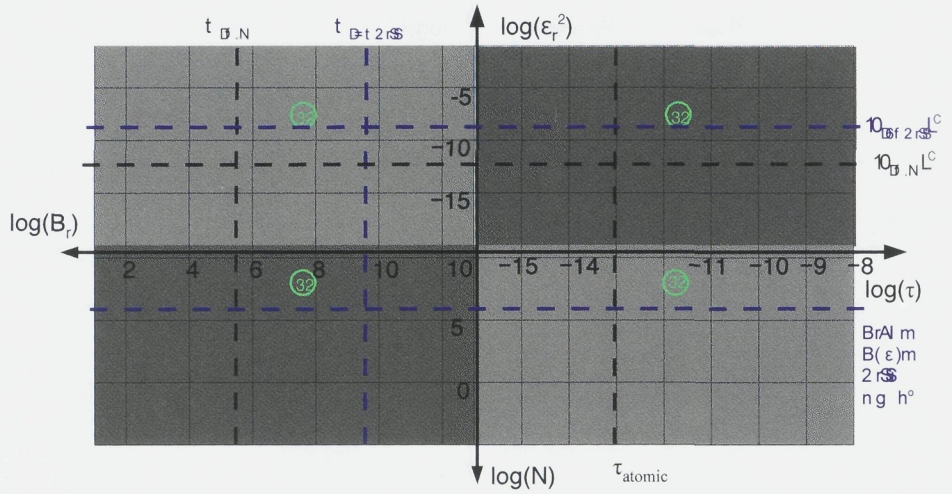

Figure 7.31: Novel RF Streak Camera arranged as per figure 7.13, here we have marked pertinent data points for imaging discussed in the text with a dashed black line and for diffraction with a dashed blue line.

to need the same $I = N_{diff}q/\tau_{atomic}$. So far this gun has been demonstrated by Musumeci in [118], and we are still waiting for real pump probe experiments.

Gun A.32 is located at UCLA and uses the Pegasus photo injector, it has $B_r = 4 \times 10^7$ A/ $(\mathrm{m}^2\mathrm{srV})$ so according to table 7.1 and shown in figure 7.31 it can perform stroboscopic imaging with $N = 1$ apart from the most demanding phase contrast imaging. From table 7.2, gun $A.32$ can perform single shot LAD, but none of the lower ϵ diffraction. The $\epsilon_r = 1.6 \times 10^{-4}$ m rad$\sqrt{(\mathrm{V})}$ is too high to perform any of the imaging the gun will need to be apertured and N severely reduced. However to perform LAD the ϵ_r is good enough.

The temporal resolution of Gun A.32 is not directly related to the laser pulse and bunch expansion like other pulses, since the streaking camera sets the temporal resolution. The N and τ are therefore not good comparators for gun $A.32$, and we should compare the N per τ_{atomic} , $N = 1.25 \times 10^8$ and $\tau = 2$ ps giving N per τ_{atomic} as 6.25×10^6 which is greater than N_{diff}. However gun A.32 has the same problems as other guns, its ϵ will grow due to stochastic interactions, and its pulse length will grow due to space charge, and it is also still limited by Child's law these last two are not important for temporal resolution since this will be determined by the streak camera, but they reduce B_r and so limit the amount of information that can be obtained. Since the gun uses an RF cavity for acceleration and relativistic speeds all of these problems are reduced, as stated in section 7.5.5. Further issues for gun A.32 are the timing between the streak camera, the RF cavity and the laser pulse, and chirp added to the pulse, these can cause a blurring of the temporal information, or if the chirp is known it can further complicate the data analysis. Gun A.32 might be improved in the same way as guns in section 7.5.5, but might also be improved by implementing the RF streak cam-

era with lower emittance source such as a (photo)field emitter. The advantage of a lower emittance source would as already discussed give access to smaller samples and perhaps other diffraction techniques in repeated mode. The physical limits of this gun remain the same however and eventually the Pauli exclusion principle or stochastic Coulomb interactions will defeat this gun, and therefore we don't expect any single shot convergent beam diffraction patterns, nor do we expect any single shot imaging to be possible.

Single Shot UED with Laser Accelerated Electrons

Gun A.31 comprises both a novel method of generating electrons and a method to compress them. The cathode is a 10 μm polyethylene film irradiated with p polarised light a few degrees away from the normal. The authors claim the electrons are then accelerated by the so called $J \times B$ heating see [119] by WL Kruer and K Estabrook. The result is that electrons with energies from around 0.1 to 1 MeV are created, those with $\approx$ 350 keV are selected and using two magnets to direct the beam through a complete circle temporal focusing can be achieved, since electrons with a higher energy travel a longer path. More details are given in figure 7.32 and its caption.

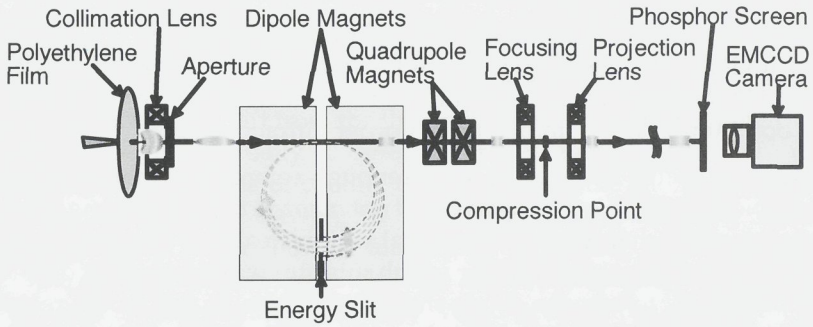

Figure 7.32: Taken from [120] Copyright 2013 American Physical Society. Schematic of the laser accelerated electrons set-up. From left to right we see the laser exciting a polyethylene film. The beam is collimated and then passed through a magnetic energy filter after which it is focused temporally and spatially onto the sample (at the compression point) and then imaged onto the phosphor screen.

So far gun A.31 has not performed any pump probe experiments however a demonstration of the pulse width ($\approx$ 600 fs) has been shown using laser scattering

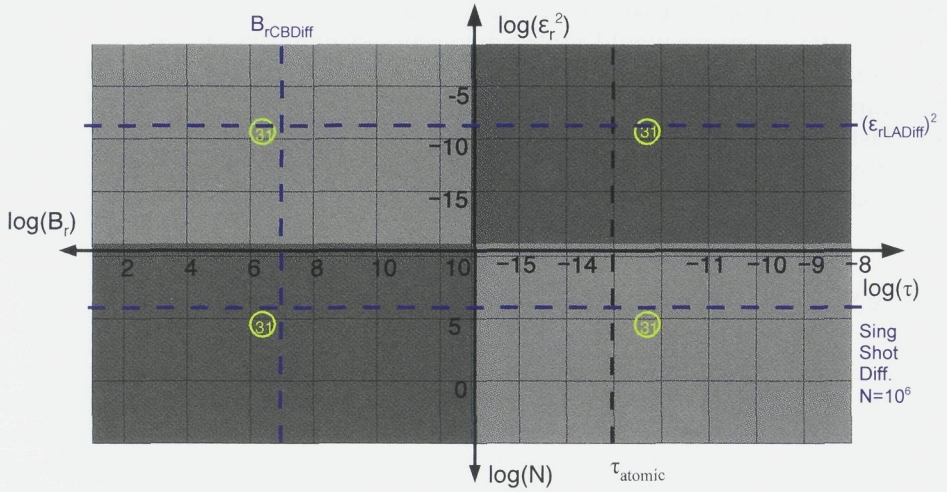

Figure 7.33: Single Shot UED with Laser Accelerated Electrons arranged as per figure 7.13, here we have marked pertinent data points for imaging discussed in the text with a dashed black line and for diffraction with a dashed blue line.

from the electron pulse, and a single shot electron pattern from an Au foil has been made.

According to our understanding this gun manages only $N = 3.75 \times 10^4$ yet in [120] Tokita et al show single shot diffraction patterns, in section 7.3.2 we set $N_{diff} = 10^6$ therefore we believe gun A.31 will struggle when noise conditions are not optimum or when finding higher order diffraction spots.

The $B_r = 2.4 \times 10^6$ A/ $\left(\mathrm{m}^2\mathrm{srV}\right)$ is high enough according to table 7.1 to perform stroboscopic with ϵ_{Aim}, but this gun could not manage the other forms of imaging. However since the energy spread is several keV the reality is this gun is not useful for imaging. In diffraction mode for which this gun was designed it does not yet have sufficient B_r to manage single shot experiments in any mode, requiring a factor of ten greater B_r, although this is only according to our requirements. The gun has sufficient B_r for repeated LAD. The pulse length is reasonable with a $\tau = 600$ fs, although this is similar to the uncompressed cathodes.

Gun A.31 is quite different from the other guns, so trying to decide what limits this gun is difficult. Since there is an extremely rapid acceleration from the laser Child's law is probably not an issue, nor since the pulse is compressed should longitudinal space charge be a problem. In this case perhaps the gun is most limited by the wide range of energies emitted by the source, and the loss of most of the electrons created when choosing an energy range. One can imagine many theoretical methods for making a more mono-energetic beam with more of the current, however most likely in practice they would be far too complex to implement. The B_r of this source should not increase with an increased laser intensity since the source is vapourised by every laser pulse and all electrons are extracted, however

more electrons will be extracted if a thicker film can be used.

This gun is interesting because of the novel, and large acceleration however as yet it's performance needs to be improved to prove it's usefulness. It can not perform single shot imaging, and will probably struggle with single shot LAD.

7.6 Conclusions

7.6.1 Summary of Guns

We have set several limits for electron guns and linked them to systems, and what they can perform.

We found that standard flat cathodes are limited by space charge expansion and that this should keep their B_r at less than 10^6 $\mathrm{A}/\left(\mathrm{m}^2\mathrm{srV}\right)$ (equation 7.30), this was respected by all cathodes except A.8 for which we found the calculated B_r doubtful. According to our two tables 7.1 and 7.2 this meant that they can only perform repeated LAD or stroboscopic amplitude contrast imaging, and we found only one exception with gun A.1, which might actually have been moved to the sharp tips in section 7.5.6 since it worked with only a single electron per pulse and so space charge expansion is not a problem.

The larger flat cathodes using temporal compression or relativity got around space charge expansion but never the less were still limited, this time by Child's law and stochastic interactions. Even with $E = 100\mathrm{MV/m}$ the maximum B_r according to Child's law (equation 7.25) is 6×10^{10} $\mathrm{A}/\left(\mathrm{m}^2\mathrm{srV}\right)$. None of the guns were able to reach this, apart from the theoretical implementation of the UCP gun A.30. Gun A.30 has essentially 40 times lower ΔE_x than the minimum we specified due to the novel idea of cooling the cathode. In the end none of the guns could perform single shot convergent beam diffraction or anything requiring a completely coherent beam. Further although they became bright enough to do some forms of repeated imaging, their huge ΔE prevents them from doing so in reality. Also it should be noted that they would need to lose a lot of the charge they created, to get to a reasonable ϵ for imaging.

The guns could perform single shot LAD and this was being demonstrated however there were no pump-probe experiments known at the time of writing.

The sharp tips had high B_r and could be used with either a laser or a blanker. These tips had mostly $N = 1$ or less, and had been performing stroboscopy since 1977 [121]. Perhaps the most interesting in terms of results came from gun A.22 which was a cold Schottky tip illuminated with a laser. The sharp tips were able to perform almost all types of stroboscopic diffraction or imaging, but creating a fully coherent beam seemed unlikely. Further although gun A.25 had enough electrons to perform single shot imaging (although nowhere near enough B_r) most of the guns with their small N could not perform anything other than stroboscopy. Gun A.25 had to sacrifice both ΔE and τ for its high I.

Finally we should note not even the novel guns got theoretically a B_r above 1.6×10^{11} A/ $(\mathrm{m}^2\mathrm{srV})$, which is two orders of magnitude less than what we required for single shot atomic imaging.

7.6.2 Final Conclusions and Outlook

It is hard to imagine that future systems will be able to perform any kind of atomic single shot imaging, and of course given its higher requirements complex diffraction is certainly ruled out.

The current trend seems to be focused on LAD, however with sharp tips stroboscopy starts to look more exciting, and the well developed techniques of static electron microscopy can be developed further in UFEM.

It is also not necessary to have a photo excited source and a traditional stable and easy to handle Schottky source can be chopped to perform Stroboscopy.

We believe that with $N = 1 \times 10^6$ there are enough electrons for single shot diffraction, and improving ϵ and τ should be the goal, so that higher B_r can be reached and new and more exciting science can be discovered.

8 CHAPTER

Electron Optics of An Ultra-fast MEMS Blanker

I could take Sean Connery in a fight... I could definitely take him.

Harrison Ford

We propose the use of miniature blankers to create sub ps pulses for ultrafast electron microscopy. This is an alternative to the presently used flat photo-emitters. We show both analytically and in simulations that for stroboscopy small blankers result in better performance than flat photo cathodes. We present our simulations of a simple non-symmetric micro blanker designed for use in Scanning Electron Microscopes. The blanker with a length of 100 μm for an electron beam of 16 nA and reduced brightness 10^8 A/ $(\mathrm{m}^2\mathrm{srV})$ can yield 400 fs pulses without significant deterioration of the brightness and only an additional 0.3eV energy spread. It is expected that this can easily be improved.

8.1 Introduction

Ultra-Fast Electron Microscopy (UFEM), is a technique allowing us to view the world on the atomic level this means Angstroms and femtoseconds.

It is a pump probe technique where typically a laser excites a sample and later a bunch of electrons probes the sample.

The basic set up is shown in figure 8.1

In chapter 7 we split UFEM into three different types based on the number of electrons N in a pulse, these are; single shot $N \geq 10^6$, repeated $N \approx 10^4$

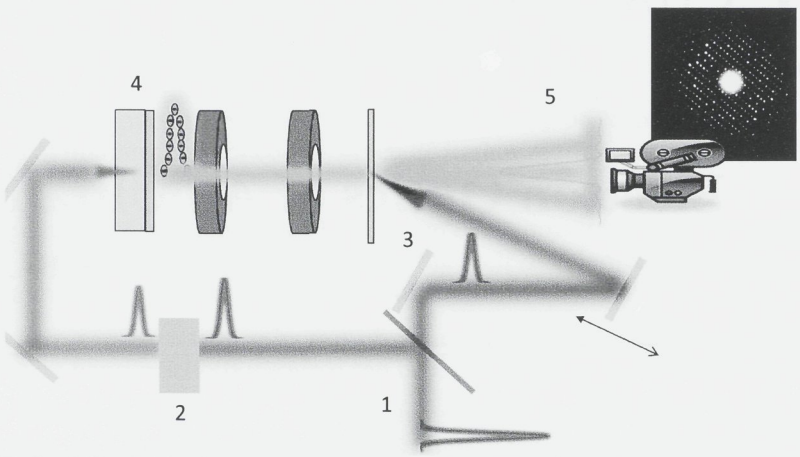

Figure 8.1: Schematic of a UFEM. Following the labels, (1) an ultra-fast (typically) infrared laser pulse is split into two pulses (2) one of which is frequency tripled by a non-linear optical crystal, the other (3) pumps the sample. The now ultra violet pulse excites the photo cathode (4) creating an electron bunch which then probes the sample (5). The delay between pump and probe is controlled by the path length of the laser.

and stroboscopy $N \approx 1$. From our literature studies in chapter 7 we find that space charge limits the first two to diffraction of large areas $\text{mm} \times \text{mm}$ with ≈ 1 ps time resolution in diffraction or $100\ \mu\text{m} \times 100\ \mu\text{m}$ and ≈ 10 ns for real space imaging. Stroboscopy uses only a single electron per pulse, so there is no space charge, allowing imaging and diffraction with $< nm$ and ≈ 100 fs resolution [122]. Unfortunately because the image/ diffraction pattern must be built up over many ($> 10^6$) pulses only repeatable processes can be viewed. The advantage of stroboscopy is that standard TEM/SEM analytical techniques can be combined with stroboscopy making it a very useful technique. For example convergent or selected area beam diffraction is useful since the thickness of a sample can vary considerably making a diffraction pattern difficult to interpret, so the pattern from a small area of constant thickness is useful [8]. In the Scanning Electron Microscope (SEM), backscattered diffraction patterns can give information on fault locations and these would be lost in a wide area diffraction pattern. Noise is a problem in stroboscopy because of the low charge per pulse. With a higher

brightness[1] (B_r) source more electrons can be delivered within the desired emittance, reducing the noise. The main group performing stroboscopy is at Caltech, where they use a laser excited LaB6 source in a TEM which we estimate to have $B_r \approx 1 \times 10^6$ A/ $(\mathrm{m}^2\mathrm{srV})$ see chapter 7 . The Caltech group can excite the LAB6 source with a spot radius of approximately 50 μm, so assuming an excess photon energy of 0.1 eV (see 2), they have 1500 electrons per 100 fs pulse. For one electron per pulse they must filter with an aperture, so before this filter and there may be enough space charge to make the electron bunch expand. There is a further temporal spreading from the initial energy spread of the electrons, which will add extra time dispersion. This is illustrated in the cartoon in figure 8.2

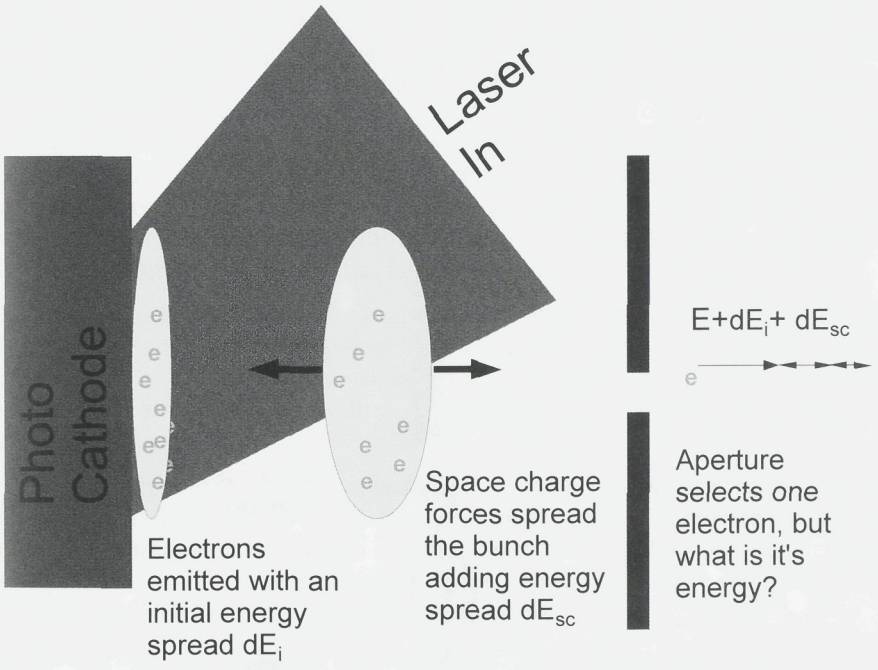

Figure 8.2: Cartoon of the emission process in a single electron gun

Decreasing the laser's spot size would help, but because the system is built into a TEM, access to the gun is difficult and probably would need a complete gun design, finally the diffraction limited spot radius would not be much less than one micron. A better solution is to use a sharp photo field emitter, here the emission area is restricted to the apex of the emitter (due to the highly localised field at this point which lowers the work function) which can be less than 1 nm in radius. Unfortunately stability data for these types of emitters is limited and we know that the stability of field emitters is poor. There is an Ultra-Fast SEM in [71], which uses a sharp tip (a cold Schottky emitter) as a source, so far this seems to function well

[1] Actually we mean the reduced brightness but to avoid being cumbersome we will refer it as brightness

but the reliability is not known. Modifying an electron microscope is expensive, and could damage this precision instrument, therefore we present our solution, an ultra fast blanker with a high brightness ZrOx Thermal Field source. The source is well tested, extremely stable, and has a measured $B_r > 1 \times 10^8$ A/ $\left(\mathrm{m}^2\mathrm{srV}\right)$ [19]. Further as we found in chapter 7 there are no sources with measured B_r greater than the Schottky source apart from cold field emitters.

Our set up is shown in figure 8.3 where the blanker is shown in an SEM, and this is where this paper focuses.

The blanker is an improvement on current systems not only because of the high B_r source but because the blanker will be closer to the sample so dispersion due to the initial energy spread will be less. Further the system is designed to be plug and play, so the SEM can be used for other tasks, and quickly adapted to be used for ultra-fast work. In figure 8.3 we can see a schematic showing how the blanker would fit into an SEM. The size of the blanker is many times exaggerated.

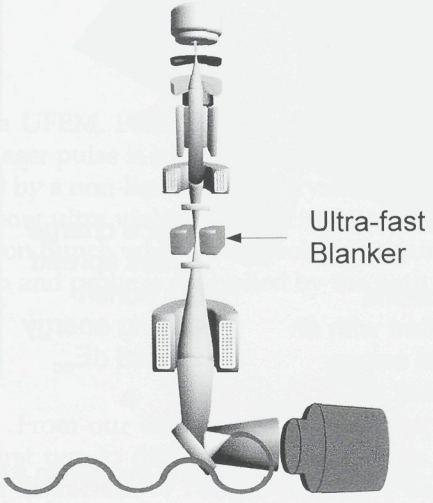

Figure 8.3: Cartoon of our blanker in an SEM.

The concept of ultra-fast blanking is not new, so why are we interested in it? The original stroboscopic ultra-fast electron microscopy with sub ps pulses was carried out by over thirty years ago by for example Hosokawa [12] and has been forgotten in the recent revival of this subject. Therefore we wish to show what can be done with a modern high brightness sources.

As well as using a high B_r source we hope to improve on previous designs

such as [12] or Sadorf [123]. These blankers were relatively large and needed the microscope column to be lengthened to accommodate a blanking module. There are no measured examples of sub ps blanking that we know about except Hosokawa in 1978 however this setup used an additional electron buncher [12]. Further the blanking process can add aberrations [124].

Our novel approach is make the blanker as small as possible so we will use MEMS (Micro Electro-Mechanical) fabrication using Silicon. The dimensions of our blanker will be $<< 1$ mm. So our blanker should fit into most columns with out any rebuilding and it will also avoid aberrations, and time dispersion. The small size will help to operate at very high frequencies, around 20 GHz which is a higher repetition rate than other blankers we know about. The blanker is designed for the case of a high brightness $> 1 \times 10^8$ A/ $\left(\mathrm{m}^2\mathrm{srV}\right)$ source, which opens new opportunities for stroboscopy. With a high B_r source we can achieve greater beam current in a pulse and it helps with the miniaturisation.

The blanker should work at the typical $30kV$ beam of an SEM. It should be used for stroboscopy, which means low charge bunches. The high frequency requires good electrical conductivity at all interfaces, in other words good matching. Further we need to make bunches below 1 ps with out adding aberrations or increasing the emittance of a low emittance source. Previous blankers, did not have this requirement, and there spatial resolution was quite poor [121].

The remainder of this paper is set out as follows, first the background - where we will discuss the various types of blankers already available, and describe how blankers work. We will derive some basic parameters for our blanker and the section will be rounded up with a comparison of our blanker to several other blankers.

Next a technical discussion which starts with a comparison of the analytical and numerical methods for simulating our blanker, which we use to show that we can expect a temporal resolution of better than 400 fs. Next we will derive and test equations to show that making a blanker smaller reduces the aberrations, and that a smaller blanker length give less dispersion.

The last section will be the conclusion and discussion.

8.2 Background

A schematic of a blanker is shown in figure 8.4. The blanker is made up of two plates, across which a lateral force F_x acts to deviate the beam, so that it hits the beam stop. The blanker is set up in conjugate mode (focus in the centre of the blanker) since we know that this mode has the least aberrations and energy spread [125] and in SEM the spot does not move whilst blanking. In an ideal situation the blanker would have a pivot point of zero size, (top line of fig 8.4) however this would imply a blanker of zero length. To blank a beam with semi-angle α the blanker must deviate it by an angle β the beam semi-angle of 2α, to achieve this F_x must act over sufficient length L. The finite length causes the beam to be blurred. In section 8.4 we will discuss this in more detail. The important parameters for a

blanker are the pulse width, the emittance increase (aberrations), and the increase in energy spread, this is summarised later in figure 8.16 for our blanker.

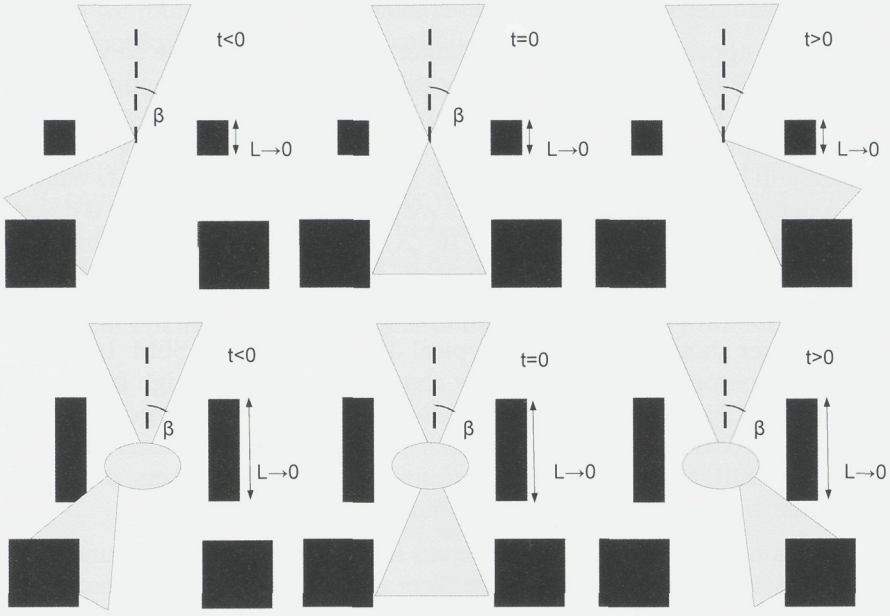

Figure 8.4: Schematic of blanker, the upper row shows a perfect zero length blanker, at three different times, the bottom row shows a blanker of length L.

There are broadly speaking two categories of blanker, oscillating and switched, and they can work with either the electric or the magnetic field. The beam of charged particles passes through the field and if it is blanked it is pushed onto a knife edge or over a slit.

Switched blankers These are suited for beams doing lithography where the beam must remain on for most of the time. In simplest form we can use a pair of parallel plates, which has a ramped voltage applied (typically 200 V) these can blank within a few 10's of nanoseconds. Some blankers in dedicated lithography machines are shaped like two horse shoes with their flat sides parallel. A voltage is applied between the two horse shoes. The beam passes first through the top corner, and is deflected but this introduces unwanted beam movement and so at the 2nd corner it sees a correcting field. All this means that the pivot point becomes conjugate. The correcting field comes from the delayed voltage signal traveling around the horse shoe. See for example [124]. It is also possible to blank with magnetic fields though these are much slower.

Oscillating blankers For stroboscopy the beam does not need to be on the entire time, but at a regular and repeated intervals to build up the image. Oscillating blankers tend to use a resonant cavity to support a radio frequency electromagnetic (EM) wave, the beam is then swept back and forth over a slit at twice the frequency of the EM wave. These use either the magnetic force or the electric force and depending of their design use different modes of the EM wave. For example [110] use the magnetic field, and [121] uses the electric field.

Finally there are traveling wave deflectors which in the simplest form send a signal down a wire which is bent such that the EM signal keeps time with the electrons in the column[126].

8.3 First Order Blanker Design

Our main design goal is to achieve sub ps electron bunches, so we now study the first order properties and determine if and how this is possible. We intend to make a sinusoidally oscillating blanker since according to table 8.1 these have the best temporal resolution. Our blanker will use two parallel plates with an electric field between them since we believe this will be the simplest to implement. One blanker plate will be grounded since this greatly easies the mechanical and electrical design, even though a blanker with a ground plane in the centre of the blanker where the beam travels would have a better electron optical performance.

We now give a first order equation for the deflection angle of an electron passing through the blanker as a function of t_0. We define t_0 as the arrival time of the electron at the centre of the blanker. We apply a sin wave to the blanker $V_{def} sin(\omega t_0)$ where V_{def} is the maximum amplitude of the voltage, ω is the angular frequency and t_0 the time the electron arrives at the centre of the deflector. If the electron arrives at the centre of the blanker with $t_0 = 0$ then it will see opposite fields; on the way in the sin wave will be negative and on the way out positive and therefore the ray will, pass through the beam stop.

From dimensional analysis we can almost guess that the deflection angle will be $\beta = \frac{V_{defL}}{V_{beam}d} sin(\omega t_0)$, where d is the distance between the two plates, V_{beam} is the voltage of the electron beam which is moving in the z direction and L is the blanker length. Using the small angle approximations β becomes

$$\beta = \frac{V_{defL}}{V_{beam}d}\omega t_0 \tag{8.1}$$

We will now try to work out what values we need to make a workable blanker. By combining equation 8.1 with an equation for the reduced brightness of a beam

$$B_r = \frac{I}{\pi^2 r_f^2 \alpha^2 V_{beam}} \tag{8.2}$$

here I is the beam current, r_f is the spot radius at a (virtual) focus and α is the half angle of the beam at such a focus. To blank the beam $\beta \geq 2\alpha$, so if we combine

Table 8.1: Comparison of Blankers, H = total height of the blanker, L = active length of Blanker, V_{beam} = energy of the electron beam, d = distance between blanking plates, V_{def} = Voltage on the blanker plates, f = frequency of blanking signal, I = beam current after chopping, T = pulse length after chopping.

Blanker	Type	H (mm)	L (mm)	V_{beam} (keV)	d (μm)	V_{def} (V)	f (GHz)	I (pA)	T (ps)	Comments
Hill 74 traveling wave deflector	traveling wave	176		12.7		0.5	9		≈ 10	
Sadorf & Kratz 1984	Impulse	60	6	3	300	1	0.25	700	10	Features two blankers to prevent voltage fall giving an unblank. Large coaxial cables will prevent very high freq signals
Hosokawa Fujioka Ura 77	Re-entrant cavity + Buncher			20			1	240	0.2	Buncher works at 4 Ghz
Hosokawa Fujioka Ura 78	Re-entrant cavity			25		2.9	1	240	10	As previous with out buncher
Gesley 93	Horse Shoe-Impulse			2.5			0.16		6000	Designed for high resolution in lithography
FEI Blanker	Two plates	10	10	30		400			5000	
Fehr et Al 2002	Coaxial Cable	13	5	10	10^4	65	18		0.1	Requires massive RF power! Pulser located below objective lens, Resolution better than 10um but temporal resolution shown to be around 10 ps
TU Delft Blanker	MEMs Parallel Plate	5	0.1	30	1	10	20	1600	0.2	Untested
Lassise et al 2012 [127]	Magnetic Cav.		17		10^4		3		0.1	A reasonably small blanker with a low power consumption.

equations (8.1) and 8.2 through this inequality and then solve for L we get 8.3

$$L > \sqrt{\frac{V_{beam}I}{B_r}}\frac{2d}{V_{def}\omega t_0 r_f \pi} \tag{8.3}$$

For a small L at high current and with fast chopping we need a high electric field (V_{def}/d) and a high B_r. Thus for our miniature blanker we need a good source and a small d. We can play further with the previous three equations to get

$$L > 2\alpha d\frac{V_{beam}I}{V_{def}}\omega t_0 \tag{8.4}$$

Which further shows that we need a very small angle for a small L. Since we need a small angle then to a good enough approximation the maximum allowable value of $r_f = d/2$ therefore

$$L > 4\epsilon\frac{V_{beam}I}{V_{def}}\omega t_0 \tag{8.5}$$

Where ϵ is the emittance of the beam. So with a high emittance source we could not use a miniature blanker.

Now we want to determine some of the parameters to make a first order design of our blanker. Working through equation 8.3, we begin with ω. It is relatively easy to create sinusoidal voltage at up to GHz frequencies, and the physics of these signals is widely understood and used for example in mobile telephones. For frequencies up to 20GHz coaxial cables work well and generators are readily available, thus we take $f = 20$ GHz. Resonant circuits can have large Q (Quality) factors see for example Hammer et al [128] who have a Q around 10^6. From table 8.1 we know that other blankers have made use of resonant free space cavities. We would like to make a small blanker, so we will make our resonance on a circuit, we hope to generate a V_{def} of 10 V meaning an amplification of around 10 times for typical rack mounted voltage source, we believe this is possible, please see appendix B for details of simulation. In radio frequency photo cathodes operating at 3 GHz fields of around 10 MV/m can be created with out significant vacuum breakdown problems, hence this field should be no problem at 20GHz, making $d = 1$ μm. Finally the SEM has the best resolution at $V_{beam} = 30$ kV.

We now have all are parameters except, we now need to find the value of L for $\beta > \alpha$. As already stated the Schottky source has a measured reduced Brightness B_r of 1×10^8 A/ $\left(\mathrm{m}^2\mathrm{srV}\right)$ [19], and again we have to define some parameters. The maximum I available in the probe of our SEM is $\approx$ 16 nA, so in a 100 fs pulse according to Poisson statistics there will be one electron once in every 101 pulses and two or more electrons once every 20, 100 pulses, thus temporal dispersion via Coulomb interactions can be ignored. The gap between our blanking plates means $r_f << d/2$, so an r_f of 100 nm seems sensible. Our beam voltage of 30 kV is already decided, and α is set from the B_r equation, now using equation 8.3 we can find the length as a function of τ, the pulse length.

We find that for a τ of 100 fs we require an $l \approx 100$ μm. A summary of our

Table 8.1: Comparison of Blankers, H = total height of the blanker, L = active length of Blanker, V_{beam} = energy of the electron beam, d = distance between blanking plates, V_{def} = Voltage on the blanker plates, f = frequency of blanking signal, I = beam current after chopping, T = pulse length after chopping.

system is shown in figure 8.5. The blanker plates indicated in black have $l = 100$ μm, $d = 1$ μm and there is a 20 GHz sin wave applied with an amplitude of 10 V. Entering the blanker in blue is the electron beam with $V_{beam} = 30$ kV, $I = 16$ nA and $r_f = 100$ nm. At the bottom in gray we see the beam stop which is set to reject all deviations $> \alpha$. Please note the fact the blanker is non-symmetric with the left plate on ground and not the centre where the beam passes.

We now have a basic set-up, for our chosen numbers the ratio of L/d is large which may cause a problem with electron beam induced contamination. However for pulse picking we probably need another slower blanker which can limit the amount of I falling on this delicate ultra-fast blanker. Since the total deflection during the sin wave is much greater than d the pulse picker will help limit secondary electrons that occur from electrons striking the blanker. However as yet we still don't know anything about the aberrations the blanker will cause, and this comes in the next sections.

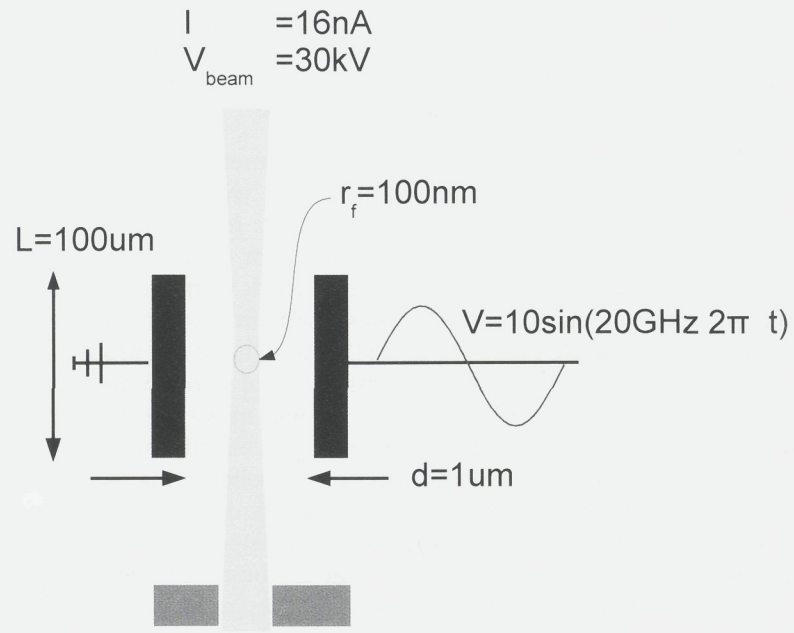

Figure 8.5: A cartoon of our proposed blanker setup.

8.4 Technical Discussion and Results

There are four things we need to know:

- The temporal resolution we can achieve.

This needs to be at least comparable to other UFM systems, as previously stated our goal is 100 fs.

- Spot displacement (can be thought of as a time independent shift, or an average shift around which the beam is blurred).

  The spot displacement should not be a problem as the SEM has deflectors which can help to realign the beam. However if the displacement is too great the beam will hit the blanker.

- The amount of lateral blurring.

  The blurring is important because it means a loss of B_r (emittance increase). Since our goal is to implement a high brightness source for UFEM a significant loss of B_r is not acceptable. Regardless of this we have decided to use a non symmetric blanker since the electronics and mechanics for this are more simple to implement. A symmetric blanker would have both plates on some voltage with ground in the centre where the electron beam should pass, our non-symmetric blanker has one plate on ground and the other provides the field.

- Energy spread. The energy spread is of importance for imaging when chromatic aberrations become important, in this situation it is the $B_r/\Delta E^2$ which determines the maximum probe current. For Ultra-fast applications the energy spread adds a temporal dispersion as $\Delta t = t\Delta E/E$ thus this needs to be kept as small as possible.

Within this next section we will show analytically that it is beneficial to have a small blanker. We will back this up with a numerical model. Now we will describe the two methods, and then compare them.

8.4.1 Analytical Model

In this model we assume that there is only a lateral (x direction) force which oscillates sinusoidally in time. The force starts and stops abruptly at the beginning of the blanker plates. We do not take into account relativity or edge effects, further the velocity of the electron in the longitudinal (z) direction does not change.

The equations of motion describing the motion of an electron in a sinusoidally oscillating electric field in the x direction, begining with the acceleration are:

$$a_x = a_0 \sin(\omega(t + t_0 - L/(2v))) \tag{8.6}$$

Where $a_0 = (-)qE_0/m$, t is time, t_0 is the time the electron passes through the centre of the blanker. The blanker has a length L , the electron has velocity v in the z direction, q is the charge on the electron and m its mass. The electric field has strength E_0 with angular frequency ω. The velocity in x is

$$u = -\frac{a_0}{\omega}\cos(\omega(t + t_0 - L/(2v))) + \frac{a_0}{\omega}\cos\left(\omega(t_0 - \frac{L}{2v})\right) + u_0 \tag{8.7}$$

where u_0 is the initial velocity. The position is given by

$$x = -\frac{a_0}{\omega^2}\sin(\omega(t+t_0-L/(2v)))+\frac{ta_0}{\omega}\cos\left(\omega(t_0-\frac{L}{2v})\right)+tu_0+a_0/\omega^2\sin\left(w(t_0-\frac{L}{2v})\right)+x_0 \tag{8.8}$$

where x_0 is the initial position. The idea is that the pulses are generated around $t_0 = 0$, so at the end of the blanker $u = u_0$, unfortunately $x \neq x_0$, and thus there is an offset. In general we assume a perfect paraxial beam focused to the centre of the blanker such that $x_0 = \frac{u_0 L}{2v}$, when we do simulations described in the next section we will also look at the affect of emittance.

Full Numerical Simulation

We now describe the numerical method of simulating the blanker. This is a two stage process where we first solve the static field, and then export it to ray tracing software where the static field is modulated. This means we are using the quasi-static approximation for the time varying electric fields.

As we have experience with a Laplace solver based on a spherical grid [65] we use this to solve the static field of our blanker. However this creates problems modeling the high aspect ratio so we must increase d to 2 μm and to compensate this we used $V_{def} = 20$ instead of $V_{def} = 10$. The result is shown in figure 8.6 where a false colour map shows the variation in potential around the blanker.

Now that we have a static field map from the Laplace solver we can export it to our ray tracer; GPT from Pulsar Physics [129]. Here a first home made custom element imports the field and a second modulates it as $E_{xyz} = E_{xyz}Ssin(\omega t)$ where S is a scaling factor. It is also worth noting that GPT takes into account relativity, and that the simulations are carried out with high accuracy such that no visible change in results could be seen when increasing the accuracy.

Comparison Methods

We now compare the analytical model to the numerical model for an on axis particle $x_0 = u_0 = 0$. We are checking equations 8.7 and 8.8 over a range of t_0 values, for figures 8.7 and 8.8 $L = 100$ μm, $f = 20$ GHz ($T = 50$ ps),and $E_0 = 10V/\mu m$, the electron has $u_0 = 0$ and starts on axis in a field free zone at $z = 390$ μm with kinetic energy of 30 keV. To improve the visualisation we plot z on the bottom axis, analytically $z = t/v - L/2$, in our simulations the middle of the blanker is at $z = 0$.

There is virtually no difference between the numerical and the analytical result. We can conclude that our initial assumptions of our analytical model were valid. The slight differences are probably explained by the change in v which was not considered, this is investigated further in section 8.4.4

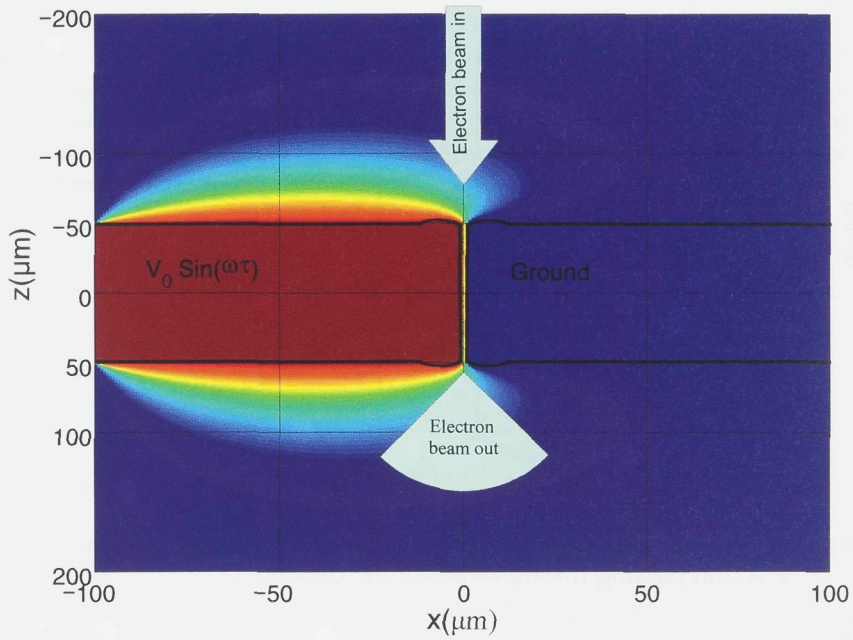

Figure 8.6: The solution of the laplace equation for the blanker, the positive plate is in red at 20V, and blue indicates ground. The blanker plates are outlined in black, the corners have been rounded to reduce their field enhancement. The gap d was increased to 2 μm since with 1 μm the simulation was not accurate, to compensate V_{def} is increased to 20V. As indicated the beam comes in at the top of the blanker and after passing through the blanker it is swept out.

8.4.2 What temporal resolution can we achieve?

Now that we are sure of our methods, we can look at the temporal resolution of the blanker. We want to know what the shortest pulse we can make is? In order to determine this we will launch three sets of electrons. Each set has a different t_0 but all the electrons within one set start at the same time and therefore have the same t_0. The sets have $t_0 = -\tau/2, 0$ or $\tau/2$, if the sets are separate in space at the end of the blanker then we can claim a resolution of τ. We know there will be some dispersion but for the moment we will not worry about this. To begin with we will use a beam with a perfect paraxial focus with zero emittance ($B_r = \infty$), then we will add emittance, and compare the differences. We will define our emittance, at the focus as a hard edged square with centre at $(0, 0)$, and top left corner at $(-r_f, \alpha)$. The corners of the square are always included and the rest of the square is filled with a random uniform distribution. This may seem overly simplistic, yet the real distribution is unknown, and we suspect that a Gaussian is a bad description. Our hard edged distribution makes a visualisation of the temporal

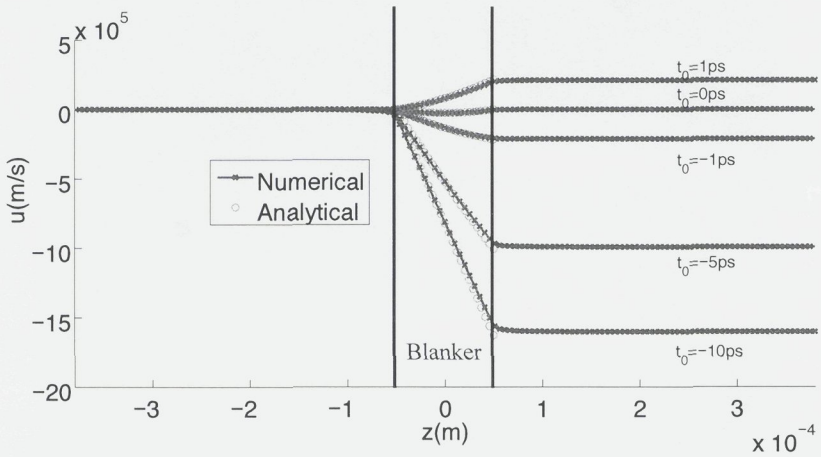

Figure 8.7: Numerical and analytical calculations showing the x velocity of an electron passing through the blanker depending on arrival time $t_0 = -10$ ps, -5 ps, -1 ps, 0 ps, 1 ps.

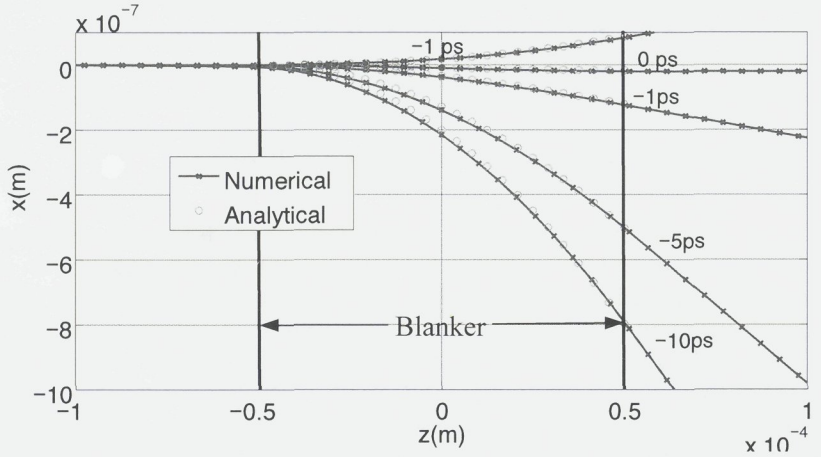

Figure 8.8: Two different calculations showing the route taken by an electron going through the blanker, depending on the arrival time $t_0 = -10$ ps, -5 ps, -1 ps, 0 ps, 1 ps.

resolution straightforward.

Let's first examine the zero emittance case shown in figure 8.9. The three sets of electrons which arrive at the centre at $t_0 = -200$ fs, $t_0 = 0$ fs and $t_0 = 200$ fs are clearly visible at the end of the blanker ($z = 50$ μm). In fact the resolution is even better, at the cross over the radius of the focused spot $r_f \approx 0$ and an aperture might be inserted and infinitely short pulses generated. This is of course supported by equation 8.4 where $L = 0$ if $\epsilon = 0$.

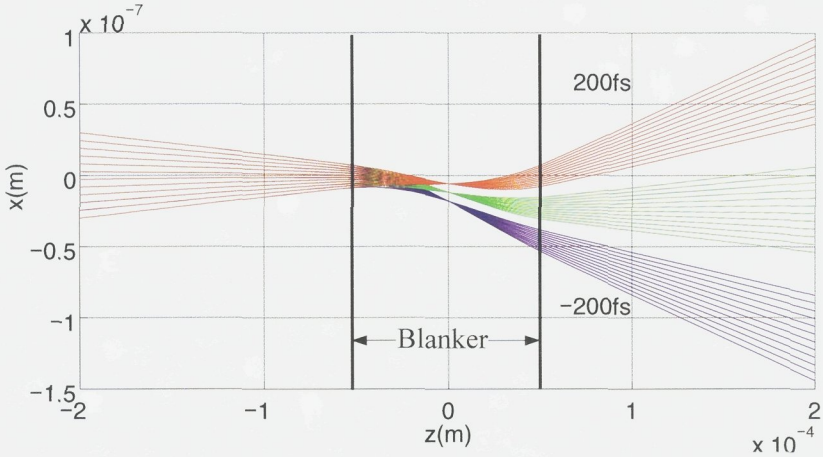

Figure 8.9: Three sets of electrons with infinite B_r The red rays all pass the centre of the blanker at $t_0 = 200$ fs, the green at $t_0 = 0$ and the blue at $t_0 = -200$ fs. The starting angle is $\alpha = 0.15$ mrad, $E = 10$ V/μ, $f = 20$ GHz and $L = 100$ μm, $V_{def} = 20$V and $d = 2$ μm

When we include the emittance in figure 8.10 we can clearly still resolve the three different t_0's and therefore conclude that our system can create a pulse of $\tau = 400$ fs. In order to achieve $\tau = 400$ fs we increased r_f to 150 nm instead of our original 100 nm, further optimisation of r_f may produce a smaller τ.

Our $\tau = 400$ fs is good enough for most UFEM experiments see chapter 7, an improved τ can come increasing E, l or ω, however in doing so we introduce dispersion and aberration, this is shown in the next sections. An other alternative is to reduce I, for example with $I = 4$ nA then $\alpha = 0.75$ mrad and we should be able to achieve 200 fs pulses.

8.4.3 x blur

We now know that our blanker can create short enough pulses for UFEM, we need to know about the aberrations, or in other words the decrease in B_r of the system. If we lose B_r our signal to noise decreases and imaging/diffraction pattern forming will take longer, in some cases it may simply become impossible. So we want to know if we create any blur whilst blanking. Since this will happen only in the x direction we will describe this as x blur. Note it is not our goal to make a complete

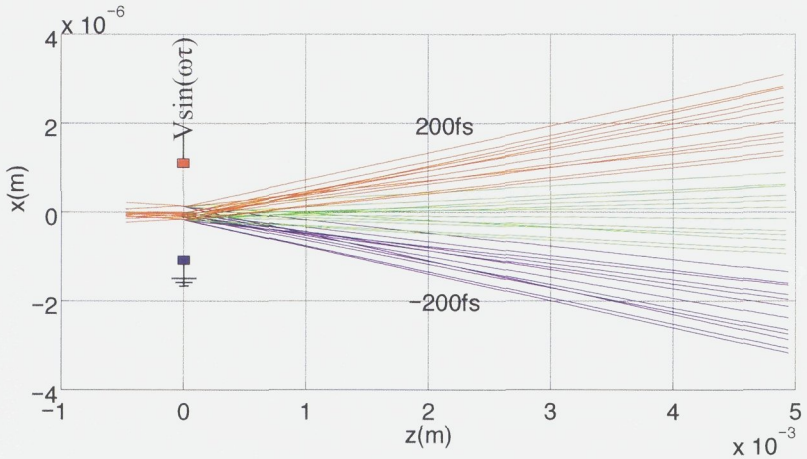

Figure 8.10: $B_r = 10^8$ A/ $\left(\mathrm{m}^2\mathrm{srV}\right)$, $I = 16$ nA, $E = 10$ MV/m, $r_f = 150$ nm, $f = 20$ GHz, $L = 100$ µm. The rays in red all passed the centre of the blanker at $t_0 = 200$ fs, the green rays at $t_0 = 0$ fs and the red rays at $t_0 = -200$ fs

theoretical study of the aberrations of blankers, just to show that a smaller blanker reduces aberrations.

As per figure 8.4 we want the electron beam to come from a perfect point, but this does not happen because of the finite L. We want an analytical formula for the blur, which we expect to grow with L, we also check this numerically. First we will look at the results for a perfect paraxial focus with no emittance, then numerically we will see the affects of emittance.

Our normal assumptions remain, no change in v so $t = z/v$, and a non-relativistic beam. We want to find the circle of least confusion (in this 1D case it actually becomes a line), or the apparent virtual focus. To do this we launch rays at $t_0 = 0, dt, -dt$, and we will also launch rays at half a cycle later i.e $t_0 + 1/f$. We then find the final angle and corresponding position, which we trace back, to find where the three lines cross. This is shown in figure 8.11, for on axis rays.

From figure 8.11, it appears that there is a blur of around 50 nm, however we expect that (as stated earlier) we will probably use another blanker as a pulse picker and therefore the 2nd pulse of the sin wave can be ignored.

We will now find an analytical solution for the blurring in x. First we approximate the ray path described by equations 8.7 and 8.8 with the small angle approximation that is equivalent to a third order Taylor expansion. Later we will expand this with a higher order Taylor expansion. With the third order Taylor expansion the equations of motion become

$$\beta = \frac{a_0\omega}{v2}(t^2 - \frac{tL}{v} + 2tt_0) + \alpha_0; \tag{8.9}$$

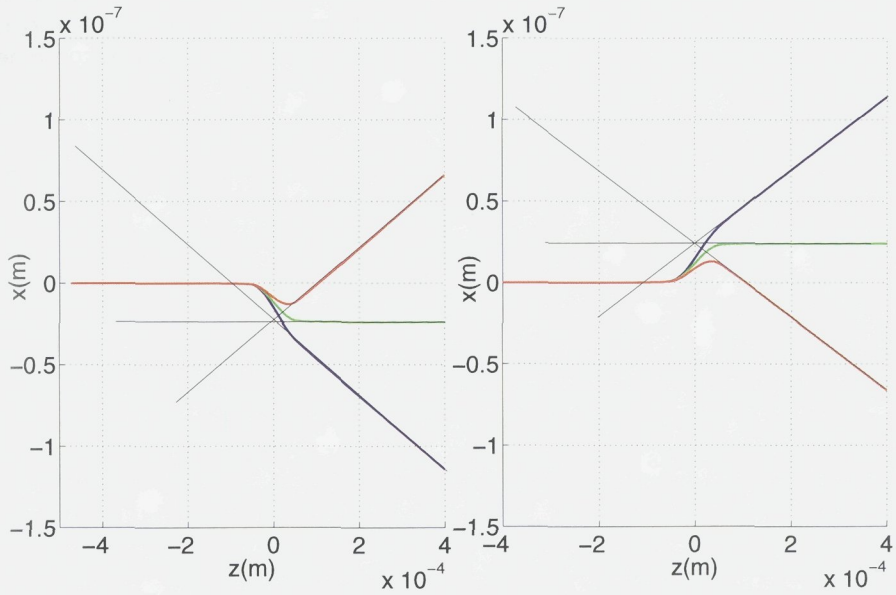

Figure 8.11: Numerically calculated ray trace of electrons passing through the blanker, on the left graph red at $t_0 = 100$ fs green $t_0 = 0$ fs and blue at $t_0 = -100$ fs, the right graph the situation at half a wavelength phase difference $t_0 = t_0 + 25$ ps. The location of the virtual focus is shown in black.

$$x = \frac{a_0\omega}{2}\left(\frac{t^3}{3} - t^2\frac{L}{2v} + t_0t^2\right) + \alpha_0 t + x_0; \tag{8.10}$$

From these we find that the virtual focus is always at the centre of the blanker and its x location $x_{SD} = \frac{-a_0\omega L^3}{12v^3}$, in this approximation there is no blurring, since there are no t_0, or α terms. Actually x_{SD} is the spot displacement discussed in point three at the start of this section.

So what about the higher order terms which presumably cause a blur? We take a 6th order expansion found using the symbolic math function in Matlab to avoid error, with commands taylor(cos(arg), 6) and taylor(sin(arg), 6) to replace cos and sin in equations 8.7 and 8.8. When we then trace back to $z = L/2$, and ignore any constant terms which do not contain α or t_0 we get equation 8.11.

$$x_b = \frac{L^3 a_0\omega^3}{24v^3}t_0^2 \tag{8.11}$$

In equation 8.11 we can see that the diameter of the spot will vary with the frequency and blanker length to the third power, and the electric field (in a_0 lin-

early). We will now take equation 8.11 further and generalise it by relating it to ϵ. First to avoid aberrations we want $r_f >> x_b$, and since $\epsilon = r_f\alpha$ then $\epsilon >> x_b\alpha$. We know already that to blank the beam $\beta \geq 2\alpha$ so we can now we can combine equations 8.11 and 8.1 to get,

$$\epsilon >> \frac{L^4 a_0 \omega^4}{48v^3} t_0^3 \frac{V_{def}}{dV_{beam}} \tag{8.12}$$

Finally recalling that $a_0 = -qV_{def}/(dm_e)$ and $V_{beam} = \frac{1}{2q} m_e v^2$ we get

$$\epsilon >> \frac{-q^2 L^4 \omega^4 V_{def}^2 t_0^3}{m_e^2 24 v^5 d^2} \tag{8.13}$$

Equation 8.13 further shows that to use a small ϵ beam the blanker must have small aberrations, and these depend on L^4. For our blanker with parameters we previously described this would mean a maximum $L = 358$ μm if we assume $>>$ means ten times greater.

We have plotted the numerical results and equation 8.11 in figure 8.12, note that we have reduced the field to only 2 MV/m in order to avoid the electrons hitting the end of the blanker for the longer blankers. All other parameters are the same as for figure 8.11 unless otherwise stated.

The result is quite remarkable, and clearly demonstrates the quality of the analytical approach. The numerical line must depart from our approximation because of fringe fields and the change in v neglected in our previous working.

Let's also see how the picture changes when we actually simulate the emittance, see figure 8.13. The effect is clearly much more pronounced and shows the merit of having a small blanker. Figure 8.13 shows that x_{blur} affects our $L = 100$ μm blanker very little, but if we let it become too long (> 0.5 mm) then x_{blur} would dominate the spot size.

8.4.4 Energy Spread

In the previous section we looked at how there is a blurring effect which scales with L^3, this decreases the brightness, so we do not want to increase the length too much. However what about the energy spread? we will now investigate this. It did not seem trivial to produce an analytical model which would accurately track the electron, so we began to investigate it numerically. We wanted to know how L effects the dispersion so we calculated the field for $L = 30$ μm to $L = 450$ μm increasing L by 70 μm for each measurement. This range was chosen because with $f = 20$ GHz the transit time through the blanker is much less than the blankers period (50 ps), and therefore low order approximations still hold. The results of this are shown in figure 8.14, we have had to reduce the electric field to only 2 MV/m to stop the electrons hitting the edge of the longer blankers. The first thing we see from 8.14 is that there is significant change in the final velocity of the electrons, luckily this is unimportant.(A Δv of 3×10^3 m/s $= 1.7$ eV) The important factor is the difference in v between the two electrons arriving at $-\tau/2$

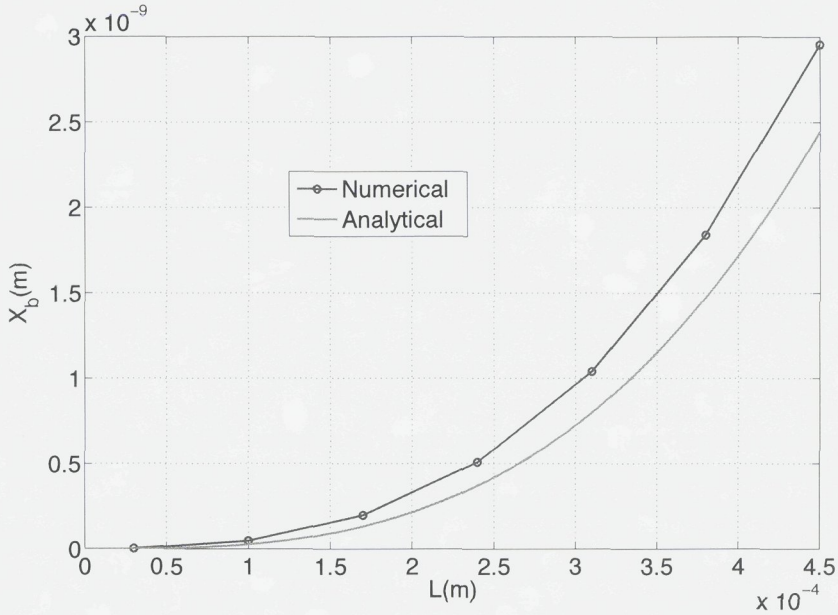

Figure 8.12: Total x blur for rays with a perfect paraxial focus ($B_r = \infty$) in as a function of L, $\tau/2 = -1$ ps and $E_0 = 2$ MV/m. Starting point of electrons is 390 μm + L

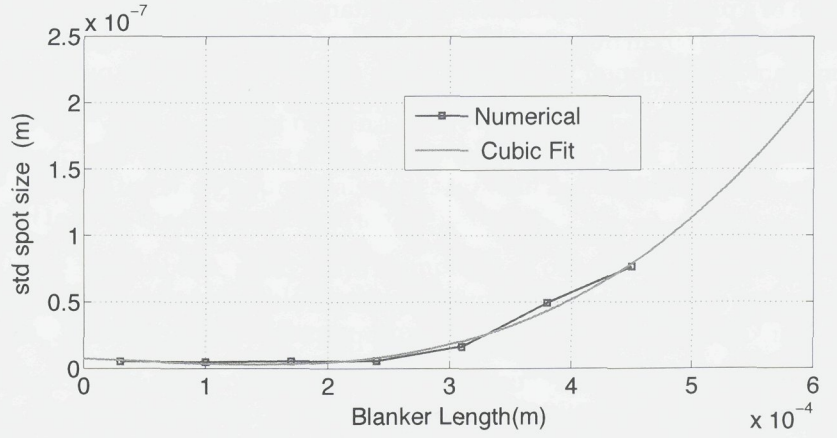

Figure 8.13: x blur verses L, because we include emittance our initial r_f is already blurred. Other parameters are $B_r = 1 \times 10^8$, $I = 16$ nA, $E = 2$ MV/m, $f = 20$ GHz

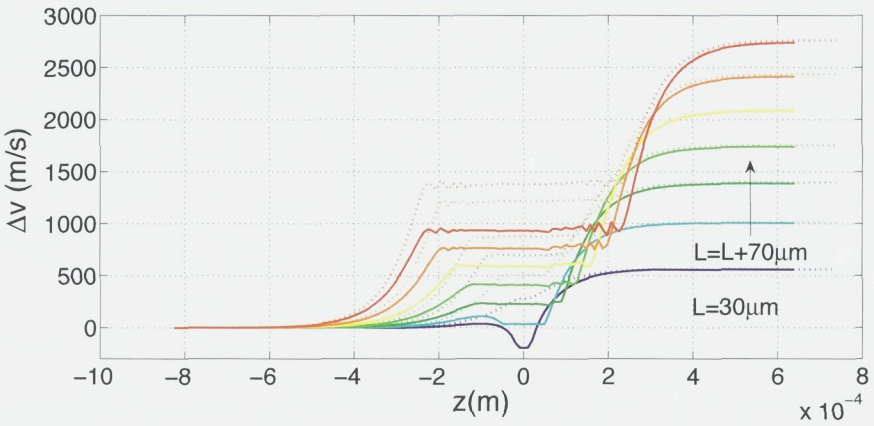

Figure 8.14: Numerical calculation of the change in v as a function of z. Different blanker lengths are shown with different colours but are also labeled on the graph, L runs from 30 μm, to 450 μm with 70 μm spacing. The dotted line is for $t_0 = -\tau/2$, and the solid line for $t_0 = \tau/2$. The frequency is $f = 20$ GHz, as usual however the E field is only 2 MV/m to stop the electrons hitting the blanker walls for the longer blankers

and $\tau/2$ (dotted line and solid line), this velocity difference D is relatively small and it is this which will cause the electron bunch to spread out as it travels.

In figure 8.15. We calculate the velocity difference between electrons at the start and finish of a pulse we have included the emittance immediately. The dispersion after traveling the 30 cm from the blanker to the sample would mean that with the 450 μm blanker a temporal increase of 300 fs almost doubling the pulse length, where as our blanker with $L = 100$ μm only increases the pulse length by around 30 fs.

8.4.5 Summary of Results

We have seen that it is possible to create sub picosecond pulse using a small 100 μm blanker, with only 10 V over a 1 μm gap at a frequency of 20 GHz.

Further we presented analytical and numerical evidence to support our idea that reducing the blanking length reduces aberrations and dispersion. The aberrations scale with L^3, and the dispersion also goes up with L

Finally we can look at a mock up system 8.16 which includes an aperture to blank the beam, this system creates bunches of total length 400 fs, and with a total energy spread of approximately 0.3 eV, and has virtually no effect on the brightness. The brightness drops as we go through the blanker since this includes

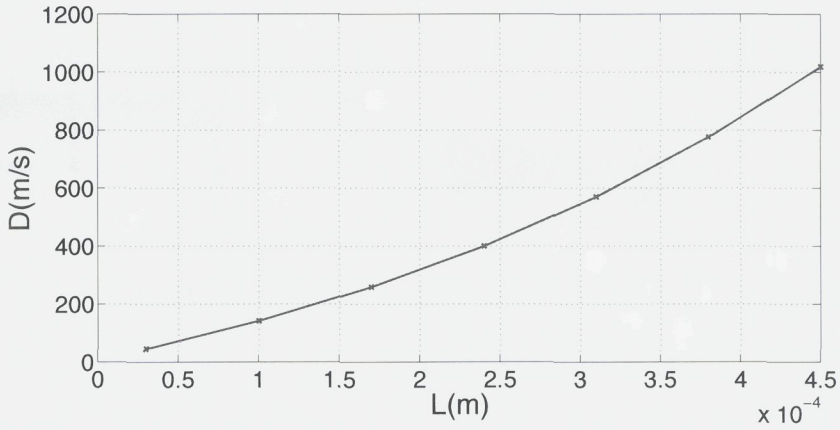

Figure 8.15: Dispersion velocity as function of blanker length calculated numerically, for a beam with $B_r = 10^8$ A/ $(\mathrm{m}^2\mathrm{srV})$, focused to a 100 nm spot. Other parameters are, $I = 16$ nA, $f = 20$ GHz, $/\tau/2 = 1$ ps and $E = 2$ MV/m

electrons that don't pass through the aperture, they are blurred because of their large t_0 (see equation 8.11). The aperture lets pass only those electrons with a small enough t_0 so the blurred electrons don't pass, however it does not change the current therefore at the aperture the B_r returns back to nearly it's original value.

8.5 Conclusions

From our results we can conclude that a micro blanker can deliver 400 fs pulses with a high B_r, at a current of 16 nA, however it will give a small increase in the energy spread. The blurring effect of a simple oscillating conjugate blanker scales with L^3, and the energy spread also goes up with L, thus this is another excellent reason to keep the blanker length small.

There are doubtless many ways to improve on our simple blanker, for example a good design should be able to reduce the fringe fields which we suspect would, decrease the blurring, and energy spreading.

There could also be some merit to optimising the frequency and the length, since both length and frequency give there own challenges, in terms of alignment, and electronics respectively.

Finally we repeat that with a simple blanker consisting of two plates of length 100 μm, at a frequency of 20 GHz with plate gap 2 μm and a voltage of 20 V pulses of total width 400 fs can be made, with out significantly disturbing a $B_r = 10^8$ A/ $(\mathrm{m}^2\mathrm{srV})$ beam, with $16nA$ of current. This represents an improvement of 2

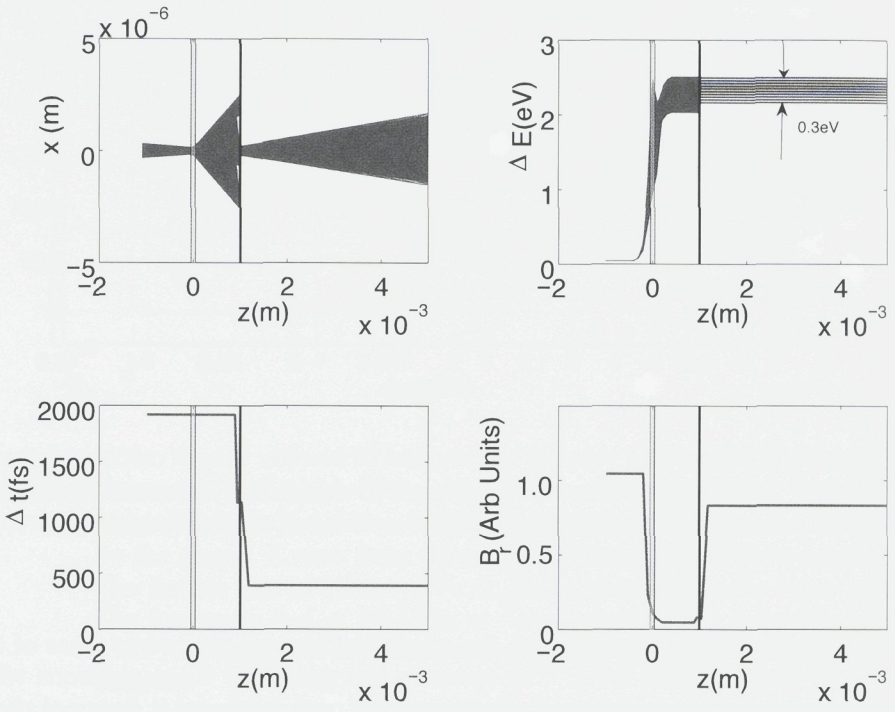

Figure 8.16: Blanking system. The blanker plates are indicated by grey shading around $z = 0$ and the aperture at $z = 1$ mm, with radius 210 nm is marked by a thick black line. Top left shows a ray trace of electrons passing through the blanker, depending on their arrival time the electrons are either stopped by the aperture, or transmitted. Top right, shows the increase in energy spread after passing through the blanker with a mono-energetic beam. Bottom left, shows the pulse length before (2 ps $\approx$ a continuous beam) and after the blanker where a pulse of total length 400 fs is created. Bottom right shows the root mean square (rms) B_r of the beam before and after the blanker.

orders of magnitude over conventional flat cathodes used for UFEM see chapter 7.

9 CHAPTER

Coulomb Interactions in Pulsed Photo Field Emitters

Electrons are like drinks when you've had one another often seems to follow

Ken Book

Photofield emitters show great potential for many single electron pulsed applications however for the brightest pulses we find that Poisson statistics and stochastic Coulomb interactions limit the brightness and energy spread even with an average of a single electron per pulse. For the systems we study we find that the energy spread is probably the limiting factor for most applications.

9.1 Introduction

In this study we will use the term photofield emitter to mean a sharp tip in a strong electric field (> 0.1 V/nm), with a laser incident. So we consider both field emission of photo excited electrons, and directly photo emitted electrons entering into a strong field.

People have suggested using photofield emitters in ultra-fast electron microscopy for many years, see for example King [15], or Hommelhoff [114], however only recently Mohammed [88] has managed to fully implement one. There is further interest in using photofield emitters in lithography, because of the fast modulation available through optical switching. At the Paul Scherer Institute there has been extensive research by for example Ganter, [130] who looked at arrays of photofield emitters for use in their new free electron laser. Photofield emitters could

also be useful as photodetectors and perhaps they could be useful in electron interferometers or other quantum experiments. Given the wide range of uses and recent interest from the groups at Caltech [88] and the Paul Scherer Institute [130], it seems that we should investigate photofield emitters in more details.

There are many areas we might like to investigate, for example we know that the stability and lifetime of field emitters is a problem for microscopy . Stability data for photofield emitters does not appear to exist, but we can assume that it is similar to a field emitter, since the processes are comparable. For photo-field emitters large laser powers can also give problems, and quickly damage sharp tips [112]. Further issues exist with thermal emission from laser heating and field emission from an unwanted field enhancement, perhaps caused by a change in shape of the tip.

Mostly these problems can only be examined with experiments, and any results given on stability or lifetime will be heavily dependent on the making of the tip, the vacuum environment and quality of the experiment.

We want to look at a specific area, the use of single electron packages for stroboscopy, and other low charge ultra-fast pulse applications like electron interferometry where beam quality, coherence, emittance and brightness are important.

We believe that Coulomb interactions, which occur after the electrons are emitted into a beam reduce its quality, and therefore why not use a single electron per pulse? For a bright photofield emitter we want a small emission area, ultra-short pulse durations and lots of charge, unfortunately in this case we expect that Poisson statistics will start to limit B_r when the average number of electrons per pulse $\langle N_e \rangle$ is less than one.

We can calculate the effect of the Coulomb interactions for a pulse of 2 electrons emitted on axis with a 10 fs spacing. Let's assume that near the surface of the tip there is a uniform field of 1 V/nm, (this is typical see for example chapter 2), the first electron emitted with no initial velocity travels 8.8 nm in the 10 fs before the next electron is emitted, the potential energy for this situation is 0.16 eV about equal to the intrinsic energy spread caused by the Fermi-Dirac distribution in the metal [46]. In this case Coulomb interactions will cause the final energy spread to be twice the intrinsic value. Things get worse when we consider that in a 10 fs pulse the electrons can be emitted at any time during the 10 fs.

Coulomb effects may already limit the emission well before other factors such as thermal effects or laser damage (ablation) start to cause problems. For an average of 1 electron in our 10 fs pulse as described we would expect a laser intensity $> 10^{10}$ GW/m^2 (assuming a quantum efficiency of $< 0.1\%$). According to Hommelhoff [114] these kind of intensities are close to the damage threshold for W tips

In [131] they experimentally investigated the Coulomb interactions in continuous photofield emitters, finding that they add a long tail to the total energy distribution, this work is probably not directly applicable to pulsed emission, or the high current densities that we will be discussing. There is also work from Qiang

[132] who looked at 30 ps pulses from nano-tips, however according to our literature study in chapter 7 for stroboscopy the maximum pulse lengths are around 1 ps . Siwick et al [133] investigated Coulomb interactions in electron pulses for ultra-fast electron diffraction, however these are for drift space and a relatively large numbers of electrons distributed over large areas. This means their results are also unlikely to be applicable.

Finally there is our own work, [63], [65] and [41] to name a few, which investigated electron-electron interactions in Schottky, cold-field and DC photo field emitters.

None of the articles we listed has investigated the ultra-short low charge pulses, suitable for stroboscopy. Therefore it is high time we understood the consequences Coulomb interactions and Poisson statistics have on photo-field emitted electron pulses.

We plan to first examine a simple system, this is a section of drift space with electrons moving at a constant velocity. We then move on to a more realistic photofield emitter. We will examine the emittance increase caused by photo emission and the increase in energy spread due to stochastic interactions, and also space charge. Hence we will show that even compensating for space charge with (for example) an RF compression cell there is still an stochastic element which can not be removed.

9.2 Coulomb Interactions in Drift Space

The arrangement for this system is shown in figure 9.1. The number of electrons in a pulse is decided by Poisson statistics from the built in Matlab distribution. Statistics are built up over many pulses with an average of 5000 electrons per data point. The initial angle=0 meaning also the emittance =0, also the initial energy spread is 0. All electrons start at $z = 0$ within a radius of 10 nm. The electrons starting positions are chosen from a Random Uniform Distribution - RUD - created by Matlab, their start times are also chosen from a RUD. The electrons initial speed is $\sqrt{2Ue/m}$ in the z direction, where $U = 1$ kV, e is the electron charge and m is the pass of an electron. Each electron travels 1 mm (a typical gun length) and at this point its data is recorded. Electrons still have influence after 1 mm, so electrons at the rear of the pulse always see the effect of those at the front. The electron-electron interactions are found using an implementation of the Barnes-Hut model in GPT_3 [129].

9.2.1 Results of Model System

We have chosen to examine a beam with a 10 nm radius since this is a typical size for a photofield emitter [114]. Larger beams have fewer interactions per electron and take considerably more time to investigate. We note that with field emitters the beam expands as it travels through the gun, however for simplicity we choose

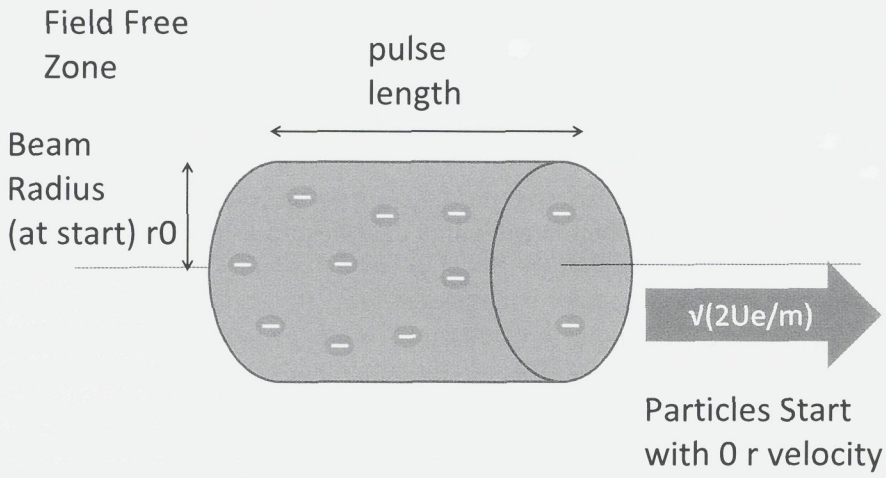

Figure 9.1: Model system used to gain insight into Coulomb interactions in pulses

a columnated beam. Further the affects of the Poisson statistics well be less noticeable. We will examine a range of pulse lengths from the ultra-short 1 fs up to 10 ps because these are used or being considered for stroboscopy. First we will examine the emittance increase in our model system.

The standard way of calculating emittance is to use the rms values, as we will show later this can give an over estimate for tall thin distributions. We prefer the $\epsilon_{50\%}$, the emittance in x or y containing 50% of the electrons. To simplify the implementation of the algorithm we first find the (virtual) focus by tracing back from $z = 1$ mm we find the smallest radius from the axis containing again 50% of the current. At the virtual focus we plot either x or y trace space and $\epsilon_{50\%}$ is the area of an ellipse containing 50% of the charge. In figure 9.2 we plotted the y trace space for the 10 ps pulse with $N = 10^4$ from 9.3. The red ellipse in the middle contains 50% of the electrons, and its area is $\epsilon_{y50\%}$.

From figure 9.3 we can see that for each pulse length we have always a sharp increase in ϵ as $\langle N_e \rangle$ approaches one. The short pulses are the worst effected since the current density is so great, the 1 fs pulse has an initial current density of $5 \times 10^{11}\mathrm{A/m^2}$ for $\langle N_e \rangle = 1$. The emittance values on the bottom left of the graph for the pulsed beams are mainly from errors in the numerical process, since the chance of 2 electrons in the pulse is virtually zero, there are no Coulomb interactions.

We also looked at how a DC beam compares for the same current. The DC

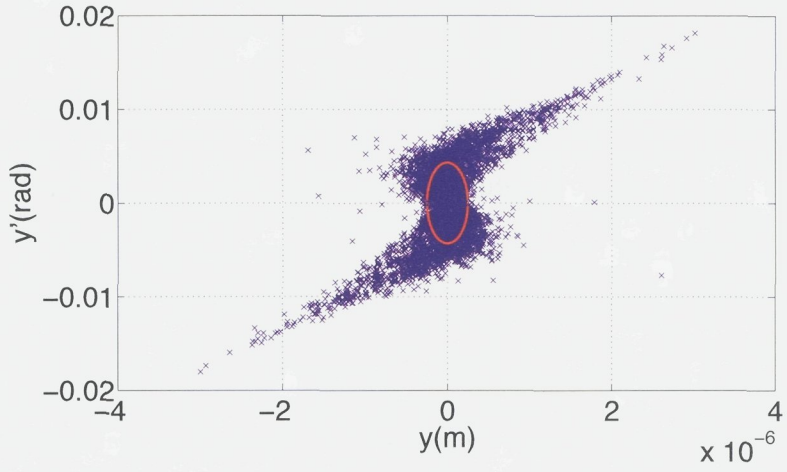

Figure 9.2: Trace space of a 10 ps pulse with $N = 10^3$. The red ellipse in the centre is the smallest ellipse containing 50% of the charge.

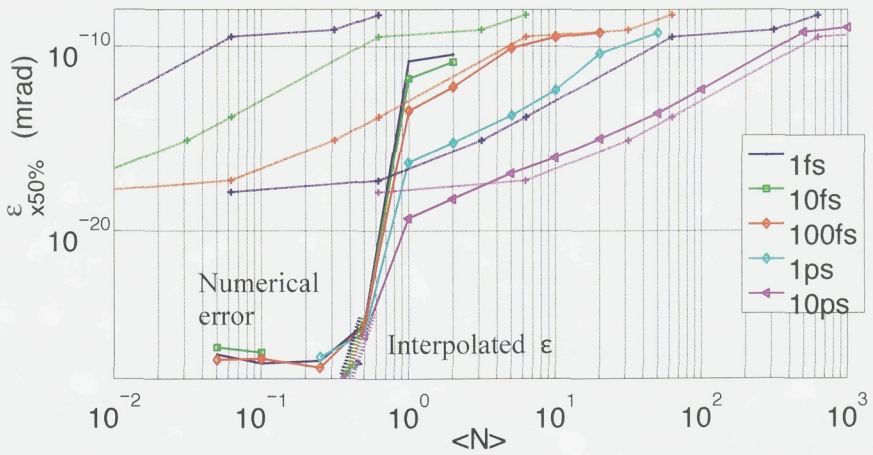

Figure 9.3: Growth in emittance due to Coulomb interactions for pulsed beams shown with solid lines and a Direct Current (DC) beam drawn with dotted lines with the same current as its pulsed partner.

beam was simulated by randomly filling a cylinder with 5000 electrons, and allowing that cylinder to travel 1 mm in drift space.

Trend on the Direct Currents and pulses

The 1 ps and 10 ps quickly start to look like the DC beam, however they have slightly more emittance. The extra emittance may come because the pulsed beam can expand giving it a large longitudinal energy spread which will cause a chromatic focusing error. The 100 fs and shorter pulses have lower emittance than their DC equivalent, this may have a similar explanation. The pulse can first have a fast none/less stochastic expansion and later Coulomb interactions are reduced due to their increased distance from one another. As the current in the beam increases we see a clear power law for the middle sections. The emittance grows with a near cubic law as expected from Jansen [52] for a pencil beam. This is in contrast to [133] who found a 0.5 power law which would according to Jansen be expected for a Gaussian beam and can be explained by the larger beam width, and much longer flight time.

The initial section of the DC beams is most likely erroneous because of the extremely small deviations involved. The last section has close to a $2/3^{rd}$ power law which is what Jansen [52] predicts for the extended beam regime in particular the Holtzmarkian beam. A pencil beam is defined $r_{es} >> z_{es}$ -radial electron spacing >> longitudinal electron spacing- this ceases to hold when $r_{es} = 10z_{es}$. For a 1 ps pulse when there are around 100 electrons $r_{es} = 10z_{es}$, which is when the power law changes.

Figure 9.2 shows an 'S' shaped distribution of trace space, that is characteristic of spherical aberration, this can only occur from non-linear space charge forces. Therefore the complete situation is a combination of stochastic and space charge forces.

What we can take away from figure 9.2 is the dramatic increase in emittance when we reach one electron per pulse, we might argue that other things will limit us long before stochastic Coulomb interactions, however we have only looked at 1 mm of drift space, and haven't considered what happens at the gun where the electrons spend more time due to their lower average velocity.

9.2.2 Brightness of the Model Beams

We will also look at the reduction in brightness due to electron-electron interactions. The brightness is important as it tells us the amount of charge we can have in a focused spot for a given time. Here we measure the reduced brightness defined as $B_r = \frac{<N>e}{\tau V \epsilon_{x50} \epsilon_{y50}}$ where $< N >$ is the mean number of electrons in the pulse, e is the electronic charge, τ is the total time of the electron pulse and V is the beam potential. We don't use the differential $B_r = \delta I/(V \delta\Omega \delta A)$ where Ω is the beam solid angle, A is the beam area and δI is the amount of current in $\delta\Omega\delta A$, because this will give different results depending on the size of δ used. In other

words, to make a meaningful measurement the infinitely small δA must become a finite sized ΔA and the same holds for I and Ω. Then B_r depends on the size of ΔA and $\Delta\Omega$. If we choose $\epsilon_{y/x50}$ then the product of A and Ω is optimised for half the current, which is probably a more general characterisation.

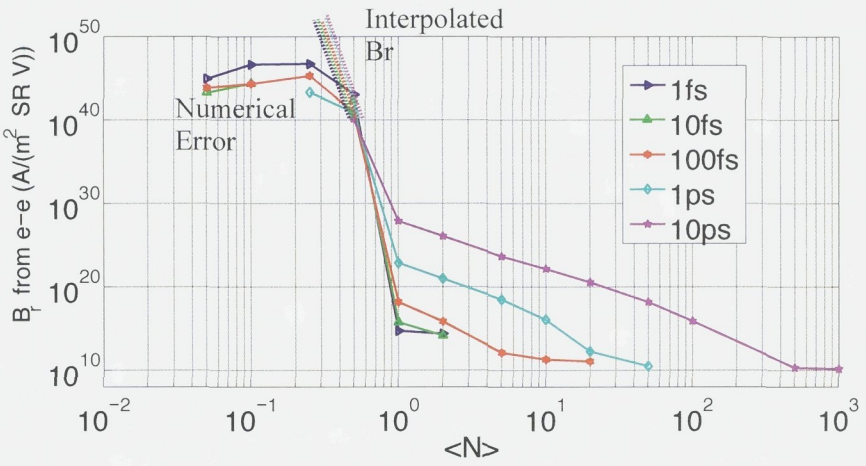

Figure 9.4: Brightness reduction of model system due to Coulomb interactions

We now look at figure 9.4, which shows the change in B_r as a function of $< N >$ for our model system. The first thing to note is that the extreme values of B_r at over 10^{40} $\mathrm{A}/\left(\mathrm{m}^2\mathrm{srV}\right)$ are a computational error and should be read as infinite. When the chance of two electrons in a pulse is essentially zero then our infinitely bright starting conditions must remain. When Coulomb interactions do not occur the beam with the highest current is the brightest, however according to 9.4 as soon as we get above a single electron per pulse the brightest beam is actually the longest. This is important since it means that it is always best to maximise τ.

9.2.3 Energy Spread of model beams

The energy spread of an electron pulse will cause it to disperse as per $\Delta_t = \Delta V/(2V)t$. For ultra-short pulses this can be big problem, in just $t = 1$ ns a $\Delta V = 1eV$, and $V = 1$ kV can have grown by a picosecond. Further in imaging applications the energy spread causes chromatic aberrations which blur the image.

To measure the energy spread we use a full width containing 50% of the electrons. The reason for this is clear when we look at figure 9.5, since the distribution is so tall and narrow the standard deviation is a huge over estimate of the distribution width. We have made no effort to seperate the stochastic effects from the general space charge effects.

This graph is less clear than the graphs for emittance and B_r this is because it is even more difficult to measure the energy spread due to the large spread in

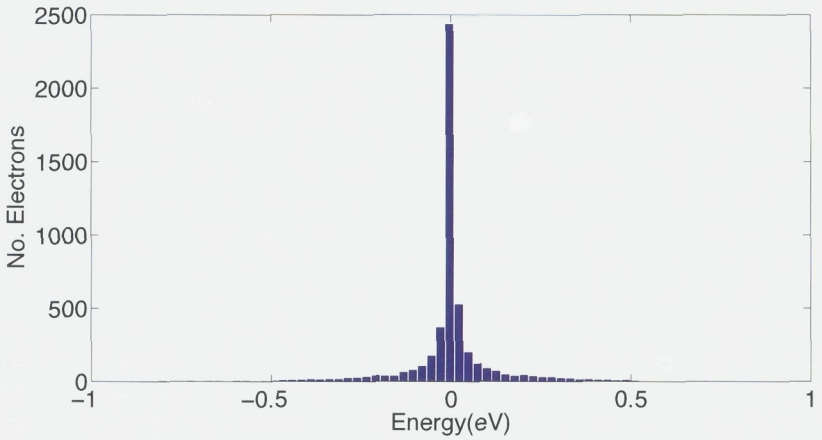

Figure 9.5: Energy Spread of Beam where RMS measurement would give misleading results about the beam size.

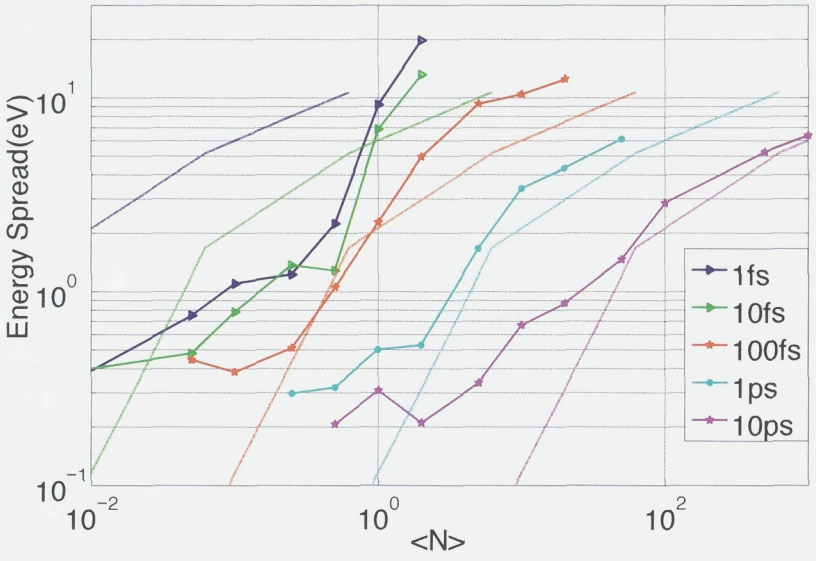

Figure 9.6: Energy spread of our model system, and indicated with dashed lines is the equivalent DC

energy and its very narrow distribution. Still clearly visible however is the jump as we move to a single electron in the pulse. This time the power laws is less clear compared with the emittance growth.

Similar to the emittance the longer pulses have a lower ΔE than their DC equivalent, and the shorter pulses eventually have a higher ΔE once space charge effects kick in. The longer pulses do not feel the space charge effects so quickly, and since there are less electrons they can have slightly fewer collisions than the DC.

One thing we can learn is that although the B_r of the short pulses is acceptable when we examine the ΔE this is too large for imaging and may also add too much dispersion (see equation 7.17 in chapter 7 and surrounding text). Therefore we should probably work at less than 1 electron per pulse for the highest resolution work.

From this model system we have learnt that the emittance of short pulses is sensitive to Poisson statistics and Coulomb interactions. For the ultra-short pulses, < 100 fs a single electron on average per pulse is enough to be noticeable. For longer pulses the increase in emittance is too small to be significant. For these longer pulses the emittance grows at a roughly cubic rate as predicted by Jansen [52]. The brightness of the ultra-short pulses is actually the worst despite having the highest current. This means that for best performance the pulse length should match the required temporal resolution. Finally we see that ΔE is the worst affected aspect and can reach up to 10 eV which is too large for high resolution imaging.

9.3 Photofield

Now that we have studied our model system it is time to move onto the more complicated photofield emitter. We expect to see similar results with the energy spread being the biggest problem. We begin by describing the manner in which we simulated the photofield emitter.Then we examine the emittance and brightness of the photofield emitter as a function of $< Ne >$, and find that there is a maximum B_r. Finally we look at the energy spread, and demonstrate that even with corrective time dependent electron optics a stochastic energy spread would still remain.

Method

As we did in [65] we will simulate our sharp tip using a Poisson solver based on a spherical grid. The system is described in [65], in figure 9.7 we see a $r_{tip} = 50$ nm tip with an extractor voltage of 650 V. The field at the tip surface is 2.97 V/nm

The emission area on the tip is limited to a radius of $r_{tip}a/4$, this maybe somewhat arbitrary but it selects most of the front of the tip which is where ideally the most current should come from. We actually start the electrons with a uniform

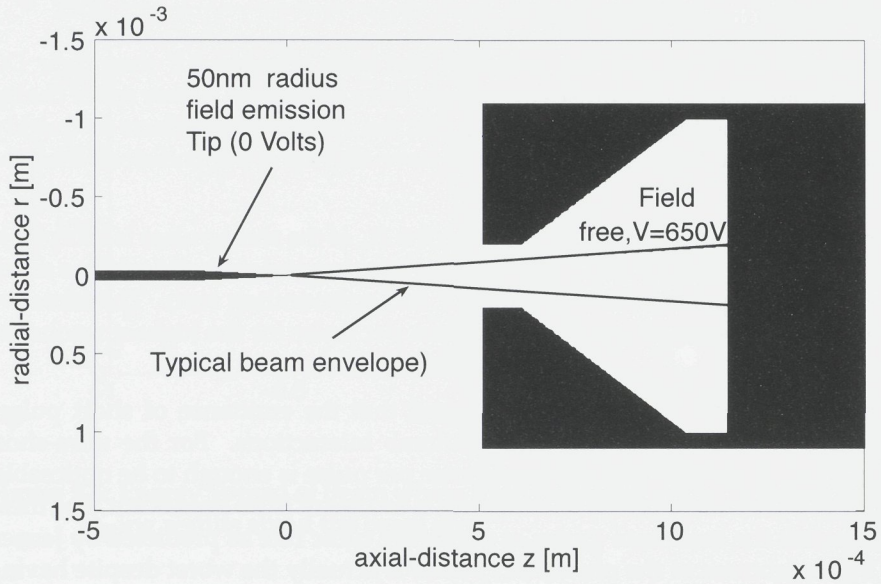

Figure 9.7: Photofield gun

spherical distribution at 10 nm from the front of the tip, as if they had come from the centre of the spherical part of the tip. The speed of the electrons is $\sqrt{2Ue/m}$ where U is the potential at their launch point. Since the electrons appear to come from a point they have zero emittance, and we assign them zero energy spread.

Emittance growth as function of N

9.3.1 Emittance growth of photofield gun

In figure 9.8 we see the emittance growth for a 50 nm tip with a 10 fs electron pulse. The emittance does not drop below 10^{-11} mrad since we are limited by aberrations and numerical errors.

According to Kruit in [20] we can expect a spherical aberration coefficient of 0.5 mm, with a $\alpha = 10$ mrad opening angle the radius due to spherical aberrations $r_{sph} = C_s\alpha^3$ is 0.5 nm which agrees well with the spot diagram in figure 9.9.

Further the spherical aberration can be seen in the trace space diagram 9.10.

Despite the aberrations the emittance clearly grows even when $< N >$ is less than one, clearly the Poisson statistics take effect at below the single electron per pulse level. This is the same as we saw with our model system, except that the

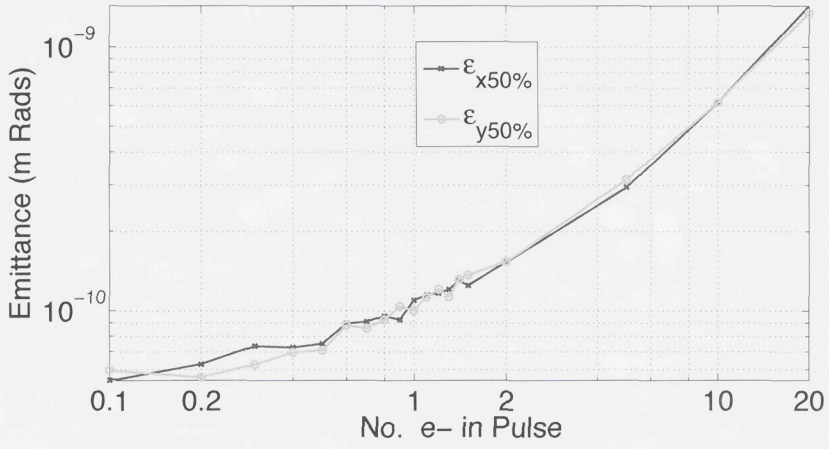

Figure 9.8: Emittance (x and y) growth due to Coulomb interactions for the photofield emitter in figure 9.7

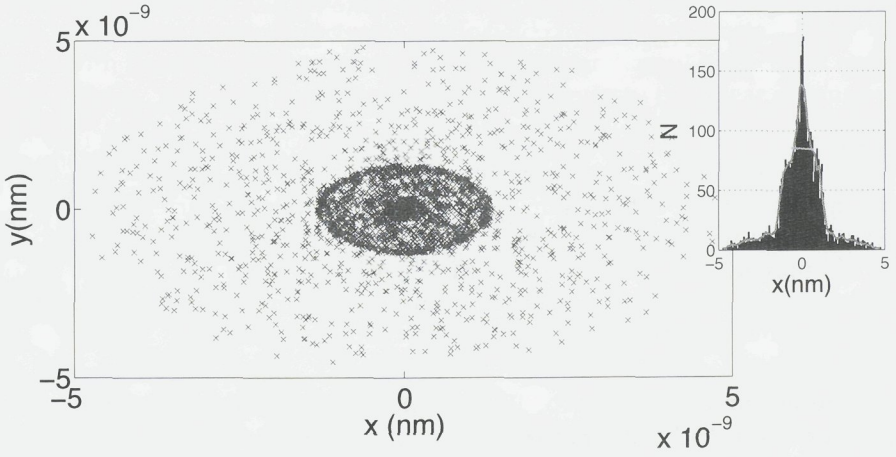

Figure 9.9: Spot Diagram with no electron-electron interactions

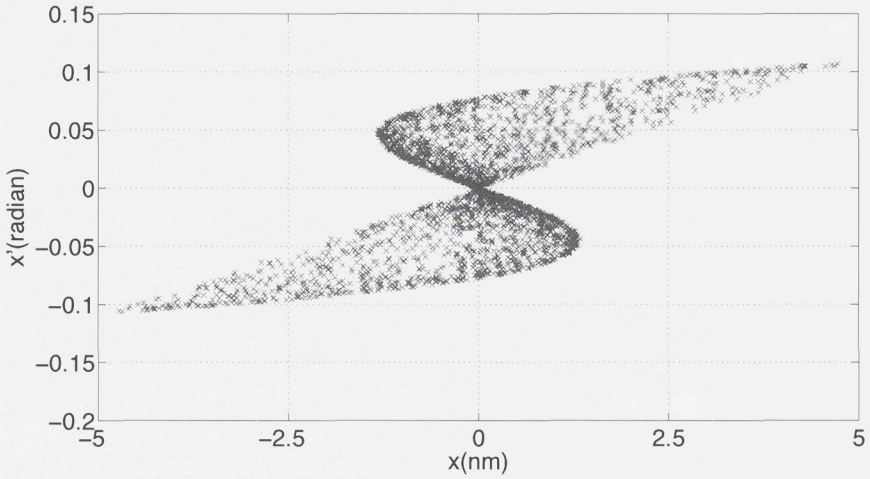

Figure 9.10: Trace space diagram with no electron-electron interactions

Coulomb interactions are greater. In an electron gun the electrons move initially very slowly as they must be accelerated from the tip surface, therefore the Coulomb interactions are greater. A sharp tip should for the same brightness, have lower Coulomb interactions than a flat cathode since the high field at the tip surface quickly accelerates the electrons. The field around a field emitter also acts laterally to spread the electrons this is shown in figure 9.7 where we can see the cone like beam envelope. The emittance values we are dealing with are not unrealistic as can be found from a back of the envelope calculation. From [46] for a pure photo emitter (i.e no field) we can write $r_{tip}^2 \delta E_x = \epsilon^2 V$, a typical excess photon energy is $\Delta E_x = 0.1$ eV making $\epsilon = 10^{-9}$ mrad.

Now let's examine how the B_r of the field emitter changes with N. If we look at figure 9.11 we see that the B_r of the emitter reaches a maximum between 0.4 and 2 electrons per pulse. However in this analysis the expansion of the pulse during it's trip through the gun is neglected therefore the current is $\frac{<Ne>q}{10 \text{ fs}}$. This result ties in with figure 9.4 where we see a sharp change in the behavior of B_r as N approaches 1, although note that here we include the intrinsic B_r of the emitter. This result also matches with our other work on Coulomb interactions with continuous current field emitters see chapters 5,4 and 6.

The maximum $B_r = 2.4 \times 10^{11}$ A/ $\left(\text{m}^2\text{srV}\right)$ is less than the Pauli/quantum limit of 1×10^{12} A/ $\left(\text{m}^2\text{srV}\right)$ for $\Delta E = 0.1$ eV given in chapter 7.4.2. This does not contradict the work of Jarvis [66] who claims to have seen individual pulses with B_r at the quantum limit, this results means that when many pulse are taken on average the B_r will probably be limited by Coulomb interactions. Therefore Poisson statistics and Coulomb interactions limit the usable B_r, in this case to $B_r = 2.4 \times 10^{11}$ A/ $\left(\text{m}^2\text{srV}\right)$.

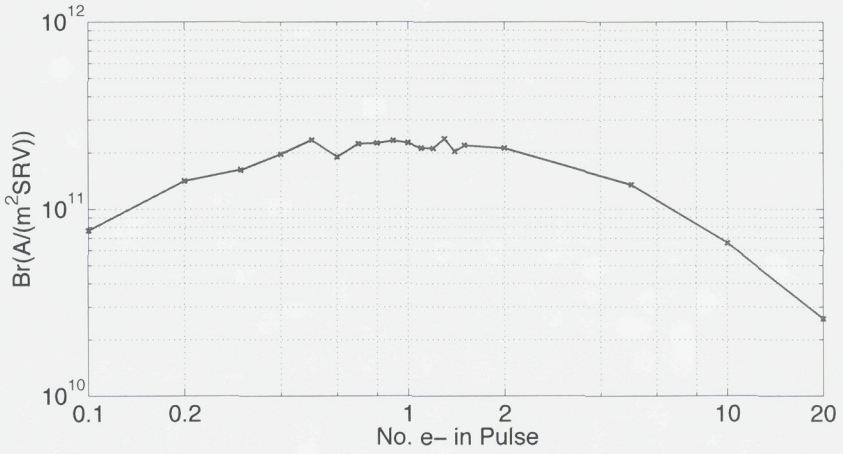

Figure 9.11: Reduced Brightness of photofield emitter in figure 9.7 as a function of the number of electrons in the pulse. The B_r is calculated without any increase in τ.

9.3.2 Energy Spread

We already identified that the energy spread is probably the area that gives the most issues. Here we will discuss the energy spread of the photofield emitter and what might be done to correct it.

Compressing the energy spread Recently it has been demonstrated that ultrafast diffraction can be performed with a bunch of electrons that have been compressed with a time varying electromagnetic field. In [96] they create a bunch of electrons with linear space charge and allow it to expand, until it reaches a radio frequency cavity, where an oscillating electric field reverses the linear expansion. We will look at the total energy spread, and also a corrected energy spread which approximates the action of the radio frequency cavity, we call the corrected energy spread the stochastic energy spread. To correct the energy spread we used the least squared method to fit a straight line through the z velocity data plotted against time. The straight line was then subtracted this from the data, and we found the FW50. The process is shown in figure 9.12.

Graph of the Energy Spread Looking at figure 9.12 the first thing we see is that the total energy spread quickly grows to a massive 8 eV yet the stochastic energy spread levels out at around 2 eV, for this region in seems that the biggest problem is space charge. Both the total and stochastic measures grow at the same rate up to around $< N >= 2.5$, thus we can assume that here the expansion is mostly stochastic. If we look closely at the bottom right part of figure 9.12 we see that initially the energy spread is 0 and just before $< N >= 1$ it starts to grow, which confirms our expectations that Coulomb interactions will start to have an effect

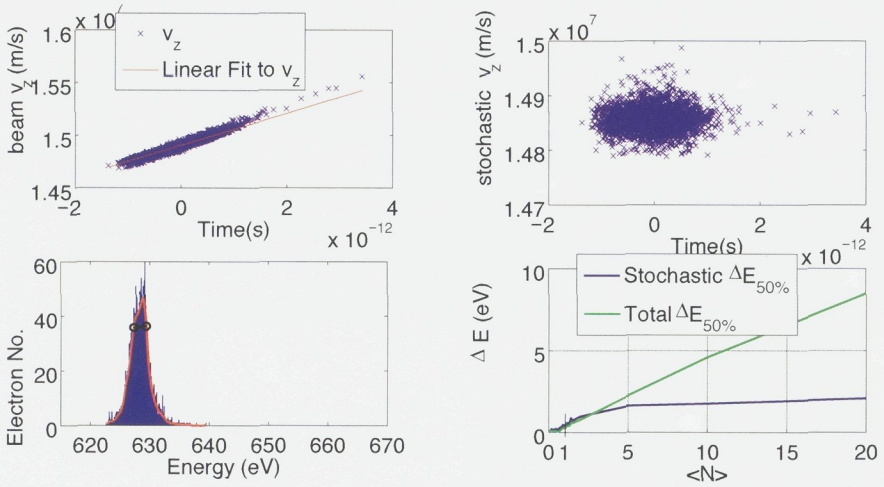

Figure 9.12: Method to apply a linear correction to the energy spread. Top left: Raw data with straight line fit shown in red. Top right: data after subtracting the linear fit. Bottom left: The F50 energy spread. Bottom right: The green line shows the total F50 energy spread before subtracting the straight line fit and the blue line is the stochastic energy spread which is left over after correction.

before $< N >= 1$ The total change ΔE appears to grow roughly linearly with the amount of charge which should be expected from the initial potential energy. The total ΔE of 8 eV at 20 electrons corresponds to emission from a lateral length of around 2 nm, which makes sense for the field at the tip.

What should be noted for the stochastic ΔE is that we did not actually compress the electrons, and when compressing the electrons they undergo further stochastic interaction which broaden the energy spread.

9.4 Conclusions

In conclusion we have seen that the energy spread and brightness of a photofield emitter are limited by Coulomb interactions. The maximum B_r of our system was $B_r = 2.4 \times 10^{11}$ A/(m^{2}srV) and the stochastic energy spread had a maximum value of ≈ 2 eV while the total energy spread grows almost linearly with $< N >$. The maximum B_r of the system was found to occur near $< N >= 1$ however in the analysis we had neglected the expansion of the pulse, which will push this back to slightly less than $< N >= 1$.

Part III

Summary and Conclusions

10 CHAPTER

Summary and Conclusions

He'd been wrong, there was a light at the end of the tunnel, and it was a flamethrower.

Terry Pratchet

It is time to bring to a close this thesis and try and wrap it up. I will first summarize what has been presented and then draw several conclusions.

10.1 Summary

Here I hope to briefly review what we did and some of the results of the preceding chapters. There will be some brief explanation of the results, but conclusions are left for the next section. The summary is presented in chronological order, thus we begin with Part 1.

In chapter 2, we were interested in improving the workings of a ZrO Schottky emitter by illuminating it with a laser to add photo emission. Therefore we first looked at electron emission from cathodes combining a mixture of photo, thermal and field effects. To do this we needed to come up with expressions for the reduced on axis differential brightness see section 2.2.1. From here we were able to show numerically that photoemission improves the B_r of Schottky tip and in some regimes without increasing the energy spread. However it must be noted that the amount of laser intensity required was in the TW/m^2 regime.

The logical follow up of chapter 2 was to look at laser heating. Chapter 3 used a simple model to compare photo emission to the thermal emission caused by laser heating. We combined a simple heat equation (3.1) with Richardson's equation

for thermal emission to get an expression for the thermal emission due to laser heating (3.5). This could then be compared to (3.2) which gave us the emission current from photo excited electrons. The results showed that sharp metal tip cathodes (When working above a reasonable B_r and current) are always going to be dominated by laser heating and not photoemission. However using pulsed lasers photoemission can be brighter than thermal, at least during the pulse.

Even ignoring laser heating we discovered in chapter 4 that statistical Coulomb interactions will degrade the quality of the beam from a photo assisted Schottky source. We did this for a particular gun design using the approximate formulas of Jansen [2]. However we believe this result is quite general, since for the same setup Coulomb interactions had less consequences for the pure Schottky tip.

After chapters 2, 3 and 4 we were convinced that a photo emitter was a lost cause. We were now interested to know how bright could we go? We decided to examine colds field emitters since many people have claimed extraordinary B_r, for example Jarvis [66] suggested B_r at the quantum limit. We expected again that Coulomb interactions would limit the B_r before reaching the high values claimed in the literature. The results are neatly summed up in figure 5.9. It turns that for our simulations and set up, the worst radius for the tip of a cold field emitter is ≈ 100 nm. An atomically sharp tip has a maximum $B_r \approx 10^{11}$ A/ $\left(\mathrm{m}^2\mathrm{srV}\right)$ limited by Coulomb interactions and for larger tips around 1 μm radius we discovered that Schottky tips do not compare so badly to CFE's which both have B_r of nearly 10^9 A/ $\left(\mathrm{m}^2\mathrm{srV}\right)$ for a tip radius of 1 μm.

The final chapter of part I showed that the work of chapter 5 on Coulomb interactions compared well to full numerical N body simulations of the same situation. In order to make the work more relevant we also looked at how the energy spread of cold field emitters was increased by Coulomb interactions and concluded that for situations where energy spread is important a cold field emitter outperforms a Schottky emitter.

Feeling as if we had done enough work on continuous sources we decided to look at Ultra-fast sources and concentrate on Ultra-Fast Electron Microscopy, with the view of examining sources for high resolution imaging and diffraction. Thus we began part II with chapter 7 a review of existing electrons sources for UFEM. We found that most guns has focused on what we called large area diffraction (LAD) and that using a well designed flat photocathode it was possible to take a diffraction pattern in a single shot with ≈ 100 fs time resolution. However we are still at the proof of concept stage. Unfortunately single shot imaging with atomic resolution (we concluded) is impossible, as are the more complex forms of diffraction which are normally used in TEM.

Stroboscopically however with a single electron in the bunch or perhaps less we can perform the same kind of imaging and diffraction as a modern high resolution TEM.

To achieve this we noted that both electron beam blankers and sharp tips illuminated by lasers were a good solution, having a high B_r and low emittance.

From chapter 7 we decided that an ultra-fast blanker combined with a high B_r source would an interesting solution for UFEM. We examined this in chapter 8, which shows the electron optics of an ultra-fast micro blanker. Here we developed analytical equations and performed numerical simulations to show that a short blanker is beneficial to reducing aberrations. Finally we were able to show that we could create pulses of around 400 fs with 16 nA, without significantly reducing the beam quality.

Finally in chapter 9 we looked at Photofield emitters, we expected that these like the cold field emitters in chapters 5 and 6 would be limited by Coulomb interactions. However we expected that in this case the limitations would be due to Poisson statistics something that is not covered in the Jansen theory. Therefore we decided to make a pure numerical study. We looked at one particular scenario and found that even an average of 1 electron per pulse reduced the B_r and increased ΔE. However the B_r that could be achieved when there was close to zero chance of a two electrons in a pulse was in our classical simulations effectively infinite. The actual limit is probably set by purely quantum mechanical effects.

10.2 Conclusions

Having summarised in chronological order this thesis it is now time to bring all the pieces together and present the conclusions. Since conclusion should be clear and decisive these are presented as a numbered list.

1. Cold field emitters are limited by electron-electrons interactions long before quantum limitations can occur.
2. For situations which require reasonable current and are not limited by energy spread, it is best to use a Schottky source, however for low current or when ΔE is a problem the cold field emitter is best.
3. We can not have continuous high brightness metal photocathodes due to heating and also electron electron interactions.
4. However with pulsed photocathodes it is possible to increase the B_r without increasing ΔE unlike thermal or field emitters.
5. Sharp tipped metal photocathodes with less than a single electron per pulse should be used for stroboscopic UFEM.
6. Another possibility for stroboscopic UFEM is a Schottky tip in combination with a micro blanker. This has the advantage over the photofield emitter of the more stable Schottky tip.
7. A short blanker is useful in reducing both aberrations and dispersion
8. Single shot ultra-fast atomic imaging or complex diffraction can never occur and more effort should be placed looking at the high resolution stroboscopic imaging.

Part IV

Appendices

A APPENDIX

Details of Gun Parameters

In this appendix we will show where the parameters of the guns discussed in chapter 7 come from. Quoting the available literature, we will show principally how we worked out the B_r of the guns, since this calculation tends to combine many other parameters.

Each section of this appendix refers to a specific gun and most will have the following order:

1. Briefly describe the purpose of the gun
2. Give the papers consulted.
3. Quote or otherwise reference the numbers used to find the B_r.
4. Calculate B_r.
5. Perform a sanity check on the numbers
6. If applicable present other methods to calculate the brightness.
7. Argue which value of B_r we find to be the most believable.

We now describe the methods used to calculate B_r. In most papers we can find information on the current $I = Q/\tau$, the source area, the work function of the cathode and the wavelength of the laser, this lets us use equation 7.8 to find B_r. Sometimes we will use equation 7.11, which links the diffractive imaging properties to the B_r. In some papers of course B_r is simply stated, in this case we will quote directly the numbers given.

Finally the energy spread of the emitted electrons will be roughly $(hc/\lambda) - \phi$.

A.1 UEM1 or the 4DTEM

This gun is called UEM1 which stands for ultrafast electron microscopy, it is however used in the 4DTEM. We will quote from reference [134] which is a patent writ-

ten by Zewail and Lobastov[1]. Since the patent is long we will quote the column and line numbers respectively as (X,X).

To use equation 7.8 first we need to find I, since this is not directly stated we must do some calculation. The UEM1 gun consists of a LaB_6 cathode(12,30) and a frequency doubled laser with $\lambda = 400$ nm (11,47). The laser gives pulses of energy 500 pJ (12,43) and $\tau \approx 10^{-13}$ s (12,39). The quantum efficiency of a LaB_6 cathode is about 10^{-3} (12,36). From the above figures we can calculate the number of photons emitted from the laser is $\frac{500\text{ pJ}}{hc/\lambda} = 10^9$, multiplying the number of photons by the quantum efficiency we find that $N = 10^6$, this gives $I = 10^6 e/(10^{-13}) = 1.6$. Next we need to find J so we need the area of the cathode. The cathode has flat emission diameter of 300 μm (12,2). However the laser spot has a diameter between 30 μm and 200 μm(12,7), meaning $J = 2.3 \times 10^9$ or $J = 5.1 \times 10^7 \text{Am}^{-2}$. Now to find B_r we need the excess energy of the photons ΔE_x given as $\Delta E = 0.1$ eV (12,42). From equation 7.8 this makes $B_r = 8 \times 10^9$ or $B_r = 1.6 \times 10^8$ A/ $\left(\text{m}^2\text{srV}\right)$.

Performing our sanity check we notice that even the lower limit $B_r = 1.6 \times 10^8$ is greater than our space charge limited maximum B_r stated in section (7.25). Also with $N = 10^6$ we know that the pulse will expand extremely rapidly (see for example the description of gun A.12 in section 7.5.5) therefore we find these two B_r's unrealistic, and start again with a new calculation.

Throughout the patent is talk of single electrons pulses. With one electron per pulse and the above figures we can calculate from equation 7.8 that $B_r = \frac{q}{\pi^2(15\times10^{-6})^2(0.1)(1\times10^{-13})} = 7.2 \times 10^3$ A/ $\left(\text{m}^2\text{srV}\right)$. More likely however is that they have a few more electrons say $N = 10$ at the cathode and then later aperture to have a single electron in the pulse, so we guess $B_r = 8 \times 10^4$ A/ $\left(\text{m}^2\text{srV}\right)$.

A.2 UED2

This gun is called UED2 which stands for ultra-fast electron diffraction 2. This set up is designed to perform averaged diffraction experiments from circa 100 μm sized crystals. We use two papers to find parameters for this gun [18] and [103]. The first [18] is a review paper by Srinivasan et al. We want to find B_r using equation 7.8 so let's find the current I. According to figure 6 of [18] we can achieve $N = 10^3$ in 1 ps or less therefore $I = 160$ μA. The beam area is defined by a 75 μm pinhole lets assume this is a radius, and further assuming a roughly collimated beam then at the cathode $J = 160\ \mu\text{A}/(\pi(75\ \mu\text{m})^2) = 9.1 \times 10^3\ \text{Am}^{-2}$. We now need the excess energy of the photons, according to Gahlmann in [103] $\Delta E_x = 0.1$ eV and so $Br = 2.8 \times 10^4$ A/ $\left(\text{m}^2\text{srV}\right)$. This number appears to be reasonable and therefore we make no further calculations.

[1]We will ignore UEM2 since as far as we can see this is simply UEM1 with a nanosecond laser for fast imaging as performed in the DTEM.

A.3 UED3

This gun is the next generation of UED2. We take information from [18] and from [103]. First as we want to use equation 7.8 we find the current I, according to figure 6 in [18] $N = 10^4$ for a $\tau < 1$ ps giving $I = 1.6$ mA. We assume the cathode radius is approximately 75 μm as defined by a pinhole, therefore $J = 9.1 \times 10^4$ Am^{-2}. Now we want the excess energy of the photons, section 3.2 of [18] tells us that the work function of the thin silver film cathode is 3.65 eV, and section 3.1.1 gives $\lambda = 267$ nm, therefore $\Delta E_x = 1$ eV, making $B_r = 2.8 \times 10^4$ $\mathrm{A}/\left(\mathrm{m}^2\mathrm{srV}\right)$, just the same as UED2 reference A.2. This is a reasonable number but maybe we should expect some improvement in B_r between generations, therefore, we can take information from [103] which says that $\Delta Ex = 0.1$, giving $B_r = 2.8 \times 10^5$ $\mathrm{A}/\left(\mathrm{m}^2\mathrm{srV}\right)$. We accept this as the best estimate for UED3.

A.4 UED4

Here we examine the gun used at Caltech in their UED4 set up which is again an update of UED3 A.3. UED4 is designed for gas-phase electron diffraction (GED). We take our data from a paper by Gahlman et al [135] and an earlier paper also by Gahlman [103]. We want to use equation 7.8 to find B_r so let's first find the current I, from the 6^{th} paragraph of [135] $N = 2 \times 10^5$ which quickly expands to around 10 ps after propagating only 200 mm, see figure 5 or figure 10 of [103], this makes $I = 3.2$ mA. Next we will find J, at the focus the beam has a $750um$ diameter, so J at focus is 7.2×10^3 Am^{-2} and we will assume that the magnification is one to one therefore J at the cathode is also $= 7.2 \times 10^3$ Am^{-2} . Now we need to find ΔE_x, from the introduction of [135] we know that the cathode is magnesium and front illuminated by a laser with $\lambda = 267$ nm. Magnesium has a work function of 3.66 eV [39], which means $\Delta E_x \approx 1$ eV. Now we can work out from equation 7.8 that $B_r = 7.2 \times 10^3$ $\mathrm{A}/\left(\mathrm{m}^2\mathrm{srV}\right)$. This however seems too small, so let's check with another method. We will use equation (7.11), but first we need to choose a value for X_{pc}. For good contrast this should be much bigger than the lattice spacing of the sample, Silicon for example has a lattice spacing of around 0.5 nm [39], so 10 times greater than this means $X_{pc} = 5$ nm. This quickly leads to $B_r = \left(\frac{5 \text{ nm}}{375 \text{ μm}}\right)^2 (\frac{2 \times 10^5 q}{10 \text{ ps}}) 10^{18} = 1.4 \times 10^5$ $\mathrm{A}/\left(\mathrm{m}^2\mathrm{srV}\right)$). This value 1.4×10^5 $\mathrm{A}/\left(\mathrm{m}^2\mathrm{srV}\right)$) makes more sense, and is more generous so we choose this.

A.5 Toronto Gun

In Toronto we have the Miller group, their set-up is designed for averaged mode diffraction. They are able to observe non-reversible processes by combining images from different sections of a crystal to produce a single diffraction pattern. We will use papers [95] by Siwick, [136] by Dwyer et al and one by Sciani [83]. As

with the other guns we want to use equation 7.8 to find B_r so we will start by finding the current I.

In the methods section of [95] by Siwick, we learn that $N = 10\ 000$ and from figure S2 of [95] we see that although the initial pulse length is around 120 fs at the sample it will have expanded to around 900 fs. This lets us calculate the current at the sample, $I = 1.8$ mA. In the same section we find the beam diameter is 200 μm, assuming that this is close to the beam size at the cathode then we can calculate $J = 6 \times 10^4$ Am^{-2}. Now to apply equation 7.8 we just need ΔE_x. Section 3.1.1 of [136] tells us they use a 257 nm laser with a thin film Ag cathode which they claim has a work function of 3.65 eV. This gives us a $\Delta E_x = 0.1$ eV. Finally we can calculate that $B_r = 2 \times 10^5$ A/ (m^{2}srV), this Br is entirely reasonable it is in the middle of our other flat cathodes, but there is further information to examine. In the paper by Sciani [83], we find what appears to be still the same gun. This time with $N = 10^4$ and an estimated FWHM $\tau = 400$ fs, this better τ improves the B_r to 4.1×10^5 A/ (m^{2}srV). Now as a final check since we know that the spot on the sample in [83] was $r = 150$ μm we can use (7.11) to calculate the B_r, if we assume a $X_{pc} = 5$ nm (approx, ten times the lattice spacing of Si) then $B_r = 10^7$ A/ (m^{2}srV) which seems too high, if however $X_{pc} = 1$ nm then $B_r = 4 \times 10^5$ A/ (m^{2}srV) which is in line with our previous estimates. We take $B_r = 4.1 \times 10^5$.

A.6 Florida State

This is a flat catode designed for performing repeated diffraction. This gun is described by two papers the first by cao [16] from 2003, and a further paper by Wang [137] from 2009.

We want to use equation 7.8 to find B_r, so we start by finding I. Figure 2 in [16] shows that this gun can easily have $N = 2000$ with $\tau < 300$ fs, which means that $I = 1.1$ mA. In [137] they discuss similar parameters, and say the beam diameter is only 100 μm at a pinhole. If we assume that this pin hole essentially corresponds to the diameter of the virtual source then we can calculate J at the cathode as 1.4×10^5 Am^{-2}. Returning to [16] where we learn that $\Delta E_x < 0.5$ eV allowing us to calculate $B_r = 8.9 \times 10^4$ A/ (m^{2}srV). As a sanity check we can use (7.11) with $X_{pc} = 5$ nm and according to [137] a beam diameter at the sample of 350 μm $B_r = \left(\frac{5\text{ nm}}{375\ \mu\text{m}}\right)^2 (\frac{2\times10^5 q}{10\text{ ps}} 10^{18} = 5.7 \times 10^5$ A/ (m^{2}srV)) $= 5.4 \times 10^4$ A/ (m^{2}srV). Since both values of B_r are quite close we choose the higher value.

A.7 Atomic UED

This flat cathode has been developed in China, and is designed for atomic UED, of large crystals (LAD). We take information from [138] by WenXi. We want to use equation 7.8, so we will first find the current I. On page 3 we find that $N = 1.9 \times 10^3$ and on page 2 the time resolution is said to be less than 500 fs this

makes $I = 0.6$ mA. Again on page 2 we discover that the beam is defined by a 100 μm diameter pinhole , this gives us a $J = 8 \times 10^4$ Am^{-2}. On the first page we see the gun is made of a 40 nm Ag film coated on sapphire plate excited by a laser $\lambda = 266$ nm as per previous guns this leads us to $\Delta E_x = 0.1$ eV and then $B_r = 2.5 \times 10^5$ $\mathrm{A}/\left(\mathrm{m}^2\mathrm{srV}\right)$. Let's perform a sanity check, and use equation 7.4 to find the B_r. From [138] we know that the cathode to sample is 17 cm and on reaching the sample the beam has expanded from around 100 μm to 400 μm this gives us a divergence angle of ≈ 2 mrad, since the beam voltage at the sample is 58 keV, then $B_r = \frac{0.6 \text{ mA}}{\pi^2(100/2\times10^{-6})^2(2e-3)^2(58e3)} = 1.1 \times 10^5$ $\mathrm{A}/\left(\mathrm{m}^2\mathrm{srV}\right)$. This matches our expectations and we take the larger B_r.

A.8 Michigan

In [82] Ruan et al discuss an LAD experiment using a flat photocathode based at Michigan state university. In this case we can not use equation 7.8, and we will try to use equation (7.11) instead. First we need to find the current I, [82] tells us that there are a maximum of 1000 electrons per pulse, and at the sample $\tau < 1$ ps, this means $I = 0.16$ mA. At the sample this is spread over a diameter of around 5 μm, if we assume $X_{pc} = 5$ nm (since this is ten times the lattice spacing of Si) then $B_r = (1 \times 10^{18})(0.16 \text{ mA})(\frac{5 \text{ nm}}{5 \text{ μm}})^2 = 1.6 \times 10^8$ $\mathrm{A}/\left(\mathrm{m}^2\mathrm{srV}\right)$. This B_r is very large compared to the other flat photo cathodes, and actually since their sample consists of 2 nm gold particles perhaps the assumption of $X_{pc} = 5$ nm is excessive, with this in mind we make $X_{pc} = 2$ nm and get that $B_r \approx 5 \times 10^6$ $\mathrm{A}/\left(\mathrm{m}^2\mathrm{srV}\right)$. However this seems too large given our space charge limitations in section 7.4.3 to B_r and the fact that this gun design is based on [95]. Therefore we do not believe it, hence we mark it as a theoretical not experimental.

A.9 Duisberg Essen Gun

Janzen in [139] describes a flat photocathode for ultrafast electron diffraction at surfaces. We want to use equation (7.8) so let's start by finding the current I, the numbered section of [139] tells us that they expect at the sample to have around $\tau = 6$ ps, and typically $N = 1500$, this gives us $I = 40$ μA. In section (IIIc) we find that the cathode has $r = 150$ μm, therefore we can calculate $J = 566$ Am^{-2}. Now finally for equation (7.8) we just need ΔE_x, which according to the abstract is $0.1eV$, this gives us $B_r = 1.8 \times 10^3$ $\mathrm{A}/\left(\mathrm{m}^2\mathrm{srV}\right)$. This B_r is believable but small.

We can check this with equation (7.4) by using the beam divergence, beam energy and focus at the sample. In section (IV) at the sample they find a spot with $r = 190$ μm and beam divergence 1.5 mrad at 15 keV therefore $B_r = \frac{40 \text{ μA}}{\pi(190 \text{ μm})^2\pi(1.5e-3)^2*15e3} = 3.3 \times 10^3$ $\mathrm{A}/\left(\mathrm{m}^2\mathrm{srV}\right)$. This value agrees well with the previous B_r, and is a little higher so we choose this one.

A.10 DC Photoelectron Gun

This gun is designed for UEM, it is based on a themal gun designed by Togawa et al. [105], Berger and collegues at the university of chicago [104] have adapated this gun to use as a front illuminated photocathode. Let's begin by trying to use equation (7.8) to find B_r we first need to find the current I. In the abstract we learn that $N = 20 \times 10^3$ and $\tau = 4$ ps, making $I = 0.8$ mA. The cathode produces an electron beam with an area of $1mm^2$, so we can calculate $J = 800\ \mathrm{Am}^{-2}$. Now we need ΔE_x, in the experimental and results sections we find that the cathode is made from tantalum with $\phi = 4.25$ eV , excited with a laser of wavelength $\lambda = 261$ nm (4.75 eV). This means that $\Delta E_x = 0.5eV$, and gives us a $B_r = 510\ \mathrm{A}/\left(\mathrm{m}^2\mathrm{srV}\right)$, which seems rather low, therefore we can use a 2nd method to check this number. In measurements they see a divergence of 5 mrad at 25 kV which they show fits with expectations based on ΔE_x. With this information we can use equation (7.4) to find B_r - we already know $J = 800\ \mathrm{Am}^{-2}$ - therefore $B_r = \frac{800\ \mathrm{Am}^{-2}}{\pi(5\mathrm{mrad})^2(25\ \mathrm{kV})} = 407.43\ \mathrm{A}/\left(\mathrm{m}^2\mathrm{srV}\right)$

A.11 Chicago Gun

In an extended abstract [140] Schroeder outlines a rough plan for a compressed source, which would be used for UEM. We want to use equation 7.8, to find B_r, Schroeder tells us that the density of electrons is about $10^4 electrons/\ \mathrm{mm}^2$ so we do not need to calculate I but J, according to figure 1 in [140] the pulse is compressed to less than 100 fs this makes $J = 1.6 \times 10^4$. He claims he needs $\Delta E_x < 1$ eV, therefore from equation (7.8) $B_r = 5.1 \times 10^3\ \mathrm{A}/\left(\mathrm{m}^2\mathrm{srV}\right)$, however this seems too small. At the cathode Schroeder suggests $\tau = 200$ fs assuming he more than meets his ΔE_x requirements let $\Delta E_x = 0.5$, then $B_r = 1.2 \times 10^4\ \mathrm{A}/\left(\mathrm{m}^2\mathrm{srV}\right)$, however according to figure 1 he is able to compress $\tau < 1$ fs and applying this means the gun should have a brightness of $B_r = 1.2 \times 10^6\ \mathrm{A}/\left(\mathrm{m}^2\mathrm{srV}\right)$. This higher figure is at the upper end of flat cathodes but not massive compared to other cathodes using compression. We therefore use this number despite the extremely small value of τ. Finally since this application is for single shot DTEM then we assume that to form an image $N = 10^8$, which probably means Coulomb Interactions will seriously reduce this B_r.

A.12 Eindhoven RF compression gun

In [69] and [96] Oudheusden describes a gun designed for single shot LAD 100 fs diffraction. This gun features RF compression, and is a front illuminated flat cathode. We want to find B_r and will try to use equation 7.8, thus we will first find the current I. From the abstract of [69] we find that each 200 fC pulse is focused to a half width of less than 100 fs, and from graphs in [69] we make the full width 160 fs giving $I = 1.25$ A . The spot radius at the cathode is according

to the abstract of [96] around 25 μm making $J = 3.2 \times 10^9$ Am^{-2}. If we calculate B_r based on the initial energy spread given in [96] $\Delta E_x = 0.6$ eV then $B_r = 1.7 \times 10^9$ $\mathrm{A}/\left(\mathrm{m}^2\mathrm{srV}\right)$. This is quite a high B_r and difficult to feel certain since Pasmans in [141] discusses the source as having $r = 50$ μm which means a reduction of 4 so $B_r = 4.25 \times 10^8$ $\mathrm{A}/\left(\mathrm{m}^2\mathrm{srV}\right)$, this newer number seems more reliable. As a further check let's try using equation 7.11 in [96] they aim for a 4 nm coherence length which for our definition means $X_{pc} = \pi 4$ nm. This focused onto the diffraction pattern in [69] with $r = 400$ μm means that the fraction of I that was coherent is
$((\pi 4 \text{ nm})/(800 \text{ μm}))^2 = 10^{-9}$ therefore
$B_r = 10^{18} \times 10^{-9} \times 0.2$ pC/160 fs $= 3 \times 10^8$ $\mathrm{A}/\left(\mathrm{m}^2\mathrm{srV}\right)$. We accept the value of $B_r = 4.25 \times 10^8$ $\mathrm{A}/\left(\mathrm{m}^2\mathrm{srV}\right)$ as the most reasonable, as it sits in between the other two values.

A.13 Max Planck - Munich

This gun is based on a paper by Fill , Veiszm, Apolonski and Krausz [142]. It is a simulation paper. The goal is to create low charge sub-relativistic pulses with $\tau < 1$ fs. The gun is a flat cathode. Given that this gun is designed for low charge it would be most suitable for stroboscopy, and therefore high resolution UEM. We would like to find the B_r and will use equation 7.8, we start by finding I. According to the conclusion of [142] this gun should produce extremely short pulses with $N = 1$ and $\tau < 1$ fs, then $I = 0.16$ mA. In section four of [142] the cathode radius is given as 10 μm making $J = 5 \times 10^5$, if as stated $\Delta E_x \approx 1$ eV then $B_r = 1.6 \times 10^5$. However here we can be more precise since they give us $\epsilon_n = 6 \times 10^{-3}$ mm mrad so we can calculate first B_n and then convert it to B_r as in equations (7.3) and (7.5).

$B_n = \frac{q}{\pi^2(6\times10^{-9})^2/1e-15} = 4.5 \times 10^{11}$ $\mathrm{A}/\left(\mathrm{m}^2\mathrm{sr}\right)$ which makes $B_r = 8.8 \times 10^5$ $\mathrm{A}/\left(\mathrm{m}^2\mathrm{srV}\right)$). These two numbers agree and seem pretty reasonable therefore we accept this higher value.

A.14 Max Planck 2: Ultrashort pulse electron gun with a MHz repetition rate

This gun is described in the experimental paper by Wytrykus et al [143]. We believe this a first step to verify the simulation paper [142]. The gun is designed for a low number of electrons per pulse to reduce space charge, the design of the cathode is a quartz plate coated with 50 nm of gold. We want to calculate B_r and we will try to use equation (7.8). First we need to find the current I, s ection 2.2 of [143] tells us the highest average current was $I = 0.8pA$ with a pulse frequency of $f = 2.7MHz$ and $\tau = 270s$ fs this means that the current in a pulse is 1.1 μA. The radius of the laser spot used was $r = 70$ μm giving us $J = 71$ Am^{-2}, we are given the excess energy of the electrons $\Delta E_x = 0.6eV$ therefore $B_r = 189$ $\mathrm{A}/\left(\mathrm{m}^2\mathrm{srV}\right)$. If

we consider this B_r it is quite small, however it doesn't seem unreasonable given the very low average current of $1.08pA$, we therefore take this number.

A.15 Reflection Compressor

From the abstract of [144] by Kassier at the university of Stellenbosch, we learn that this gun is designed for femtosecond UED experiments and should operate in the $30 - 100$ keV regime. It features a pulse compression method based on a reflectron concept.

We will now try to find this gun's B_r, from the abstract of [144] we realize that the best method is to use equation (7.11). We start by finding I which given $N = 200 \times 10^3$ and $\tau = 2 * 130$ fs, then $I = \frac{q200\times10^3}{2\times130 \text{ fs}} = 0.123$ A, the sample radius is 140 μm and $X_{pc} = 1.5$ nm, this makes the coherent current $0.123 \text{ A} \left(\frac{1.5 \text{ nm}}{140 \text{ μm}}\right)^2 = 14$ pA. Finally we get $B_r = 14 \text{ pA} \times 10^{18} = 1.3 \times 10^7$. This number seems reasonable and therefore passes our sanity check.

A.16 Femtosecond RF-gun

In Rimjaem's paper [145] he simulates producing sub-picosecond bunches using a thermal RF cathode. The bunches are compressed, and the system works at relativistic speeds. This gun would be suitable for single shot LAD.

The useful information is neatly summarised in table 1 page 263 of [145] and in part reproduced here. We want to know B_r, which we can find from equations

Parameter	Measure	Units
Max. beam momentum, cp	2.91	MeV
Cathode Emission Current	2.9	A
Cathode Radius	3.0	cm
Charger per bunch	94	pC
Charger per bunch	94	pC
Peak current	707	A
Norm. beam emittance, rms	3.8	$mmmrad$

Table A.1: Rim

(7.3) and (7.5). First we need to find I, using full width measures $\tau = 103.6$ fs and from the charge per bunch 94 pC, we calculate the mean current in the pulse $I = Nq/\tau = 907$ A, now using equations (7.3) and (7.5) $B_n = 907/(\pi^2(3.8 \times 10^{-6})^2) = 6.3641 \times 10^{12}$ A/ $\left(\text{m}^2\text{sr}\right)$, or $B_r = 1.25 \times 10^7$ A/ $\left(\text{m}^2\text{srV}\right)$, which we conclude is reasonable, given the relativistic speed and the compression. Interestingly section 6 suggests that actually the emittance is improved from 3.8×10^{-6} to 3.17 mm mrad thus $B_n = 9.145 \times 10^{12}$ A/ $\left(\text{m}^2\text{srV}\right)$ or $B_r = 1.79 \times 10^7$ A/ $\left(\text{m}^2\text{srV}\right)$, this number is also reasonable and we take this higher value.

A.17 SLAC Gun

The SLAC gun is used primarily to produce electrons for generating GeV beams for a variety of experiments, however it can also be used for UED, and is one of the most optimised guns available. The table from the front cover of [146] by Akre et al is reproduce in table A.2

Parameter	Measure	Units
Final Injector e^- energy	135	MeV
Bunch Charge	1	nC
Initial Bunch length	11	ps
Final Bunch	0.4-11	ps
Project Norm. $\epsilon_{95\%}$	1.2	μm
Slice Norm.$\epsilon_{95\%}$	1	μm
Slice Energy Spread (rms)	> 6	keV
Single Bunch f	30	Hz
rf gun field at cathode	115	MV/m
Laser Spot Diameter	1.3	mm

Table A.2: SLAC details

We want to calculate B_r thus we quickly calculate from equations (7.3) and (7.5) that $B_n = \frac{1\text{ nC}}{\pi^2(1\text{ mm mrad})^2 0.4\text{ ps}} = 2.5330 \times 10^{14}\text{ A}/\left(\text{m}^2\text{sr}\right)$ and converting that to B_r gives $5 \times 10^8\text{ A}/\left(\text{m}^2\text{srV}\right)$.

A.18 SLAC 2

Hastings used gun A.17 to perform a single shot LAD experiment, which is described in [70], at the rear of this paper is a table with gun parameters which we reproduce in table A.3.

This allows us as with gun A.17 to calculate $B_r = 7 \times 10^6$, this is a lot less than gun A.17, however this experiment may not have been carried out under optimum conditions, therefore we accept it.

A.19 Osaka

This gun is described in two papers Yang [147] gives us simulation details from 2009 and the experimental realisation of this is from Morooka [98] in 2011. The gun is designed to perform single shot LAD at relativistic speeds. We want to find the B_r of this gun, from the abstract of [147] we see that we have the information to use equations 7.3 and 7.5. Lets first find I, which given $\tau = 100$ fs and a maximum N of $\frac{2\text{ pC}}{Q}$ makes the maximum $I = 16$ A. The normalised emittance is quoted as 0.1 mm mrad giving $B_r = 4 \times 10^8$. This number is quite reasonable and we can

Parameter	Value	Units
Bunch Charge	2.9	pC
Energy	5.4	MeV
Energy Spread (rms)	¡6	keV
rms pulse length	560	fs
Long. Emittance	2.5	keVps
Norm. Emittance	0.85	μm
Geometric emittance	0.075	μm
Minimum rms divergence	45	45 μrad
Solenoid field	1.7	kG
Gun gradient	104	MV/m
Laser gun phase	40	degrees

Table A.3: Details of beam parameters from Hastings single shot Diffraction experiment

also compare it with the experimental paper [98]. The information in Murooka's paper [98] suggests using equation (7.16). Normally we first find I, but this time we want to find J. The abstract tells us that $\tau = 100$ fs, and later we learn that each pulse has a density of $5.3 \times 10^8 e/cm^2$ at the sample making $J = 8.5 \times 10^8$ Am^{-2}. Further in the abstract the beam energy of $V = 3.0$ MeV is given and from the rest of their article we learn that the beam at the sample has a divergence angle of 5×10^{-5}rad

Therefore $B_r = \frac{5.3 \times 10^{12} q}{\pi^2 (5 \times 10^{-5})^2 (1.2 \times 10^7)(120 \text{ fs})} = 2.8 \times 10^7$ A/ $(\mathrm{m}^2 \mathrm{srV})$. This number is also reasonable, but it is a factor of 10 less than the simulated B_r so we choose the higher B_r.

A.20 Guncher

For this gun we examine a review paper by Musumeci [148]. The Guncher is designed for relativistic LAD. Most of the useful information is found in table 1 of [148] which we reproduce here.

Parameter	Guncher	Hybrid
Bunch Charge	3 pC	3 pC
Pulse length	60 fs	50 fs
rms beam size	500 μm	400 μm
rms beam divergence	45 μrad	45 μrad
Peak Brightness	1.2×10^{15} A/ $(\mathrm{m}^2\mathrm{sr})$	1.5×10^{15} A/ $(\mathrm{m}^2\mathrm{sr})$
rms ϵ_n	0.18 μm	0.14 μm
Laser rms spot size	100 μm	50 μm
Laser rms pulse length	600 fs	1.2 ps

Table A.4: Details of the Guncher and Hybrid Guns

We want to find B_r, but do not take it directly from this table for the following reason. Table A.4 contains information about two guns the Guncher and the Hybrid if $B_n = 2Nq/(\tau k \epsilon_n^2)$ where k is a constant relating the pulse length measure τ to the actual width of the beam used for the calculation, then k should be the same for both guns, however each gun has a different k. In other words we are not sure how the B_n in the table has been calculated and therefore will calculate it ourselves. We should first note that Musumeci defines ϵ_n with a factor of π included (we define it as the area of the $ellipse/\pi$), using equations 7.3 and 7.5 we calculate the B_r of the Guncher as
$B_r = \frac{1}{m_0 c^2} \frac{3 \text{ pC}}{60 \text{ fs}(1.8^{-7} \text{ mrad})^2} = 3 \times 10^9 \text{ A}/\left(\text{m}^2\text{srV}\right)$.

A.21 Hybrid

The Hybrid like the Guncher in appendix A.20 is designed for single shot LAD. Appendix A.20 contains all the information for this gun. We calculate the B_r of the Hybrid as
$B_r = \frac{1}{m_0 c^2} \frac{3 \text{ pC}}{50 \text{ fs}(1.4^{-7} \text{ mrad})^2} = 5 \times 10^9 \text{ A}/\left(\text{m}^2\text{srV}\right)$.

A.22 Ultra Fast SEM With Laser Illuminated Schottky Tip

In a paper by Yang [71] in 2010 and [88] by Mohammed in 2011 we find out results about a laser illuminated Schottky tip designed for stroboscopic UEM. This tip has been implemented into an ultrafast SEM.

We want to find a value for the B_r of this tip, we would normally do that with equation (7.8), however it is not not straight forward since according to [88] the tip is illuminated by a $\lambda = 565$ nm ($= 2.2$ eV) laser. According to [71] the work function of the Schottky source is 3.3 eV including the Schottky lowering of the barrier, since the laser photon energy is below the work function this means that that in [88] the tip is used in photofield emission mode and equation 7.8 does not apply. If we instead take an example operation from [71] where the laser is frequency tripled to 357 nm, meaning direct emission over the barrier with $\Delta E = 0.3$ eV.

We know from appendix A.26 that the Schottky source when used normally has $B_r = 10^8 \text{ A}/\left(\text{m}^2\text{srV}\right)$ and from van Veen's [19] measurements of the virtual source the radius appears to be about 20 nm as limited by Coulomb interactions, with out interactions r could be half this. Therefore we will now use (7.8), first we find I, assuming single electron emission with $\tau = 200$ fs [88], $I = 0.8$ μA. The current density given the virtual source radius of 10 nm is $J = \frac{0.8 \text{ μA}}{\pi(10 \text{ nm})^2} = 2.6 \times 10^9 \text{ Am}^{-2}$. Finally we have $\Delta E = 0.3$ eV and then $B_r = \frac{q}{\pi^2 (10nm)^2 (0.3 \text{ eV})} = 5.4 \times 10^9 \text{ A}/\left(\text{m}^2\text{srV}\right)$.

A.23 Photofield

Hommelhoff in [114] looks at two different types of emission, both photofield emission and optical field emission. We now look at the photofield emission. This gun is a sharp tungsten tip illuminated by infra-red laser , with sub workfunction energy (making ΔE_x negative), this set up could be used for stroboscopic UEM or high resolution UED applications due to low charge per pulse, and it's small emittance. We want to find B_r, in this case as per chapter 2 we could numerically find the B_r, but in keeping with the spirit of the rest of this chapter, we can take a guess based on our previous experience calculating the brightness of field and photofield emitters. Let's begin by calculating I, first the laser used to excite this gun has $\tau = 70$ fs [114] , and we assume the electron pulse has the same τ. The 40 nm tip had an averaged current of 40 fA spread over an 80MHz repetition rate meaning $N = 0.0031$, and the current in the pulse was $I = 7$ nA. Now we will try to find J, using field ion microscopy the emission area was imaged and the size deduced to be around 1 nm, from the 30 nm tip. This is in line with other measurements of the virtual source size of field emitters, however we do not know how big the virtual source is during photofield emission, so to be cautious we will double it, making $J \approx 5.625 \times 10^8$ Am^{-2}. From previous experience we know that J and B_r are often similar so for simplicity so we assume the same value for $B_r = 5.625 \times 10^8$ $\mathrm{A}/\left(\mathrm{m}^2\mathrm{srV}\right)$.

A.24 Optical field

We now examine optical field emission using [114] by Hommelhoff. As per appendix A.23, this embodiment of a sharp tip plus laser has a much larger N then photofield or photo-Schottky emission, however it is still not enough for repeated diffraction, and due to the low emittance should be used for UEM and high resolution UED. As proof of optical field emission not photofield emission, they demonstrate the non-linearity of laser power vs current dependence as function of the polarisation angle, noting that this is different from that expected by photofield emission from surface states (see for example Venus [149]). We of course want to find B_r, and will do so as per the previous gun A.23, we start with the current, $N = 200$ in a 70 fs pulse, which would make $I = 0.5$ mA. Now we will find J, the optical field emission current came from a 1 μm radius tip with some sharp features so assuming a 1 μm source size then $J = 1.5 \times 10^8$ Am^{-2}. This could give a similar B_r, however perhaps with $N = 200$ Coulomb interactions destroy this B_r, so let's look further.

In a later publication [45] Hommelhoff was able to demonstrate an extremely short pulse length of only 8 fs by using a interferometer with the laser tip at the centre, this showed that when two pulses from the two paths of the interferometer overlap there is a strong non-linearity, suggesting that the pulse length is at least as short as the laser pulse. If the measured current of 900 nA in a pulse (see figure 2a part 1) comes from $r = 2$ nm as suggested in A.23 then as before we assume

$J \approx B_r \approx 10^{11}$ A/ $(\mathrm{m}^2\mathrm{srV})$ with still less than a single electron in the pulse, and therefore no Coulomb interactions.

A.25 Laser-Photofield Emission

This photofield emitter is being developed for use at the free electron laser at the Paul Scherrer Institute in Switzerland. It is a ZrC needle with around 50 μm emitting radius and it has a large N, therefore it could be used for single shot LAD but it's emittance is probably not suitable for more high resolution applications. We examine a paper by Ganter [111], and to find the B_r we can use equation 7.4. We start by finding I although in the abstract they state a peak current of 2.9 A they also give the bunch charge as $< 150\ pC$ from a 16 ps rms laser pulse which by our previous calculation methods would mean $I = \frac{150\ pC}{16\ \mathrm{ps}} = 4.7\mathrm{A}$. They also give the emittance as 0.05 mm mrad, which was achieved at 27 keV, so from 7.4 we get $B_r = \frac{4.7}{\pi^2 * 0.05e-6^2 \times 27e3} = 7.0550 \times 10^9$ A/ $(\mathrm{m}^2\mathrm{srV})$. This is not an unreasonable number, however it is quite high and we wonder what is shown in the body of the paper, for example at what current was the emittance measured?.

Looking further in figure 1 of [111] $\epsilon_n = 0.3$ mm mrad with $I = 150pC/32$ ps $=$ 4.7 A and from equations (7.3) and (7.5)

$B_n = \frac{4.7}{5.3 \times 10^{12}}$ A/ $(\mathrm{m}^2\mathrm{sr})$

which translates to $B_r = 10^7$ A/ $(\mathrm{m}^2\mathrm{srV})$. This number seems extremely reasonable so we accept it.

A.26 Schottky Source

The Schottky tip is tungsten tip covered with a work function lowering coating of ZrO. It is normally used in continuous current mode, however it can be pulsed using for example an electrostatic chopper / blanker. The Schottky tip is routinely used for many high resolution applications in state of the art TEM's, it is not suitable for high current applications with a maximum current of a few hundred micro amperes. We examine a paper by Fransen [57] who measured the B_r of a Schottky tip in a TEM. The measured radius of the Schottky tip was 900 nm, it achieved a $B_r = 1.2 \times 10^8$ A/ $(\mathrm{m}^2\mathrm{srV})$ at an extractor voltage of 4 kV. There was a field enhancement factor of $1.9 \times 10^5 \mathrm{m}^{-1}$ assumed, therefore the field at the tip surface was 0.76 V/nm.

In this experiment the I was apertured to give only 0.4 nA, however similar results have been found by Van Veen et al [19], with a current of up to 16 nA.

All of these measurements used a continuous beam, however chapter 8 of my thesis demonstrates with simulations that an $I = 16$ nA of current from a Schottky emitter at 30 keV can be chopped with $\tau > 500$ fs.

The energy spread of a Schottky emitter was measured by Fransen et al [29] to have an ΔE of around 0.5 eV at a temperature of 1850 K, and a $J = 10^8$ A/m^2.

A.27 Tungsten Hairpin

The tungsten hairpin is an old style of emitter not often used except for low budget applications. It is simply not as bright as the more modern Schottky emitters. These emitters are well documented and have a max $B_r < 10^6$ A/ $(\mathrm{m}^2\mathrm{srV})$ which can be found in virtually any text book on electron microscopy. Since the tungsten emitter is a thermal emitter it is not normally pulsed, however in [12] Hosokawa et al report $\tau = 0.2$ ps blanking at $I = 240$ pA, $f = 1$ GHz and $V = 20$ keV.

A.28 Carbon Nanotube Field Emitter

Cold field emitters have been known to have a high B_r for around a 100 years. Normally they are made from a sharpened tungsten tip, however recently carbon nanotubes have been used, since it is thought they should give an even higher brightness. The field emitter is not suitable for high current applications since they can at best manage a maximum (continuous) current of a few micro amperes, yet they have been used in high resolution electron microscopes for many years. As per the Schottky tip A.26 they can be pulsed.

One of the best measurements of any cold field emitter is from de Jonge et al [58] who gave the $B_r = 3 \times 10^9$ A/ $(\mathrm{m}^2\mathrm{srV})$ for a carbon nanotube with continuous current they measured X_c and I. This B_r is quite believable.

The diameter of the carbon nanotube was measured to be 2.7 nm and the emitted current measured in a Faraday cup was 14 nA.

Measurements by Fransen [150] give the energy spread (FWHM) for a 9 nm carbon nanotube give $\Delta E = 0.3$ eV, see figure 9 in [150].

Pulsing is as per the Schottky Source in section A.26.

A.29 Eindhoven Ultra-cold Plasma

This is an ultra cold gas in a magneto-optical trap, it has a relatively large source radius, and is suitable for LAD see section 7.5.7 for more. From chapter 7 of Taban's thesis [117] we find the following table. (this information is available in other publications such as [151] and [152])

Source	Rms Size μm	Temp K	Charge fC	Bunch len. ns	ϵ_n $mm\ mrad$	B_n A/ $(\mathrm{m}^2\mathrm{sr})$	Ref
Pulsed1	50	15	10	2	2.5×10^{-3}	8×10^9	Ch.4
Pulsed2	30	10	10	0.85	1.2×10^{-3}	8×10^{10}	Ch.5
DC-RF		10	100	1×10^{-8}	1×10^{-3}	8×10^{16}	Ch.7

Table A.5: Ultra Cold Plasma Details

From this we have all the information we require to calculate B_r using equation 7.5 which gives an experimentally measured value of 1.57×10^5 A/ $(\mathrm{m}^2\mathrm{srV})$, which seems quite reasonable.

The bottom line of table A.5 is a reference to the gun described in appendix A.30.

A.30 Ultra-cold Plasma Bunched

For the ultra-cold Plasma source described in gun A.29 van der Geer et al [153] propose to switch from DC fields to an RF Cavity. This gun is also described in the final line of table A.5 using equation 7.5 we can calculate the B_r of this gun, giving $B_r = 1.57 \times 10^{11}$ A/ $(\mathrm{m}^2\mathrm{srV})$. This is a massive number however in this case as a simulation we can accept it.

A.31 Laser-Accelerated Electron Source

In [120] Kyoto Tokita et al describe a new type of source in which electrons are excited by an intense laser beam on a polyethylene film. This gun is suitable for LAD and they demonstrate a single shot diffraction pattern taken with this gun. We want to find B_r, and to do this the data in [120] suggests using equation 7.11. Let's first find the current I according to [120] after filtering, a charge of 6 fC is available for diffraction, and that is contained in pulse of length $\tau = 500$ fs making $I = 12$ mA. Next we need to find the current in a coherent area so assuming $X_{pc} = 5$ nm and given their beam size of 560 µm × 890 µm which is a sort of half circle, let's make the area$(500\ \mu\mathrm{m})^2\pi/2$ then according to equation 7.11 $B_r = 2.4 \times 10^6$, this number seems pretty reasonable. What we find strange is the single shot diffraction with such a small $N = 3.75 \times 10^4$.

A.32 RF Streak Camera based relativistic UED

In [118] Musumeci discusses using a single pulse to gather information about a whole time series of information. The gun is an RF Flat cathode, in an accelerator beam line. It is best used for LAD experiments. With this gun it is not immediately clear how well our parameters will help to evaluate this style of gun. Nicely Musumeci summarises this gun in table one in [118] which we have reproduced here in table A.6. The gun is further described in [154] where we find at the end of the paper an $\epsilon_n = 0.7$ mm mrad and $B_n = \approx 10^{14}$ A/ $(\mathrm{m}^2\mathrm{sr})$, although we calculate from equation 7.3 that $B_n = 2 \times 10^{13}$ based on the table A.6 and the emittance reported in [154], from equation 7.5 we calculate $B_r = 1.25 \times 10^8$ A/ $(\mathrm{m}^2\mathrm{srV})$

Beam Energy	3.3 MeV
E	75 MV/m
Injection Phase	40°
Beam charge	20 pC
Laser Spot size (rms)	400 μm
UV laser pulse length (rms)	40 fs
total bunch length at target	2 ps

Table A.6: Pegasus photoinjector parameters for the rf streak camera based UED

B APPENDIX

MEMs Blanker -Additional Information

B.1 Blanker Electronics Simulation

For completeness we show some of the work done designing the electronics of the blanker. We simulated a resonant circuit made of 50 Ω transmission lines using a capacitor to model the blanker. This is shown in the screen print figure B.1. To the right of the image is a 50 Ω voltage source (+/ − 1 V) which supplies the open ended transmission line stub labeled TL1, this creates a resonance with the transmission line attached to the capacitor. The resonance can be tuned by adjusting the length of the transmission lines, this is shown as E=28.51 for the stretcher and E=77.19 the units are degrees. In parallel with the capacitor is a voltmeter made up of a ammeter and 10^{10} Ω resistor. The capacitor is grounded through a small resistor labeled R7 to mimic loses on the substrate.

Figure B.2 shows the (correctly scaled) output of the voltmeter in figure B.1. There is a strong peak near 20 GHz reaching a voltage of 1400 V. In reality we would not expect such a strong peak however the value of the resistor R7 is perhaps in reality a little too small. The simulation and result however is a proof of principle.

B.1.1 MEMs Blanker

In order to create the high aspect ratio we created the blanker from two pieces of silicon wafer glued together with insulating 1 μm spacers in between to create our one micron gap. Since the dimensions of the blanker where too small to be easily worked the two blanker plates where actually much bigger. The electrons travel first through a trench before meeting the blanker, as shown in figure B.3. The blanker plates are formed between the top chip (transparent blue) and the signal line on the bottom chip in red.

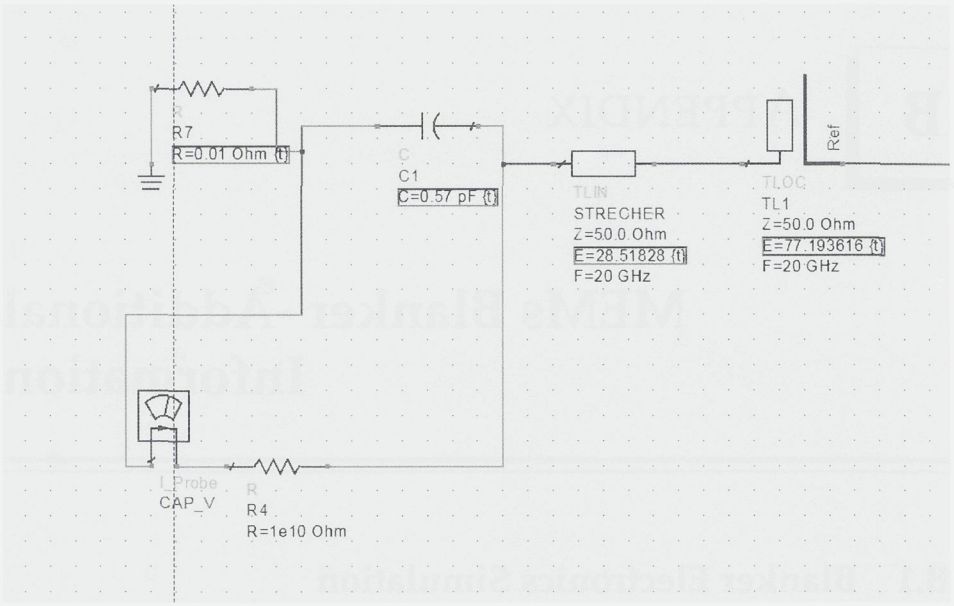

Figure B.1: Screen Print From ADS(An Electronics design suite from Agilent). The circuit is mock up of the resonator attached to the blanker which is represented by a capacitor, more information in the main text.

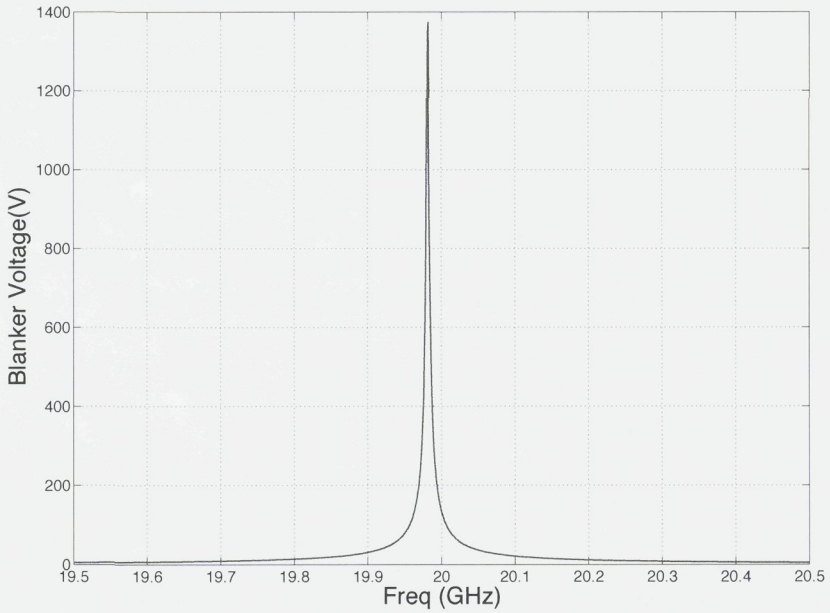

Figure B.2: The (scaled) output of the voltmeter in figure B.1

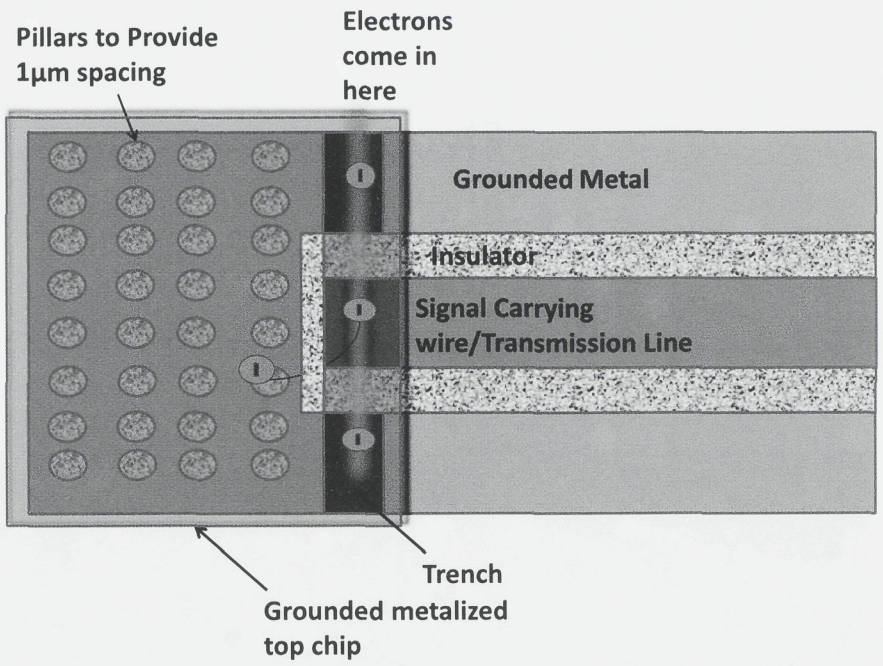

Figure B.3: Schematic of the MEMs designed blanker chip which consist of two patterned and metalized silicon chips placed one on top of the other. The blanker plates are the cross over of the top chip in transparent blue and the red transmission line

The realization of this is shown in figure B.4 where we can see the bottom chip of the blanker, and also figure

We also managed to fabricate and place one or two blankers into the SEM this is shown in figures B.6 and B.7. In figure B.6 we see the SEM and the blanker attached to a stick or holder which can be inserted into the labeled hole on the SEM. In figure B.7 we see the blanker in close up. The large hole visible on the right is to help with alignment, and the electron beam should actually pass through the two chips roughly at the right side of the upper most chip.

Unfortunately we had difficulties to align the chip, and so no images are available.

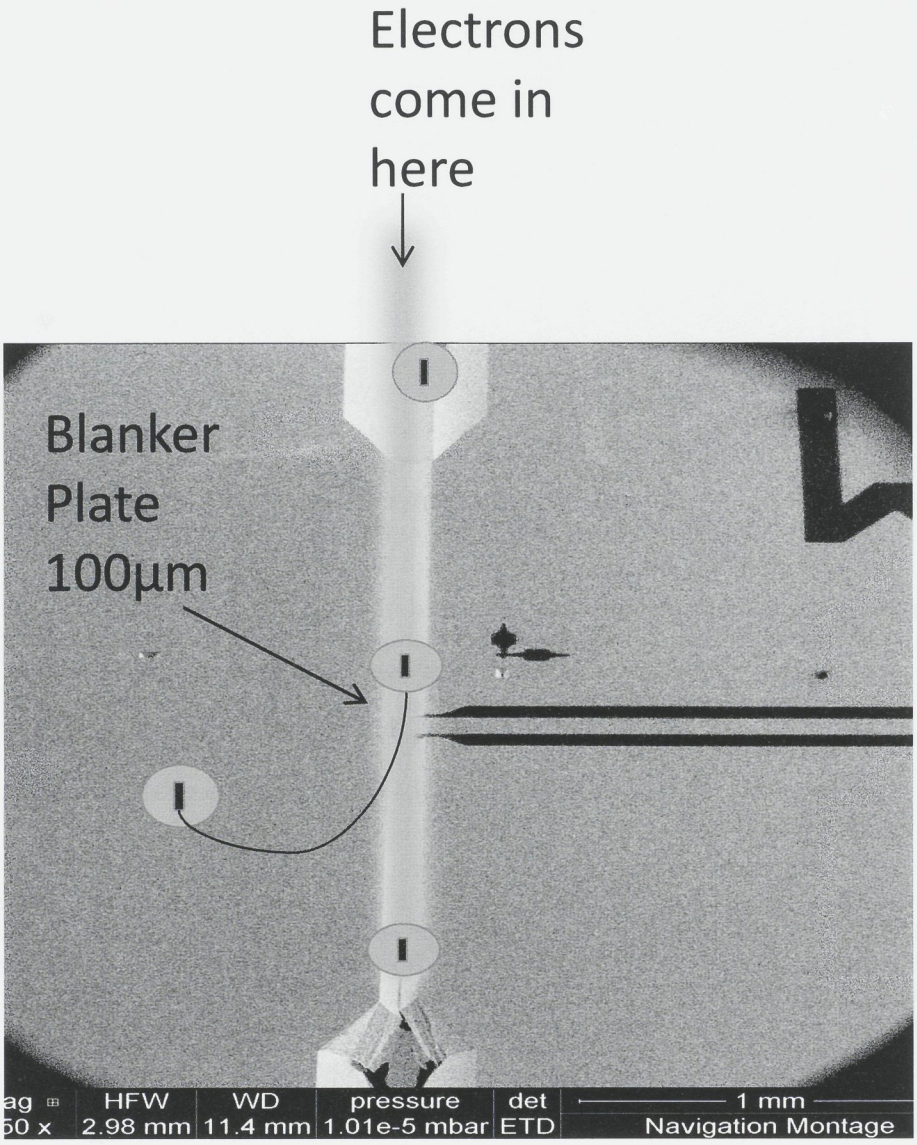

Figure B.4: SEM image of the bottom chip, shown in green is the electron path through the trench.

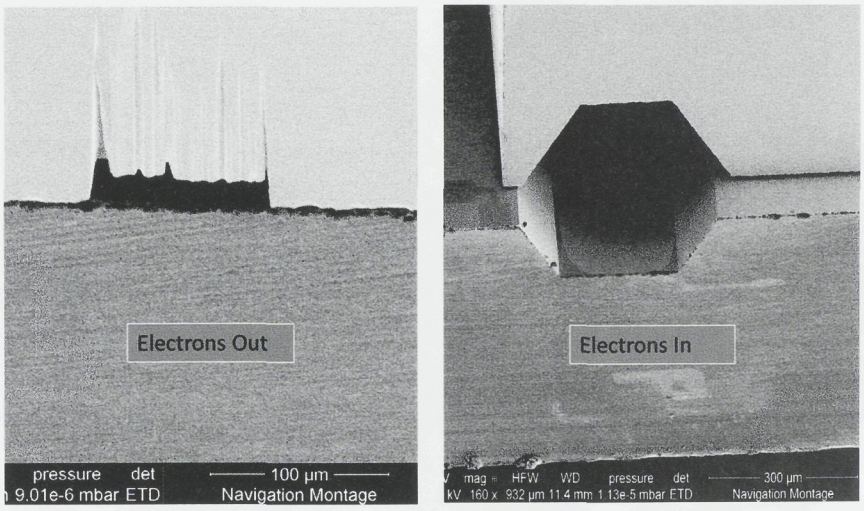

Figure B.5: On the left we see where the electrons should exit from the two chips this aperture forms the beam stop, on the right we see where the electrons enter the trench.

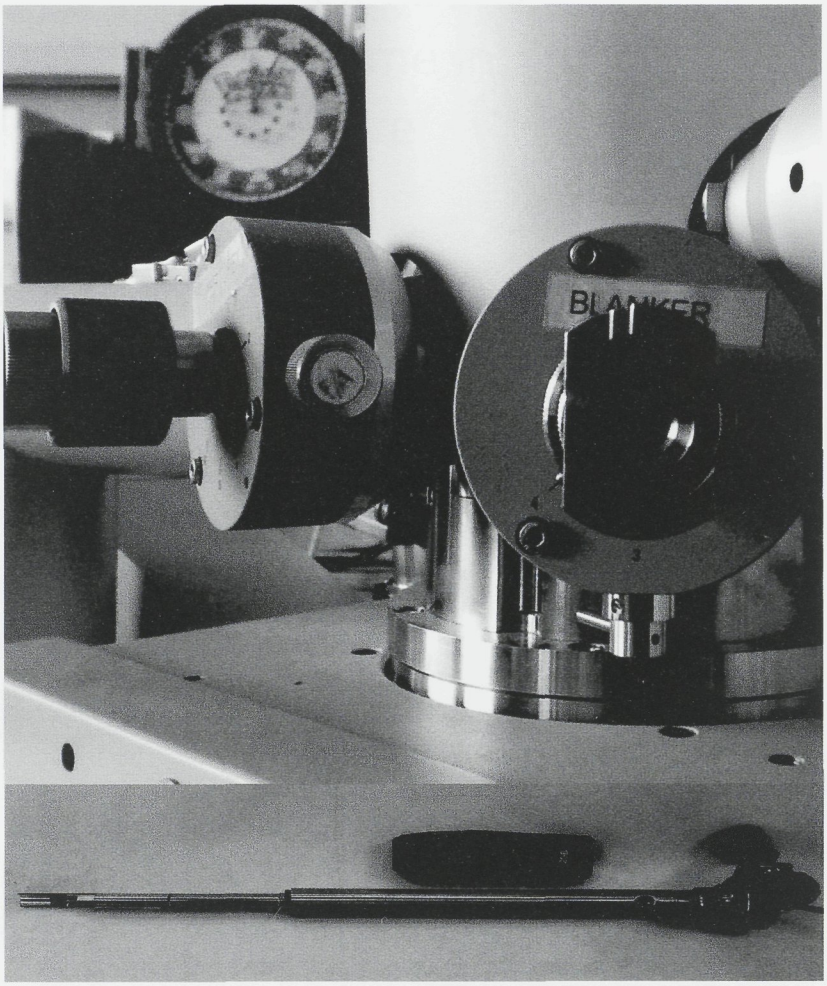

Figure B.6: In the lower picture we see the blanker mounted on a stick/holder which can be inserted into the SEM in the labeled hole shown in the above picture. For sizing there is also a standard USB pen included in the lower picture.

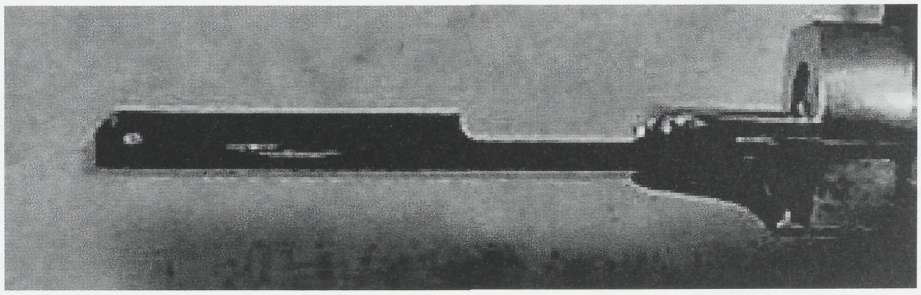

Figure B.7: The Blanker chip attached glued to electrical connector.

C APPENDIX

Appendix C: Curriculum Vitae

Ben Cook was born to parents Michael and Julie Cook, he grew up in a small village in Northamptonshire England where he attended the local village schools until the summer of his 18^{th} year when he received his A-levels in Mathematics, Physics and Computer Science.

He then made a one year internship at Willett Industrial Printers in the embedded software department, where he worked on testing, assisting with the programming of bespoke software and was in charge of the local languages project. He spent the next three years studying physics at Imperial College London, graduating with a BSc (Hons) in 2003. After this he decided to take a Gap year and teach physics in Sichuan China, unfortunately to teach the local children physics required that they first learnt English so he instead spent one year teaching English.

On returning to the UK he examined many different career possibilities and whilst doing so worked in the accounts department at DHL. Eventually he decided to return to Imperial College to get a Masters in Optics and Photonics. He had the good fortune to be able to do his thesis work at the Max Planck Inst. Göttingen Germany on super resolution STED (STimulated Emission Depletion) microscopy.

Early in the next year he discovered Delft and the charged particle optics group and spent the next five years there working on this thesis.

Ben now works at Applied Materials in Munich helping to design and build electron microscope columns specialized for the computer chip industry.

Bibliography

[1] J van Zuylen. The microscopes of antoni van leeuwenhoek. *J Microsc*, 121(3):309, Mar 1981.

[2] G.H Jansen. Coulomb interactions in particle beams. volume 21 of *Advances in Electronics and Electron Physics*. Academic Press, 1990.

[3] O. W. Richardson. Problems of physics. *Science*, 54(1396):283–291, 1921.

[4] Louis de Broglie. The reinterpretation of wave mechanics. *Foundations of Physics*, 1:5–15, 1970. 10.1007/BF00708650.

[5] R. H. Fowler and L. Nordheim. Electron emission in intense electric fields. *Proceedings of the Royal Society of London. Series A, Containing Papers of a Mathematical and Physical Character*, 119(781):173–181, 1928.

[6] Clinton Davisson. Nobel prize lecture the discovery of electron waves, 1937.

[7] R. H. Fowler. The analysis of photoelectric sensitivity curves for clean metals at various temperatures. *Phys. Rev.*, 38(1):45–56, Jul 1931.

[8] David B. Williams and C. Barry Carter. *Transmission Electron Microscopy-A Textbook for Materials Science*. Springer, 2009.

[9] Allan J. Melmed. Recollections of Erwin Mller's laboratory: the development of fim (19511956). *Applied Surface Science*, 9495(0):17 – 25, 1996. Proceedings of IFES 42.

[10] A. V. Crewe, J. Wall, and J. Langmore. Visibility of single atoms. *Science*, 168(3937):1338–1340, 1970.

[11] T. Hosokawa, H. Fujioka, and K. Ura. Gigahertz stroboscopy with the scanning electron microscope. *Review of Scientific Instruments*, 49(9):1293–1299, 1978.

[12] T. Hosokawa, H. Fujioka, and K. Ura. Generation and measurement of subpicosecond electron beam pulses. *Review of Scientific Instruments*, 49(5):624–628, 1978.

[13] O. Bostanjoglo and Th. Rosin. Ultrasonically induced magnetic reversals observed by stroboscopic electron microscopy. *Optica Acta: International Journal of Optics*, 24(6):657–664, 1977.

[14] R Melinda. A history of the laser: A trip through the light fantastic. *Photonics Spectra*, May 2010.

[15] W. E. King, G. H. Campbell, A. Frank, B. Reed, J. F. Schmerge, B. J. Siwick, B. C. Stuart, and P. M. Weber. Ultrafast electron microscopy in materials science, biology, and chemistry. *Journal of Applied Physics*, 97(11):111101, June 2005.

[16] J. Cao, Z. Hao, H. Park, C. Tao, D. Kau, and L. Blaszczyk. Femtosecond electron diffraction for direct measurement of ultrafast atomic motions. *Applied Physics Letters*, 83(5):1044–1046, 2003.

[17] B. J. Siwick, J. R. Dwyer, R. E. Jordan, and R. J. D. Miller. An Atomic-Level View of Melting Using Femtosecond Electron Diffraction. *Science*, 302:1382–1385, November 2003.

[18] Ramesh Srinivasan, Vladimir A. Lobastov, Chong-Yu Ruan, and Ahmed H. Zewail. Ultrafast electron diffraction (ued). a new development for the 4d determination of transient molecular structures. *ChemInform*, 34(40), 2003.

[19] A.H.V van Veen, C.W Hagen, J.E Barth, and P Kruit. Reduced brightness of the zro/w schottky electron emitter. *Journal of Vacuum Science & Technology B*, 19(6):2038–2044, NOV-DEC 2001.

[20] P Kruit, M Bezuijen, and J.E Barth. Source brightness and useful beam current of carbon nanotubes and other very small emitters. *Journal Of Applied Physics*, 99(2), Jan 15 2006.

[21] M. S. Bronsgeest, J. E. Barth, L. W. Swanson, and P. Kruit. Probe current, probe size, and the practical brightness for probe forming systems. *Journal of Vacuum scince & Technology B*, 26(3):949–955, May 2008.

[22] H. Shimoyama and S. Maruse. Theoretical considerations on electron optical brightness for thermionic, field and t-f emissions. *Ultramicroscopy*, 15(3):239–254, Feb 1984.

[23] Lee A. DuBridge. Theory of the energy distribution of photoelectrons. *Phys. Rev.*, 43(9):727–741, May 1933.

[24] K. L. Jensen. *Electron Emission Physics*, volume 149 of *Advances in Imaging and Electron Physics*. Academic Press, 2007.

[25] W Schottky. *Physik. Z.*, 15:872, 1914.

[26] E Kasper and P Hawkes. *Principles of Electron Optics*. Academic Press, 1996.

[27] R Gomer. *Field Emission and Field Ionization*. Harvard Univesity Press, 1961.

[28] J. H. Bechtel. Heating of solid targets with laser pulses. *Journal of Applied Physics*, 46(4):1585–1593, 1975.

[29] M. J. Fransen, J. S. Faber, Th. L. van Rooy1, P. C. Tiemeijer1, and P. Kruit. Experimental evaluation of the extended schottky model for zro/w electron emission. *Journal of Vacuum Science & Technology B: Microelectronics and Nanometer Struct*, 16:2063–2072, July 1998.

[30] K. L. Jensen, D. W. Feldman, and P. G. O'Shea. Advanced photocathode simulation and theory. *Nuclear Instruments & Methods in Physics Research Section a-Accelerators Spectrometers Detectors and Associated Equipment*, 507(1-2):238–241, 2003. 11 Elsevier Science BV.

[31] K. L. Jensen, N. A. Moody, D. W. Feldman, E. J. Montgomery, and P. G. O'Shea. Photoemission from metals and cesiated surfaces. *Journal of Applied Physics*, 102(7):19, 2007. Jensen, Kevin L. Moody, N. A. Feldman, D. W. Montgomery, E. J. O'Shea, P. G. 121 Amer. Inst. Physics.

[32] K. L. Jensen, D. W. Feldman, N. A. Moody, and P. G. O'Shea. Field-enhanced photoemission from metals and coated materials. *Journal of Vacuum Science & Technology B*, 24(2):863–868, 2006. 33 A V S Amer. Inst. Physics.

[33] MJG Lee. Field emission of hot electrons from tungsten,. *Physical Review Letters*, 30(24):1193–1196, June 1973.

[34] Alvin B. Cardwell. Photoelectric and thermionic properties of nickel. *Phys. Rev.*, 76(1):125–127, Jul 1949.

[35] J. H. Bechtel, W. Lee Smith, and N. Bloembergen. Two-photon photoemission from metals induced by picosecond laser pulses. *Phys. Rev. B*, 15(10):4557–4563, May 1977.

[36] Alvin B. Cardwell. The photoelectric properties of tantalum. *Phys. Rev.*, 38(11):2041–2048, Dec 1931.

[37] R Ganter et al. Laser-photofield emission from needle cathodes for low-emittance electron beams,. *Physical Review Letters*, 100:064801, Feb 2008.

[38] Neil W Ashcroft and N.David Mermin. *Solid State Physics*. Harcourt Inc, 1976.

[39] David R. Lide, editor. *CRC Handbook Of Chemistry and Physics*. CRC Press, 2007-2008.

[40] W.E. Spicer and A. Herrera-Gomez. Modern theory and applications of photocathodes. *online*, Aug 1993.

[41] M. S. Bronsgeest, J. E. Barth, P.Kruit, G.A. Schwind, and L.W. Swanson. Extracting the boersch effect contribution from experimental energy spread measurements for schottky electron emitters. *Jnl Vac. Sci. & Tech B*, 25(6):2049–2054, Nov 2007.

[42] von Ardenne. *Tabellen Der ElecktronenPhysik und Ubermikroskopie.* Deutscher Verlag Der Wissenschaften Berlin, 1956.

[43] C. Kittel. *Introduction to Solid State Physics.* Wiley, 8 edition, 2004.

[44] K. L. Jensen, D. W. Feldman, N. A. Moody, and P. G. O'Shea. A photoemission model for low work function coated metal surfaces and its experimental validation. *Journal of Applied Physics*, 99(12):19, 2006. 62 Amer. Inst. Physics.

[45] P. Hommelhoff, C. Kealhofer, and M. A. Kasevich. Ultrafast electron pulses from a tungsten tip triggered by low-power femtosecond laser pulses. *Physical Review Letters*, 97(24):4, 2006. Hommelhoff, Peter Kealhofer, Catherine Kasevich, Mark A. 26 AMERICAN PHYSICAL SOC.

[46] Ben Cook, Merijn Bronsgeest, Kees Hagen, and Pieter Kruit. Improving the energy spread and brightness of thermal-field (schottky) emitters with phast–photo assisted schottky tip. *Ultramicroscopy*, 109(5):403 – 412, 2009. IFES 2008, Proceedings of the 51th International Field Emission Symposium.

[47] X. Cao, M. Jahazi, J.P. Immarigeon, and W. Wallace. A review of laser welding techniques for magnesium alloys. *Journal of Materials Processing Technology*, 171(2):188 – 204, 2006.

[48] A. K. Dokania, J. F. M. Velthuis, Y. Zhang, and P. Kruit. Thermal model of miniaturized Schottky emitter for parallel electron beam lithography. *Journal of Vacuum Science Technology B: Microelectronics and Nanometer Structures*, 25:504, 2007.

[49] W. B. Nottingham. Remarks on energy losses attending thermionic emission of electrons from metals. *Phys. Rev.*, 59:906–907, Jun 1941.

[50] M.J.G Lee, R Reifenberger, E.S Robins, and H.G Lindenmayr. Thermally enhanced field emission from a laser illuminated tungsten tip - temperature rise of tip. *Journal of Applied Physics*, 51(9):4996–5006, 1980.

[51] M. J. G. Lee and E. S. Robins. Thermal relaxation of a laser illuminated field emitter. *Journal of Applied Physics*, 65(4):1699–1706, 1989.

[52] G.H. Jansen and P. Kruit. *Handbook of Charged Particle Optics -Chapter 7.* CRC Press, 1997.

[53] G.A. Schwind and L.W. Swanson. *Handbook of Charged Particle Optics - Chapter 1.* CRC Press, 1997.

[54] H. Shimoyama and S. Maruse. Theoretical considerations on electron optical brightness for thermionic, field and t-f emissions. *Ultramicroscopy*, 15(3):239–254, Feb 1984.

[55] C. A. Brau. High-brightness electron beams - small free-electron lasers. *Nuclear Instruments and Methods in Physics Research Section A: Accelerators, Spectrometers, Detectors and Associated Equipment*, 407(1-3):1 – 7, 1998.

[56] J.C.H Spence, T. Vecchione, U. Weierstall, and G. Hembree. A monochromatic laser-pulsed picosecond electron field-emitter. *Microscopy and Microanalysis*, 11(Supplement):480–481, 2005.

[57] M. J. Fransen, M. H. F. Overwijk, and P. Kruit. Brightness measurements of a zro/w schottky electron emitter in a transmission electron microscope. *Applied Surface Science*, 146(1-4):357 – 362, 1999.

[58] N de Jonge, Y Lamy, K Schoots, and TH Oosterkamp. High brightness electron beam from a multi-walled carbon nanotube. *Nature*, 420(6914):393–395, NOV 28 2002.

[59] W. Qian, M. R. Scheinfein, and J. C. H. Spence. Brightness measurements of nanometer-sized field-emission-electron sources. *Journal of Applied Physics*, 73:7041–7045, June 1993.

[60] X Jiang. *Coulomb Interactions in Charged Particle Optical Columns*. PhD thesis, Delft University of Technical, 1996.

[61] N. K. Kang, J. Orloff, L. W. Swanson, and D. Tuggle. An improved method for numerical analysis of point electron and ion source optics. *Journal of Vacuum Science and Technology*, 19(4):1077–1081, 1981.

[62] Jos Thijssen. *Computational Physics*. Cambridge University Press, 2007.

[63] *Statistical coulomb interactions in PHoto Assisted Schottky Emission- (PHASE)*, 2008.

[64] Merijn Bronsgeest. *The Physics of Schottky Emitters*. PhD thesis, Deflt Univeristy of Technology, 2009.

[65] B. Cook, T. Verduin, C. W. Hagen, and P. Kruit. Brightness limitations of cold field emitters caused by coulomb interactions. *Journal of Vacuum Science & Technology B: Microelectronics and Nanometer Structures*, 28(6), 2010.

[66] J. D. Jarvis, H. L. Andrews, B. Ivanov, C. L. Stewart, N. de Jonge, E. C. Heeres, W.-P. Kang, Y.-M. Wong, J. L. Davidson, and C. A. Brau. Resonant tunneling and extreme brightness from diamond field emitters and carbon nanotubes. *Journal of Applied Physics*, 108(9):094322, 2010.

[67] http://www.pulsar.nl/gpt Pulsar Physics.

[68] Josh Barnes and Piet Hut. A hierarchical o(n log n) force-calculation algorithm. *Nature*, 324:446, 1986.

[69] T. van Oudheusden, P L E M. Pasmans, S. B. van der Geer, M. J. de Loos, M. J. van der Wiel, and O. J. Luiten. Compression of subrelativistic space-charge-dominated electron bunches for single-shot femtosecond electron diffraction. *Phys Rev Lett*, 105(26):264801, Dec 2010.

[70] J. B. Hastings, F. M. Rudakov, D. H. Dowell, J. F. Schmerge, J. D. Cardoza, J. M. Castro, S. M. Gierman, H. Loos, and P. M. Weber. Ultrafast time-resolved electron diffraction with megavolt electron beams. *Applied Physics Letters*, 89(18):184109, 2006.

[71] Ding-Shyue Yang, Omar F. Mohammed, and Ahmed H. Zewail. Scanning ultrafast electron microscopy. *Proc Natl Acad Sci U S A*, 107(34):14993–14998, Aug 2010.

[72] Brian Spear. J.J. Thomson, the electron and the birth of electronics. *World Patent Information*, 28(4):330 – 335, 2006.

[73] Brett Barwick, Hyun Soon Park, Oh-Hoon Kwon, J Spencer Baskin, and Ahmed H. Zewail. 4d imaging of transient structures and morphologies in ultrafast electron microscopy. *Science*, 322(5905):1227–1231, Nov 2008.

[74] Aycan Yurtsever and Ahmed H. Zewail. 4d nanoscale diffraction observed by convergent-beam ultrafast electron microscopy. *Science*, 326(5953):708–712, 2009.

[75] R. J. Miller et. al. 'Making the molecular movie': first frames. *Acta Crystallographica Section A*, 66(2):137–156, Mar 2010.

[76] Ahmed H. Zewail. Four-dimensional electron microscopy. *Science*, 328(5975):187–193, Apr 2010.

[77] H.-Y. Hao and H. J. Maris. Study of phonon dispersion in silicon and germanium at long wavelengths using picosecond ultrasonics. *Phys. Rev. Lett.*, 84:5556–5559, Jun 2000.

[78] Peter Baum and Ahmed H. Zewail. Attosecond electron pulses for 4d diffraction and microscopy. *Proceedings of the National Academy of Sciences*, 104(47):18409–18414, 2007.

[79] H.N. Chapman et. al. Femtosecond X-ray protein nanocrystallography. *Nature*, 470:73–77, February 2011.

[80] Anton Barty et. al. Ultrafast single-shot diffraction imaging of nanoscale dynamics. *Nature Photonics*, 2:415–419, June 2008.

[81] Peter Baum, Ding-Shyue Yang, and Ahmed H. Zewail. 4d visualization of transitional structures in phase transformations by electron diffraction. *Science*, 318(5851):788–792, Nov 2007.

[82] Chong-Yu Ruan, Yoshie Murooka, Ramani K. Raman, and Ryan A. Murdick. Dynamics of size-selected gold nanoparticles studied by ultrafast electron nanocrystallography. *Nano Letters*, 7(5):1290–1296, 2007.

[83] Germain Sciaini et. al. Electronic acceleration of atomic motions and disordering in bismuth. *Nature*, 458(7234):56–59, Mar 2009.

[84] D. Alloyeau, B. Freitag, S. Dag, Lin W. Wang, and C. Kisielowski. Atomic-resolution three-dimensional imaging of germanium self-interstitials near a surface: Aberration-corrected transmission electron microscopy. *Phys. Rev. B*, 80:014114, Jul 2009.

[85] N.D. Browning, M.A. Bonds, G.H. Campbell, J.E. Evans, T. LaGrange, K.L. Jungjohann, D.J. Masiel, J. McKeown, S. Mehraeen, B.W. Reed, and M. Santala. Recent developments in dynamic transmission electron microscopy. *Current Opinion in Solid State and Materials Science*, 16(1):23 – 30, 2012. Advances in Electron Microscopy and its Application to Materials.

[86] D von der Linde, K Sokolowski-Tinten, and J Bialkowski. Lasersolid interaction in the femtosecond time regime. *Applied Surface Science*, 109110(0):1 – 10, 1997.

[87] C V Drysdale. "stroboscopy". *Transactions of the Optical Society*, 7(1):1, 1905.

[88] Omar F. Mohammed, Ding-Shyue Yang, Samir Kumar Pal, and Ahmed H. Zewail. 4d scanning ultrafast electron microscopy: visualization of materials surface dynamics. *J Am Chem Soc*, 133(20):7708–7711, May 2011.

[89] M. Ligges, I. Rajkovic, P. Zhou, O. Posth, C. Hassel, G. Dumpich, and D. von der Linde. Observation of ultrafast lattice heating using time resolved electron diffraction. *Applied Physics Letters*, 94(10):101910, 2009.

[90] T. LaGrange, M. R. Armstrong, K. Boyden, C. G. Brown, G. H. Campbell, J. D. Colvin, W. J. DeHope, A. M. Frank, D. J. Gibson, F. V. Hartemann, J. S. Kim, W. E. King, B. J. Pyke, B. W. Reed, M. D. Shirk, R. M. Shuttlesworth, B. C. Stuart, B. R. Torralva, and N. D. Browning. Single-shot dynamic transmission electron microscopy. *Applied Physics Letters*, 89(4):044105, 2006.

[91] John C.H. Spence. *High-Resolution Electron Microscopy*. Oxford University Press, 2009.

[92] A Rose. Television pickup tubes and the problem of vision. volume 1 of *Advances in Electronics and Electron Physics*, pages 131 – 166. Academic Press, 1948.

[93] Dong-Hua Chen, Joanita Jakana, Xiangan Liu, Michael F. Schmid, and Wah Chiu. Achievable resolution from images of biological specimens acquired from a 4k x 4k ccd camera in a 300-kv electron cryomicroscope. *Journal of Structural Biology*, 163(1):45 – 52, 2008.

[94] C. Kisielowski et Al. Detection of single atoms and buried defects in three dimensions by aberration-corrected electron microscope with 0.5- information limit. *Microscopy and Microanalysis,*, 14:469, 2008.

[95] B. J. Siwick, J. R. Dwyer, R. E. Jordan, and R. J. D. Miller. An Atomic-Level View of Melting Using Femtosecond Electron Diffraction. *Science*, 302:1382–1385, November 2003.

[96] T. van Oudheusden, E. F. de Jong, S. B. van der Geer, W. P. E. M. Op 't Root, O. J. Luiten, and B. J. Siwick. Electron source concept for single-shot sub-100 fs electron diffraction in the 100 kev range. *Journal of Applied Physics*, 102(9):093501, 2007.

[97] Ralph Ernstorfer, Maher Harb, Thibault Dartigalongue, Christoph T. Hebeisen, Robert E. Jordan, Lili Zhu, and R. J. Dwayne Miller. Femtosecond electron diffraction study on the heating and melting dynamics of gold. In Paul Corkum, David M. Jonas, R. J. Dwayne. Miller, Andrew M. Weiner, F.P. Schafer, J.P. Toennies, and W. Zinth, editors, *Ultrafast Phenomena XV*, volume 88 of *Springer Series in Chemical Physics*, pages 755–757. Springer Berlin Heidelberg, 2007.

[98] Y. Murooka, N. Naruse, S. Sakakihara, M. Ishimaru, J. Yang, and K. Tanimura. Transmission-electron diffraction by mev electron pulses. *Applied Physics Letters*, 98(25):251903, 2011.

[99] K. L. Jensen, D. W. Feldman, N. A. Moody, and P. G. O'Shea. A photoemission model for low work function coated metal surfaces and its experimental validation. *Journal of Applied Physics*, 99(12):124905, June 2006.

[100] C. D. Child. Discharge From Hot Cao. *Physical Review Series I*, 32:492–511, May 1911.

[101] I. Langmuir. The Effect of Space Charge and Initial Velocities on the Potential Distribution and Thermionic Current between Parallel Plane Electrodes. *Physical Review*, 21:419–435, April 1923.

[102] Á. Valfells, D. W. Feldman, M. Virgo, P. G. O'Shea, and Y. Y. Lau. Effects of pulse-length and emitter area on virtual cathode formation in electron guns. *Physics of Plasmas*, 9:2377–2382, May 2002.

[103] Andreas Gahlmann, Sang Tae Park, and Ahmed H. Zewail. Ultrashort electron pulses for diffraction, crystallography and microscopy: theoretical and experimental resolutions. *Physical Chemistry Chemical Physics*, 10:2894, 2008.

[104] Joel A. Berger, John T. Hogan, Michael J. Greco, W. Andreas Schroeder, Alan W. Nicholls, and Nigel D. Browning. Dc photoelectron gun parameters for ultrafast electron microscopy. *Microscopy and Microanalysis*, 15(04):298–313, 2009.

[105] K. Togawa, T. Shintake, T. Inagaki, K. Onoe, T. Tanaka, H. Baba, and H. Matsumoto. ceb_6 electron gun for low-emittance injector. *Phys. Rev. ST Accel. Beams*, 10:020703, Feb 2007.

[106] Peter Baum and Ahmed Zewail. Femtosecond diffraction with chirped electron pulses. *Chemical Physics Letters*, 462(1-3):14 – 17, 2008.

[107] F.B Kiewiet, A.H Kemper, O.J Luiten, G.J.H Brussaard, and M.J van der Wiel. Femtosecond synchronization of a 3ghz rf oscillator to a mode-locked ti:sapphire laser. *Nuclear Instruments and Methods in Physics Research Section*

A: Accelerators, Spectrometers, Detectors and Associated Equipment, 484(1-3):619 – 624, 2002.

[108] W. D. Kilpatrick. Criterion for vacuum sparking designed to include both rf and dc. *Review of Scientific Instruments*, 28(10):824–826, 1957.

[109] B. Cook, T. Verduin, C. W. Hagen, and P. Kruit. Brightness limitations of cold field emitters caused by coulomb interactions. *Journal of Vacuum Science & Technology B: Microelectronics and Nanometer Structures*, 28(6), 2010.

[110] O.J. Luiten A. Lassise, P.H.A. Mutsaers. High repetition ultrafast electron bunches, October 2010.

[111] R. Ganter, R. Bakker, C. Gough, S. C. Leemann, M. Paraliev, M. Pedrozzi, F. Le Pimpec, V. Schlott, L. Rivkin, and A. Wrulich. Laser-photofield emission from needle cathodes for low-emittance electron beams. *Phys. Rev. Lett.*, 100:064801, Feb 2008.

[112] C. Ropers, D. R. Solli, C. P. Schulz, C. Lienau, and T. Elsaesser. Localized multiphoton emission of femtosecond electron pulses from metal nanotips. *Phys Rev Lett*, 98(4):043907, Jan 2007.

[113] B Barwick, C Corder, J Strohaber, N Chandler-Smith, C Uiterwaal, and H Batelaan. Laser-induced ultrafast electron emission from a field emission tip. *New Journal of Physics*, 9(5):142, 2007.

[114] P. Hommelhoff, Y. Sortais, A. Aghajani-Talesh, and M. A. Kasevich. Field emission tip as a nanometer source of free electron femtosecond pulses. *Physical Review Letters*, 96(7):4, 2006. 30 Amer. Phys. Soc.

[115] T. Verduin, B. Cook, and P. Kruit. Influence of gun design on Coulomb interactions in a field emission gun. *Journal of Vacuum Science Technology B: Microelectronics and Nanometer Structures*, 29(6):060000, 2011.

[116] S.B. van der Geer, M.J. de Loos, E.J.D. Vredenbregt, and O.J. Luiten. Ultracold electron source for single-shot, ultrafast electron diffraction. *Microscopy and Microanalysis*, 15(04):282–289, 2009.

[117] G. Taban. *A Cold Atom Electron Source*. PhD thesis, Eindhoven University of Technology, 2009.

[118] P. Musumeci, J. T. Moody, C. M. Scoby, M. S. Gutierrez, and T. Tran. Rf streak camera based ultrafast relativistic electron diffraction. *Review of Scientific Instruments*, 80(1):013302, 2009.

[119] W. L. Kruer and K. Estabrook. J $\times$ B heating by very intense laser light. *Physics of Fluids*, 28:430–432, January 1985.

[120] Shigeki Tokita, Masaki Hashida, Shunsuke Inoue, Toshihiko Nishoji, Kazuto Otani, and Shuji Sakabe. Single-shot femtosecond electron diffraction with laser-accelerated electrons: Experimental demonstration of electron pulse compression. *Phys. Rev. Lett.*, 105:215004, Nov 2010.

[121] K. Ura, H. Fujioka, and T. Hosokawa. Stroboscopic scanning electron microscope to observe two-dimensional and dynamic potential distribution of semiconductor devices. In *Proc. Int. Electron Devices Meeting*, volume 23, pages 502–505, 1977.

[122] Vladimir A. Lobastov, Ramesh Srinivasan, and Ahmed H. Zewail. Four-dimensional ultrafast electron microscopy. *Proceedings of the National Academy of Sciences of the United States of America*, 102(20):7069–7073, 2005.

[123] H. Sadorf and H.A Katz. Plug-in fast electron beam chopping system. *Review of Scientific Instruments*, 56(4):567, December 1984.

[124] M. Gesley, D. Colby, F. Raymond, D. McClure, and F. Abboud. Electrodynamics of fast beam blankers. *Journal of Vacuum Science & Technology B: Microelectronics and Nanometer Structures*, 11(6):2378–2385, 1993.

[125] J. T. L. Thong. Picosecond electron pulse generation via beam deflection-chopping in the SEM. *Measurement Science and Technology*, 2:207–216, March 1991.

[126] M S Hill and A Gopinath. Probing gunn domains at x-band microwave frequencies using a scanning microscope. *Journal of Physics D: Applied Physics*, 7(1):69, 1974.

[127] A. Lassise, P. H. A. Mutsaers, and O. J. Luiten. Compact, low power radio frequency cavity for femtosecond electron microscopy. *AIP*, Marchs 2012.

[128] G Hammer, S Wuensch, K Ilin, and M Siegel. Ultra high quality factor resonators for kinetic inductance detectors. *Journal of Physics: Conference Series*, 97(1):012044, 2008.

[129] Pulsar Physics. Gpt.

[130] R. Ganter, R. J. Bakker, R. Betemps, M. Dehler, T. Gerber, J. Gobrecht, C. Gough, M. Johnson, E. Kirk, G. Knopp, F. Le Pimpec, K. Li, M. Paraliev, M. Pedrozzi, L. Rivkin, H. Sehr, L. Schulz, and A. Wrulich. Nanoseconds field emitted current pulses from zrc needles and field emitter arrays. *Journal of Vacuum Science & Technology B: Microelectronics and Nanometer Structures*, 24(2):974–978, 2006.

[131] Lee M. J. G. Donders P. J. Coulomb scattering in field and photofield emission. *phys rev. B*, 35:6578–6587, May 1987.

[132] J. Qiang, J. Corlett, S. Lidia, H. A. Padmore, W. Wan, A. Zholents, M. Zolotorev, and A. Adelmann. Numerical study of coulomb scattering effects on electron beam from a nano-tip. In *Proc. PAC Particle Accelerator Conf. IEEE*, pages 1185–1187, 2007.

[133] B. J. Siwick, J. R. Dwyer, R. E. Jordan, and R. J. D. Miller. Ultrafast electron optics: Propagation dynamics of femtosecond electron packets. *Journal of Applied Physics*, 92:1643–1648, August 2002.

[134] A. Zewail and Vladimir A. Lobastov. Method and system for ultrafast photoelectron microscope, 2008.

[135] Andreas Gahlmann, Sang Tae Park, and Ahmed H. Zewail. Structure of isolated biomolecules by electron diffraction-laser desorption: Uracil and guanine. *Journal of the American Chemical Society*, 131(8):2806–2808, 2009. PMID: 19055399.

[136] Ralph ernstorfer & Thibault Dartigalongue & R. J. Dwayne Miller Jason R. Dwyer & Robert E. Jordan & Christoph T. Hebeisen & Maher Harb. Experimental basic for femtosecond electron diffraction studies. *Journal of Modern Optics*, 54(7):923–942, 2007.

[137] Xuan Wang, Shouhua Nie, Hyuk Park, Junjie Li, Rick Clinite, Renkai Li, Xijie Wang, and Jianming Cao. Measurement of femtosecond electron pulse length and the temporal broadening due to space charge. *Review of Scientific Instruments*, 80(1):013902, 2009.

[138] Liang Wen-Xi, Zhu Peng-Fei, Wang Xuan, Nie Shou-Hua, Zhang Zhong-Chao, Clinite Rick, Cao Jian-Ming, Sheng Zheng-Ming, and Zhang Jie. Ultrafast electron diffraction with spatiotemporal resolution of atomic motion. *Chinese Physics Letters*, 26(2):020701, 2009.

[139] A. Janzen, B. Krenzer, O. Heinz, P. Zhou, D. Thien, A. Hanisch, F.-J. Meyer Zu Heringdorf, D. von der Linde, and M. Horn von Hoegen. A pulsed electron gun for ultrafast electron diffraction at surfaces. *Review of Scientific Instruments*, 78(1):013906, January 2007.

[140] WA Schroeder. Optimization of ultrafast photo-electron sources for dtem. *Microscopy and Microanalysis*, 14(Supplement S2):32–33, 2008.

[141] Peter Pasmans, Thijs van Oudheusden, Marieke de Loos, Bas van der Geer, Arjan Klessens, and Jom Luiten. Single-shot, femtosecond electron diffraction. In *International Conference on Ultrafast Phenomena*, page MA4. Optical Society of America, 2010.

[142] Ernst Fill, Laszlo Veisz, Alexander Apolonski, and Ferenc Krausz. Sub-fs electron pulses for ultrafast electron diffraction. *New Journal of Physics*, 8(11):272, 2006.

[143] D. Wytrykus, M. Centurion, P. Reckenthaeler, F. Krausz, A. Apolonski, and E. Fill. Ultrashort pulse electron gun with a mhz repetition rate. *Applied Physics B: Lasers and Optics*, January:X, 2009.

[144] G. H. Kassier, K. Haupt, N. Erasmus, E. G. Rohwer, and H. Schwoerer. Achromatic reflectron compressor design for bright pulses in femtosecond electron diffraction. *Journal of Applied Physics*, 105(11):113111, 2009.

[145] Sakhorn Rimjaem, Ruy Farias, Chitrlada Thongbai, Thiraphat Vilaithong, and Helmut Wiedemann. Femtosecond electron bunches from an rf-gun. *Nuclear Instruments and Methods in Physics Research Section A: Accelerators, Spectrometers, Detectors and Associated Equipment*, 533(3):258 – 269, 2004.

[146] R. Akre, D. Dowell, P. Emma, J. Frisch, S. Gilevich, G. Hays, Ph. Hering, R. Iverson, C. Limborg-Deprey, H. Loos, A. Miahnahri, J. Schmerge, J. Turner, J. Welch, W. White, and J. Wu. Commissioning the linac coherent light source injector. *Phys. Rev. ST Accel. Beams*, 11:030703, Mar 2008.

[147] Jinfeng Yang, Koichi Kan, Nobuyasu Naruse, Yoichi Yoshida, Katsumi Tanimura, and Junji Urakawa. 100-femtosecond mev electron source for ultrafast electron diffraction. *Radiation Physics and Chemistry*, 78(12):1106 – 1111, 2009. APSRC-2008, The Second Asia-Pacific Symposium on Radiation Chemistry, August 29 September 1, 2008.

[148] P. Musumeci, L. Faillace, A. Fukasawa, J.T. Moody, B. O'Shea, J.B. Rosenzweig, and C.M. Scoby. Novel radio-frequency gun structures for ultrafast relativistic electron diffraction. *Microscopy and Microanalysis*, 15(04):290–297, 2009.

[149] D. Venus and M.J.G. Lee. Polarization dependence of photoexcitation in photofield emission. *Surface Science*, 125(2):452 – 472, 1983.

[150] M. Fransen. Field emission energy distributions from individual multiwalled carbon nanotubes. *Applied Surface Science*, 146:312–327, May 1999.

[151] G. Taban, M. P. Reijnders, B. Fleskens, S. B. van der Geer, O. J. Luiten, and E. J. D. Vredenbregt. Ultracold electron source for single-shot diffraction studies. *EPL (Europhysics Letters)*, 91(4):46004, 2010.

[152] B. J. Claessens, M. P. Reijnders, G. Taban, O. J. Luiten, and E. J. D. Vredenbregt. Cold electron and ion beams generated from trapped atoms. *Physics of Plasmas*, 14(9):093101, 2007.

[153] S. B. van der Geer, M. P. Reijnders, M. J. de Loos, E. J. D. Vredenbregt, P. H. A. Mutsaers, and O. J. Luiten. Simulated performance of an ultracold ion source. *Journal of Applied Physics*, 102(9):094312, 2007.

[154] P. Musumeci, J. T. Moody, R. J. England, J. B. Rosenzweig, and T. Tran. Experimental generation and characterization of uniformly filled ellipsoidal electron-beam distributions. *Phys. Rev. Lett.*, 100:244801, Jun 2008.

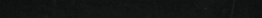
TU Delft
Technische Universiteit Delft


FEI™ Explore. Discover. Resolve.


FOM